MEASUREMENT OF THE NEUTRON (^{3}He) SPIN STRUCTURE FUNCTIONS AT LOW Q^2: A CONNECTION BETWEEN THE BJORKEN AND GERASIMOV-DRELL-HEARN SUM RULE

A Dissertation
Presented to
The Faculty of the Department of Physics
The College of William and Mary in Virginia

In Partial Fulfillment
Of the Requirements for the Degree of
Doctor of Philosophy

by
Pibero Djawotho
2002

APPROVAL SHEET

This dissertation is submitted in partial fulfillment of
the requirement for the degree of

Doctor of Philosophy

Pibero Djawotho

Approved, December 2002

John Michael Finn

Todd D. Averett

David S. Armstrong

Keith A. Griffioen

John Dirk Walecka

Jian-Ping Chen
Thomas Jefferson National Accelerator Facility

To Mom and Dad,
Mundara, Afoyo, Djamundu, and Utembi

TABLE OF CONTENTS

ACKNOWLEDGMENTS

This dissertation would not have been possible without the enormous assistance and guidance of my advisor, Prof. J.M. Finn. This document is a testament to his wisdom and patience. I would also like to acknowledge the Jefferson Laboratory E94-010 Collaboration for providing a nurturing environment in which I was able to grow as a physicist. I especially enjoyed working with the graduate students, Karl, Alexander, Stephen, and Ioannis. To my parents, I am eternally grateful for emphasizing at an early stage the importance of education and providing me relentless support throughout the years. Much love to my little sister and brothers for reminding me how blessed I am.

Life would not be bearable without the warmth and support of friends. In particular, I have enjoyed the friendships of Fefo and Paolo during my stay in Williamsburg. I thank them for the experience and hope that the camaraderie only grows stronger with time. Many thanks to Vittorio and Elio from Sal's for providing me with a place "where everybody knows your name". I would also like to thank Gary, Lucho, and Tatiana from my undergraduate days for remaining good friends throughout the years. Thanks also to Jojo, Carlos, Fanculo, Hovanes, and Claudio.

Last but not least, I would like to acknowledge the invaluable help of the administrative staff, Sylvia, Paula, and Dianne, in navigating effortlessly through the College of William and Mary's bureaucracy. It is an understatement to assert that I will never truly know how much I benefited from their assistance. Finally, thanks to countless other people who are just too numerous to name and have contributed in one way or another in making this achievement a reality.

LIST OF TABLES

LIST OF FIGURES

ABSTRACT

This dissertation presents results of experiment E94-010 performed at Jefferson Laboratory (simply known as JLab) in Hall A.

The experiment aimed to measure the low Q^2 evolution of the Gerasimov-Drell-Hearn (GDH) integral from $Q^2 = 0.1$ to 0.9 GeV^2. The GDH sum rule at the real photon point provides an important test of Quantum Chromodynamics (QCD). The low Q^2 evolution of the GDH integral contests various resonance models, Chiral Perturbation Theory (χPT) and lattice QCD calculations, but more importantly, it helps us understand the transition between partonic and hadronic degrees of freedom. At high Q^2, beyond 1 GeV^2, the difference of the GDH integrals for the proton and the neutron is related to the Bjorken sum rule, another fundamental test of QCD. In addition, results of the measurements for the spin structure functions g_1 and g_2, cross sections, and asymmetries are presented.

E94-010 was the first experiment of its kind at JLab. It used a high-pressure, polarized ^{3}He target with a gas pressure of 10 atm and average target polarization of 35%. For the first time, the polarized electron source delivered an average beam polarization of 70% with a beam current of 15 μA. The limit on the beam current was only imposed by the target. The experiment required six different beam energies from 0.86 to 5.1 GeV. This was the first time the accelerator ever reached 5.1 GeV. Both High-Resolution Spectrometers of Hall A, used in singles mode, were positioned at 15.5° each.

MEASUREMENT OF THE NEUTRON (^{3}He) SPIN STRUCTURE FUNCTIONS AT LOW Q^2: A CONNECTION BETWEEN THE BJORKEN AND GERASIMOV-DRELL-HEARN SUM RULE

Chapter 1

PHYSICS MOTIVATION

1.1 Introduction

Jefferson Laboratory experiment E94-010 [1], also known as the GDH experiment, with co-spokepersons Z.-E. Meziani, G. Cates, and J.-P. Chen (for a complete list of collaborators and institutions represented, see the addendum) was an experiment with many firsts: It was the commissioning experiment for the newly formed polarized ^{3}He collaboration at the Thomas Jefferson National Accelerator Facility (Jefferson Laboratory), in Newport News, Virginia. It was the first experiment to run at this laboratory requiring both polarized beam and a polarized target from September 25 to December 24, 1998. The purpose of this experiment was to explore the connection between two powerful sum rules of hadronic physics, a Gerasimov-Drell-Hearn (GDH) sum rule $I(0)$ applicable to the real photon limit corresponding to a vanishing four-momentum transfer squared ($Q^2 = 0$) and a virtual photon Bjorken sum rule valid at high Q^2. It was the successor of the high energy work at SLAC, involving many of the same people, which studied both neutron and proton scattering at high Q^2 to test the fundamental Bjorken sum rule. The present experiment proposed to test the Q^2 evolution of a generalized GDH sum rule $I(Q^2)$ to see if the gap between the low energy and high energy theorems could be bridged. In ^{3}He, the two protons couple to zero spin as a first approximation. Therefore, polarized ^{3}He is a good approximation to a free neutron target; see Fig. 1.1. As compared to the other choice of using polarized deuterium as a source for polarized neutrons, ^{3}He targets are easier to make and require a weak holding field compared to current deuterated ammonia

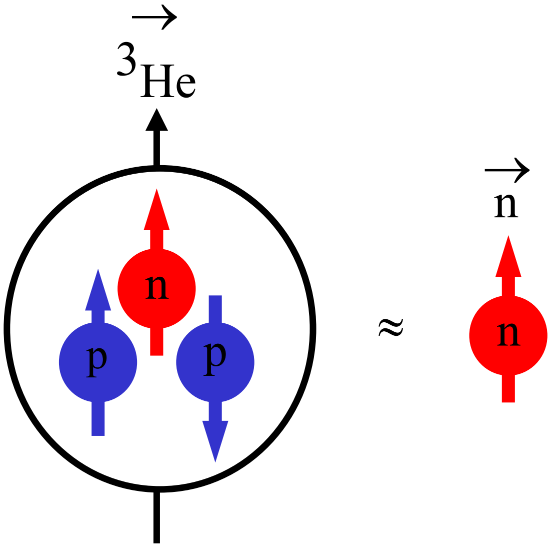

Figure 1.1: The ^{3}He nucleus is composed of two protons with opposite spins most of the time and one neutron whose spin dictates the overall spin of the nucleus. Thus, to a fair approximation, a polarized ^{3}He nucleus behaves much like a polarized neutron.

targets, which must be brute force polarized by using superconducting magfnets at high fields which can have the effect of distorting incident and outgoing electron momenta. Furthermore, the targets can be made in relatively pure form, avoiding the severe dilution effects of ND_3 ammonia cells. However, the nuclear corrections are more pronounced in ^{3}He and require sophisticated corrections to the data.

Three essential pieces of apparatus were needed to carry out this effort: first the high intensity polarized electron source of the Continuous Electron Beam Accelerator Facility (CEBAF) at Jefferson Laboratory was used to provide electrons of the desired energies (1-5 GeV) with the needed high currents. Secondly, a polarized target of sufficient density and polarization had to be developed by this collaboration. Finally, the Hall A High Resolution Spectrometers were employed to detect the data. In order to acquire data over an extended region of Q^2 and energy transfer $\nu = E - E'$, the run plan called for measurements of data at multiple beam energies and spectrometer settings, as shown in the kinematics diagram of Fig. 1.2. Data were acquired at six incident beam energies of 0.86, 1.7, 2.6, 3.4, 4.2, and 5.1 GeV, and interpolations were made to extract results at six constant Q^2 values ranging from 0.1 to 0.9 GeV^2. The average target polarization was 35%, while the average beam polarization was 70%.

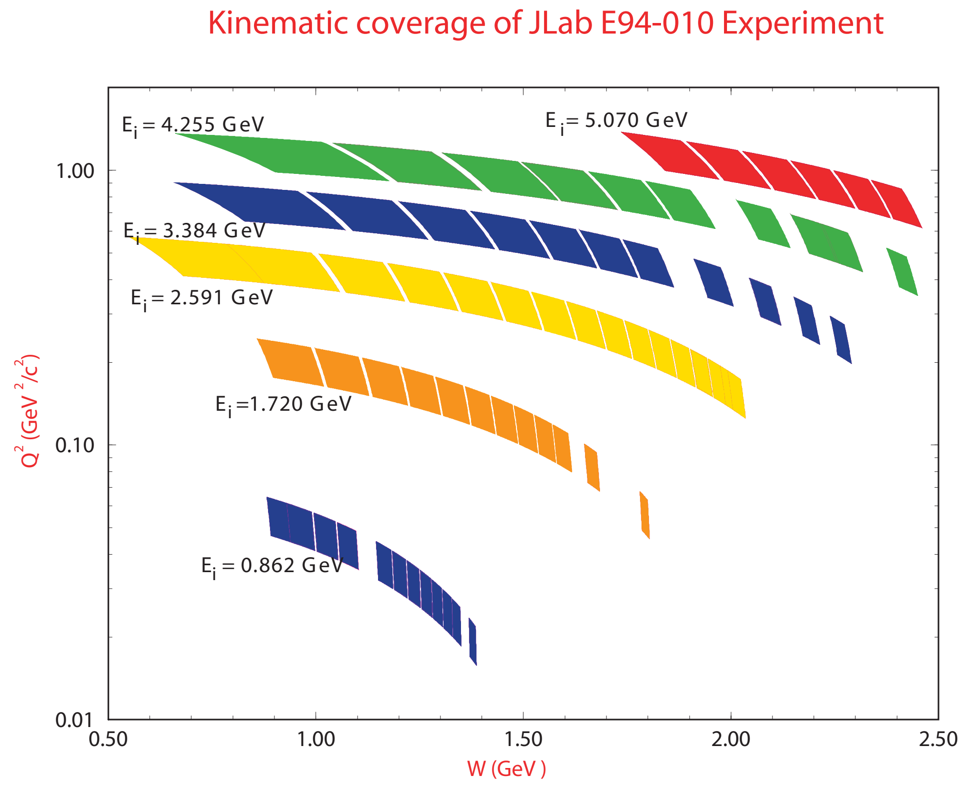

Figure 1.2: Kinematic coverage of Jefferson Laboratory experiment E94-010. Plotted in the figure are the Q^2, W range of our experiment with each bin indicating different setting of E, E'. The different colored bands represent the six different beam energies. The nominal scattering angle was fixed throughout the experiment at 15.5°. Each block represents one E, E' spectrometer setting.

Because any discussion of sum rules is deeply theoretical in nature and requires a basic understanding of quantum electrodynamics, the remainder of this chapter will be spent on the development of the mathematical formalism and a review of the essential physical concepts. The second chapter will then present a detailed description of the physical apparatus. The third chapter will present the analysis of the data, which forms the core subject matter of this Ph.D. dissertation, while the final chapter presents a discussion of the experimental results and their significance.

The success of this experiment has opened the door to a large, active experimental program of polarized ^{3}He studies at Jefferson Laboratory. The present and future directions of this program will be briefly reviewed as part of the concluding remarks.

1.2 Kinematics

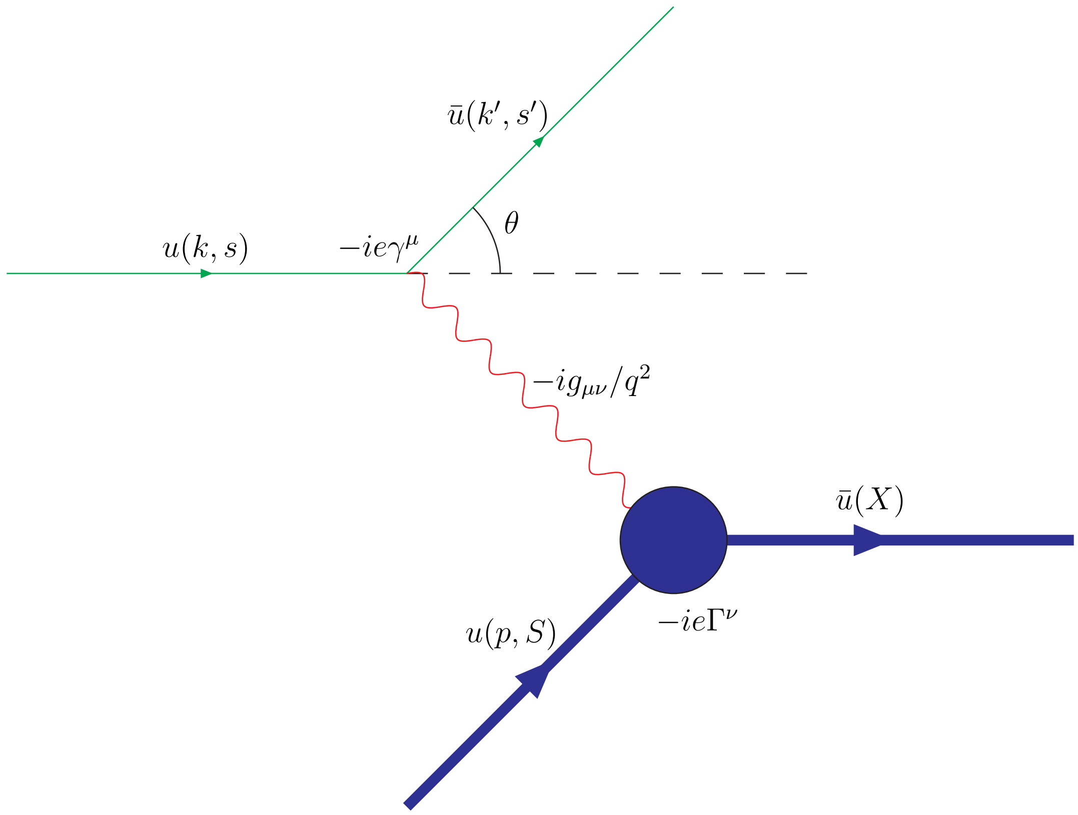

Figure 1.3: Kinematics for inelastic electron-nucleon scattering in the one-photon exchange approximation. Here the four-momentum transfer is carried by the virtual photon and is absorbed on a nucleon of mass M leading to an excited system of invariant mass W which is in the continuum.

Fig. 1.3 shows a typical Feynman diagram for inclusive inelastic electron-nucleon scattering. The incident electron has four-momentum $k = (E, \mathbf{k})$ and spin four-vector s. The scattered electron has four-momentum $k' = (E', \mathbf{k}')$ and spin four-vector s'.

The scattering angle θ is with respect to the incident momentum direction. The exchanged virtual photon has four-momentum $q = (\nu, \mathbf{q})$. The energy transfer or energy loss is ν. The preferred Lorentz frame is the lab frame where the target nucleon is at rest before the collision and has four-momentum $p = (M, \mathbf{0})$ and spin four-vector S satisfying $S^2 = -1$ and $S \cdot p = 0$. M is the target nucleon rest mass. The recoiling hadronic system X has four-momentum W known as the invariant mass. Energy-momentum conservation at the leptonic vertex requires $q = k - k'$, that is,

$$q^2 = (k - k')^2 = k^2 + k'^2 - 2k \cdot k' = m^2 + m^2 - 2EE' + 2|\mathbf{k}||\mathbf{k}'|\cos\theta, \tag{1.1}$$

where $m = 0.511$ MeV is the mass of the electron. The lowest beam energy for E94-010 was 862 MeV which is much larger than the rest mass of the electron. Therefore the mass terms can be safely dropped from Eq. (1.1). Einstein's energy-momentum relation $E^2 = |\mathbf{k}|^2 + m^2$ may also forgo the mass term at high energies and becomes $E = |\mathbf{k}|$. The net result is a simpler expression for Eq. (1.1):

$$q^2 = -2EE' + 2EE'\cos\theta = -2EE'(1 - \cos\theta) = -4EE'\sin^2\frac{\theta}{2}, \tag{1.2}$$

It is customary to introduce a new Lorentz invariant Q^2 to do away with the minus sign in Eq. (1.2):

$$Q^2 = -q^2 = 4EE'\sin^2\frac{\theta}{2}. \tag{1.3}$$

Energy-momentum conservation at the hadronic vertex gives:

$$W^2 = (p + q)^2 = p^2 + q^2 + 2p \cdot q = M^2 - Q^2 + 2M\nu. \tag{1.4}$$

1.3 Cross Section

The differential cross section for the scattering process $A + B \to 1 + 2 + \cdots + n$ is [2]

$$d\sigma = \frac{1}{F}|\mathcal{M}(A + B \to \{p_i\})|^2 d\Pi_n \tag{1.5}$$

where $F = |\mathbf{v}_A - \mathbf{v}_B| 2E_A \cdot 2E_B = 4\left[(p_A \cdot p_B) - m_A^2 m_B^2\right]^{\frac{1}{2}}$ is the incident flux for a general collinear collision between A and B,

$$d\Pi_n = (2\pi)^4 \delta^4(p_A + p_B - \sum_{i=1}^{n} p_i) \prod_{i=1}^{n} \frac{d^3 p_i}{(2\pi)^3 2E_i} \tag{1.6}$$

is the relativistically invariant n-body phase space or Lorentz invariant phase space, and $\mathcal{M}(p_A + p_B \to \{p_i\})$ is the invariant amplitude. The amplitude $\mathcal{M}$ isolates the dynamics of the particular scattering process under study from the kinematics in the cross section. $\mathbf{v}_A$ and $\mathbf{v}_B$ are the velocities of the initial states in the laboratory frame.

1.4 Leptonic and Hadronic Tensors

The Feynman rules of quantum electrodynamics (QED) for Dirac particles summarized in [2] give, for the differential cross section of the inelastic electron-nucleon scattering process of Fig. 1.3

$$\begin{aligned} d\sigma &= \frac{1}{(2E)(2M)} \sum_{spins} \sum_{X} \left| \bar{u}(k', s')(-ie\gamma^\mu) u(k, s) \left(\frac{-ig_{\mu\nu}}{q^2} \right) \bar{u}(X)(-ie\Gamma^\nu) u(p, S) \right|^2 \\ &\times \frac{d^3k'}{(2\pi)^3 2E'} \prod_{i=1}^{N} \frac{d^3p'_i}{(2\pi)^3 2E'_i} (2\pi)^4 \delta^4(p + q - \sum_{i=1}^{N} p'_i), \end{aligned} \tag{1.7}$$

where the sum $\sum_X$ includes all possible many-particle states X. u and $\bar{u}$ are Dirac spinors and the structure of the hadron vertex is encapsulated in Γ^ν. The phase space factor for the scattered electron is

$$\frac{d^3k'}{(2\pi)^3 2E'} = \frac{E'^2 dE' d\Omega}{(2\pi)^3 2E'} = \frac{E' dE' d\Omega}{2(2\pi)^3}. \tag{1.8}$$

Futhermore, the invariant amplitude can be separated into the leptonic tensor $L^{\mu\nu}$ and the hadronic tensor $W^{\mu\nu}$ [3] where

$$L^{\mu\nu} = \sum_{s,s'} \left| \bar{u}(k', s') \gamma^\mu u(k, s) \right|^2, \tag{1.9}$$

$$\begin{aligned} W^{\mu\nu} &= \frac{1}{4\pi M} \sum_{spins} \sum_{N} \left| \bar{u}(X) \Gamma^\mu u(p, S) \right|^2 \int \prod_{i=1}^{N} \frac{d^3p'_i}{(2\pi)^3 2E'_i} \\ &\times (2\pi)^4 \delta^4(p + q - \sum_{i=1}^{N} p'_i). \end{aligned} \tag{1.10}$$

Finally, the differential cross section can be written as

$$\frac{d^2\sigma}{d\Omega dE'} = \frac{\alpha^2}{Q^4} \frac{E'}{E} L^{\mu\nu} W_{\mu\nu}, \tag{1.11}$$

where the definition of the fine-structure constant $\alpha = e^2/4\pi$ was used.

1.4.1 Leptonic Tensor $L^{\mu\nu}$

The leptonic tensor can be completely calculated in QED since the electron is a Dirac point particle. In polarized experiments, the incident electron is ususally polarized along the beam direction (Transverse polarizatin states are smaller by a factor of $1/\gamma$ relative to the longitudinal part). Let $\downarrow$ denote the helicity of a left-handed electron and $\uparrow$ denote the helicity of a right-handed electron. The corresponding projection operators $P_L = (1-\gamma^5)/2$ and $P_R = (1+\gamma^5)/2$ must be applied to the spinor $u(k,s)$ to obtain the respective helicity states. The leptonic tensor is then summed over all final spin states since the detectors are typically insensitive to polarization. Eq. (1.9), with the aid of trace technology, is transformed into [2]

$$\begin{aligned} L^{\mu\nu}(\downarrow) &= \sum_{s,s'} \left| \bar{u}(k',s')\gamma^\mu \left(\frac{1-\gamma^5}{2}\right) u(k,s) \right|^2, & (1.12) \\ &= 2(k^\mu k'^\nu + k'^\mu k^\nu - g^{\mu\nu} k\cdot k' + i\epsilon^{\mu\nu\alpha\beta} k_\alpha k'_\beta), & (1.13) \end{aligned}$$

where all mass terms were dropped in the high energy limit. $\epsilon^{\mu\nu\alpha\beta}$ is the totally antisymmetric tensor. The leptonic tensor can be separated into symmetric and antisymmetric parts under μ,ν interchange.

$$\begin{aligned} L_S^{\mu\nu}(\downarrow) &= 2(k^\mu k'^\nu + k'^\mu k^\nu - g^{\mu\nu} k\cdot k'), & (1.14) \\ L_A^{\mu\nu}(\downarrow) &= 2i\epsilon^{\mu\nu\alpha\beta} k_\alpha k'_\beta. & (1.15) \end{aligned}$$

Similarly, for a right-handed incident electron,

$$\begin{aligned} L_S^{\mu\nu}(\uparrow) &= 2(k^\mu k'^\nu + k'^\mu k^\nu - g^{\mu\nu} k\cdot k'), & (1.16) \\ L_A^{\mu\nu}(\uparrow) &= -2i\epsilon^{\mu\nu\alpha\beta} k_\alpha k'_\beta. & (1.17) \end{aligned}$$

1.4.2 Hadronic Tensor $W^{\mu\nu}$

The form of the hadronic tensor is constrained by gauge invariance and symmetry principles. It can be formulated as [4]

$$\begin{aligned} W_{\mu\nu} = {} & W_1(\nu,Q^2)\left(-g_{\mu\nu} + \frac{q_\mu q_\nu}{q^2}\right) \\ & + \frac{W_2(\nu,Q^2)}{M^2}\left(p_\mu - \frac{p\cdot q}{q^2} q_\mu\right)\left(p_\nu - \frac{p\cdot q}{q^2} q_\nu\right) \\ & + i\epsilon_{\mu\nu\alpha\beta} q^\alpha S^\beta M G_1(\nu,Q^2) \\ & + i\epsilon_{\mu\nu\alpha\beta} q^\alpha (p\cdot q S^\beta - q\cdot S p^\beta) \frac{G_2(\nu,Q^2)}{M}, \qquad (1.18) \end{aligned}$$

where W_1 and W_2 are the spin-averaged structure functions. G_1 and G_2 are the spin-dependent structure functions. All structure functions depend only on the variables ν and Q^2. G_1 and G_2 are the only structure functions multiplying terms with the nucleon spin S, hence the nomenclature. In analogy to the leptonic case, the hadronic tensor also lends itself to partition into symmetric and antisymmetric sections,

$$\begin{aligned} W^S_{\mu\nu} &= W_1(\nu, Q^2)\left(-g_{\mu\nu} + \frac{q_\mu q_\nu}{q^2}\right) \\ &\quad + \frac{W_2(\nu, Q^2)}{M^2}\left(p_\mu - \frac{p\cdot q}{q^2}q_\mu\right)\left(p_\nu - \frac{p\cdot q}{q^2}q_\nu\right), \\ W^A_{\mu\nu} &= i\epsilon_{\mu\nu\alpha\beta}q^\alpha S^\beta M G_1(\nu, Q^2) \\ &\quad + i\epsilon_{\mu\nu\alpha\beta}q^\alpha(p\cdot q S^\beta - q\cdot S p^\beta)\frac{G_2(\nu, Q^2)}{M}. \end{aligned} \tag{1.19}$$

Note that the symmetric part involves the unpolarized structure functions while the antisymmetric part involves the polarized structure functions only.

1.4.3 Contraction of $L^{\mu\nu}$ and $W_{\mu\nu}$

The cross section is proportional to the contraction of the leptonic and hadronic tensors (1.11). The contraction of a symmetric and antisymmetric tensor is zero, that is, $L^{\mu\nu}_S W^A_{\mu\nu} = L^{\mu\nu}_A W^S_{\mu\nu} = 0$, resulting in,

$$L^{\mu\nu}W_{\mu\nu} = L^{\mu\nu}_S W^S_{\mu\nu} + L^{\mu\nu}_A W^A_{\mu\nu}. \tag{1.20}$$

First, contraction of the symmetric (spin-averaged) tensors is considered.

$$\begin{aligned} L^{\mu\nu}_S W^S_{\mu\nu} &= 2(k^\mu k'^\nu + k'^\mu k^\nu - g^{\mu\nu} k\cdot k') \\ &\quad \times \left[2W_1\left(-g_{\mu\nu} + \frac{q_\mu q_\nu}{q^2}\right)\right. \\ &\quad \left. + \frac{W_2}{M^2}\left(p_\mu - \frac{p\cdot q}{q^2}q_\mu\right)\left(p_\nu - \frac{p\cdot q}{q^2}q_\nu\right)\right] \qquad (1.21) \\ &= 2W_1\left[k\cdot k' + \frac{2(k\cdot q)(k'\cdot q)}{q^2}\right] \\ &\quad + \frac{2W_2}{M^2}\left[2\left(k\cdot p - \frac{(p\cdot q)(k\cdot q)}{q^2}\right)\left(k'\cdot p - \frac{(p\cdot q)(k'\cdot q)}{q^2}\right)\right. \\ &\quad \left. - (k\cdot k')\left(p^2 - \frac{(p\cdot q)^2}{q^2}\right)\right]. \qquad (1.22) \end{aligned}$$

In the high energy limit and in the target nucleon rest frame, $k^2 = k'^2 = 0$, and $|\mathbf{k}| = E$ and $|\mathbf{k}'| = E'$. Therefore,

$$
\begin{aligned}
Q^2 &= -q^2 = 4EE' \sin^2 \frac{\theta}{2}, && (1.23)\\
k \cdot k' &= \frac{1}{2} Q^2, && (1.24)\\
k \cdot q &= -\frac{1}{2} Q^2, && (1.25)\\
k' \cdot q &= \frac{1}{2} Q^2, && (1.26)\\
k \cdot p &= ME, && (1.27)\\
k' \cdot p &= ME', && (1.28)\\
p \cdot q &= M\nu, && (1.29)\\
p^2 &= M^2. && (1.30)
\end{aligned}
$$

The contraction becomes

$$
L_S^{\mu\nu} W_{\mu\nu}^S = 8W_1 EE' \sin^2 \frac{\theta}{2} + 4W_2 EE' \cos^2 \frac{\theta}{2}. \tag{1.31}
$$

The spin-averaged cross section is then

$$
\frac{d^2\sigma}{d\Omega dE'} = \frac{4\alpha^2}{Q^4} E'^2 \left[2W_1(\nu, Q^2) \sin^2 \frac{\theta}{2} + W_2(\nu, Q^2) \cos^2 \frac{\theta}{2} \right]. \tag{1.32}
$$

Second, contraction of the antisymmetric (spin-dependent) tensors yields

$$
\begin{aligned}
L_A^{\mu\nu} W_{\mu\nu}^A &= \pm i\epsilon^{\mu\nu\alpha\beta} k_\alpha k'_\beta \left[i\epsilon_{\mu\nu\rho\sigma} q^\rho S^\sigma M G_1 + i\epsilon_{\mu\nu\rho\sigma} q^\rho (p \cdot q S^\sigma - q \cdot S p^\sigma) \frac{G_2}{M} \right] \\
&= \pm 4[(k \cdot q)(k' \cdot S) - (k \cdot S)(k' \cdot q)] M G_1 \\
&\quad \pm 4[(k \cdot q)(k' \cdot S)(p \cdot q) - (k \cdot S)(k' \cdot q)(p \cdot q) \\
&\quad -(k \cdot q)(k' \cdot p)(q \cdot S) + (k \cdot p)(k' \cdot q)(q \cdot S)] \frac{G_2}{M}. && (1.33)
\end{aligned}
$$

where + (-) stands for a left-handed (right-handed) incident electron. In a typical double-polarization experiment, the spin of the incident electron is flipped pseudo-randomly along the beam line. The spin of the target nucleon is held stationary in a direction parallel or perpendicular to the beam line. Thus the four polarized cross sections of interest are $\sigma^{\downarrow\uparrow}$, $\sigma^{\uparrow\uparrow}$, $\sigma^{\downarrow\rightarrow}$, and $\sigma^{\uparrow\rightarrow}$ where the first arrow superscript denotes electron polarization and the second arrow superscript denotes target nucleon polarization. For the case of a longitudinally polarized target and left-handed

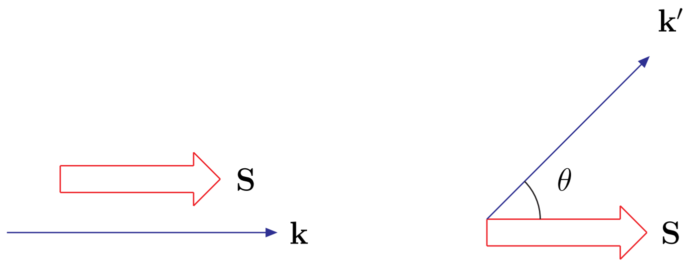

Figure 1.4: Incident ($\mathbf{k}$) and scattered ($\mathbf{k}'$) electron momentum with nucleon spin ($\mathbf{S}$) longitudinal with respect to beam line in nucleon rest frame.

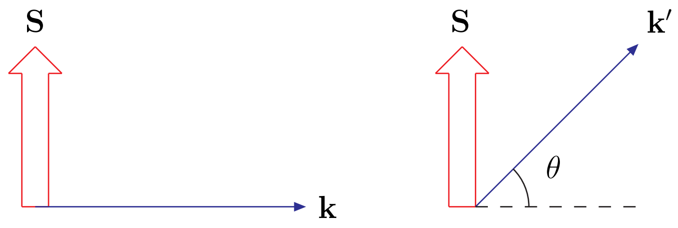

Figure 1.5: Incident ($\mathbf{k}$) and scattered ($\mathbf{k}'$) electron momentum with nucleon spin ($\mathbf{S}$) transverse with respect to beam line in nucleon rest frame.

electron, the nucleon spin can be chosen to be $S = (0, 0, 0, 1)$ as shown in Fig. 1.4. It follows that

$$k \cdot S = -E, \tag{1.34}$$

$$k' \cdot S = -E' \cos\theta, \tag{1.35}$$

$$q \cdot S = -E + E' \cos\theta. \tag{1.36}$$

The contraction of the spin-dependent leptonic and hadronic tensors becomes

$$L_A^{\mu\nu}(\downarrow) W_{\mu\nu}^A(\uparrow) = 2Q^2(E + E' \cos\theta) M G_1 - 2Q^4 G_2. \tag{1.37}$$

The right-handed electron counterpart differs only by a minus sign,

$$L_A^{\mu\nu}(\uparrow) W_{\mu\nu}^A(\uparrow) = -2Q^2(E + E' \cos\theta) M G_1 + 2Q^4 G_2. \tag{1.38}$$

For the case of a transversely polarized target and left-handed electron, the nucleon spin can be chosen to be either $S = (0, 1, 0, 0)$ or $S = (0, 0, 1, 0)$ as shown in Fig. 1.5.

This time, it follows that

$$\begin{aligned} k \cdot S &= 0, && (1.39)\\ k' \cdot S &= -E' \sin\theta, && (1.40)\\ q \cdot S &= E' \sin\theta. && (1.41) \end{aligned}$$

The contraction of the spin-dependent leptonic and hadronic tensors now becomes

$$L_A^{\mu\nu}(\downarrow) W_{\mu\nu}^A(\rightarrow) = 2Q^2 E' \sin\theta (MG_1 + 2EG_2). \quad (1.42)$$

Again, the right-handed counterpart differs only by a minus sign,

$$L_A^{\mu\nu}(\uparrow) W_{\mu\nu}^A(\rightarrow) = -2Q^2 E' \sin\theta (MG_1 + 2EG_2). \quad (1.43)$$

For the purpose of forming asymmetries, the sum and differences of polarized cross sections are of interest.

$$\begin{aligned} \Delta\sigma_{\parallel} &= \frac{d^2\sigma}{d\Omega dE'}(\downarrow\uparrow - \uparrow\uparrow) = \frac{4\alpha^2}{Q^2}\frac{E'}{E}[(E + E'\cos\theta)MG_1 - Q^2 G_2], && (1.44)\\ \Sigma\sigma_{\parallel} &= \frac{d^2\sigma}{d\Omega dE'}(\downarrow\uparrow + \uparrow\uparrow) = \frac{8\alpha^2}{Q^4}E'^2\left[2W_1 \sin^2\frac{\theta}{2} + W_2\cos^2\frac{\theta}{2}\right], && (1.45)\\ \Delta\sigma_{\perp} &= \frac{d^2\sigma}{d\Omega dE'}(\downarrow\rightarrow - \uparrow\rightarrow) = \frac{4\alpha^2}{Q^2}\frac{E'^2}{E}\sin\theta[MG_1 + 2EG_2], && (1.46)\\ \Sigma\sigma_{\perp} &= \frac{d^2\sigma}{d\Omega dE'}(\downarrow\rightarrow + \uparrow\rightarrow) = \frac{8\alpha^2}{Q^4}E'^2\left[2W_1 \sin^2\frac{\theta}{2} + W_2\cos^2\frac{\theta}{2}\right]. && (1.47) \end{aligned}$$

Note $\Sigma\sigma_{\parallel} = \Sigma\sigma_{\perp}$ because they do not dependent on beam and target polarizations (involve only unpolarized structure functions W_1 and W_2).

1.5 Virtual Photon-Nucleon Total Cross Section

Consider real photon-nucleon scattering as shown in Fig. 1.6. For an incident real photon ($q^2 = 0$) with energy K, transverse polarization $\epsilon_\lambda^\mu(q)$, and helicity $\lambda = \pm 1$, the cross section defined in section 1.3 and the Feynman rules of QED [2] yield

$$\begin{aligned} d\sigma &= \frac{1}{(2K)(2M)}|\epsilon_\lambda^\mu(q)\bar{u}(X)(-ie\Gamma_\mu)u(p,S)|^2 \int \prod_{i=1}^{N} \frac{d^3p_i'}{(2\pi)^3 2E_i'}\\ &\quad \times (2\pi)^4 \delta^4(p + q - \sum_{i=1}^{N} p_i'). && (1.48) \end{aligned}$$

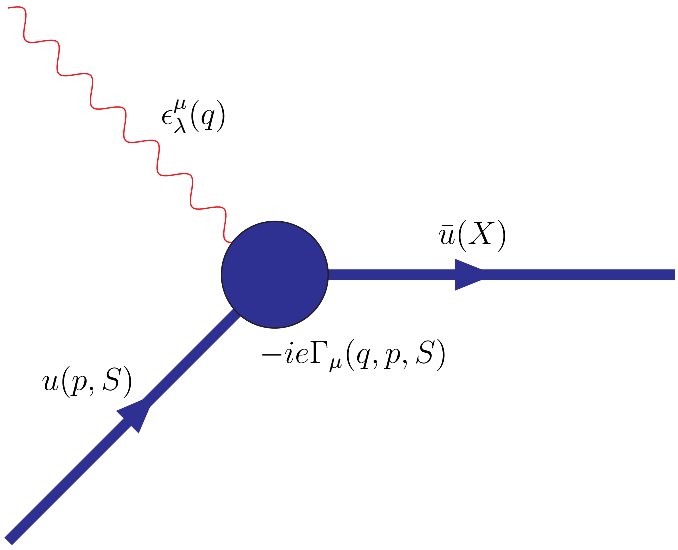

Figure 1.6: Real photon-nucleon scattering. X can be any excited final state.

Using the definition of the hadronic tensor in Eq. (1.10), the total cross section is written as

$$\sigma(\gamma N \to X) = \frac{4\pi^2\alpha}{K}\epsilon^{\mu *}W_{\mu\nu}\epsilon^{\nu}. \tag{1.49}$$

The invariant mass W of the final state is:

$$W^2 = (p+q)^2 = M^2 + 2MK. \tag{1.50}$$

Real photons possess two transverse polarization states. A common convention is to use [2]:

$$\epsilon_{+} = \frac{1}{\sqrt{2}}(0,1,i,0), \tag{1.51}$$

$$\epsilon_{-} = \frac{1}{\sqrt{2}}(0,1,-i,0). \tag{1.52}$$

Virtual photons have an additional polarization state chosen as:

$$\epsilon_0 = \frac{1}{\sqrt{Q^2}}(\sqrt{\nu^2+Q^2},0,0,\nu). \tag{1.53}$$

Generalizing the total cross section to virtual photon-nucleon scattering ($q^2 \neq 0$) raises one difficulty: the flux factor $4MK$ is ill-defined or arbitrary. One particular convention is to preserve Eq. (1.50) in defining the virtual photon flux:

$$K = \frac{W^2 - M^2}{2M} = \nu - \frac{Q^2}{2M}. \tag{1.54}$$

This is known as the Hand convention [5]. Another convention commonly used is the Gilman convention [6]:

$$K = |\mathbf{q}| = \sqrt{\nu^2 + Q^2}. \tag{1.55}$$

The leptonic tensor is well-known and completely computable in QED. The interesting hadronic physics happens at the hadronic vertex. By way of the optical theorem, the virtual photon-nucleon (photoabsorption) total cross section may be related to the imaginary (absorptive) part of the forward virtual Compton amplitude, $\mathcal{M}_{ab\to cd}$, where a, b, c and d represent helicities of the incident virtual photon and nucleon and scattered virtual photon and nucleon respectively. The forward virtual Compton amplitudes are related to the hadronic tensor by helicity decomposition:

$$\mathcal{M}_{ab\to cd} = \epsilon^{\mu *}(\lambda_c) W_{\mu\nu} \epsilon^{\nu}(\lambda_a), \tag{1.56}$$

where $\epsilon^{\mu}(\lambda)$ is the photon polarization four-vector of helicity λ. The virtual photon of spin 1 has three helicity states: two transverse, +1 and -1, and one longitudinal, 0. The nucleon of spin 1/2 has two helicity states: +1/2 and -1/2. Angular momentum conservation restricts the number of possible amplitudes to ten. Additional symmetry laws futher reduce the number of independent amplitudes to four, the number of independent structure functions. There are three helicity-preserving amplitudes ($\mathcal{M}_{1\frac{1}{2}\to 1\frac{1}{2}}$, $\mathcal{M}_{1-\frac{1}{2}\to 1-\frac{1}{2}}$ and $\mathcal{M}_{0\frac{1}{2}\to 0\frac{1}{2}}$) and one helicity-flip amplitude ($\mathcal{M}_{0\frac{1}{2}\to 1-\frac{1}{2}}$) with respect to nucleon polarization. The relationships between the photoabsorption cross sections and the structure functions result from combining (1.49) and (1.56):

$$\begin{aligned}
\sigma_{1/2} &= \frac{4\pi^2\alpha}{K}\mathcal{M}_{1-\frac{1}{2}\to 1-\frac{1}{2}} = \frac{4\pi^2\alpha}{K}\left[W_1 + M\nu G_1 - Q^2 G_2\right], && (1.57)\\
\sigma_{3/2} &= \frac{4\pi^2\alpha}{K}\mathcal{M}_{1\frac{1}{2}\to 1\frac{1}{2}} = \frac{4\pi^2\alpha}{K}\left[W_1 - M\nu G_1 + Q^2 G_2\right], && (1.58)\\
\sigma_L &= \frac{4\pi^2\alpha}{K}\mathcal{M}_{0\frac{1}{2}\to 0\frac{1}{2}} = \frac{4\pi^2\alpha}{K}\left[W_2\left(1+\frac{\nu^2}{Q^2}\right) - W_1\right], && (1.59)\\
\sigma_{LT} &= \frac{4\pi^2\alpha}{K}\mathcal{M}_{0\frac{1}{2}\to 1-\frac{1}{2}} = \frac{4\pi^2\alpha}{K}\sqrt{Q^2}\left[M G_1 + \nu G_2\right]. && (1.60)
\end{aligned}$$

The numerical subscripts, 1/2 and 3/2, on the transverse photoabsorption cross sections designate the total angular momentum projection along the q axis. The longitudinal photoabsorption cross section is σ_L and the photoabsorption cross section resulting from transverse and longitudinal interference is σ_{LT}. The total transverse photoabsorption cross section is defined by:

$$\sigma_T = \frac{1}{2}(\sigma_{1/2} + \sigma_{3/2}) = \frac{4\pi^2\alpha}{K} W_1. \tag{1.61}$$

The transverse-transverse interference photoabsorption cross section is defined by:

$$\sigma_{TT} = \frac{1}{2}(\sigma_{1/2} - \sigma_{3/2}) = \frac{4\pi^2\alpha}{K}(M\nu G_1 - Q^2 G_2). \tag{1.62}$$

1.6 Virtual Photon-Nucleon Asymmetries

Having introduced virtual photoabsorption cross sections, these may be used to define virtual photoabsorption asymmetries A_1 and A_2:

$$A_1 = \frac{\sigma_{1/2} - \sigma_{3/2}}{\sigma_{1/2} + \sigma_{3/2}} = \frac{\sigma_{TT}}{\sigma_T} = \frac{1}{W_1}(M\nu G_1 - Q^2 G_2), \tag{1.63}$$

$$A_2 = \frac{2\sigma_{LT}}{\sigma_{1/2} + \sigma_{3/2}} = \frac{\sigma_{LT}}{\sigma_T} = \frac{\sqrt{Q^2}}{W_1}(M G_1 + \nu G_2). \tag{1.64}$$

1.7 Experimental Cross Sections and Asymmetries

The longitudinal, $A_{\parallel}$, and transverse, $A_{\perp}$ asymmetries are defined as:

$$A_{\parallel} = \frac{\sigma^{\downarrow\uparrow} - \sigma^{\uparrow\uparrow}}{\sigma^{\downarrow\uparrow} + \sigma^{\uparrow\uparrow}} = \frac{\Delta\sigma_{\parallel}}{\Sigma\sigma_{\parallel}}, \tag{1.65}$$

$$A_{\perp} = \frac{\sigma^{\downarrow\rightarrow} - \sigma^{\uparrow\rightarrow}}{\sigma^{\downarrow\rightarrow} + \sigma^{\uparrow\rightarrow}} = \frac{\Delta\sigma_{\perp}}{\Sigma\sigma_{\perp}}. \tag{1.66}$$

The measured asymmetries and cross sections can be related to the corresponding virtual photoabsorption quantities with:

$$A_{\parallel} = D(A_1 + \eta A_2), \tag{1.67}$$

$$A_{\perp} = d(A_2 - \zeta A_1), \tag{1.68}$$

and

$$\frac{d^2\sigma}{d\Omega dE'} = \Gamma(\sigma_T + \epsilon\sigma_L), \tag{1.69}$$

$$\frac{d^2\sigma}{d\Omega dE'}(\downarrow\uparrow - \uparrow\uparrow) = 2\Gamma D(1 + \epsilon R)(\sigma_{TT} + \eta\sigma_{LT}), \tag{1.70}$$

$$\frac{d^2\sigma}{d\Omega dE'}(\downarrow\rightarrow - \uparrow\rightarrow) = 2\Gamma d(1 + \epsilon R)(\sigma_{LT} - \zeta\sigma_{TT}), \tag{1.71}$$

where

$$\begin{aligned}
\Gamma &= \frac{\alpha}{4\pi^2}\frac{K}{Q^2}\frac{E'}{E}\frac{2}{1-\epsilon}, &(1.72)\\
\frac{1}{\epsilon} &= 1+2\left(1+\frac{1}{\gamma^2}\right)\tan^2\frac{\theta}{2}, &(1.73)\\
\gamma &= \sqrt{Q^2}/\nu, &(1.74)\\
D(1+\epsilon R) &= 1-E'\epsilon/E, &(1.75)\\
d(1+\epsilon R) &= \sqrt{2\epsilon/(1+\epsilon)}, &(1.76)\\
\eta &= \epsilon\sqrt{Q^2}/(E-E'\epsilon), &(1.77)\\
\zeta &= \eta(1+\epsilon)/2\epsilon, &(1.78)\\
R &= \sigma_L/\sigma_T. &(1.79)
\end{aligned}$$

The polarization of the virtual photon in the laboratory frame is ϵ and the photon depolarization factor is D. A typical doubly-polarized experiment would measure $\sigma^{\downarrow\uparrow}$, $\sigma^{\uparrow\uparrow}$, $\sigma^{\downarrow\rightarrow}$ and $\sigma^{\uparrow\rightarrow}$ from which σ_{TT} and σ_{LT} can be extracted using the set of equations above. Note σ_{TT} is needed for the GDH sum rule.

1.8 The Bjorken Sum Rule

A sum rule is a comparison between an integral over all excitation energies invoking closure, which is then compared to a specific experimental result. For example, the Bjorken sum rule is a sum of inelastic electron scattering from the nucleon which, in the infinite Q^2 limit, can be related to the β decay of the nucleon. In the limit $Q^2 \to \infty$ and $\nu \to \infty$, yet finite Bjorken scaling variable $x = Q^2/2M\nu$, the structure functions scale as:

$$\begin{aligned}
MW_1(\nu,Q^2) &\to F_1(x), &(1.80)\\
\nu W_2(\nu,Q^2) &\to F_2(x), &(1.81)\\
M^2\nu G_1(\nu,Q^2) &\to g_1(x), &(1.82)\\
M\nu^2 G_2(\nu,Q^2) &\to g_2(x). &(1.83)
\end{aligned}$$

The Bjorken sum rule, radiatively corrected to finite Q^2, is fundamental to our understanding of Quantum Chromodynamics (QCD). The importance of QCD sum rules is that they are model-independent. The Bjorken sum rule relates the first moments of

Experiment	Q^2	$\Gamma_1^p - \Gamma_1^n$	Bjorken sum rule
CERN SMC [11]	5 GeV^2	$0.181^{+0.012+0.018+0.015}_{-0.011-0.018-0.006}$	0.181 ± 0.003
SLAC E154 [12]	5 GeV^2	$0.171 \pm 0.005 \pm 0.010 \pm 0.006$	0.181 ± 0.003

Table 1.1: Tests of the Bjorken sum rule [10]. The errors for $\Gamma_1^p - \Gamma_1^n$ are statistical, systematic, and theoretical. The Bjorken sum rule is calculated to order α_s^2 [13].

the polarized spin structure functions with the ratio of axial to axial-vector coupling constants of neutron β-decay [7]:

$$\Gamma_1^p - \Gamma_1^n = \int_0^1 \left(g_1^p(x) - g_1^n(x)\right) dx = \frac{1}{6}\left|\frac{g_A}{g_V}\right|, \tag{1.84}$$

where $\Gamma_1^N = \int_0^1 g_1^N(x)dx$ is the first moment of the structure function g_1^N for the nucleon N, g_A and g_V are the axial and vector neutron β-decay coupling constants, respectively. Their ratio is $g_A/g_V = -1.2601 \pm 0.0025$ [8]. The Bjorken sum rule was initially derived in the framework of $U(6) \otimes U(6)$ current algebra of Gell-Mann, Feynman, and Zweig [9], then was later rederived in QCD under the Operator Product Expansion (OPE) formalism. Historically, its is rather amusing to note that Bjorken referred to his sum rule as a "worthless equation" due to the absence of polarized experiments at the time. In an attempt to "salvage" the sum rule, he chose to emphasize an inequality involving unpolarized cross sections instead [7]. Nowadays, with the aid of rapid technological advances in both polarized sources and targets, the Bjorken sum rule has been verified to better than 10% [10]. Experiments are always performed at finite Q^2. The OPE method can be used to extend the validity of the Bjorken sum rule to finite Q^2 [4]. In fact, QCD radiative corrections to the Bjorken sum rule have been calculated to third order in the strong coupling constant [13]. In this respect, the Bjorken sum rule provides validation for the QCD radiative corrections:

$$\begin{aligned}\Gamma_1^{p-n}(Q^2) &= \int_0^1 \left(g_1^p(x,Q^2) - g_1^n(x,Q^2)\right) dx \\ &= \frac{1}{6}\left|\frac{g_A}{g_V}\right| \left[1 - \left(\frac{\alpha_s}{\pi}\right) - 3.5833\left(\frac{\alpha_s}{\pi}\right)^2 - 20.2153\left(\frac{\alpha_s}{\pi}\right)^3\right]\end{aligned} \tag{1.85}$$

where $\alpha_s(Q^2) = 12\pi/(33 - 2n_f)\ln(Q^2/\Lambda^2)$ is the strong coupling constant. $n_f = 3$ is the number of flavors: u, d, and s. Λ is a free parameter fixed by experiment. It determines the transition from quark and gluonic degrees of freedom to hadronic and mesonic degrees of freedom. Λ is believed to lie in the range 0.1 to 0.5 GeV [3]. Estimates of QCD corrections to order α_s^4 have been made in Ref. [14].

Conversely, assuming the validity of the Bjorken sum rule, a value for the strong coupling constant can be extracted. It is standard convention to quote this value at the mass of the Z boson $M_Z = 91.19$ GeV [15],

$$\alpha_s(M_Z) = 0.118^{+0.010}_{-0.024}. \tag{1.86}$$

1.9 The Gerasimov-Drell-Hearn Sum Rule

1.9.1 Introduction

In the limit $Q^2 \to 0$ (real photon scattering), the Gerasimov-Drell-Hearn sum rule [16] relates the helicity structure of the sum over all nucleon photo-excitations with its anomalous magnetic moment. It is based on general physics principles: Lorentz and gauge invariance, crossing symmetry, causality, and unitarity.

$$I_{GDH} = \int_{\nu_{thr}}^{\infty} \frac{d\nu}{\nu}(\sigma_{1/2} - \sigma_{3/2}) = -\frac{2\pi^2\alpha}{M^2}\kappa^2 = \begin{cases} -204.5\ \mu\text{b for the proton} \\ -232.8\ \mu\text{b for the neutron} \end{cases}, \tag{1.87}$$

where $\nu_{thr} = m_\pi^2/2M + m_\pi \approx 150$ MeV is the threshold energy for pion photoproduction. $\sigma_{1/2}$ and $\sigma_{3/2}$ are the photoabsorption cross sections of total helicity 1/2 and 3/2, respectively. $\alpha = e^2/4\pi \approx 1/137$ is the fine structure constant, M is the nucleon mass ($M_p = 938.3$ MeV/c^2 and $M_n = 939.6$ MeV/c^2), and κ is the anomalous magnetic moment of the nucleon defined by $\mu_p/\mu_N = 1 + \kappa_p = 2.793$ for the proton and $\mu_n/\mu_N = \kappa_n = -1.913$ for the neutron. μ_p and μ_n are the proton and neutron magnetic moment, respectively. $\mu_N = e\hbar/2M_pc$ is the nuclear magneton.

1.9.2 Derivation

The starting point for deriving the GDH sum rule is the forward Compton amplitude [17,18] depicted in Fig. 1.7. The form of the amplitude used is that of Drell and Hearn [16].

$$T(\nu) = \chi^\dagger[f_1(\nu)\hat{\boldsymbol{\epsilon}}^* \cdot \hat{\boldsymbol{\epsilon}} + i\nu f_2(\nu)\boldsymbol{\sigma} \cdot (\hat{\boldsymbol{\epsilon}}^* \times \hat{\boldsymbol{\epsilon}})]\chi, \tag{1.88}$$

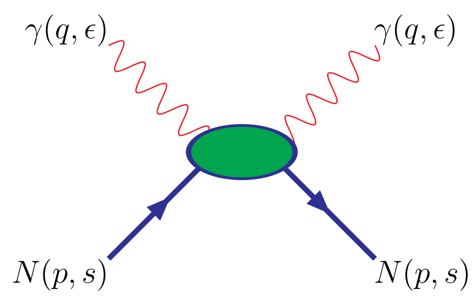

Figure 1.7: Feynman diagram for forward Compton scattering. The photon γ has four-momentum q and spin ϵ, and the nucleon N has four-momentum p and spin s.

where ν is the photon energy, χ is the spin of the nucleon, $\hat{\boldsymbol{\epsilon}}$ is photon polarization vector, and $\boldsymbol{\sigma}$ is the Pauli spin matrices vector. Crossing symmetry requires that $f_1(\nu)$ and $f_2(\nu)$ are even.

Consider a photon of helicity $\lambda = +1$ and polarization four-vector

$$\epsilon_+ = (0, 1, i, 0)/\sqrt{2}. \tag{1.89}$$

It follows that:

$$\begin{aligned} \hat{\boldsymbol{\epsilon}}^* \cdot \hat{\boldsymbol{\epsilon}} &= 1, & (1.90)\\ \hat{\boldsymbol{\epsilon}}^* \times \hat{\boldsymbol{\epsilon}} &= i\hat{\boldsymbol{e}}_3, & (1.91) \end{aligned}$$

For a nucleon with spin axis quantized along the photon polarization vector, $\chi_+ = \binom{1}{0}$ for spin $+\frac{1}{2}$ and $\chi_- = \binom{0}{1}$ for spin $-\frac{1}{2}$. Therefore the amplitudes $T_{3/2}$ and $T_{1/2}$ where the photon and nucleon spins are parallel and antiparallel, respectively, are:

$$\begin{aligned} T_{3/2} &= f_1 - \nu f_2, & (1.92)\\ T_{1/2} &= f_1 + \nu f_2. & (1.93) \end{aligned}$$

The Low Energy Theorem (LET) of Low, Gell-Mann, and Goldberger [19] asserts that the forward Compton amplitude can be expanded in powers of the frequency and the expansion coefficients are expressed in terms of macroscopic properties of the nucleon [20]:

$$\begin{aligned} f_1(\nu) &= -\frac{\alpha}{M} + (\alpha_E + \beta_M)\nu^2 + O(\nu^4), & (1.94)\\ f_2(\nu) &= -\frac{\alpha\kappa^2}{2M^2} + \gamma\nu^2 + O(\nu^4), & (1.95) \end{aligned}$$

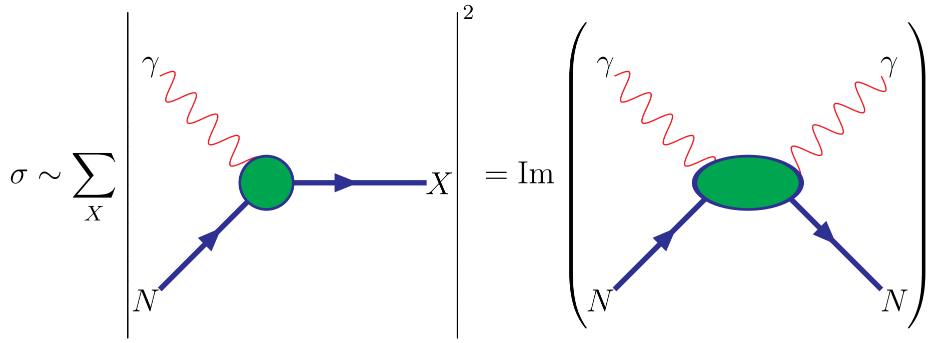

Figure 1.8: Feynman diagram for the optical theorem. The total cross section is related to the absorptive (imaginary) part of the forward amplitude.

where α_E and β_M are the electric and magnetic polarizabilities of the nucleon, respectively. κ is the anomalous magnetic moment of the nucleon and γ is the vector polarizability of the nucleon.

The optical theorem [2] connects the forward Compton amplitude to the total photoabsorption cross section:

$$\text{Im } T_{1/2(3/2)} = \frac{\nu}{4\pi}\sigma_{1/2(3/2)}. \tag{1.96}$$

This is illustrated in Fig. 1.8. Thus,

$$\text{Im } f_1 = \frac{\nu}{8\pi}(\sigma_{1/2} + \sigma_{3/2}), \tag{1.97}$$

$$\text{Im } f_2 = \frac{1}{8\pi}(\sigma_{1/2} - \sigma_{3/2}). \tag{1.98}$$

If the additional assumption is made that $|f_2(\nu)| \longrightarrow 0$ as $\nu \longrightarrow \infty$ (no subtraction hypothesis) so that the half-circles at ∞ do not contribute to the Cauchy integral, then an unsubtracted dispersion relation emerges for $f_2(\nu)$:

$$\text{Re } f_2(\nu) = \frac{2}{\pi}\int_{\nu_{thr}}^{\infty} \frac{\nu' d\nu'}{\nu'^2 - \nu^2} \text{ Im } f_2(\nu'). \tag{1.99}$$

Combining Eqs. (1.95), (1.98) and (1.99), and taking the limit $\nu \longrightarrow 0$ results in:

$$-\frac{\alpha\kappa^2}{2M^2} = \text{Re } f_2(0) = \frac{1}{4\pi^2}\int_{\nu_{thr}}^{\infty} \frac{d\nu}{\nu}(\sigma_{1/2} - \sigma_{3/2}). \tag{1.100}$$

In a similar fashion, other sum rules may be derived [21]. Baldin's sum rule [22] is:

$$\alpha_E + \beta_M = \frac{1}{2\pi^2}\int_{\nu_{thr}}^{\infty} \frac{d\nu}{\nu^2}\sigma_{total}, \tag{1.101}$$

where $\sigma_{total} = (\sigma_{1/2} + \sigma_{3/2})/2$. The forward spin polarizability [18] is:

$$\gamma = \frac{1}{4\pi^2} \int_{\nu_{thr}}^{\infty} \frac{d\nu}{\nu^3} (\sigma_{1/2} - \sigma_{3/2}). \tag{1.102}$$

1.9.3 Experimental Verification

Up until very recently, the only experimental verification of the GDH sum rule available was from phase shift analysis of pion photoproduction data. Recently real photon experiments have been completed at both Mainz and Bonn, but the data is not yet analyzed or published. Karliner [23] used isospin decomposition of the anomalous magnetic moments of the proton and neutron:

$$\kappa_p = \frac{1}{2}\kappa_S + \frac{1}{2}\kappa_V, \tag{1.103}$$

$$\kappa_n = \frac{1}{2}\kappa_S - \frac{1}{2}\kappa_V, \tag{1.104}$$

into isoscalar (κ_S) and isovector (κ_V) components. Three GDH sum rules immediately follow. They are the isovector-isovector (VV), isoscalar-isoscalar (SS), and isovector-isoscalar (VS) interference or mixed sum rules. They may be written down as:

$$I_{VV} = \int_{\nu_{thr}}^{\infty} \frac{d\nu}{\nu} \left(\sigma_{1/2}^{VV} - \sigma_{3/2}^{VV}\right) = \frac{2\pi^2\alpha}{M^2} \left(\frac{1}{2}\kappa_V\right)^2 = -218.5\ \mu\text{b}, \tag{1.105}$$

$$I_{SS} = \int_{\nu_{thr}}^{\infty} \frac{d\nu}{\nu} \left(\sigma_{1/2}^{SS} - \sigma_{3/2}^{SS}\right) = \frac{2\pi^2\alpha}{M^2} \left(\frac{1}{2}\kappa_S\right)^2 = -0.3\ \mu\text{b}, \tag{1.106}$$

$$I_{VS} = \int_{\nu_{thr}}^{\infty} \frac{d\nu}{\nu} \left(\sigma_{1/2}^{VS} - \sigma_{3/2}^{VS}\right) = \frac{2\pi^2\alpha}{M^2} \left(\frac{1}{2}\kappa_V\kappa_S\right) = +14.7\ \mu\text{b}. \tag{1.107}$$

The proton and neutron GDH sum rules can be recovered from the individual isospin components:

$$I^p = I_{VV} + I_{SS} + I_{VS}, \tag{1.108}$$

$$I^n = I_{VV} + I_{SS} - I_{VS}. \tag{1.109}$$

Single-pion photoproduction amplitudes can be decomposed into amplitudes of definite isospin [23–25]:

$$M(\gamma + p \to \pi^+ + n) = \frac{1}{\sqrt{3}} \left[M^{(3)} - \sqrt{2}\left(M^{(1)} - M^{(0)}\right)\right], \tag{1.110}$$

$$M(\gamma + p \to \pi^0 + p) = \frac{1}{\sqrt{3}} \left[\sqrt{2}M^{(3)} + \left(M^{(1)} - M^{(0)}\right)\right], \tag{1.111}$$

$$M(\gamma + n \to \pi^- + p) = \frac{1}{\sqrt{3}} \left[M^{(3)} - \sqrt{2}\left(M^{(1)} + M^{(0)}\right)\right], \tag{1.112}$$

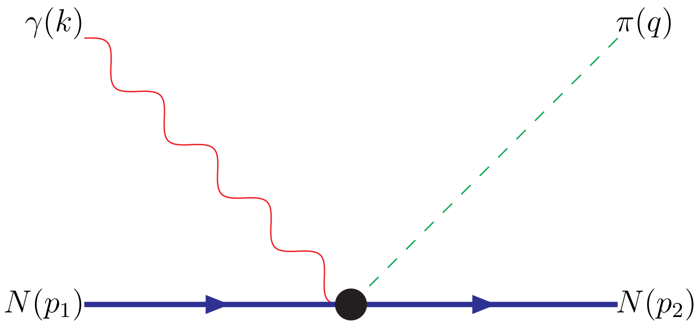

Figure 1.9: Feynman diagram for pion photoproduction $\gamma + N \to \pi + N$.

where $M^{(3)}$ is the amplitude for isospin 3/2, $M^{(1)}$ for isospin 1/2, and $M^{(0)}$ is the isoscalar amplitude. The cross sections for different isospin states are related to the isospin amplitudes:

$$\sigma^{VV} \propto |M^{(3)}|^2 + |M^{(1)}|^2, \tag{1.113}$$
$$\sigma^{SS} \propto |M^{(0)}|^2, \tag{1.114}$$
$$\sigma^{VS} \propto -[(M^{(0)})^* M^{(1)} + M^{(0)}(M^{(1)})^*]. \tag{1.115}$$

The cross sections of definite helicity can be separated into terms with amplitudes of definite parity and angular momentum [23]:

$$\sigma_{1/2} = \frac{8\pi q}{k} \sum_{l=0}^{\infty} (l+1) \left(|A_{l+}|^2 + |A_{(l+1)-}|^2 \right), \tag{1.116}$$
$$\sigma_{3/2} = \frac{8\pi q}{k} \sum_{l=0}^{\infty} \frac{1}{4}[l(l+1)(l+2)] \left(|B_{l+}|^2 + |B_{(l+1)-}|^2 \right), \tag{1.117}$$

where $A_{l\pm}$ and $B_{l\pm}$ are amplitudes for a state with pion orbital angular momentum l, parity $P = (-1)^{l+1}$, and total angular momentum $j = l \pm 1/2$. See Fig. 1.9 for a definition of kinematic variables. Isospin and angular momentum decomposition as outlined above permit us to estimate the GDH sum rule from pion photoproduction cross sections. Table 1.2 summarizes the experimental situation at the time. Clearly, the isovector-isovector sum rule is saturated and the isoscalar-isoscalar sum rule is small. Only the interference term seems in disagreement and even carries the wrong sign! Nonetheless the conclusion was that the GDH sum rule held and more precise measurements were needed.

GDH Integral	Experiment (μb)	Theory (μb)
I_{VV}	-219	-218.5
I_{SS}	-2.92	-0.3
I_{VS}	-39	+14.7
I^p	-261	-204.1
I^n	-183	-233.5

Table 1.2: Early experimental tests of the GDH sum rule from analysis of pion photo-production data [23]. The column titled Experimental is an evaluation of the integral $\int_{\nu_{thr}}^{\infty} d\nu/\nu(\sigma_{1/2} - \sigma_{3/2})$ from $\nu = 0.8$ GeV to $\nu = 1.2$ GeV. The column titled Theory represents the quantity $-2\pi^2\alpha\kappa^2/M^2$.

1.10 The Generalized GDH Integral

Let us recall the definitions of the virtual photoabsorption cross sections defined earlier:

$$\sigma_T = \frac{1}{2}(\sigma_{3/2} + \sigma_{1/2}), \tag{1.118}$$

$$\sigma'_{TT} = \frac{1}{2}(\sigma_{3/2} - \sigma_{1/2}), \tag{1.119}$$

and their relations to the structure functions:

$$\sigma_T = \frac{4\pi^2\alpha}{MK}F_1, \tag{1.120}$$

$$\sigma_L = \frac{4\pi^2\alpha}{K}\left[\frac{F_2}{\nu}\left(1 + \frac{1}{\gamma^2}\right) - \frac{F_1}{M}\right], \tag{1.121}$$

$$\sigma'_{LT} = -\frac{4\pi^2\alpha}{MK}\gamma(g_1 + g_2), \tag{1.122}$$

$$\sigma'_{TT} = -\frac{4\pi^2\alpha}{MK}(g_1 - \gamma^2 g_2), \tag{1.123}$$

where $\gamma = \sqrt{Q^2}/\nu$, $\sigma'_{LT} = -\sigma_{LT}$, and $\sigma'_{TT} = -\sigma_{TT}$. The virtual photon flux factor is:

$$K = \begin{cases} \nu(1-x) & \text{for the Hand convention [5]} \\ \nu\sqrt{1+\gamma^2} & \text{for the Gilman convention [6]} \end{cases} . \tag{1.124}$$

Different model dependent conventions exist. However, here we use the Hand convention because it is related to the Compton amplitude. Drechsel *et al.* [26] generalized the GDH integral with the following Q^2-dependence:

$$I_1(Q^2) = \frac{2M^2}{Q^2}\int_0^{x_0} g_1(x,Q^2)dx \rightarrow \begin{cases} -\frac{1}{4}\kappa_N^2 & \text{for } Q^2 \rightarrow 0 \\ \frac{2M^2}{Q^2}\Gamma_1 + \mathcal{O}(1/Q^4) & \text{for } Q^2 \rightarrow \infty \end{cases}, \tag{1.125}$$

where $x_0 = Q^2/(2Mm_\pi + m_\pi^2 + Q^2)$ is the threshold of single-pion production. The integral I_1 can be recast in terms of the virtual photoabsorption cross sections:

$$I_1(Q^2) = \frac{M^2}{8\pi^2\alpha}\int_{\nu_0}^{\infty} \frac{1-x}{1+\gamma^2}(\sigma_{1/2} - \sigma_{3/2} - 2\gamma\sigma'_{LT})\frac{d\nu}{\nu}, \tag{1.126}$$

where $\nu_0 = m_\pi + (m_\pi^2 + Q^2)/2M$ is the threshold energy for single-pion production. The term $\gamma\sigma'_{LT}$ is of order Q^2 and vanishes in the real photon limit. At finite Q^2, however, the contribution of σ'_{LT} to $I_1(Q^2)$ is significant. To remedy this situation, several alternate definitions of the GDH integral have been proposed [17, 26]:

$$\begin{aligned} I_A(Q^2) &= \frac{M^2}{8\pi^2\alpha}\int_{\nu_0}^{\infty}(1-x)(\sigma_{1/2} - \sigma_{3/2})\frac{d\nu}{\nu} \\ &= \frac{2M^2}{Q^2}\int_0^{x_0}(g_1 - \gamma^2 g_2)dx, \qquad (1.127) \\ I_B(Q^2) &= \frac{M^2}{8\pi^2\alpha}\int_{\nu_0}^{\infty}\frac{1-x}{\sqrt{1+\gamma^2}}(\sigma_{1/2} - \sigma_{3/2})\frac{d\nu}{\nu} \\ &= \frac{2M^2}{Q^2}\int_0^{x_0}\frac{1}{\sqrt{1+\gamma^2}}(g_1 - \gamma^2 g_2)dx, \qquad (1.128) \\ I_C(Q^2) &= \frac{M^2}{8\pi^2\alpha}\int_{\nu_0}^{\infty}(\sigma_{1/2} - \sigma_{3/2})\frac{d\nu}{\nu} \\ &= \frac{2M^2}{Q^2}\int_0^{x_0}\frac{1}{1-x}(g_1 - \gamma^2 g_2)dx. \qquad (1.129) \end{aligned}$$

Plots of the different GDH integrals, as produced with MAID 2000 extended version [27], are shown in Fig. 1.10. Note that variations between the different GDH integrals are significant. Therefore when comparing results from various theoretical models and experimental data, it is paramount to specify which definition is being employed.

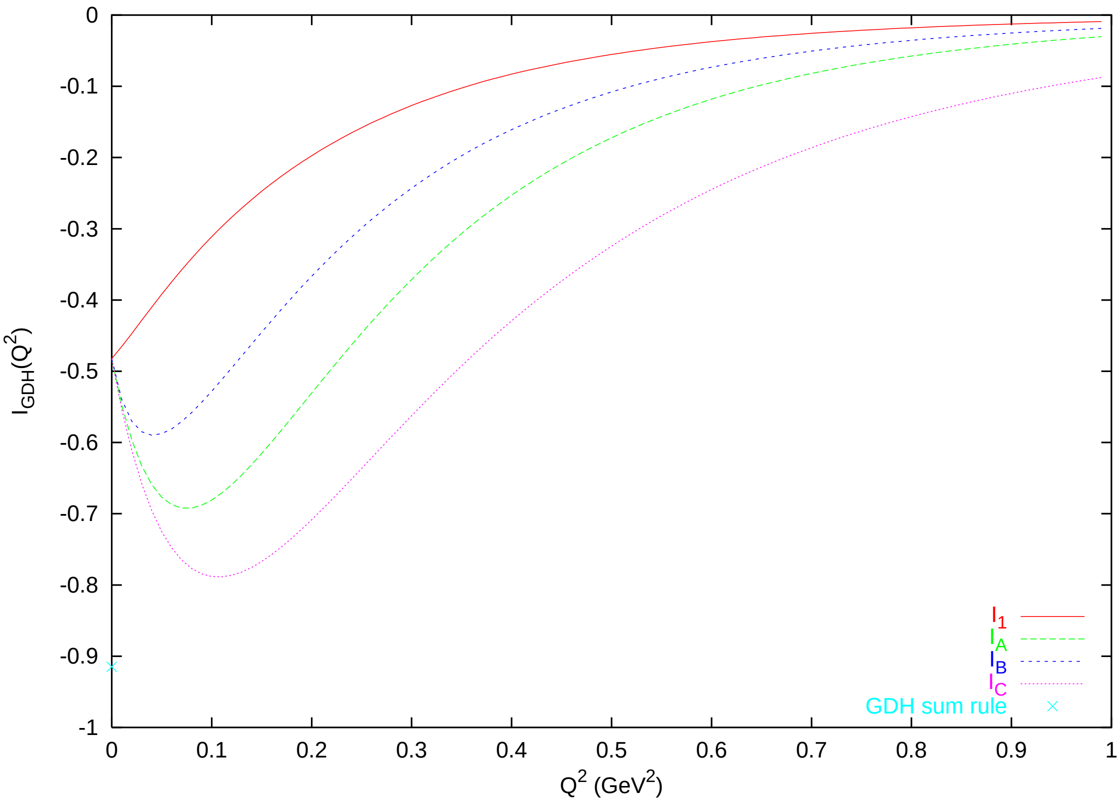

Figure 1.10: The GDH integrals I_1, I_A, I_B, and I_C for the neutron, integrated up to $W_{\rm max} = 2$ GeV, generated with MAID 2000 extended version [27]. The $\times$ at the real photon point ($Q^2 = 0$) is the value of the GDH sum rule.

1.11 Chiral Perturbation Theory

1.11.1 Chiral Symmetry

The Lagrangian for a massless Dirac particle is [28]

$$\mathcal{L} = \overline{\psi} i \partial\!\!\!/ \psi. \tag{1.130}$$

The Dirac wave function ψ can be separated into components of definite chirality (handedness),

$$\psi = \psi_L + \psi_R, \quad \psi_{L,R} = \Gamma_{L,R}\psi, \tag{1.131}$$

where $\Gamma_{L,R} = (1 \pm \gamma^5)/2$ are the left- and right-handed chirality projection operators, respectively. They obey the following relationships:

$$\Gamma_L + \Gamma_R = 1, \quad \Gamma^2_{L,R} = \Gamma_{L,R}, \quad \Gamma_L\Gamma_R = \Gamma_R\Gamma_L = 0, \tag{1.132}$$

which follow from properties of the Dirac γ-matrices [3]. A massless particle's chirality is a Lorentz-invariant. Two observers in different frames of reference will see the same chirality for a particle. A typical example in the Standard Model is the neutrino which always appears left-handed. The Lagrangian $\mathcal{L}$ is invariant under the global chiral phase transformations

$$\psi_{L,R}(x) \to \exp(-i\alpha_{L,R})\psi_{L,R}(x), \tag{1.133}$$

where $\alpha_{L,R}$ are arbitrary real constants. By virtue of Noether's theorem, the following conserved currents result:

$$J^\mu_{L,R} = \overline{\psi}_{L,R}\gamma^\mu\psi_{L,R}. \tag{1.134}$$

The corresponding chiral charges are defined as

$$Q_{L,R} = \int d^3x J^0_{L,R}(x). \tag{1.135}$$

Linear combinations of the chiral currents provide the vector current,

$$V^\mu = J^\mu_L + J^\mu_R = \overline{\psi}\gamma^\mu\psi, \tag{1.136}$$

and the axial-vector current,

$$A^\mu = J^\mu_L - J^\mu_R = \overline{\psi}\gamma^\mu\gamma^5\psi. \tag{1.137}$$

In a similar fashion, the vector charge Q and axial-vector charge Q_5 are

$$Q = Q_L + Q_R, \quad Q_5 = Q_L - Q_R. \tag{1.138}$$

The vector charge Q and axial-vector charge Q_5 are simply the sum and difference, respectively, of left- and right-handed particles.

1.11.2 Chiral Perturbation Theory

Chiral Perturbation Theory (ChPT) [28, 29] is an effective field theory that requires global chiral symmetry of the Lagrangian. The quarks are considered massless particles. Pions and kaons are the Goldstone bosons under SU(3) symmetry breaking. They are the degrees of freedom of the effective theory. In Heavy Baryon Chiral Perturbation Theory (HBχPT) the nucleons are considered infinitely heavy.

1.11.3 The GDH Sum Rule at Low Q^2

From $Q^2 = 0$ to about 0.2 GeV^2, the GDH sum rule can be described in the language of ChPT in terms of hadronic degrees of freedom. Bernard *et al.* [30] calculated the slope of I_C at $Q^2 = 0$ in ChPT to order p^3 where p is an arbitrary external momentum. They obtained[1]:

$$I'_C(0) = \frac{1}{6} M^2 \left(\frac{g_A}{4\pi m_\pi f_\pi} \right)^2 = 9.1 \text{ GeV}^{-2}, \tag{1.139}$$

where $g_A = 1.26$ is the axial coupling constant, $f_\pi = 92.4$ MeV is the pion decay constant, $M = 938$ MeV is the proton mass, and $m_\pi = 138$ MeV is the pion mass. Ji

[1] The exact relationship between I_C and Bernard *et al.* [30] GDH integral is $I_C(Q^2) = \frac{M^2}{8\pi^2\alpha} I_{BKM}(q^2)$. Moreover, their slope for the GDH integral is taken with respect to $q^2 = -Q^2$. Hence, the sign flip.

et al. [31] performed the order p^4 calculation and found:

$$\begin{aligned} I'_A(0) &= \frac{1}{6}M^2\left(\frac{g_A}{4\pi m_\pi f_\pi}\right)^2\left[1-\frac{\pi}{4}\frac{m_\pi}{M}(13+2\tau_3+2\kappa_V)\right] \\ &= \begin{cases} -14.5\ \mathrm{GeV}^{-2} \text{ for the proton} \\ -10.3\ \mathrm{GeV}^{-2} \text{ for the neutron} \end{cases}, \end{aligned} \tag{1.140}$$

$$\begin{aligned} I'_1(0) &= \frac{1}{6}M^2\left(\frac{g_A}{4\pi m_\pi f_\pi}\right)^2\frac{\pi}{8}\frac{m_\pi}{M}[1+3\kappa_V+2\tau_3(1+3\kappa_S)] \\ &= \begin{cases} 7.0\ \mathrm{GeV}^{-2} \text{ for the proton} \\ 5.7\ \mathrm{GeV}^{-2} \text{ for the neutron} \end{cases}, \end{aligned} \tag{1.141}$$

where $\kappa_V = 3.706$ and $\kappa_S = -0.120$ are the isovector and isoscalar components of the anomalous magnetic moment, respectively. The isospin τ_3 is +1 and -1 for the proton and neutron, respectively. The difference between the $\mathcal{O}(p^3)$ and $\mathcal{O}(p^4)$ calculations is quite significant. In fact, the next-to-leading order contribution to the GDH integral is more than twice the leading order and of opposite sign! This explains the sign reversal of the slope when going from order p^3 to order p^4.

1.12 GDH Integral from ^{3}He

1.12.1 Introduction

C. Ciofi degli Atti and S. Scopetta [32,33] pointed out that the neutron spin structure function $g_1^n(x)$, asymmetry $A_n(x)$, and Gerasimov-Drell-Hearn (GDH) integral may be reasonably extracted from those of ^{3}He in the resonance and deep inelastic scattering (DIS) region if nuclear effects are taken into account.

1.12.2 No Nuclear Effects

To a good approximation, the ^{3}He nucleus sits in a pure symmetric S state and the spin structure functions and asymmetries are simply:

$$g_1^{^3\mathrm{He}}(x) = g_1^n(x), \tag{1.142}$$

$$A_{^3\mathrm{He}}(x) = f_n A_n(x), \tag{1.143}$$

where $x = Q^2/2M\nu$ is the Bjorken variable, $A_n(x) = 2xg_1^n(x)/F_2^n(x)$ is the neutron asymmetry, and $f_n = F_2^n(x)/(2F_2^p(x) + F_2^n(x))$ is the neutron dilution factor.

1.12.3 The Effective Nucleon Polarizations

In a more realistic model of the ^{3}He nucleus, the ^{3}He wave function is an admixture of a symmetric S state, a state S' of mixed symmetry, and a state D of mixed symmetry. The ^{3}He nucleus has even parity ($J^P = \frac{1}{2}^+$). Conservation of parity requires that the P-state only enters in second order in the wave function. Hence the P-state contribution is negligible (see pp. 180-190 of Ref. [34] and p. 320 of Ref. [35]). If Fermi motion and binding effects are ignored, the spin structure functions and asymmetries are written:

$$g_1^{^3\mathrm{He}}(x) = 2p_p g_1^p(x) + p_n g_1^n(x), \tag{1.144}$$

$$A_{^3\mathrm{He}}(x) = 2f_p p_p A_p + f_n p_n A_n, \tag{1.145}$$

where

$$f_N = F_2^N(x)/(2F_2^p(x) + F_2^n(x)), \tag{1.146}$$

$$A_N(x) = 2xg_1^N(x)/F_2^N(x). \tag{1.147}$$

Here, f_N is the nucleon dilution factor, $A_N(x)$ is the nucleon asymmetry, and p_N is the effective nucleon polarization given by:

$$p_p = P_p^{(+)} - P_p^{(-)} = -0.028 \pm 0.004, \tag{1.148}$$

$$p_n = P_n^{(+)} - P_n^{(-)} = 0.86 \pm 0.02, \tag{1.149}$$

where $P_n^{(+)} = 1 - \Delta$ and $P_n^{(-)} = \Delta$ are the probabilities of having a neutron with spin parallel and antiparallel with the spin of the ^{3}He nucleus, respectively. $P_p^{(\pm)} = \frac{1}{2} \mp \Delta'$ are the equivalent quantities for the proton. The quantities $\Delta = \frac{1}{3}(P_{S'} + 2P_D)$ and $\Delta' = \frac{1}{6}(P_D - P_{S'})$ are model-dependent. A fit on world calculations of the three-nucleon system yields $\Delta = 0.07 \pm 0.01$ and $\Delta' = 0.014 \pm 0.002$ [36]. Afnan and Birrell [37] solved the Faddeev equations [38–41] in momentum space with a unitary pole expansion (UPE) of a Reid soft core (RSC) nucleon-nucleon potential [42] using the partial wave decomposition of Derrick and Blatt [35] involving basis states of definite symmetry (S=symmetric, A=antisymmetric, and M=mixed) for the ^{3}He wave function. They obtained the percentage probabilities $P_S = 89.2\%$, $P_{S'} = 1.6\%$, and $P_D = 9.1\%$ for the three-body system. The ^{3}He nucleus is mostly in the S state, in which both protons carry opposite spins and cancel each other. The effective polarization of the neutron contributes the most to the overall nuclear polarization.

1.12.4 The Convolution Approach

Fermi motion and binding effects are included by using the convolution approach of C. Ciofi degli Atti *et al.* [32] in which the spin structure functions of the individual nucleons are weighted by the nuclear spectral functions of ^{3}He, integrated over energy, momentum, and the Bjorken variable, then finally summed over all constituent nucleons. The full expression is presented in Ref. [32]. The formula is based on two different prescriptions from Refs. [41] and [44], that nonetheless yield the same result in the Bjorken limit. The nuclear spectral functions are related to the effective nucleon polarizations. The spin structure functions obtained with the convolution approach differ from those of Eq. (1.144) by at most 4% for $x \leq 0.9$ in the DIS region. The disagreement is more pronounced in the resonance region where Fermi motion smears the peaks of the dominant resonances (see Fig. 1.11).

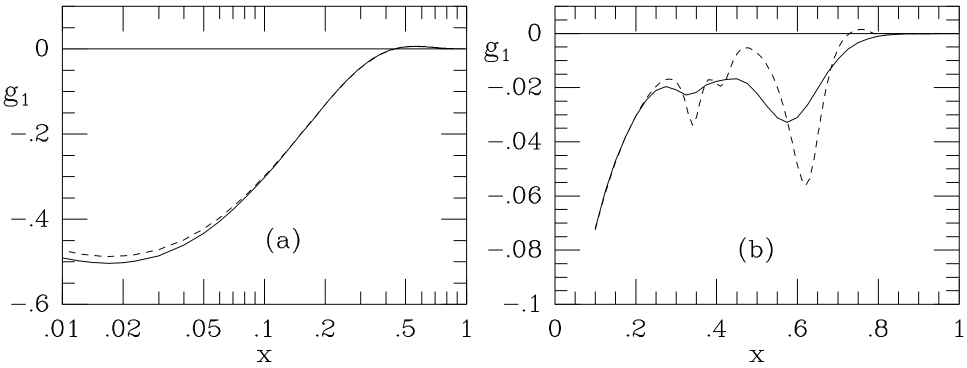

Figure 1.11: Comparison of $g_1^{^3\mathrm{He}}$ calculated with Fermi motion and binding effects (solid curve) vs. effective nucleon polarizations only (dashed curve) in (a) DIS at $Q^2 = 10$ GeV^2 and (b) resonance at $Q^2 = 1$ GeV^2. The figure is taken from Ref. [33].

1.12.5 First Moment and the GDH Integral

The first moment $\Gamma^N = \int_0^1 g_1^N(x)dx$ of the structure function $g_1^N(x)$ is of interest because it enters the expression for the Bjorken sum rule [7]:

$$\Gamma^p - \Gamma^n = \int_0^1 \left(g_1^p(x) - g_1^n(x)\right) dx = \frac{1}{6}\frac{g_A}{g_V}\left(1 - \frac{\alpha_S}{\pi}\right) \tag{1.150}$$

where g_A and g_V are the axial and vector coupling constants respectively from neutron beta decay, and α_S is the strong coupling constant. The importance of the Bjorken

Sum Rule as a proving ground for our present knowledge of Quantum Chromodynamics (QCD) in the high Q^2 regime can hardly be overemphasized. At low Q^2, the integrated quantity of interest is the Gerasimov-Drell-Hearn sum rule [16]:

$$I_{\rm GDH}(Q^2=0) = \int_{\nu_{thr}}^{\infty} \frac{d\nu}{\nu} \left(\sigma_{1/2}(\nu, Q^2=0) - \sigma_{3/2}(\nu, Q^2=0)\right) = -\frac{2\pi^2\alpha}{M^2}\kappa^2 \quad (1.151)$$

where $\nu_{thr} = (Q^2 + 2m_\pi M + m_\pi^2)/2M$ is the pion production threshold energy, $\sigma_{1/2}$ and $\sigma_{3/2}$ are the virtual photoabsorption cross sections with photon-nucleon total helicity 1/2 and 3/2, respectively, α is the fine structure constant, M is the hadron mass, and κ is the anomalous magnetic moment of the nucleon. The GDH integral:

$$I_{\rm GDH}(Q^2) = \int_{\nu_{thr}}^{\infty} \frac{d\nu}{\nu} \left(\sigma_{1/2}(\nu, Q^2) - \sigma_{3/2}(\nu, Q^2)\right) \quad (1.152)$$

is measured at finite Q^2 and can be related to the spin structure function $g_1^A(\nu, Q^2)$ of a spin 1/2 target A by:

$$I^A(Q^2) = \frac{8\pi^2\alpha}{M} \int_{\nu_{thr}}^{\infty} \frac{d\nu}{\nu} \frac{(1+Q^2/\nu^2)}{K} g_1^A(\nu, Q^2) \quad (1.153)$$

where K is the virtual photon flux. The integrated quantities, $\Gamma^N(Q^2)$ and $I^A(Q^2)$, differ by at most 5% when Fermi motion and binding effects are compared with the nuclear effects of effective nucleon polarizations only. See Fig. 1.12. Therefore the following expressions:

$$\tilde{\Gamma}^n(Q^2) = \frac{1}{p_n}\left(\Gamma^{^3{\rm He}}(Q^2) - 2p_p\Gamma^p(Q^2)\right), \quad (1.154)$$

$$\tilde{I}^n(Q^2) = \frac{1}{p_n}\left(I^{^3{\rm He}}(Q^2) - 2p_p I^p(Q^2)\right) \quad (1.155)$$

were used to extract integrated quantities of the neutron from ^{3}He. g_1^p from the MAID model [27] was used as input.

1.13 The GDH Integral for the Proton

The GDH integral for the proton has recently been measured at MAMI (Mainz) by direct measurement of the total photoabsorption cross section of circularly polarized real photons produced by bremsstrahlung of longitudinally polarized electrons, in the

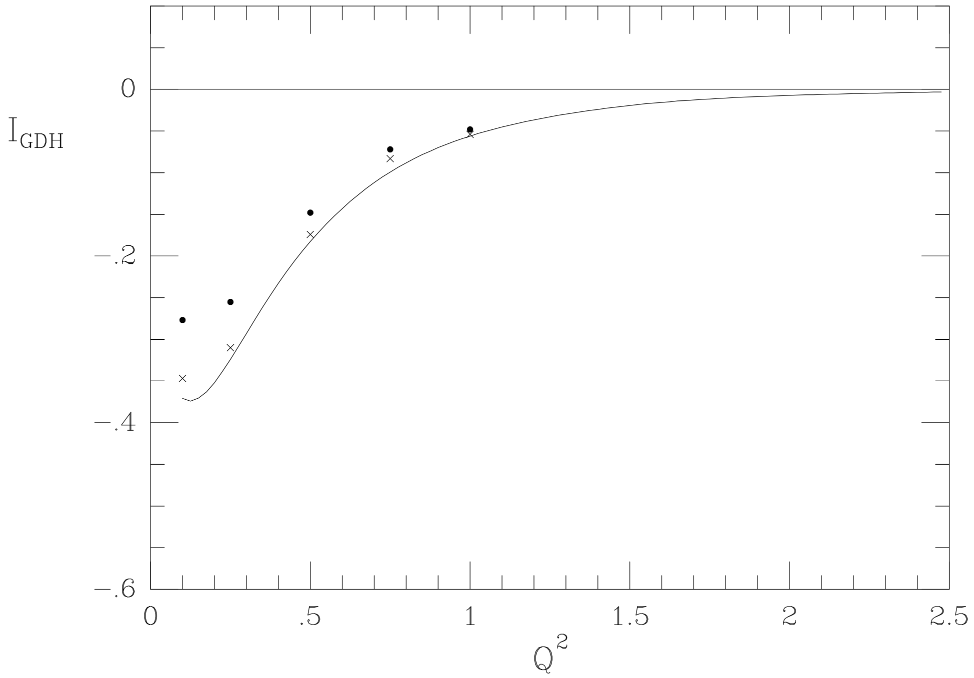

Figure 1.12: The crosses represent the GDH integral for the neutron $\tilde{I}^n(Q^2)$ obtained with Eq. (1.155) where the model of Burkert *et al.* [45] was used for g_1^p and the convolution formula of Ciofi degli Atti *et al.* [33] for $g_1^{^3\mathrm{He}}$ coupled with Eq. (1.153) to get $I^p(Q^2)$ and $I^{^3\mathrm{He}}(Q^2)$, respectively. The solid curve represents the GDH integral for the neutron $I^n(Q^2)$ obtained with the model of Burkert *et al.* [45] for g_1^n and Eq. (1.153). The dots represent the GDH integral for ^{3}He as acquired previously. Note $\tilde{I}^n(Q^2)$ and $I^n(Q^2)$ differ only by at most 5%. The figure is taken from Ref. [33].

energy range $200 < E_\gamma < 800$ MeV, on longitudinally polarized protons [46]. The GDH sum rule for the proton is

$$\int_{\nu_0}^{\infty} \frac{d\nu}{\nu}(\sigma_{3/2} - \sigma_{1/2}) = \frac{2\pi^2\alpha}{M^2}\kappa^2 = 205\ \mu\mathrm{b}, \tag{1.156}$$

where the integral on the left is adopted for the GDH integral. The Mainz measurement for the GDH integral between 200 and 800 MeV was 226±5 (stat)±12 (syst) μb. Outside the measured range of energies, theoretical models may be reasonably employed to predict the missing contributions to the GDH integral. The UIM model [27] (also known as the MAID model) gives -30 μb below 200 MeV and 40 μb in the range $800 < E_\gamma < 1650$ MeV. Beyond 1650 MeV, Bianchi and Thomas [47] predict a contribution of -26 μb. The resulting GDH integral is 210 μb, a value consistent with the GDH sum rule of 205 μb within experimental errors. Fig. 1.13 shows the GDH inte-

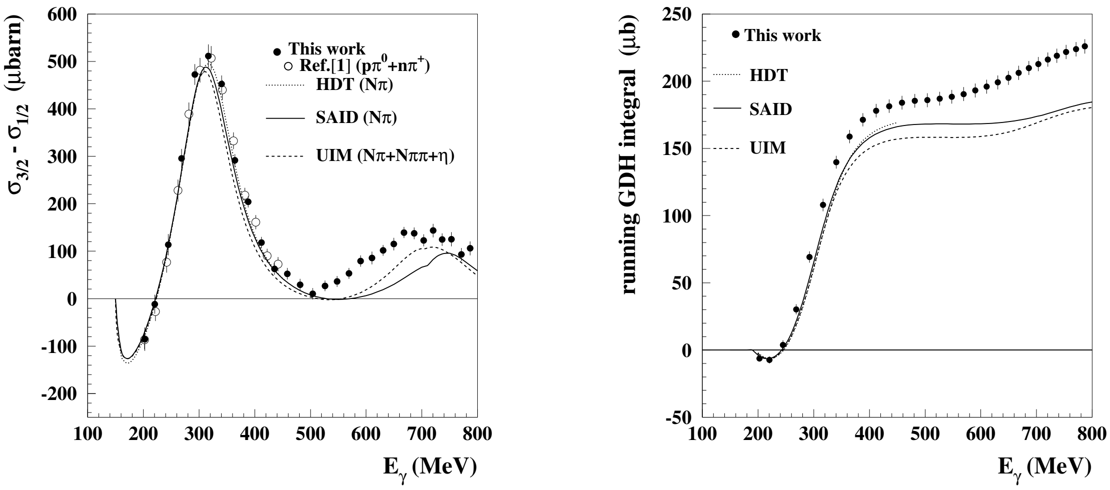

Figure 1.13: GDH integrand for the proton (left) and running GDH integral (right). "This work" refers to the data of Mainz [46] and "Ref.[1]" is a reference to an earlier measurement by the same group but at a more restricted range of photon energies. HDT [48] and SAID [49] are multipole analysis models and UIM [27] is a unitary isobar model.

grand (left) and the running GDH integral (right) along with some theoretical model predictions. Notice that the MAID model (curve labeled UIM in Fig. 1.13) gives a reasonable fit over the bulk of the data region. The contribution to the GDH integral at higher photon energies, where the theory begins to diverge from the data, is in fact suppressed by a factor of $1/\nu$. This gives us confidence that we can make a reasonable correction to the ^{3}He data using the MAID model. In the final result, systematic errors due to this correction are included in the analysis of the GDH integrand for the neutron.

Chapter 2

EXPERIMENTAL SETUP

2.1 Continuous Electron Beam Accelerator Facility

2.1.1 Injector, Linac, and ARC

The Continuous Electron Beam Accelerator Facility (CEBAF), shown in Figure 2.1 is an electron accelerator with a 45-MeV injector and two 500-MeV linear accelerators (linacs) that can deliver high duty cycle, polarized electron beams simultaneously in three end stations (Hall A, B, and C) after a maximum of five recirculation passes. The polarized beam is produced by a strained GaAs photocathode. A chopper with slits of different sizes is placed in front of the beam to allow for delivery of different currents in each hall. The chopper's frequency is 1.497 GHz. After the chopper, the beam enters the injector, a set of two and a quarter cryomodules, where it is accelerated to 45 MeV. Each cryomodule consists of eight superconducting niobium cavities maintained at 2 K by liquid helium supplied by the Central Helium Liquefier. The beam then enters the North Linac, a set of twenty cryomodules, where it is accelerated by an additional 0.5 GeV. Before entering the recirculation arcs, the beam is split into components of different momenta (from different number of recirculation passes). This is done because each momentum requires a different bending magnetic field. Hence, there are five separate arcs with different magnet settings. The beam, as a whole, is bent by the East Arc in a half-circle. The beam is then recombined and enters the South Linac, another string of twenty cryomodules, where it is accelerated

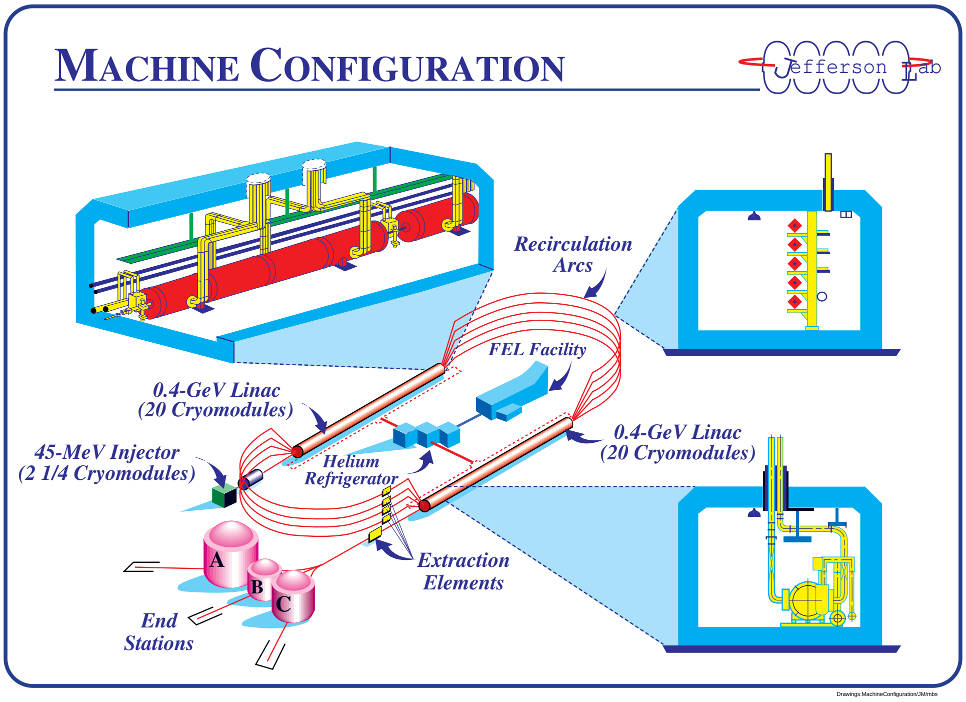

Figure 2.1: The Continuous Electron Beam Accelerator Facility (CEBAF) features a 45-MeV injector and two 500-MeV linear accelerators (linacs) that can deliver high duty cycle, polarized electrons beam simultaneously in three end stations (Hall A, B, and C) after a maximum of five recirculation passes.

by an additional 0.5 GeV. Now, the beam is bent in another half-circle, the West Arc, back to the North Linac. The cycle is repeated up to a total of five recirculation passes or until the desired beam energy is achieved. At which point the beam is extracted from the accelerator and split among the halls at the Beam Switch Yard (BSY).

2.1.2 Beam Energy and Spin Precesssion

The actual relationship between single linac energy and final beam energy at an end station is:

$$E = (2n + \alpha)E_l, \tag{2.1}$$

with some minor corrections due to synchrotron radiation at the recirculating arcs. E_l is the single linac energy, n is the number of recirculation passes, and $\alpha = 0.1125$

is the ratio of injector energy to linac energy. In addition, the spin of the electron in its rest frame will precess due to Thomas precession [52]:

$$\Delta\theta = \gamma \left(\frac{g-2}{2}\right) \Delta\phi, \tag{2.2}$$

where $\Delta\theta$ is the precession of the spin in the electron rest frame, $\gamma = E/m_e c^2$ and $m_e = 0.510998902$ MeV/c^2 is the electron rest mass, $(g-2)/2 = (115965.77 \pm 0.35) \times 10^{-8}$ is the anomalous magnetic moment of the electron, and $\Delta\phi$ is the rotation angle of the momentum in the lab frame. The single linac energy can be conveniently adjusted anywhere from 200 to 600 MeV in order to allow for maximal longitudinal polarization of the beam in all three halls [53–55].

2.1.3 Mott Polarimeter

The Mott polarimeter is a device used to measure beam polarization at the injector. It is based on the principle of Mott polarimetry in which the left-right asymmetry in the cross sections of the scattered electrons is exploited to infer the polarization of the initial incident beam. The Injector Group [56] at Jefferson Lab operates a 5 MeV Mott polarimeter [57–59]. The projectile is a polarized electron beam and the target is a gold foil (Au, Z=79) of thickness 1 μm. The rate achieved is 1 kHz/μA. The scattering angle is at 172.6° where the analyzing power is at a maximum, -0.52, but there is a dilution factor of 0.006 due to multiple scatterings. A schematic of the polarimeter is shown in Fig. 2.2. The polarimeter is equipped with two detectors shown in Fig 2.3.

Principle of Operation

The differential cross section for Mott scattering of a polarized electron from a heavy nucleus is given by [60]:

$$\sigma(\theta, \phi) = I(\theta)[1 + S(\theta)\boldsymbol{P} \cdot \hat{\boldsymbol{n}}], \tag{2.3}$$

where $I(\theta) = |f|^2 + |g|^2$ is the differential cross section for a beam with no initial transverse polarization.

$$S(\theta) = i\frac{fg^* - f^*g}{|f|^2 + |g|^2} = \frac{2\ \mathrm{Im}(f^*g)}{|f|^2 + |g|^2} \tag{2.4}$$

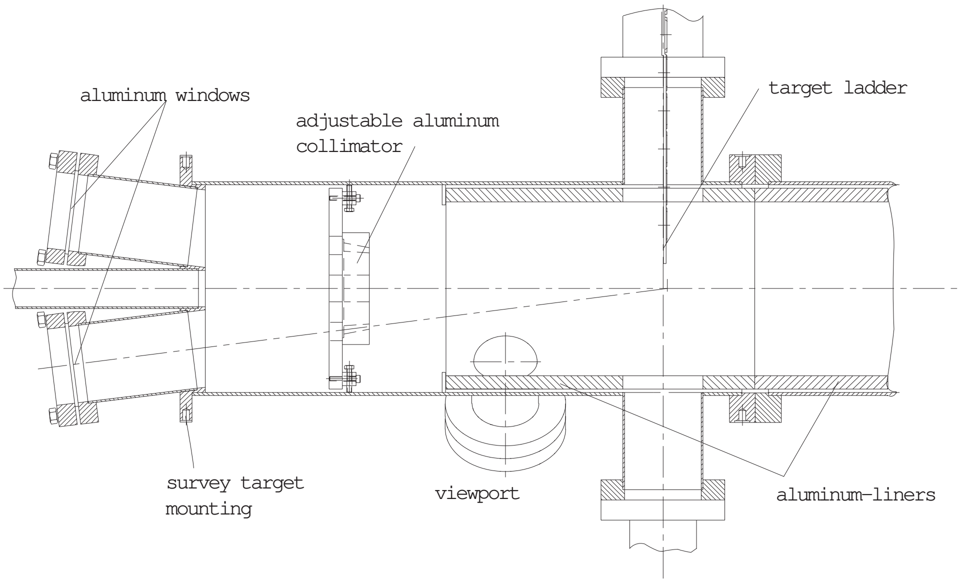

Figure 2.2: Cross section of the Jefferson Lab 5 MeV Mott polarimeter. The polarized electron beam enters through an entrance on the left and travels along the central axis. The beam is scattered by a gold foil target lowered into the scattering chamber with a target ladder. The scattered electrons are registered by two detectors placed at $\pm 172.6°$ from the incident beam direction.

is real and is the so-called Sherman function [61] or analyzing power. It establishes the link between asymmetry and polarization. Plots of the Sherman function $S(\theta)$ for several electron kinetic energies are graphed in Fig. 2.4. Note the location in scattering angle $\theta = 172.6°$ of the Jefferson Lab Mott polarimeter which corresponds to a maximum analyzing power $S(\theta)$. The complex scattering amplitudes f and g, defined in Ref. [60], are matrix elements of the scattering matrix, and $\boldsymbol{P}$ is the initial polarization vector of the electron. Other useful combinations of the functions f and g are the so-called spin-rotation functions:

$$T(\theta) = \frac{|f|^2 - |g|^2}{|f|^2 + |g|^2}, \tag{2.5}$$

$$U(\theta) = \frac{fg^* - f^*g}{|f|^2 + |g|^2} = \frac{2\ \mathrm{Re}(fg^*)}{|f|^2 + |g|^2}. \tag{2.6}$$

S, T and U satisfy the identity $S^2 + T^2 + U^2 = 1$. Together they determine how the polarization $\boldsymbol{P}$ is altered by scattering.

A derivation of the differential cross section for Mott scattering has traditionally been carried out by solving the Dirac equation with a Coulomb potential. The am-

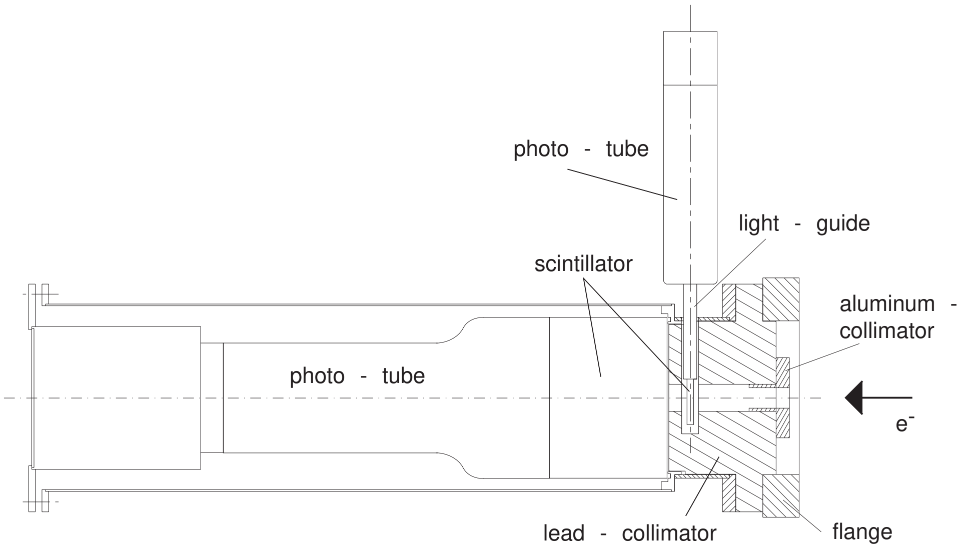

Figure 2.3: Cross section of a detector for the Jefferson Lab 5 MeV Mott polarimeter. The scattered electron enters through an aluminum collimator, with an angular acceptance of 1° in θ and 40° in ϕ, on the right and triggers a signal in a NE102a plastic scintillator attached to a phototube. A second phototube is mounted at right angle to the primary one. Its signal is used as a trigger and serves to eliminate background noise from stray radiation.

plitudes are broken down in partial-wave analysis. The literature on the subject is extensive; see Refs. [60, 63–65].

Experimental Technique

Consider the equipment setup shown in Fig. 2.5 for a Mott polarimeter. Assume perfect alignment and negligible instrumental errors. The number of counts in D_1 and D_2 for a spin-up electron $e\uparrow$ is [60]

$$L_\uparrow = nN\epsilon_1\Omega_1 I(\theta)(1 + PS(\theta)), \tag{2.7}$$

$$R_\uparrow = nN\epsilon_2\Omega_2 I(\theta)(1 - PS(\theta)), \tag{2.8}$$

respectively. Here, n is the number of incident electrons, N is the number of target nuclei per unit area, and P is the polarization of the incident beam. ϵ and Ω are the detector efficiency and angular acceptance, respectively. If the polarization of the incident electron beam is reversed, the number of counts for a spin-down electron $e\downarrow$

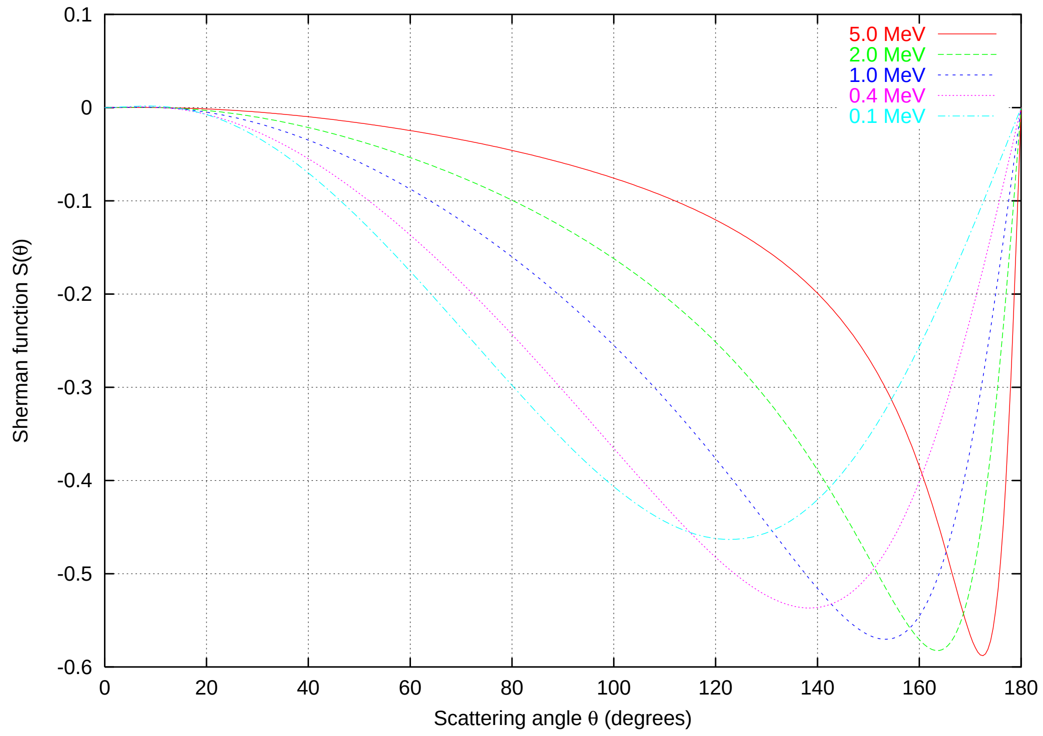

Figure 2.4: Plots of the Sherman function $S(\theta)$ for electron kinetic energies of 5.0, 2.0, 1.0, 0.4 and 0.1 MeV generated with Formula (1A-402) of Ref. [62] for a point nucleus with no screening.

is

$$L_\downarrow = n'N'\epsilon_1\Omega_1 I(\theta)(1 - PS(\theta)), \tag{2.9}$$

$$R_\downarrow = n'N'\epsilon_2\Omega_2 I(\theta)(1 + PS(\theta)). \tag{2.10}$$

By introducing the quantities N^+ and N^-,

$$N^+ = \sqrt{L_\uparrow R_\downarrow} = \sqrt{nn'NN'\epsilon_1\epsilon_2\Omega_1\Omega_2} I(1 + PS), \tag{2.11}$$

$$N^- = \sqrt{R_\uparrow L_\downarrow} = \sqrt{nn'NN'\epsilon_1\epsilon_2\Omega_1\Omega_2} I(1 - PS), \tag{2.12}$$

the asymmetry A can be written as

$$A = \frac{N^+ - N^-}{N^+ + N^-} = \frac{(1 + PS) - (1 - PS)}{(1 + PS) + (1 - PS)} = PS. \tag{2.13}$$

This equation is affectionately called the "APS rule" and relates the polarization P to the asymmetry A via the Sherman function S. Note that all instrumental systematics cancel out.

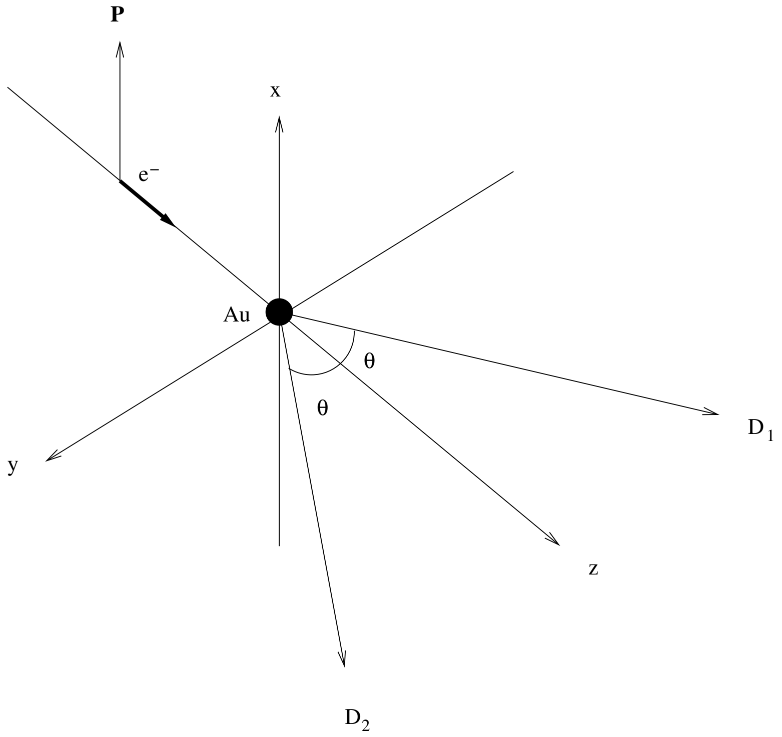

Figure 2.5: Detector arrangement for Mott polarimetry. The incident electron e^- with polarization $\boldsymbol{P}$ is elastically scattered from nuclei in a gold foil and picked up by detectors D_1 and D_2 at an angle θ to the left and right of the beam line, respectively.

Using the 5 MeV Mott polarimeter, the Injector Group can measure beam polarization at the injector with an instrumental precision of 0.5% and with an instrumental helicity-correlated false asymmetry of $(4 \pm 6) \times 10^{-4}$ [59].

2.2 Beamline in Hall A

Hall A [50], the largest of the three end stations, has a diameter of 53 m. The layout of the Hall showing the two High Resolution Spectrometers is shown in Fig. 2.6. The electron beam from the beamline is incident upon the target on the target platform in the center of the hall. The beam is then scattered into one of the spectrometers. The two spectrometers were designed for coincidence (e,e'X) experiments with the nominal Electron arm to the left looking from above and the Hadron arm to the right. For this experiments both spectrometers were used to detect electrons in single arm data acquisition (DAQ) mode and the Electron and Hadron arms will be referred to as the

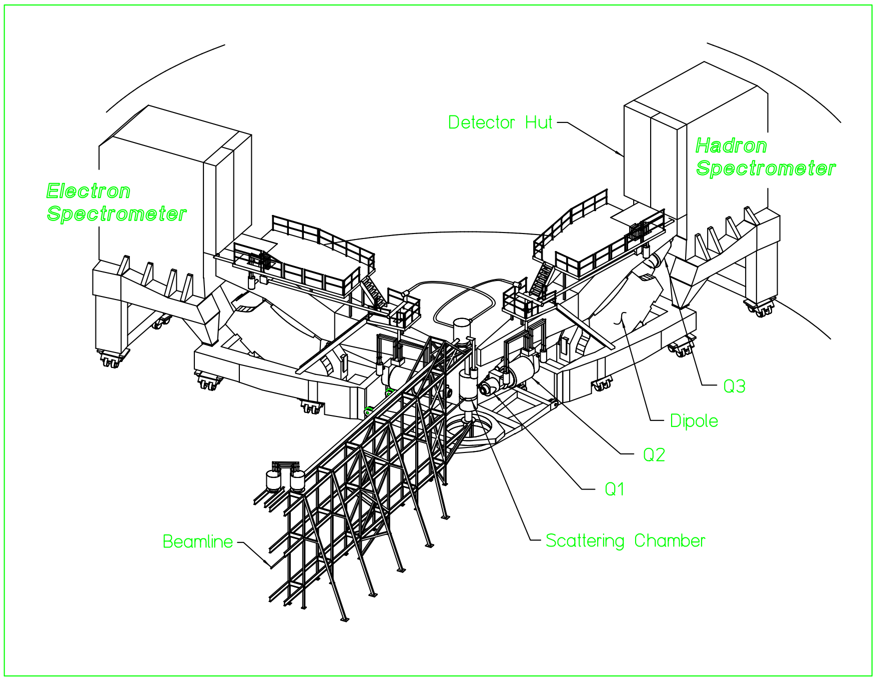

Figure 2.6: Layout of Hall A showing the beamline, the target platform in the center, and the Electron and Hadron spectrometers.

Left and Right spectrometers, respectively. The scattered electrons are then detected in detectors housed in the detector hut of each spectrometer. The left spectrometer can be moved to a central scattering angle from 12.5° to 165° from the beamline. The Right spectrometer has an angular range of 12.5° to 130°.

2.2.1 Beamline

Fig. 2.7 shows the schematic of the main elements of the beamline. The beam parameters are summarized in Table 2.1 [66].

2.2.2 Absolute Beam Energy Measurement

The ARC Method

The beam enters Hall A through a 40-m arc section with a bend angle $\theta = 34.3318°$ as shown in Fig. 2.8. A series of eight dipoles and nine quadrupoles are stationed along the arc section to bend and focus the beam, respectively. The beam energy can be calculated from accurate knowledge of the bend angle and magnetic field in the

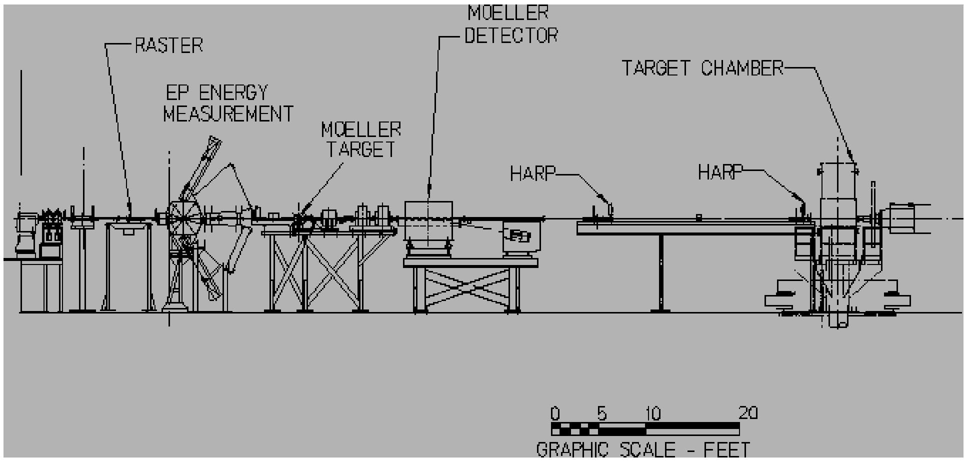

Figure 2.7: Hall A beamline elements from shield wall to target chamber.

Energy	0.8 – 6.0 GeV
Energy spread	2.5×10^{-5}
Current	1 – 190 μA
Emittance	2×10^{-9} m-rad
Duty cycle	100% CW
Instantaneous size	35 μm

Table 2.1: Beam parameters.

dipoles.

An electron carrying charge e and velocity $\boldsymbol{v}$ in a magnetic field $\boldsymbol{B}$ is subject to the Lorentz force $\boldsymbol{F}$:

$$\boldsymbol{F} = \frac{d\boldsymbol{p}}{dt} = e\boldsymbol{v} \times \boldsymbol{B}. \tag{2.14}$$

The incremental change in momentum Δp for a small time increment Δt is

$$\Delta p = e\Delta l_{\parallel} B_{\perp}, \tag{2.15}$$

where $\Delta l_{\parallel}$ is the component of the displacement along the path length and $B_{\perp}$ is the magnetic field component orthogonal to the path length. The change in momentum defines a small angle $\theta = \Delta p/p$. In addition, at high enough energy, the energy of the electron E is simply $E = pc$. It therefore follows that

$$E = \frac{0.299792}{\theta} \int dl_{\parallel} B_{\perp}, \tag{2.16}$$

where distances are measured in meters, magnetic fields in teslas, angles in radians, and the resulting energy is in GeV. ARC energy measurements taken in Hall A during E94-010 are shown in Table 2.2. The ARC method covers a beam energy range of 0.5

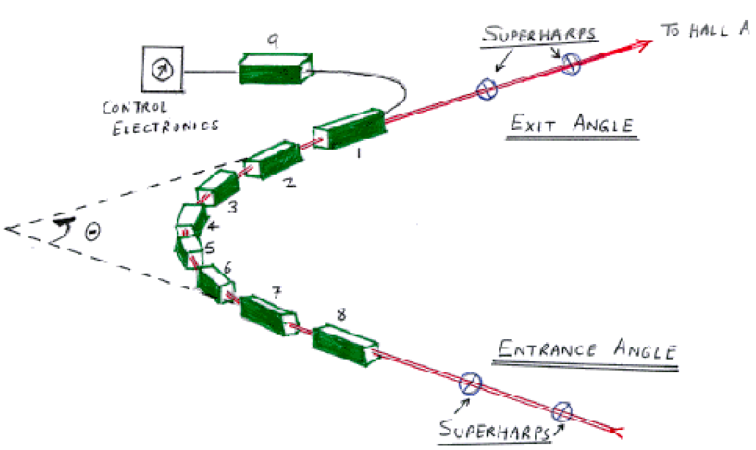

Figure 2.8: ARC equipment for absolute beam energy measurement in Hall A.

to 6 GeV with an accuracy of $\Delta p/p \leq 2 \times 10^{-4}$ (FWHM). The ARC equipment was built and installed by a group from CEA/DAPNIA of Saclay, France. Much technical information about the ARC apparatus in Hall A is available in Ref. [67].

The eP Method

The eP method for measuring beam energies utilizes the elastic reaction $p(e, e'p)$. The target is a rotating tape of CH_2 of thickness 10-30 μm. The electron and proton are detected in coincidence in silicon strip detectors with pitch 100 μm, augmented with scintillators and gas Cherenkov counters (CO_2). The eP equipment was built and installed by a group from CNRS/IN2P3 of Clermont-Ferrand, France. The beam energy is given by

$$E = M\left(\frac{\cos\theta_e + \sin\theta_e/\tan\theta_p - 1}{1 - \cos\theta_e}\right), \tag{2.17}$$

where θ_e and θ_p are the angles from the beamline of the scattered electron and scattered proton, respectively. The angle θ_p is fixed at 60° and θ_e varies with incident beam energy from 9° to 41°. The energy range covered is 0.5 to 6 GeV. The accuracy achieved is $\Delta p/p \leq 2 \times 10^{-4}$ (FWHM). A schematic of the eP apparatus is shown in Fig 2.9.

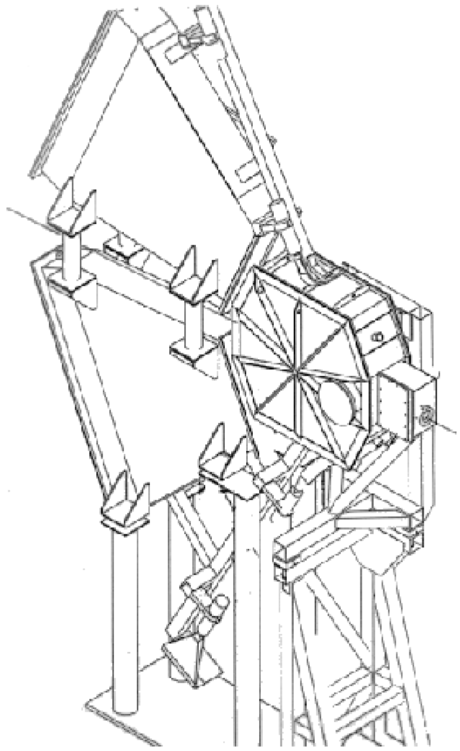

Figure 2.9: eP equipment for absolute beam energy measurement in Hall A. Beam enters from the right and exits from the left. The scattered electrons and protons are detected in the two vertical detection chambers.

2.2.3 Beam Position Monitors

The beam position monitors (BPMs) measure the beam position in the xy-plane (transverse to the beamline). This measurement is noninvasive, thus allowing continuous monitoring and adjustement of the beam position. Five BPMs are located between the Hall A shield wall and the target. However, the BPMs of primary interest for Hall A are IPM1H03A, located 7.524 m upstream of the target, and IPM1H03B, located 1.286 m upstream of the target. A BPM consists of a cavity with a four-wire antenna array tuned to the fundamental beam frequency of 1.497 GHz. Two wires are for the x-position and the other two for the y-position. A beam of charged particles

Hall A Beam Energy Measurements
E94-010 Oct-Dec 1998

Date	Mode	E_{nominal}	E_{eP}	E_{ARC}
Oct 24	Disp		3385	3379.7
Nov 3	Disp			1709.1
Nov 6	Disp	4255	4236.2	4232.64
Nov 20	Achr			4233.2
Dec 8	Disp	2594	2581.1	2578.8
Dec 8	Achr	2594		2582.33
Dec 17	Achr			5055.16
Dec 22	Achr			5055.82

Table 2.2: Table of energy measurements made in Hall A during E94-010. The mode indicates whether the energy tune was dispersive (Disp) or achromatic (Achr). All energies are in MeV.

(current) induces a signal in each wire. The asymmetry between the induced signals from the wires is proportional to the distance from the beam. The beam position can be determined within 100 μm for currents above 1 μA. A diagram of the Hall A BPM subsystem and its associated electronics is shown in Fig. 2.10.

2.2.4 Beam Current Monitors

The beam current monitors (BCMs) allow measurement of the beam current in Hall A. The Hall A beam current monitors consist of one Unser (Parametric Current Transformer) and two radio-frequency (RF) cavity monitors tuned at 1.497 GHz (beam frequency). The Unser has an absolute accuracy of $\pm$ 300 nA at 100 μA. The RF cavities have a non-linearity of less than 0.2%. A block diagram of the Hall A beam current monitors are shown in Fig. 2.11 and currents obtained with the BCMs during a typical run is shown in Fig. 2.12.

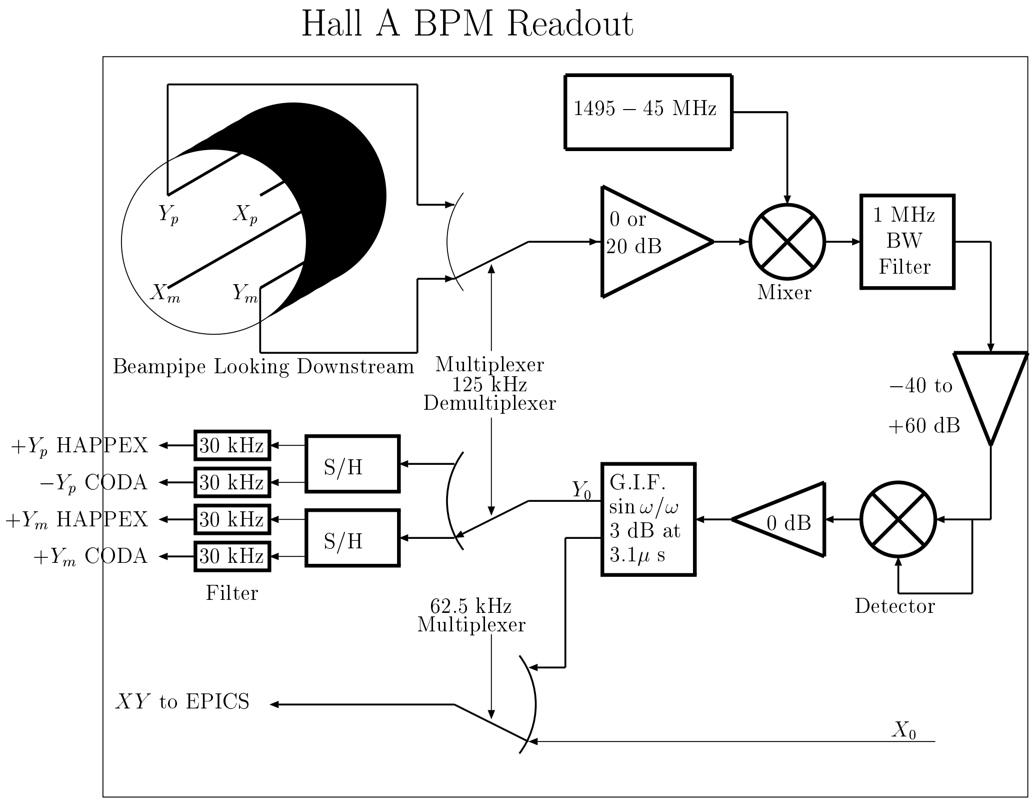

Figure 2.10: Hall A beam position monitors. The wire strip chambers use four wires pickup coils. Sums and differences are taken from the outputs to determine the average current and the mean beam x and y displacements from the central axis.

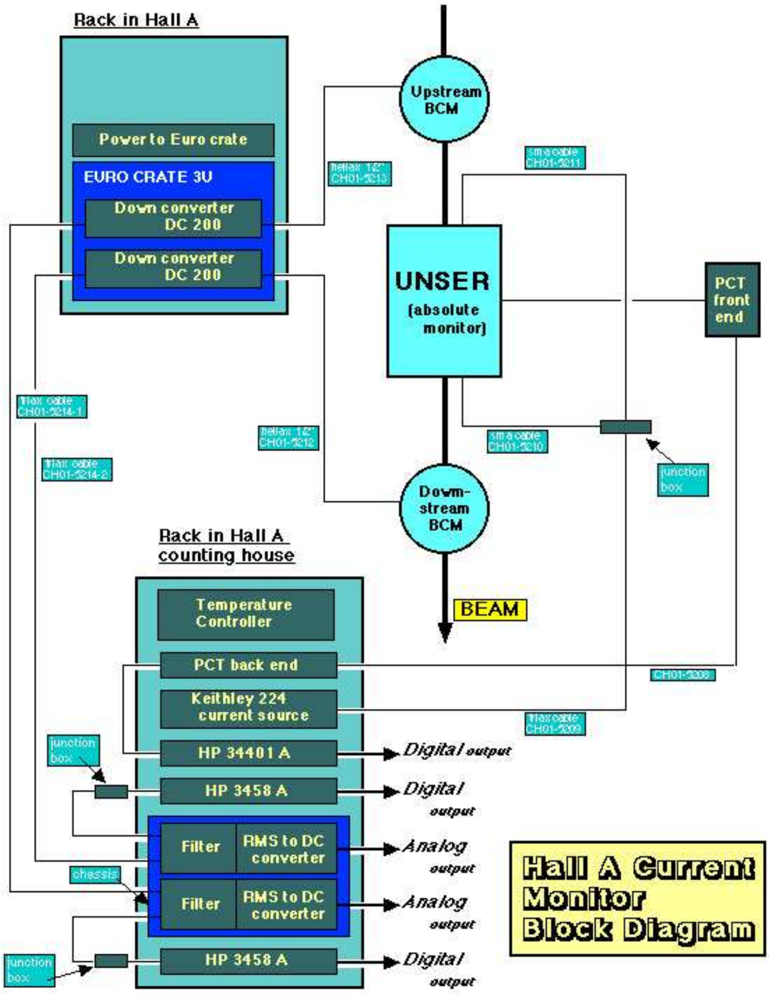

Figure 2.11: Block diagram of the Hall A beam current monitors.

2.2.5 Møller Polarimeter

Møller polarimetry [68] is a method for measuring beam polarization at high energies at the target based on the reaction $\vec{e} + \vec{e} \rightarrow e + e$, known as Møller scattering. The Møller spin-dependent cross section is

$$\frac{d\sigma}{d\Omega} = \frac{d\sigma_0}{d\Omega}\left[1 + \sum_{i,j} P_i^b A_{ij} P_j^t\right], \tag{2.18}$$

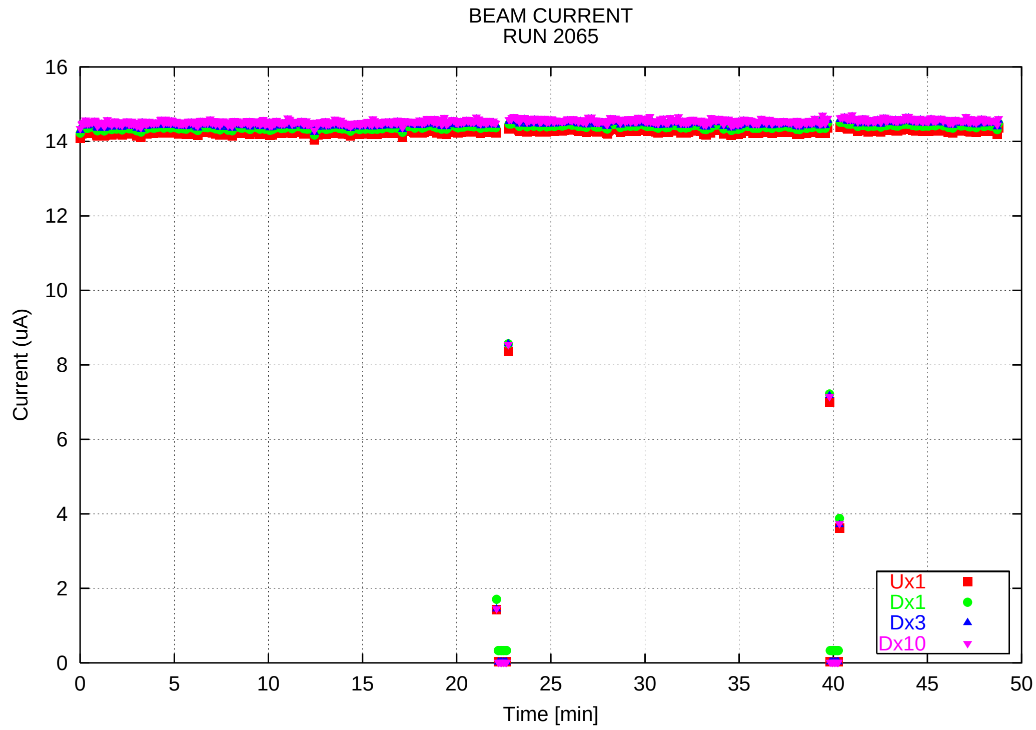

Figure 2.12: Beam current in Hall A during E94-010 for a typical run. Note that the beam is relatively constant except at dips occuring at 23 and 40 minutes usually caused by RF trips.

where

$$\frac{d\sigma_0}{d\Omega} = \frac{\alpha^2}{4m^2}\frac{1}{\xi^2}\frac{(4-\sin^2\theta)^2}{\sin^4\theta}, \tag{2.19}$$

$$A_{zz} = -\frac{(7+\cos^2\theta)\sin^2\theta}{(3+\cos^2\theta)^2}, \tag{2.20}$$

$$A_{xx} = -A_{yy} = -\frac{1}{\xi}\frac{2\sin^3\theta\cos\theta}{(3+\cos^2\theta)^2}, \tag{2.21}$$

$$A_{xy} = A_{yx} = A_{yz} = A_{zy} = 0, \tag{2.22}$$

$$\xi = \sqrt{\frac{E+m}{2m}}, \tag{2.23}$$

$$i,j = x,y,z, \tag{2.24}$$

where $d\sigma_0/d\Omega$ is the unpolarized cross section in the ultrarelativistic limit ($E \gg m$). The quantities P_i^b and P_j^t are components of the beam and target polarizations respectively. The A_{ij} are asymmetry parameters. The asymmetry parameters assume

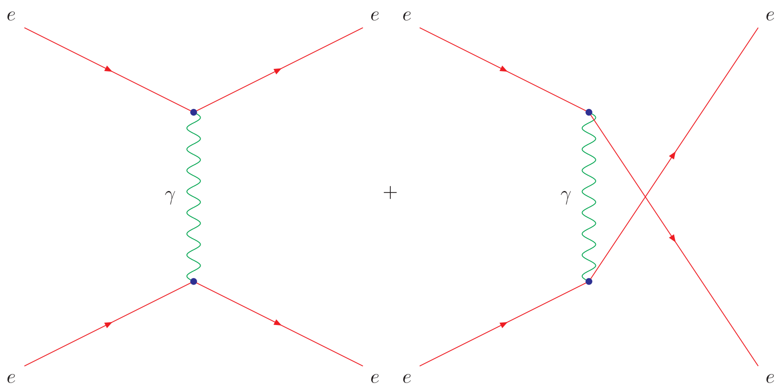

Figure 2.13: Tree-level Feynman diagrams for Møller scattering $\vec{e} + \vec{e} \rightarrow e + e$.

maxima at $\theta = 90°$:

$$A_{zz} = -\frac{7}{9}, \tag{2.25}$$

$$A_{xx} = -A_{yy} = -\frac{1}{9}, \tag{2.26}$$

at which point $d\sigma_0/d\Omega = 9\alpha^2/4m^2 = 0.179$ barn/sr. A_{xx} and A_{yy} are suppressed by a factor of $1/\xi$. Therefore, at high energy, A_{zz} becomes the dominant term. A Monte Carlo simulation of the Møller spectrometer acceptance gives $A_{zz} = 0.76$. The raw asymmetry along the longitudinal beam direction is:

$$A_{\mathrm{raw}} = \frac{\sigma^{\uparrow\uparrow} - \sigma^{\uparrow\downarrow}}{\sigma^{\uparrow\uparrow} + \sigma^{\uparrow\downarrow}} = P_b A_{zz} P_t \cos\theta_t, \tag{2.27}$$

where the arrow superscripts denote target and beam polarizations respectively, and θ_t is the angle between the beam direction and the target foil. The beam polarization can then be inferred:

$$P_b = \frac{A_{\mathrm{raw}}}{P_t \cos\theta_t A_{zz}}. \tag{2.28}$$

The Hall A Møller polarimeter is situated 17.5 m upstream of the Hall A target platform. The target is a foil made of Supermendur, a ferromagnetic Fe-Co alloy (49% Fe, 49% Co, 2% V by weight), with thickness 12.5 μm. Polarization is induced on the target electrons by applying an external magnetic field of 300 Gauss which forces alignment of the electron spins along the field direction. The target polarization is obtained from:

$$P_t = \frac{M}{n_e \mu_B} \frac{g' - 1}{g'} \frac{g_e}{g_e - 1}, \tag{2.29}$$

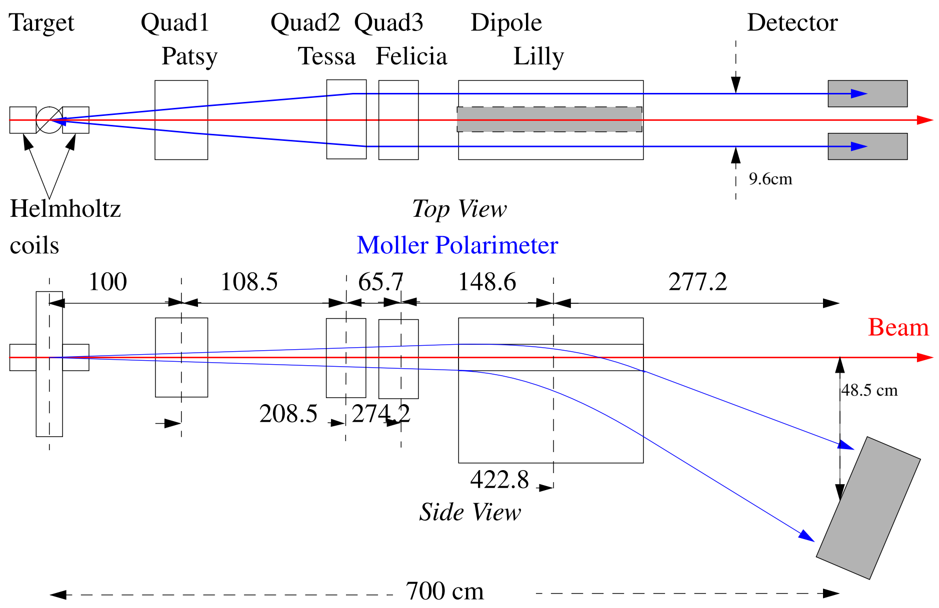

Figure 2.14: The optics of the Møller polarimeter is QQQD. The target on the left is a foill of ferromagnetic Fe-Co alloy called Supermendur. The detector on the right is a lead-glass calorimeter.

where M is the foil magnetization, n_e is the electron density, $g_e = 2.002319$ is the free electron g-factor, $\mu_B = 9.273 \times 10^{-21}$ G cm^3 is the Bohr magneton, and $g' = 1.916 \pm 0.002$ is the magnetomechanical ratio due to the orbital contribution to magnetization for a 50-50 Fe-Co alloy, assuming the Vanadium's contribution to be negligible. A target polarization of $7.60 \pm 0.23\%$ was achieved. The scattered electrons are focused by a QQQD spectrometer and detected in coincidence in lead-glass calorimeters. The optics of the Møller polarimeter is shown in Fig. 2.14. A Møller measurement is an invasive procedure that takes about an hour and an additional forty minutes to alter magnet settings. The results of the Møller polarimeter measurements along with the Mott polarimeter measurements from the injector, for comparison, obtained during E94-010 are displayed in Fig. 2.15. The average beam polarization was about 72% during this experiment.

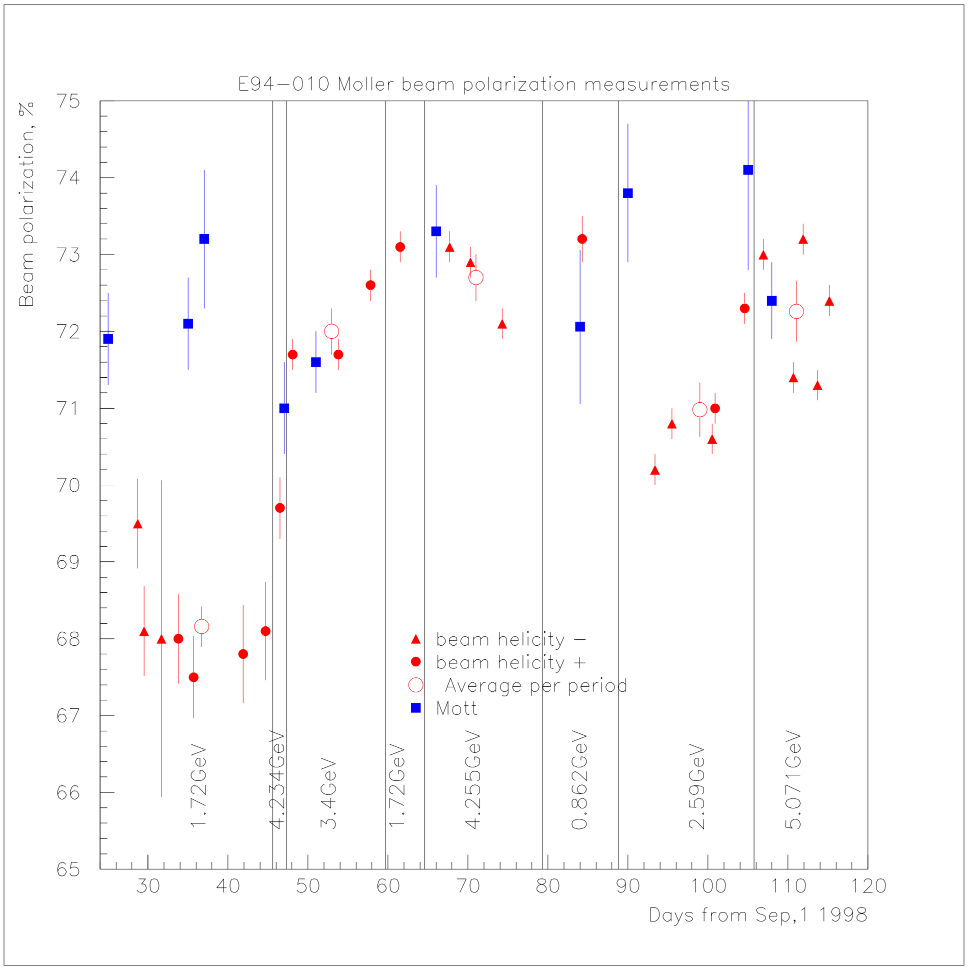

Figure 2.15: Møller and Mott polarimeter measurements taken during E94-010. The average beam polarization is about 72%. The Møller measurements were carried out in the Hall A end station, whereas the Mott measurements were made at the injecter.

2.2.6 Fast Raster

The Hall A fast raster is a couple of horizontal (X) and vertical (Y) air-core dipole magnets located 23 m upstream of teh target. It rasters the beam on target with an amplitude of several millimeters to prevent overheating due to prolonged application of the beam at a single spot. The fast raster can be operated in either sinusoidal or amplitude modulated mode.

In sinusoidal mode, both the X and Y dipole pairs are driven with pure sine waves. The ratio of frequencies is irrational (not a ratio of integers) so that the beam sweeps the targeted area in a non-Lissajous pattern, *i.e.*, the entire phase space is filled at a

Figure 2.16: Target ladder containing the main polarized target cell (top), the seven ^{12}C foils (center middle), the BeO target window (front middle), and the reference cell (bottom).

pseudo-random but predictable way.

In the amplitude modulated scheme, both the X and Y dipole pairs are driven at 18 kHz with a 90° relative phase. The resulting pattern is circular. Furthermore, the radius is modulated at 1 kHz.

For this experiment, the amplitude modulated scheme was used to raster the beam.

2.2.7 Target Scattering Chamber

The targets are enclosed in the target scattering chamber which is made of a high-density polymer. Inside the target scattering chamber are several targets:

- The polarized ^3He cell is the main target used throughout most of the production runs. The target is a 40-cm long gas cylinder oriented along the beam axis. In addition to helium, the target cell contains traces of nitrogen gas used to quench depolarization of helium from photons emitted during the optical pumping process and traces of rubidium. The target cell is described in more detail in a later section.

- The reference cell is of identical construction to the main target cell. It is used in one of two modes. When used as an empty reference cell, it maintains a vacuum and is used to estimate the backgound from the glass windows. When used as a nitrogen reference cell, it is filled with nitrogen gas and used to estimate the backgound from nitrogen contamination.

- The BeO (beryllium oxide) target is used as a bull's-eye for beam position and spot size alignment before any production run is taken.

- The optics alignment target consists of an array of seven ^{12}C foils. Since this was the first time that such a long cell had been used in Hall A, additional optics studies were required to extend the optics database used to map the particle trajectories. Results of measurements made with this target will be shown in the section discussing spectrometer optics.

A diagram of the target ladder is shown in Fig. 2.16.

2.2.8 Beam Exit Channel and Beam Dump

After the target chamber the beam is channeled into the beam dump. This exit beam pipe is made of a thin walled aluminum spiral corrugated pipe of welded construction. The diameter varies from 6 inches to 36 inches. The pipe is maintained at a vacuum of 10^{-5} Torr with a turbomolecular pump. A diffuser with a beryllium window is connected via a 12-inch port to this exit of the pipe. The beam dump can sustain 1 MW of power (200 μA at 5 GeV).

2.3 High Resolution Spectrometers

The High-Resolution Spectrometers (HRS) [69] consist of nearly identical Electron and Hadron arms shown in Fig. 2.6, and can be operated in singles or coincidence mode. Each arm has a QQDQ configuration of magnetic elements shown in Fig. 2.17. All quadrupole (Q) and dipole (D) magnets are superconducting magnets. General characteristics of the HRS are summarized in Table 2.3. The layout of the detector package in both spectrometer arms are displayed in Figs. 2.18 and 2.19. In the Electron arm, E94-010 utilized the Vertical Drift Chamber (VDC) for reconstruction of

Momentum range	0.3-4.0 GeV/c
Configuration	QQDQ
Bend angle	45°
Optical length	23.4 m
Momentum acceptance	±4.5%
Dispersion (D)	12.4 cm/%
Radial linear magnification (M)	2.5
D/M	5
Momentum resolution (FWHM)	1×10^{-4}
Angular acceptance:	
Horizontal	±28 mr
Vertical	±60 mr
Solid angle:	
Rectangular approximation	6.7 msr
Elliptical approximation	5.3 msr
Angular resolution (FWHM):	
Horizontal	0.6 mr
Vertical	2.0 mr
Transverse length acceptance	±5 cm
Transverse position resolution (FWHM)	1.5 mm
Spectrometer angle determination accuracy	0.1 mr

Table 2.3: Hall A HRS general characteristics.

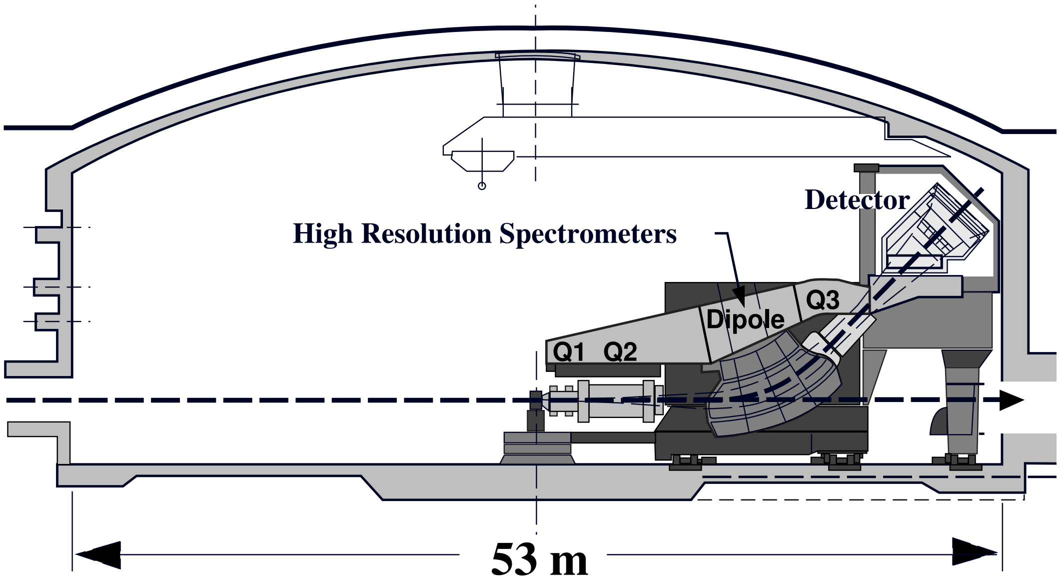

Figure 2.17: QQDQ configuration of magnetic elements for HRS in Hall A.

particle tracks, the scintillator planes S1 and S2 for triggering, the gas Cherenkov for pion rejection, and the preshower and shower counters for scattered energy measurement. The aerogel Cherenkov was not used for this experiment; see Fig. 2.18. In the Hadron arm, the experiment used the Vertical Drift Chamber (VDC) for reconstruction of particle tracks, the scintillator planes S1 and S2 for triggering, and the gas Cherenkov for pion rejection. The aerogel Cherenkov, the carbon analyzer or focal-plane polarimeter (FPP), and the scintillator plane S3, typically used in coincidence experiments, were not utilized in this experiment. However, a lead glass calorimeter (not shown in the figure) was added in the rear for particle identification; see Fig. 2.19.

2.3.1 Coordinate Systems

The spectrometer optics allows one to reconstruct physical variables at the target from physical quantities measured at the focal plane in the detector hut, as illustrated in Fig. 2.20. Even though five different coordinate systems are described in the ESPACE manual [70], only two will be considered here.

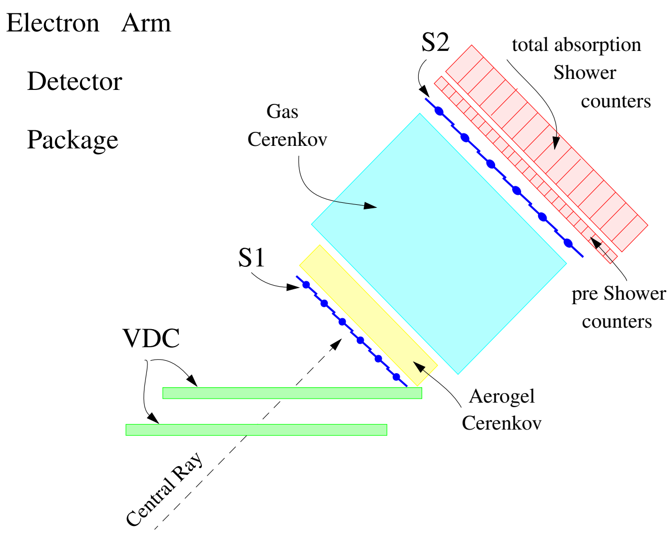

Figure 2.18: Hall A HRS Electron arm detector package. E94-010 made use of the Vertical Drift Chamber (VDC) for reconstruction of particle tracks, the scintillator planes S1 and S2 for triggering, the gas Cherenkov for pion rejection, and the preshower and shower counters for scattered energy measurement. The aerogel Cherenkov was not used for this experiment.

Spectrometer Reconstructed Coordinate System

The origin of this coordinate system is defined as a point at a distance of 1.25 m from the center of the central sieve-slit hole. The z-axis $\hat{\boldsymbol{z}}_{tg}$ points from the origin to the center of the central sieve-slit hole. The x-axis $\hat{\boldsymbol{x}}_{tg}$ is orthogonal to the z-axis and points downwards. The angle in the horizontal plane (yz-plane) is ϕ_{tg} and the angle in the vertical plane (xz-plane) is θ_{tg}. The spectrometer angle between the beam line and the z-axis is Θ_0. The spectrometer reconstructed coordinate system is illustrated in Fig. 2.21.

Spectrometer Focal-Plane Coordinate System

The origin of this coordinate system is defined by the intersection of wire 184 in the first wire plane of the drift chamber and the projection on the first wire plane of wire 184 in the second plane. The z-axis $\hat{\boldsymbol{z}}_{fp}$ is the projection of the central ray in the vertical plane. The x-axis $\hat{\boldsymbol{x}}_{fp}$ is perpendicular to the z-axis and points downward.

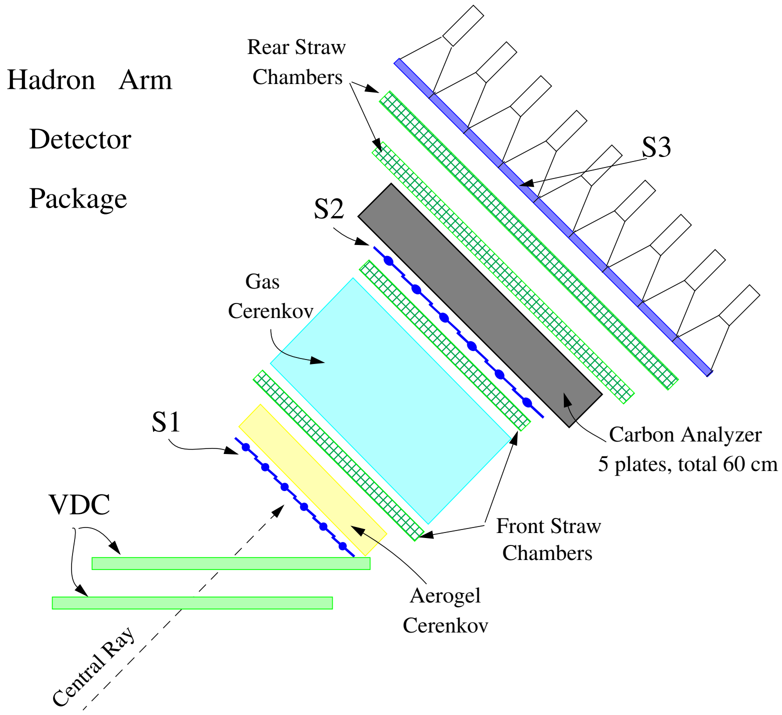

Figure 2.19: Hall A HRS Hadron arm detector package. E94-010 made use of the Vertical Drift Chamber (VDC) for reconstruction of particle tracks, the S1 and S2 scintillator planes for triggering, and the gas Cherenkov for pion rejection. The carbon analyzer or focal-plane polarimeter (FPP) was not utilized in this experiment. Neither was the aerogel Cherenkov nor the S3 scintillator plane, typically used in coincidence experiments. However, a lead glass calorimeter (not shown in the figure) was added in the rear for particle identification.

As a result, the x- and z-axis vary with fractional momentum $\Delta p/p$ of the charged particle. The spectrometer focal-plane coordinate system is illustrated in Fig. 2.22.

2.3.2 Transport

Kinematic variables at the focal plane can be mapped to kinematic variables at the target using the spectrometer optics tensor [71, 72]. Assuming mid-plane symmetry

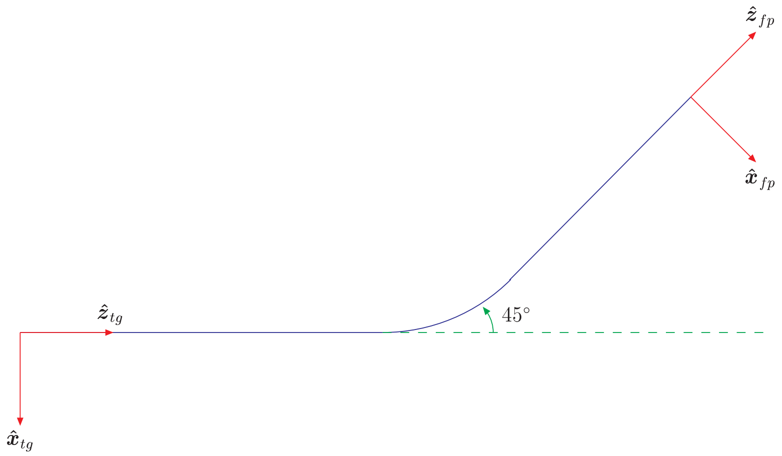

Figure 2.20: The spectrometer central ray is scattered at the target. The central ray is then deflected by an angle of 45° at the dipole magnet (not shown). The position of the central ray is finally measured at the focal plane with the aid of the vertical drift chamber (VDC). The matrix elements of the spectrometer optics tensor map the kinematic variables at the focal plane (fp) to those at the target (tg).

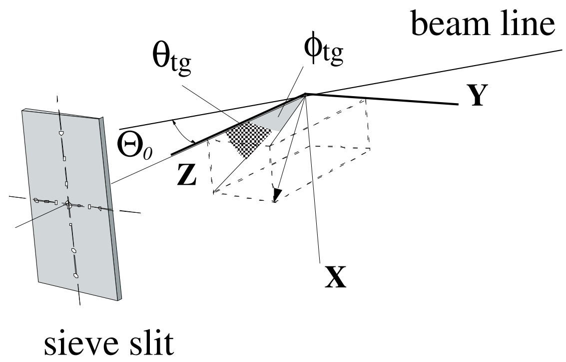

Figure 2.21: Spectrometer reconstructed coordinate system. The origin is a point 1.25 m from the center of the sieve slit located at the entrance of the spectrometer.

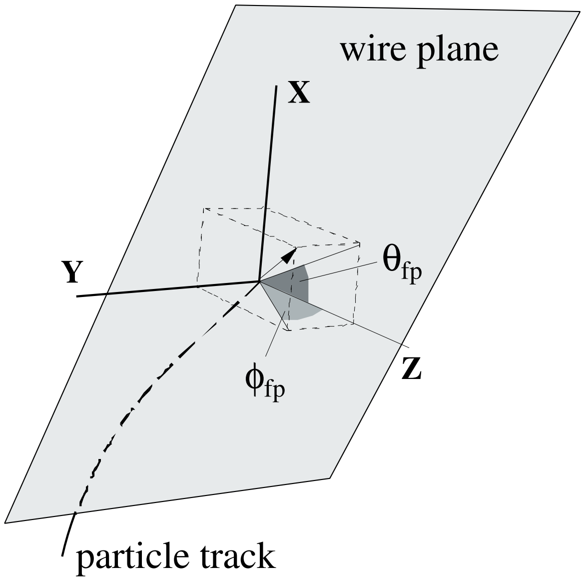

Figure 2.22: Spectrometer focal-plane coordinate system.

and setting $x_{tg} = 0$, a first-order approximation to this matrix is:

$$\begin{bmatrix} \delta \\ \theta \\ y \\ \phi \end{bmatrix}_{tg} = \begin{bmatrix} \langle\delta|x\rangle & \langle\delta|\theta\rangle & 0 & 0 \\ \langle\theta|x\rangle & \langle\theta|\theta\rangle & 0 & 0 \\ 0 & 0 & \langle y|y\rangle & \langle y|\phi\rangle \\ 0 & 0 & \langle\phi|y\rangle & \langle\phi|\phi\rangle \end{bmatrix} \begin{bmatrix} x \\ \theta \\ y \\ \phi \end{bmatrix}_{fp}, \tag{2.30}$$

where $\delta = (p - p_0)/p_0$ is the fractional momentum of the particle, p is the momentum, and p_0 is the central momentum of the spectrometer. This simple matrix assumes a block-diagonal form because of mid-plane symmetry. In practice, the matrix above poorly describes the spectrometer optics. Instead, each target variable is expanded as a power series (up to fifth order) in the focal plane variables. That is:

$$y_{tg} = \sum_{j,k,l} Y_{jkl}\theta^j_{fp} y^k_{fp} \phi^l_{fp}, \tag{2.31}$$

$$\theta_{tg} = \sum_{j,k,l} T_{jkl}\theta^j_{fp} y^k_{fp} \phi^l_{fp}, \tag{2.32}$$

$$\phi_{tg} = \sum_{j,k,l} P_{jkl}\theta^j_{fp} y^k_{fp} \phi^l_{fp}, \tag{2.33}$$

$$\delta_{tg} = \sum_{j,k,l} D_{jkl}\theta^j_{fp} y^k_{fp} \phi^l_{fp}, \tag{2.34}$$

(2.35)

where the transfer tensors Y_{jkl}, T_{jkl}, P_{jkl}, and D_{jkl} are polynomials in x_{fp}, *i.e.* $Y_{jkl} = \sum_i C_i x^i_{fp}$. The subscripts j, k, and l of the transfer tensors are just powers of the focal plane variables θ_{fp}, y_{fp}, and ϕ_{fp}, respectively. The C_i's are the matrix elements of the spectrometer optics tensor. Optimum values for the transfer tensors are obtained by minimizing the χ^2 of the following aberration functions:

$$\Delta(y) = \sum_s \left[\frac{\sum_{j,k,l} Y_{jkl} \theta^j_{fp} y^k_{fp} \phi^l_{fp} - y^0_{tg}}{\sigma^s_y} \right]^2, \tag{2.36}$$

$$\Delta(\theta,\phi) = \sum_s \left[\frac{\sum_{j,k,l} T_{jkl} \theta^j_{fp} y^k_{fp} \phi^l_{fp} - \theta^0_{tg}}{\sigma^s_\theta} \right]^2 + \sum_s \left[\frac{\sum_{j,k,l} P_{jkl} \theta^j_{fp} y^k_{fp} \phi^l_{fp} - \phi^0_{tg}}{\sigma^s_\phi} \right]^2, \tag{2.37}$$

$$\Delta(\delta) = \sum_s \left[\frac{\sum_{j,k,l} D_{jkl} \theta^j_{fp} y^k_{fp} \phi^l_{fp} - \delta^0_{tg}}{\sigma^s_\delta} \right]^2, \tag{2.38}$$

where σ is the resolution of the subscript variable.

2.3.3 Optics

The evolution of the transport matrix elements as a function of optical path length (z) is shown in Fig. 2.23. The $\langle x|\theta_0\rangle$ term is large in the dipole to provide good momentum resolution at the moderate bending angle of 45°. The $\langle y|y_0\rangle$ term remains small inside the entire spectrometer to allow the use of extended targets (10 cm at 90°). The spectrometer is a double-focusing design providing point-to-point focus in the dispersive direction, $\langle x|\theta_0\rangle = 0$, and point-to-point focus in the transverse direction, $\langle y|\phi_0\rangle = 0$, at the focal plane, $z \approx 20$ m. There is a transverse crossover in the middle of the dipole to keep the transverse elements $\langle y|y_0\rangle$ small.

2.3.4 Extended Target Optics Studies

In previous measurements, the longest target used in Hall A was a 15-cm long hydrogen cryotarget. The polarized ^{3}He target cells are limited in density due to the need to obtain long polarization lifetimes. This led us to the design of a 40-cm long cell to obtain the desired luminosity. This, in turn, requires a new set of optics measurements to obtain a database over a larger range of $y_{\rm tg}$. Measurements were undertaken

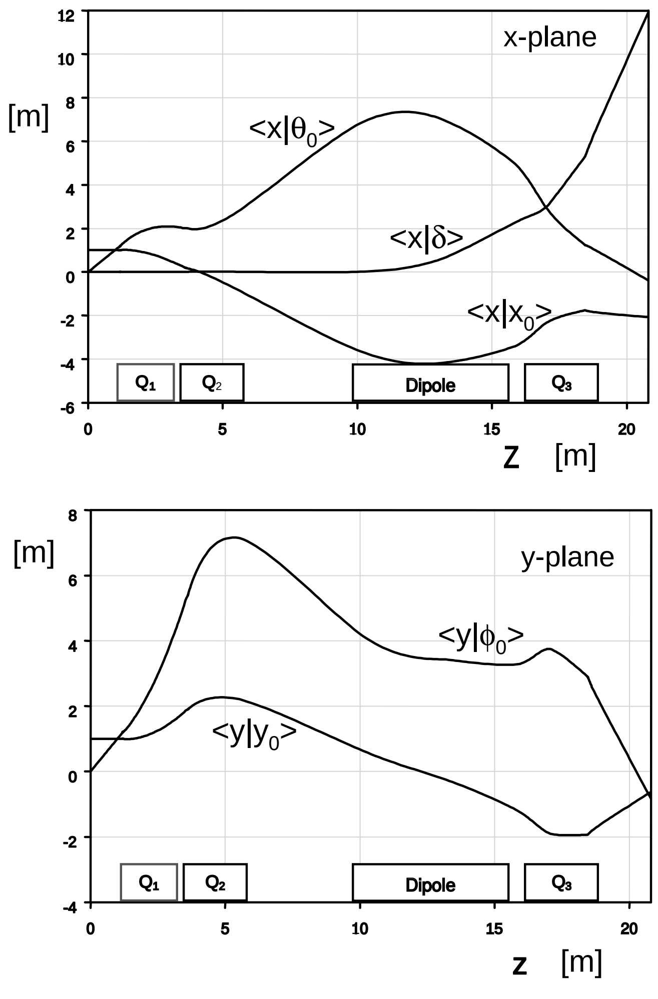

Figure 2.23: Evolution of the first-order transport matrix elements along the optical path length of the HRS.

at the beginning of our experiment using an array of thin ^{12}C foils spanning the target length of helium in conjunction with the installation of a sieve slit collimator in front of the first quadrupole of the spectrometer. Measurements were taken on elastic scattering on ^{12}C at various positions of the focal plane. The methodology used was to obtain a simultaneous bid to a collection of dispersive, angular, and extended target matrix elements. Although the measurements were taken simultaneously, the experimental procedure conceptually can be broken down into three tasks:

1. Measurements of the elastic scattering from ^{12}C at the center of the focal plane were used to obtain the best momentum focus, then the peak was scanned to obtain a set of dispersive matrix elements. By this mean, a central momentum resolution better than 10^{-4} was obtained.

2. The angular matrix elements were constrained by the passage of the electrons through the holes in the sieve slit as shown in Fig. 2.24. The fitting routine required both a good resolution of the virtual image and a proper spacing of the holes in the spectrum. As shown in the figure, the sieve slit consists of a 7×7 array of small holes machined through a lead collimator. Two of the holes were enlarged to resolve ambiguities in the orientation of the collimator coordinate system. As shown in the reconstructed image in the right of the collimator, these two holes are clearly resolved. After correcting the matrix elements, the holes are aligned exactly as predicted.

3. The critical item for this set of measurements was to obtain an extended set of y_{tg} matrix elements. This requires a simultaneous fit to optimize y_{tg}. As shown in Fig. 2.25 only the central five foils are visible in the acceptance of the spectrometer. At a forward scattering angle of 15.5°, the resolution along the z direction is not very good, only about 1.5 cm (FWHM). However, this corresponds to a 4 mm (FWHM) resolution in the y_{tg} direction. Again the observed array spacing is exactly as predicted.

The target is sufficiently long that the end windows are usually out of the acceptance. Although in some cases, one or both of the target windows can be seen. Using the new set of matrix elements, we can cut the windows out of the analysis using the analysis software. This totally eliminates the major source of background to the experiment. Further details on spectrometer optics can be found in Ref. [50].

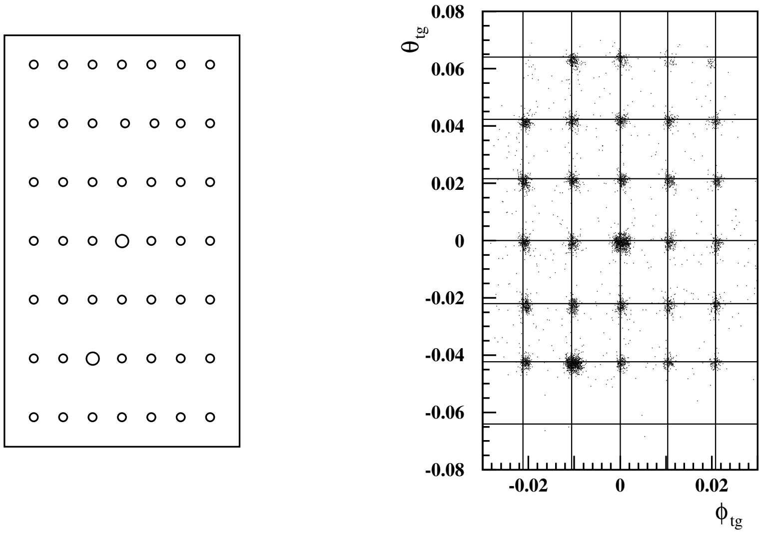

Figure 2.24: Geometric (left) and reconstructed (right) configurations of the sieve slit. The two large holes, which allow for an unambiguous identification of the orientation of the image at the focal plane, can be clearly identified in the right figure.

2.4 Focal Plane Instrumentation

2.4.1 Vertical Drift Chamber

The Vertical Drift Chamber (VDC) [73], designed and constructed by the Nuclear Interactions Group at the MIT Laboratory for Nuclear Science, is used for particle tracking. Each spectrometer has one VDC mounted on rails and inserted between the exit of the quadrupole magnet Q3 and the entrance of the detector hut. Each VDC is capable of achieving a resolution of 145 μm FWHM when operated at -4.8 kV or 225 μm FWHM at -4.0 kV.

Description

A layout of a VDC is shown in Figs. 2.26 and 2.27. Each VDC has a lower and an upper chamber. The lower chamber is upstream of the central ray and the upper chamber is downstream. The dimensions of the active area of each chamber are 211.8 cm (dispersive direction) $\times$ 28.8 cm (transverse direction). The distance between corresponding planes in each chamber is 33.5 cm. The placement of each chamber is such that the central ray passes through the center of the active area. Each chamber

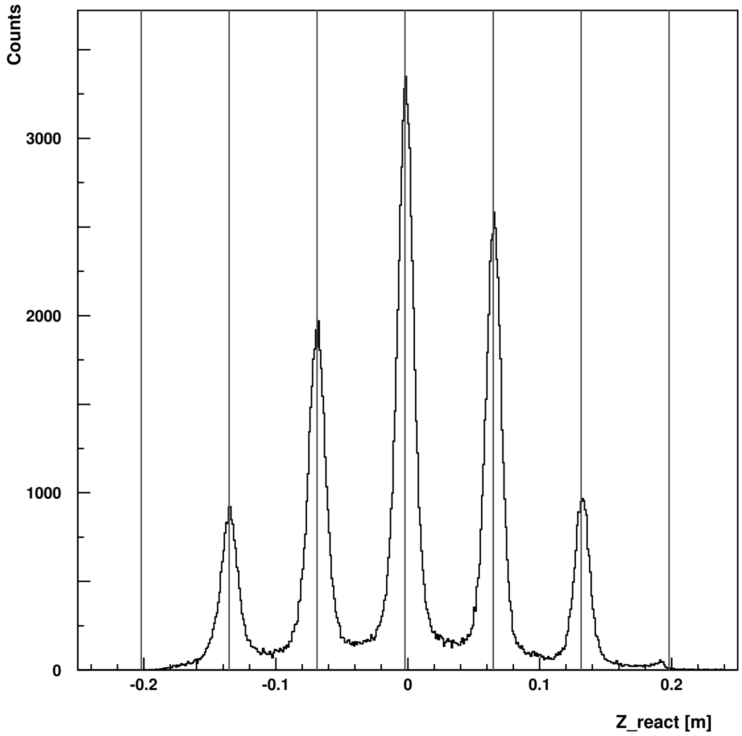

Figure 2.25: Reconstructed position along the beam line (z_{react}) for 862 MeV electrons scattered from the set of ^{12}C foil targets. The lines indicate the expected positions of the foils. The central five of seven thin foils are visible within the y_{tg} acceptance of the HRS.

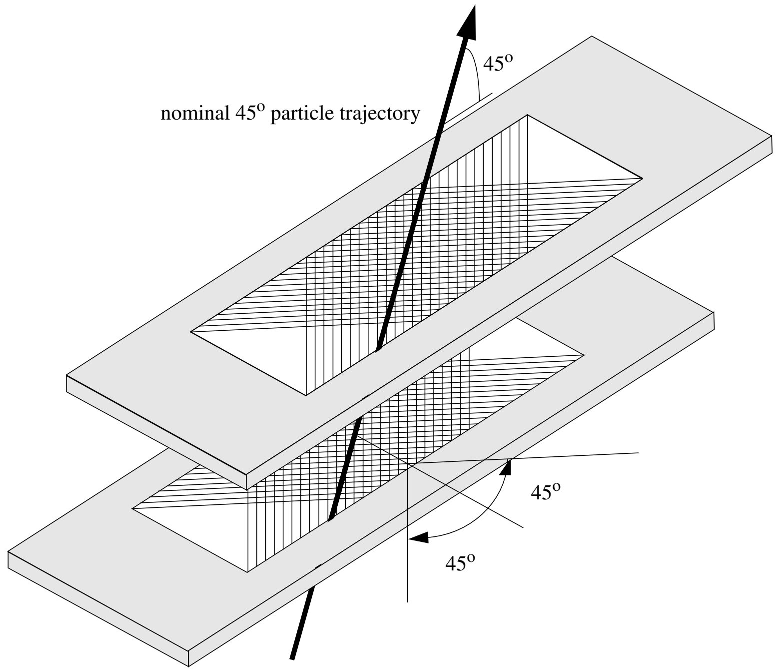

Figure 2.26: Layout of the Hall A VDC. The lower and upper chambers lie in the horizontal plane and are aligned in such a way that the central ray passes through the center of the active area of each chamber.

has three high-voltage planes in the horizontal. Sandwiched between two high-voltage planes is a wire plane. Each wire planes contains 368 sense wires at 45° from the dispersive direction; wires from different wire planes are orthogonal to each other. Each sense wire is made of gold-plated tungsten and is 20 μm in diameter. The sense wire-to-sense wire distance is 4.243 mm.

Principle of Operation

A VDC consists of a plane of evenly spaced, anode wires. Directly above and below the wires are two conducting planes kept at a negative high voltage. A $1/r$ electric field is generated near each wire; see Fig. 2.29. The entire chamber is filled with an argon-ethane gas mixture at 50%/50% proportion by volume. A charged particle traveling through the chamber leaves behind a trail of electrons and ions from the gas mixture. As these electrons approach the anode wires along the electric field lines, an avalanche of electrons and ions is created that induces a negative signal in the conducting wire. This signal is captured by dedicated electronics, amplified, discriminated, and read

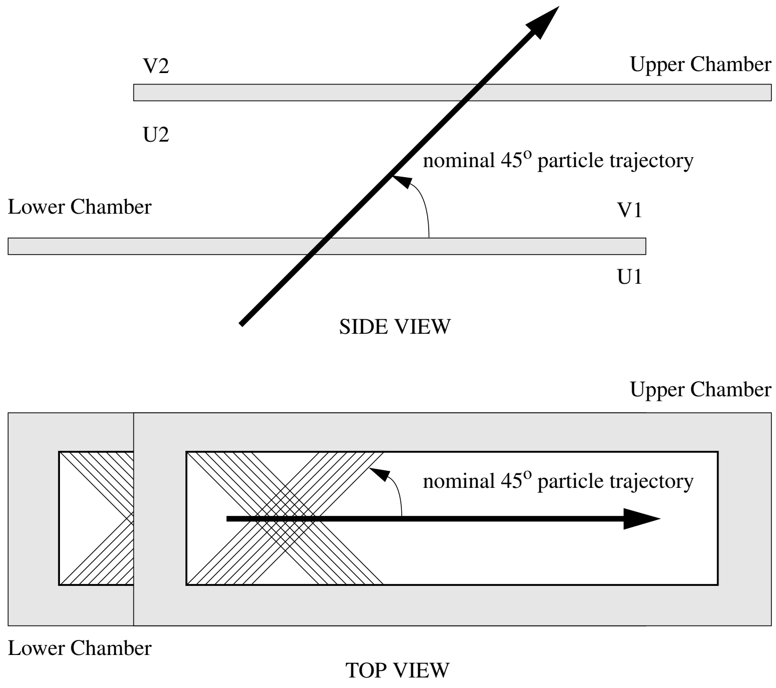

Figure 2.27: Side and top view of the Hall A VDC. The lower and upper chambers lie in the horizontal plane of the hall. The central ray is angled at 45° from each chamber and crosses the center of the active area of each chamber. Each chamber has two wire planes where one set of sense wires is angled at 45° from the particle trajectory and the other set is angled at −45°. The lower (upstream) wire plane is identified as the U-plane and the upper (downstream) wire plane is identified as the V-plane.

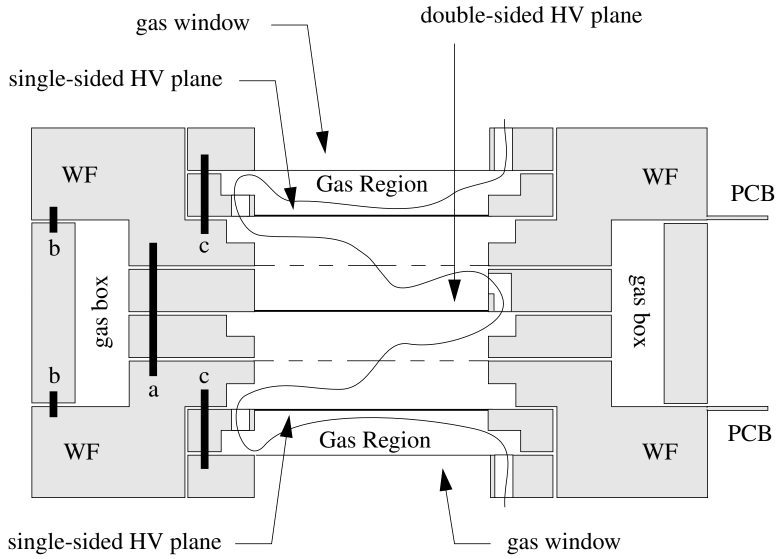

Figure 2.28: Cross-sectional view of a Vertical Drift Chamber (VDC). A VDC has three high-voltage (HV) planes (solid lines) and two wire planes (dashed lines). The flow of the argon-ethane gas mixture is indicated by the wiggly line. The wire frames are labelled WF. The printed circuit boards (PCB) relay the signals to the readout electronics.

out by the data acquisition system. The VDC readout electronics is pictured in Fig. 2.30. The particle track is angled at 45° from the wire plane and typically induces signals in five neighboring wires. By using the triggers from the scintillators and some Time-to-Digital Converters (TDC), the drift time of the electrons from the particle track to the anode wire can be estimated, and subsequently the distance of the particle track to the anode wire. A single-wire drift-time spectrum is shown in Fig. 2.31. The number of events per time bin is

$$\frac{dN}{dt} = \frac{dN}{ds}\frac{ds}{dt}, \tag{2.39}$$

where dN/ds is constant. The relationship between drift distance and drift time is shown in Fig. 2.32. Finally, a drift-distance spectrum is shown in Fig. 2.33.

2.4.2 Scintillator Planes

Each HRS contains two scintillator planes, S1 and S2. Each scintillator plane in turn consists of six paddles. The active area on each S1 paddle is 29.cm × 35.5 cm. The active area on each S2 paddle is 54.0 cm × 37.0 cm. Each paddle is made of 5

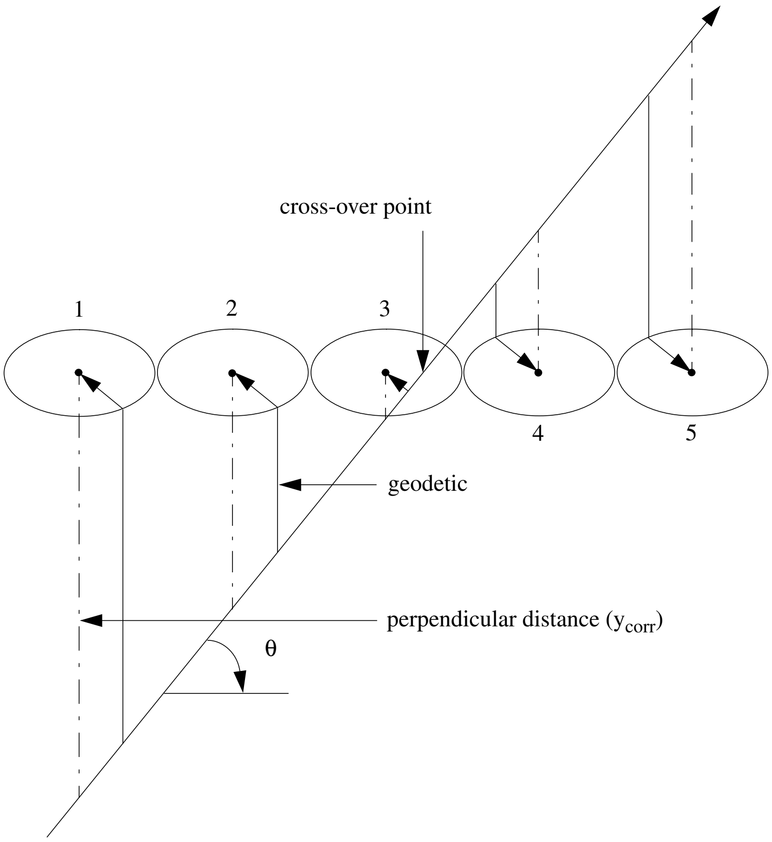

Figure 2.29: A particle track through a VDC wire plane resulting in avalanches of drift electrons in five sense wires. The paths of the drift electrons are the paths of least time and are called geodetics. The ellipses drawn around each sense wires are loci of transition where the electric fields change from linear to $1/r$. The drift times measured and knowledge of the drift velocities due to properties of the gas mixture provide the perpendicular distances from the charged particle track to each sense wire. A least square fit of these distances is finally used to reconstruct the particle track.

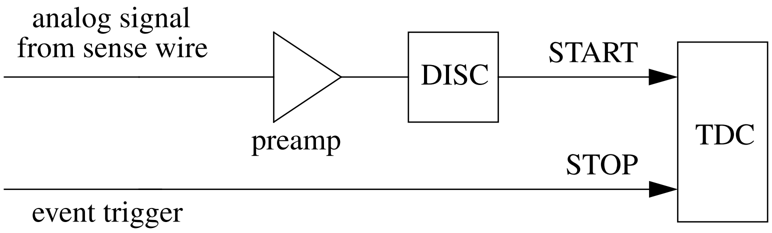

Figure 2.30: VDC readout electronics block diagram. The pulse induced by the charged particle in the sense wire is first amplified, then discriminated. This signal is used as a START signal to a time-to-digital converter (TDC). The STOP signal comes from the event trigger in the S2 scintillator plane. The output of the TDC is the drift time, the interval of time between initial ionization in the drift chamber and induction of the signal in the sense wire.

mm-thick BICRON 408 plastic scintillator and use multi-strip adiabatic light guides ending in a long cylindrical spool. At both ends of each paddle, at the cylindrical spools, are 2-inch Burle 8575 photomultiplier tubes (PMT). There is a 10 mm overlap between S1 paddles and a 5 mm overlap between S2 paddles.

Operation

Each PMT in a S2 scintillator paddle registers about 400-500 photons per passage of a single charged particle. This yields about 80-100 photoelectrons in a fresh PMT. The discriminator threshold is typically set to 45 mV. A typical PMT gain is 3×10^6. The high voltage (HV) is set to about 1.8-2.0 kV. The time resolution achieved is about 0.2 ns.

2.4.3 Gas Cherenkov Counter

Principle

The Hall A CO_2 gas Cherenkov counters, built by Saclay and INFN, operate by detecting Cherenkov radiation. Cherenkov radiation is emitted when a charged particle travels faster than light in a medium (in this case carbon dioxide) with a certain index of refraction ($n = 1.00041$ at atmospheric pressure). This radiation is emitted in a forward cone about the particle's track at a well-defined angle as shown in Fig. 2.34. After a time t, the charged particle has traveled a distance βct and electromagnetic

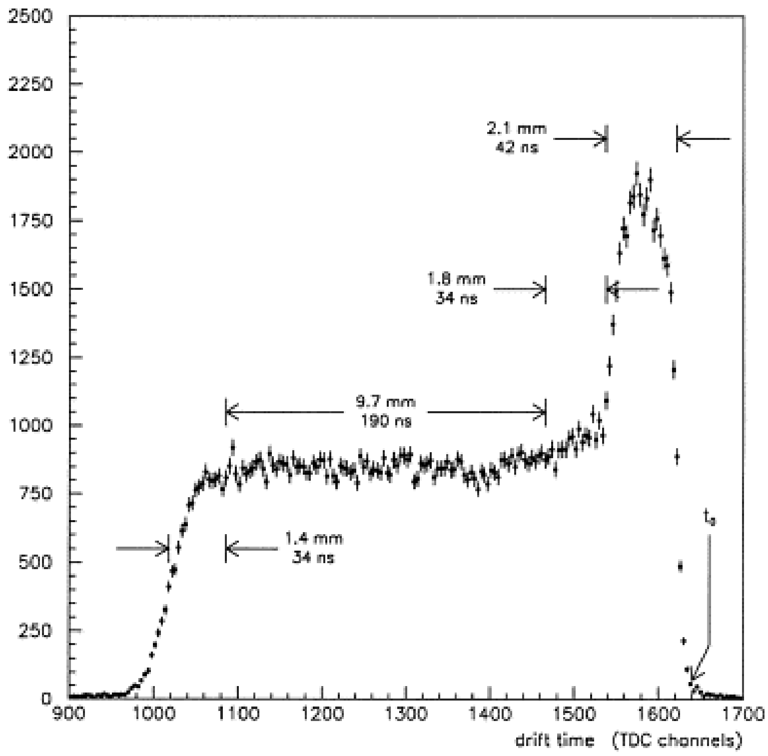

Figure 2.31: A single-wire drift-time spectrum.

radiation emitted from the moving particle forms a coherent wavefront with radius ct/n. The angle θ of the cone is related to the speed of the particle by:

$$\cos\theta = \frac{ct/n}{\beta ct} = \frac{1}{\beta n}. \tag{2.40}$$

The threshold of production for Cherenkov radiation is $\beta = 1/n$, *i.e.*, $\theta = 0$. The threshold momentum for a particle of mass m is $p = \gamma\beta mc$, where $\gamma = 1/\sqrt{1-\beta^2}$. Using $m_e = 0.511$ MeV/c^2 for the electron and $m_\pi = 139.6$ MeV/c^2 for the charged pion, the threshold momenta for emission of Cherenkov radiation are 17.84 MeV/c and 4.875 GeV/c for electrons and pions, respectively. In E94-010, the momentum settings never exceeded the threshold for pions. Therefore, the Cherenkov counters can be used effectively, in theory, for pion rejection. The Cherenkov counters were designed achieve pion rejection of 1000:1.

Description

The Electron spectrometer detector is a tank filled with CO_2 of dimension 1.996 m $\times$ 0.558 m $\times$ 1.5 m. The Cherenkov light is reflected by 10 spherical mirrors and

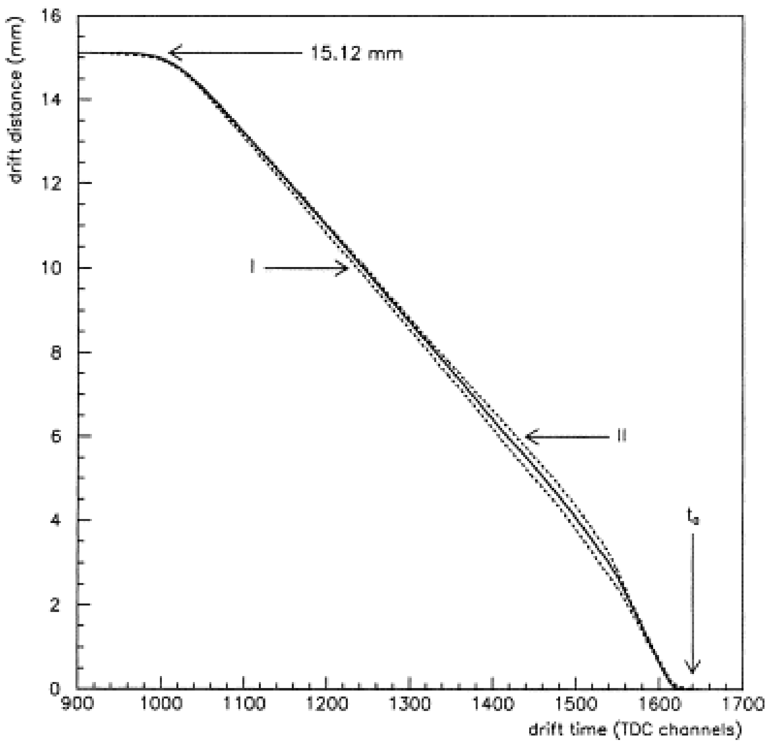

Figure 2.32: Drift distance vs. drift time conversion. The dotted curves represent the possible range of fits for different angles of incidence.

collected by 5-inch PMTs of type Burle 8854. The signals are discriminated and sent to scalers and the trigger electronics.

2.4.4 Lead-glass Calorimeter

Principle

An electron hitting a lead-glass calorimeter or shower counter will trigger an electromagnetic shower in the detector. This happens when a high-energy electron enters the lead-glass and emmits bremstrahlung radiation. These photons in turn create electron-positron pairs that emits more photons by bremstrahlung radiation. The cycle is repeated until there is not enough energy left to create any electron-positron pair. Visible light emitted by Cherenkov radiation is detected by PMTs at the end of each lead-glass block.

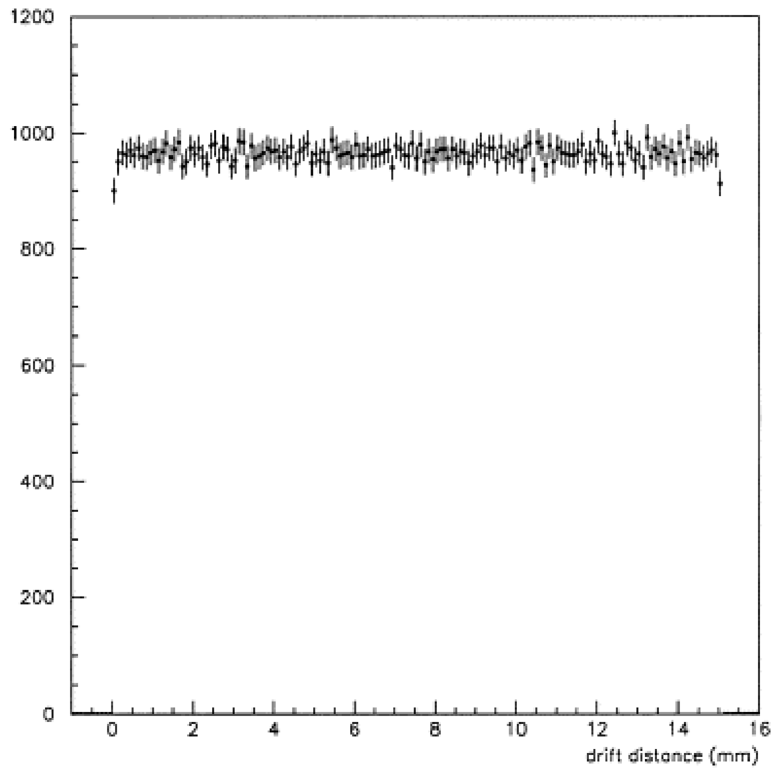

Figure 2.33: Drift-distance spectrum. Show is the drift time spectrum for Fig. 2.31 after making the drift-distance to drift-time conversion shown in Fig. 2.32. The resulting spectrum is flat as expected when scattering in the structureless deep inelastic region.

Description

The Electron arm has two layers of lead-glass blocks. The first layer constitutes the preshower and the second layer the shower counter. Together, these two layers make a total absorption calorimeter, *i.e.* the electron will lose all of its kinetic energy in the detector in the form of radiation. A similar lead-glass detector was built for the Hadron arm but unlike the Electron arm it was not total absorption.

2.5 Data Acquisition

Upon completion of E94-010, over 4 terabytes of raw data were successfully archived in mass storage. A schematic of the Hall A DAQ (Data Acquisition) system is shown in Fig. 2.35. The workhorse behind the data acquisition process is the CODA (CEBAF

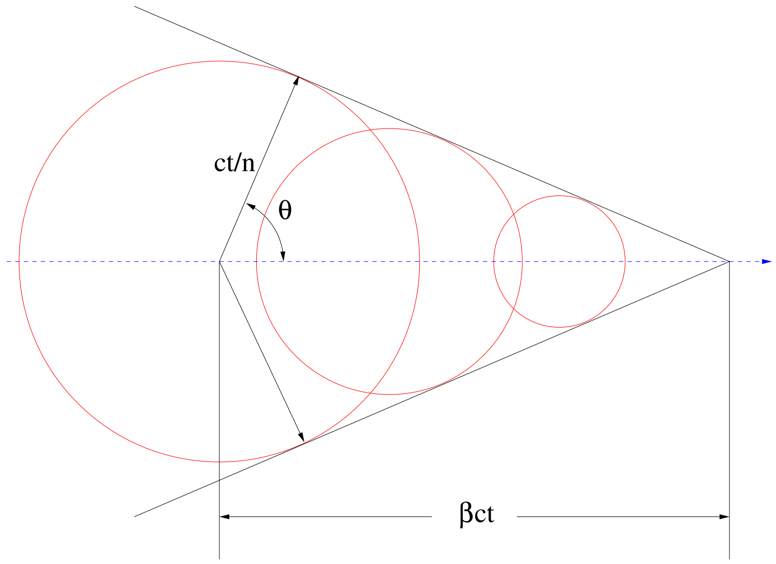

Figure 2.34: Cherenkov radiation. A charged particle in a medium with index of refraction n travels from left to right at speed βc greater than the speed of light c/n in that medium. A shock wave is created and propagates in a coherent wavefront defined by the angle θ.

Online Data Acquisition) [74] software package.

2.5.1 Description

The Electron arm has one FASTBUS crate and the Hadron Arm has two FASTBUS crates. The second FASTBUS crate in the Hadron Arm houses the FPP (Focal Plane Polarimeter) electronics. The FPP was not used during this experiment. The crates provide power to their modules and coordinate the flow of data between modules. The crates house different types of modules:

- LeCroy 1877 TDCs operating in common-stop mode with 0.5 ns resolution for the vertical drift chambers
- LeCroy 1875A TDCs operating in common-start mode with 0.1 ns resolution for the trigger scintillators and Cherenkov counters
- LeCroy 1881M ADCs for the trigger scintillators, Cherenkov counters, and lead glass counters

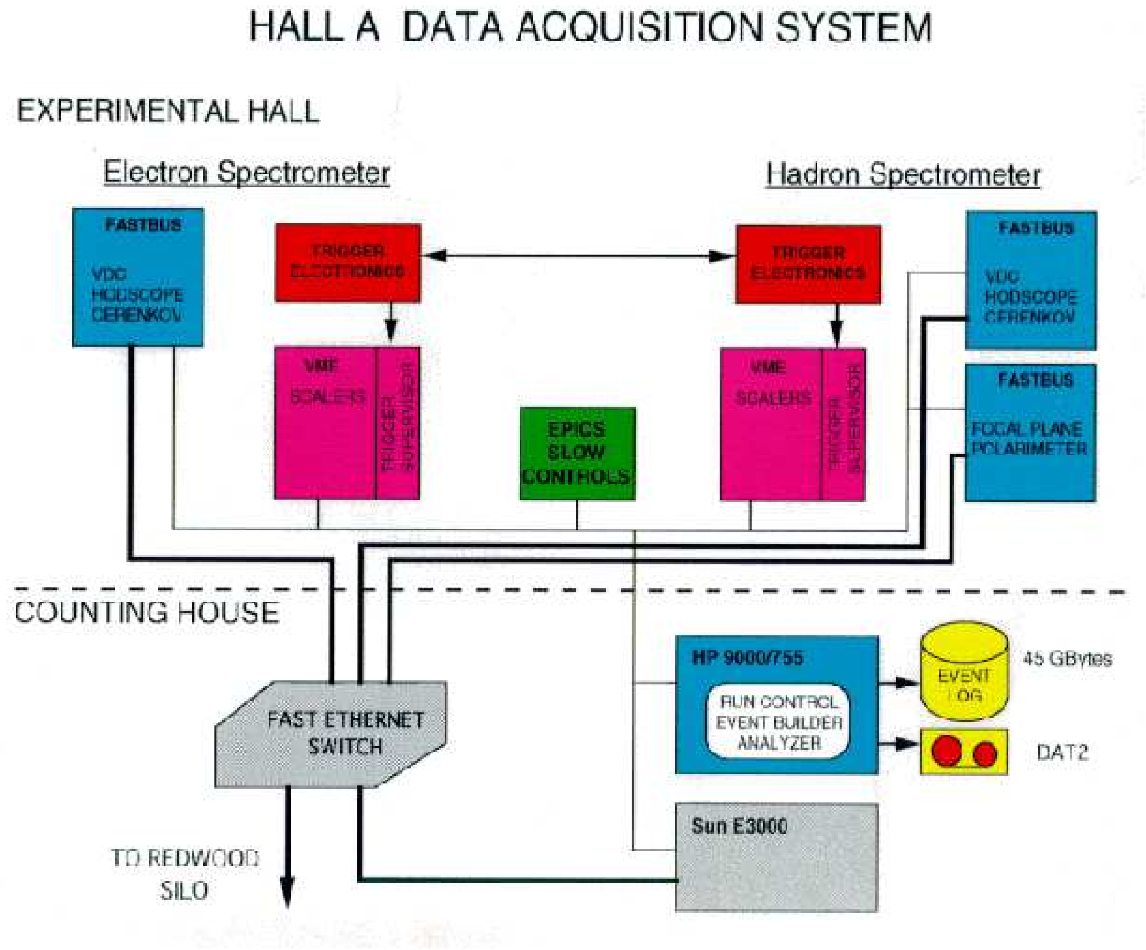

Figure 2.35: The passage of a charged particle through one of the spectrometers causes the Trigger Supervisor to initiate readouts of all ADCs, TDCs, and scalers in the corresponding FASTBUS and VME crates. The Event Builder then assembles the many fragments into a single event. Events are written into a CODA file which is later sent to mass storage. The user controls the data acquisition system via a GUI (Graphical User Interface) called Run Control running on a Unix workstation located in the Counting House.

Each spectrometer is equiped with a VME crate for BPM (Beam Position Monitor) and raster data. The following nomenclature is used for refering to the readout controllers (ROCs) in different crates in Hall A:

- **ROC1:** FASTBUS on E-arm
- **ROC2:** FASTBUS on H-arm
- **ROC3:** FASTBUS on H-arm for FPP (not used during E94-010)
- **ROC14:** VME on H-arm
- **ROC15:** VME on E-arm

The Trigger Supervisor is an electronic module developed by the Jefferson Lab Data Acquisition Group to synchronize readouts and prescale trigger inputs. Each spectrometer has its own TS and can therefore be run independently. Experiments can choose to run in 1-TS or 2-TS mode. In single Trigger Supervisor mode, only the Trigger Supervisor in the Hadron Arm is operated. The naming scheme for Trigger Supervisors is:

- **TS0:** TS on E-arm
- **TS1:** TS on H-arm

2.5.2 CODA

The CODA software package [74] is a toolkit developed by the Jefferson Lab Data Acquisition Group to control complex data acquisition systems. The User's Manual for CODA 1.4 is a rich source of information about elementary concepts in CODA [74].

A charged particle incident upon one of the spectrometers generates electronic signals in the detectors (vertical drift chambers, trigger scintillators, Čerenkov counters, and lead glass counters). These signals are sent to ROCs (Readout Controllers). After suitable discrimination, signals from S1 and S2 scintillator planes, and Cherenkov counters are utilized by the trigger electronics to classify the event as a possible trigger type; T1 or T2 for the Electron Arm, and T3 or T4 for the Hadron Arm. In case an event was registered, the Trigger Supervisor initiates readouts from all ROCs as well as scaler in VME crates. The CODA Event Builder then bundles the multitude

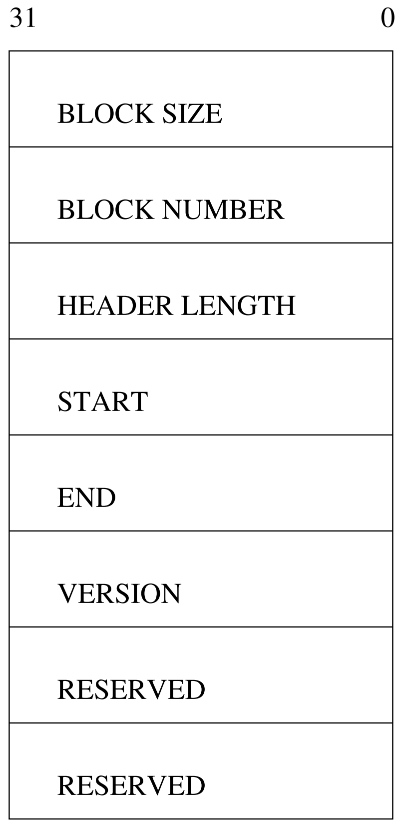

Figure 2.36: CODA physical record format. Shown here is the header for a CODA physical structure. The actual elements of the data block are self-describing as to type of data and length of arrays.

of readouts into a CODA event. Finally, the event is saved into a CODA file to be archived later in mass storage. The CODA Data Distribution system can be used effectively as a powerful tool that allows real-time display of scalers and histogramming of detector signals to monitor the quality of data during the running of the experiment. In addition, the codes DHIST and DATASPY, based on the DD system, are used in Hall A for real-time data monitoring [75].

2.5.3 CODA File Format

A CODA file is a series of fixed-size physical records. Typically a physical record would have size of 32,768 words where a word is 4 bytes (32 bits), thus the record size is 128 KB. Each physical record has the structure shown in Fig. 2.36.

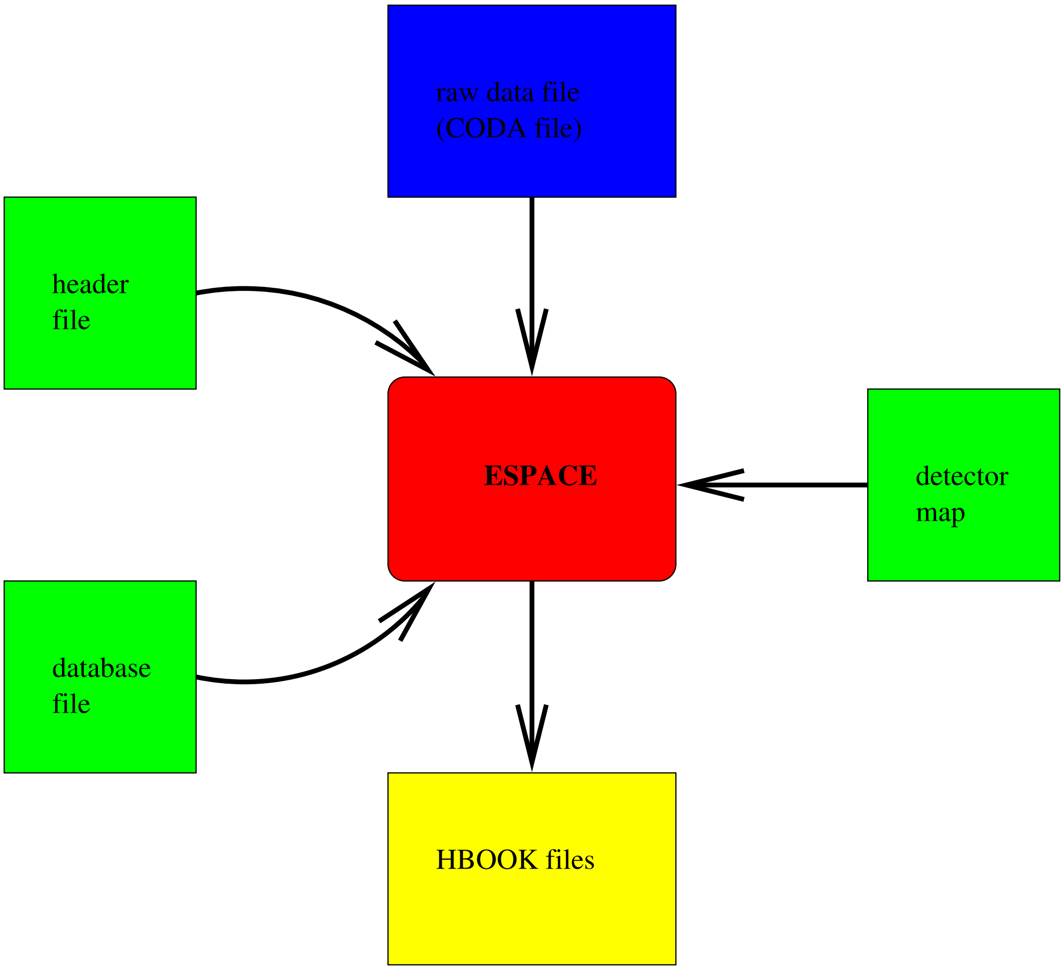

Figure 2.37: ESPACE reads in a raw data file, a header file, a database file, and a detector map, then writes several HBOOK files to disk.

2.5.4 ESPACE

ESPACE (Experiment Scanning Program for hall A Collaboration Experiments) [70] is the *de facto* off-line analyzer for Hall A. ESPACE was originally developed by Eddy Offermann and based on an earlier analyzer from Mainz. Much documentation about ESPACE can be found on its website [70]. ESPACE accepts the following files for input:

- **Raw data file** as output by CODA during each run
- **Header file** which contains information needed to construct some of the variables

- **Database file** which contains spectrometer constants and detectors
- **Detector map** which catalogs a comprehensive mapping between detector readouts and electronic channels.

A KUMAC file is a macro file for the KUIP [76] command interpreter which provides ESPACE with a PAW-like [77] interface. ESPACE executes the commands in the KUMAC file then outputs several HBOOK files with ntuples and histograms. The entire process is diagrammed in Figure 2.37.

2.6 Polarized ^{3}He Target

2.6.1 Introduction

Experiment E94-010 utilized a polarized ^{3}He target cell as a source of polarized neutrons. Polarization of the target cell is a two-step process: optical pumping and spin exchange.

2.6.2 Optical Pumping

Alkali metals have a single electron in their outer shell. The ground state of that electron is denoted $^2S_{1/2}$. In the spectroscopic notation $n^{2S+1}L_J$ with n the principal quantum number, S is the spin, L is the orbital angular momentum, and J is the total angular momentum. $2S+1$ is the multiplicity of the state. Electrons have spin $S = 1/2$ so the multiplicity is 2. L takes on the values $S = 0$, $P = 1$, $D = 2$, $F = 3$, $G = 4$, etc. $J = |L \pm S|$ is the sum of the orbital and spin angular momenta. So for a P-state electron, $J = |1 \pm 1/2| = 1/2$ or $3/2$. It follows that alkali metals also have an excited state split by spin-orbit coupling: $^2P_{1/2}$ and $^2P_{3/2}$. These states undergo further Zeeman splitting by the introduction of an external magnetic field. An electron in one of the excited states will drop down to the ground state via optical transitions D_1 ($^2P_{1/2} \rightarrow {}^2S_{1/2}$) and D_2 ($^2P_{3/2} \rightarrow {}^2S_{1/2}$). These spectral lines are termed a doublet (see Fig. 2.38), the most famous of which is the sodium doublet appearing in the optical spectrum as two distinct lines at $D_1 = 589.59$ nm and $D_2 = 588.96$ nm. In optical pumping of alkali metals, right circularly polarized photons, tuned to the wavelength of the D_1 line are applied to a sample in a holding magnetic

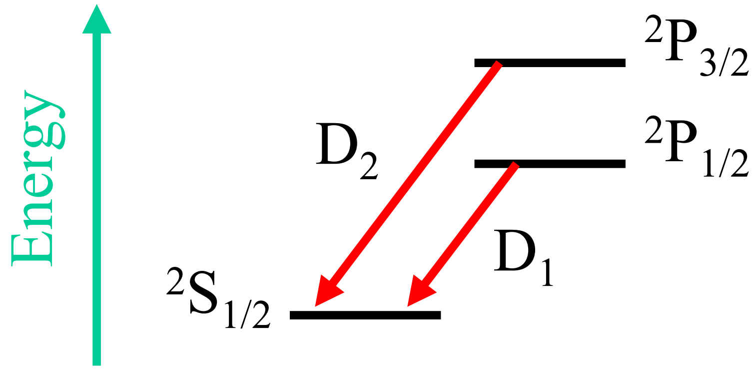

Figure 2.38: The doublet D_1 and D_2 of alkali metals are optical transitions from the excited states $^2P_{1/2}$ and $^2P_{3/2}$ respectively to the ground state $^2S_{1/2}$.

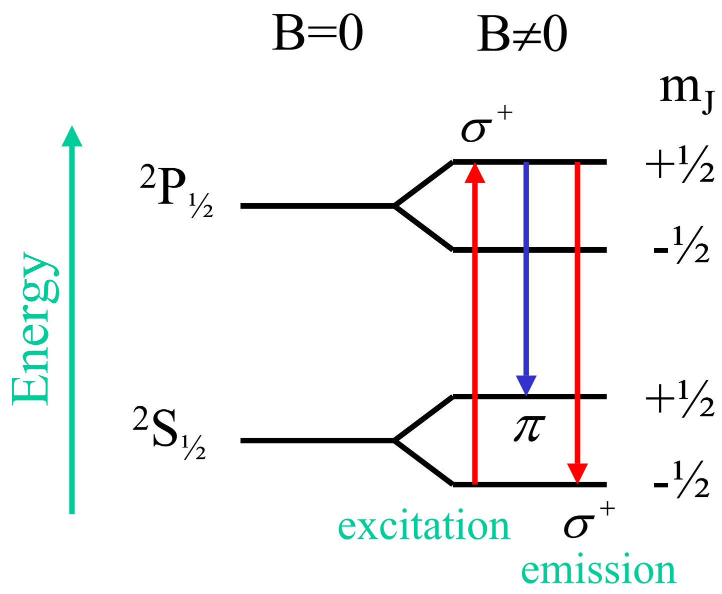

Figure 2.39: A circularly polarized beam of light tuned to the D_1 line forces atoms from the $m_J = -1/2$ ground state to the $m_J = +1/2$ excited state. They in turn decay back to both levels $m_J = -1/2$ and $m_J = +1/2$ of the ground state. Eventually, the pumping cycle depopulates the $m_J = -1/2$ ground state in favor of the $m_J = +1/2$ ground state. This technique is known as optical pumping.

field. These pumping photons must be in the direction of the applied magnetic field. Because of selection rules in optical transitions, only transitions from the ground state $^2S_{1/2},\ m_J = -1/2$ to the excited state $^2P_{1/2},\ m_J = +1/2$ are induced. Transitions back to the ground states $^2S_{1/2},\ m_J = +1/2$ and $^2S_{1/2},\ m_J = -1/2$ occur by emission of linearly polarized light π and right circularly polarized light σ^+, respectively, as shown in Fig. 2.39. In time, the pumping cycle will depopulate the ground state $m_J = -1/2$ in favor of $m_J = +1/2$. The polarization of the alkali metal can be reduced by relaxation processes that include collisions between atoms and collisions with the wall of the container. Moreover, when the excited electrons radiatively decay back to the ground state, they do so by emitting unpolarized fluorescence photons at the D_1 or D_2 line. That is they would tend to populate the $m_J = +1/2$ and $m_J = -1/2$ ground state equally. To quench this depolarization process, trace amounts of a buffer gas, in this case nitrogen (N_2), are introduced into the target cell. This way, the excited electrons are able to decay radiationlessly, by transferring energy to the vibrational, rotational, and translational degrees of freedom of the N_2 molecule, to the ground state. Unfortunately, since the introduction of nitrogen dilutes the ^{3}He cross section, there is a tradeoff between its quenching ability and its polluting of the ^{3}He cross section. Typically, the nitrogen to ^{3}He number density ratio is about 1:80. The alkali metal used in E94-010 was rubidium. Its D_1 line is at 795 nm and D_2 line at 780 nm [78]. The natural abundance of the two stable isotopes of rubidium is 72.165% for ^{85}Rb ($I = 5/2$) and 27.835% for ^{87}Rb ($I = 3/2$) [43].

2.6.3 Spin Exchange

The spin exchange process involves the hyperfine interaction of the electronic spin of Rb with the nuclear spin of ^{3}He. Schematically, the reaction is

$$\mathrm{Rb}(\uparrow) + {}^3\mathrm{He}(\downarrow) \rightarrow \mathrm{Rb}(\downarrow) + {}^3\mathrm{He}(\uparrow). \tag{2.41}$$

The magnetic dipole moment $\mu_{\mathbf{n}}$ of the neutron in the ^{3}He nucleus is [79, 80]

$$\mu_{\mathbf{n}} = \frac{g_n e}{2m_p}\mathbf{I} = g_n \mu_N \mathbf{I} \tag{2.42}$$

where g_n is the neutron g-factor, $\mathbf{I}$ is the nuclear spin, and $\mu_N = e/2m_p$ is the nuclear magneton. The magnetic dipole moment $\mu_{\mathbf{e}}$ of the rubidium valence electron is

$$\mu_{\mathbf{e}} = -\frac{e}{m_e}\mathbf{S} = -2\mu_B \mathbf{S} \tag{2.43}$$

where $\mathbf{S}$ is the electronic spin and $\mu_B = e/2m_e$ is the Bohr magneton. The magnetic field generated by $\mu_{\mathbf{n}}$ is [52]

$$\mathbf{B} = \frac{3(\mu_{\mathbf{n}} \cdot \hat{\mathbf{r}}) - \mu_{\mathbf{n}}}{r^3} + \frac{8\pi}{3}\mu_{\mathbf{n}}\delta(\mathbf{r}) \tag{2.44}$$

The potential energy of a dipole in an external magnetic field is $U = -\mu \cdot \mathbf{B}$, therefore the interaction Hamiltonian is

$$H_{SE} = -\left[\frac{3(\mu_{\mathbf{n}} \cdot \hat{\mathbf{r}})(\mu_{\mathbf{e}} \cdot \hat{\mathbf{r}}) - (\mu_{\mathbf{n}} \cdot \mu_{\mathbf{e}})}{r^3}\right] - \frac{8\pi}{3}(\mu_{\mathbf{n}} \cdot \mu_{\mathbf{e}})\delta(\mathbf{r}) \tag{2.45}$$

For an electron in a spherically symmetric s state, the expectation value of the first term vanishes and the spin exchange Hamiltonian becomes [81]

$$H_{SE} = \frac{16\pi}{3} g_n \mu_N \mu_B \mathbf{I} \cdot \mathbf{S} |\psi_e(0)|^2 \tag{2.46}$$

The time evolution of the ^{3}He polarization is [81, 89]

$$P_{He}(t) = \langle P_{Rb} \rangle \left[\frac{\gamma_{SE}}{\gamma_{SE} + \Gamma_1}\right] \left[1 - e^{-(\gamma_{SE}+\Gamma_1)t}\right] \tag{2.47}$$

where $\langle P_{Rb} \rangle$ is the average Rb polarization, γ_{SE} is the spin exchange rate, and Γ_1 is the ^{3}He polarization relaxation rate excluding spin exchange.

2.6.4 NMR Polarimetry

Consider a magnetic dipole with moment $\boldsymbol{\mu}$ immersed in a magnetic field $\mathbf{B}$. The torque $\boldsymbol{\tau}$ experienced by the magnetic dipole in the presence of the magnetic field is given by

$$\boldsymbol{\tau} = \boldsymbol{\mu} \times \mathbf{B}. \tag{2.48}$$

If $\mathbf{S}$ is the spin that gives rise to the dipole, then

$$\boldsymbol{\mu} = \gamma \mathbf{S} \tag{2.49}$$

where γ is the gyromagnetic ratio. Since torque is the rate of change of angular momentum,

$$\frac{d\boldsymbol{\mu}}{dt} = \gamma \boldsymbol{\mu} \times \mathbf{B}. \tag{2.50}$$

In a macroscopic medium with many dipoles, it is customary to introduce the magnetization $\mathbf{M}$ as the magnetic dipole moment per unit volume. The magnetization is given by [82]

$$\frac{d\mathbf{M}}{dt} = \gamma \mathbf{M} \times \mathbf{B} \tag{2.51}$$

Eq. 2.51 describes the vector $\mathbf{M}$ as precessing in an inertial frame with angular velocity $\boldsymbol{\omega} = -\gamma \mathbf{B}$. In a physical sample, spin-lattice relaxation or longitudinal relaxation involves the exchange of energy with other degrees of freedom (lattice). This relaxation mode is characterized by a relaxation time T_1 and relaxes M_z to an equilibrium value M_0. Spin-spin relaxation or transverse relaxation involves destructive interference with other spins. This relaxation mode is characterized by a relaxation time T_2 and relaxes M_x and M_y to 0 [83]. Phenomenologically, the equation of motion is modified to provide the Bloch equations, first introduced by Felix Bloch in 1946 [84]:

$$\left.\begin{aligned} dM_x/dt &= \gamma(M_y B_z - M_z B_y) - M_x/T_2 \\ dM_y/dt &= \gamma(M_z B_x - M_x B_z) - M_y/T_2 \\ dM_z/dt &= \gamma(M_x B_y - M_y B_x) - (M_z - M_0)/T_1 \end{aligned}\right\} \tag{2.52}$$

2.6.5 EPR Polarimetry

Principle

The EPR (Electron Paramagnetic Resonance) sometimes known as ESR (Electron Spin Resonance) principle is very similar to NMR (Nuclear Magnetic Resonance). Whereas NMR relies on the interaction of the nuclear spin with an external magnetic field, EPR is a result of the electronic spin of paramagnetic substances interacting with an external magnetic field. A paramagnetic material is one possessing an unpaired outer shell electron producing a net, non-zero electronic spin. The case of paired outer shell electrons with zero net spin or closed shell atoms is termed a diamagnetic substance. The energy splitting ΔE in the presence of the magnetic field B provides the fundamental equation of EPR [85]

$$h\nu = \Delta E = g_S \mu_B B \tag{2.53}$$

where $h = 4.135\ 667\ 27(16) \times 10^{-15}$ eV s is the Planck constant, ν is the frequency in Hz, $g_S = -2.002\ 319\ 304\ 3737(82)$ is the Landé g-factor of the electron, and

$\mu_B = e\hbar/2m_e = 5.788\ 381\ 749(43) \times 10^{-5}$ eV T^{-1} is the Bohr magneton [86–88]. During E94-010, the holding field was set around 18 G. This puts the resonance frequency at about 50 MHz, in the RF (Radio Frequency) region.

EPR polarimetry involves measuring the shift of the Rb Zeeman resonance line induced by the magnetic field created by polarized ^{3}He [89]. There are two processes responsible for shifting the Rb Zeeman resonance: Rb-He spin exchange and ^{3}He magnetization. The hyperfine structure Hamiltonian for an atom in a magnetic field $\mathbf{B}$ is [90,91]

$$\begin{aligned}\mathcal{H} &= hA\mathbf{I}\cdot\mathbf{S} + B\frac{3(\mathbf{I}\cdot\mathbf{S})^2 + \frac{3}{2}(\mathbf{I}\cdot\mathbf{S}) - I(I+1)S(S+1)}{2I(2I-1)S(2S-1)} \\ &\quad + g_S\mu_B\mathbf{S}\cdot\mathbf{B} + g_I\mu_N\mathbf{I}\cdot\mathbf{B} \qquad (2.54)\end{aligned}$$

where $\mathbf{I}$ is the nuclear spin and $\mathbf{S}$ is the electronic spin. A is the magnetic dipole interaction constant and B is the electric quadrupole interaction constant. Its is zero for $S = 0$ or $1/2$ because the electron distribution is spherically symmetric for these cases. g_I is the Landé g-factor of the Rb nucleus. The quantity $\mu_N = e\hbar/2m_p = 3.152\ 451\ 238(24) \times 10^{-8}$ eV T^{-1} is the nuclear magneton [86]. The ratio $\mu_I/\mu_N = +1.353\ 351\ 5$ and $I = 5/2$ for ^{85}Rb [43]. Furthermore, since $\mu_I = g_I\mu_N I$ [85], $g_I = 0.541\ 340\ 6$. The Rb-He spin-exchange process contributes a $\mathbf{K}\cdot\mathbf{S}$ term to the Hamiltonian [78]

$$\mathcal{H} = hA\mathbf{I}\cdot\mathbf{S} + h\alpha\mathbf{K}\cdot\mathbf{S} + g_S\mu_B\mathbf{S}\cdot\mathbf{B} + g_I\mu_N\mathbf{I}\cdot\mathbf{B} \qquad (2.55)$$

where $\mathbf{K}$ is the nuclear spin of ^{3}He and α is the frequency shift parameter. The bulk magnetization of the polarized ^{3}He adds an effective static field δB to the external magnetic field $\mathbf{B}$

$$\delta B = G\mu_{He}[He]P_{He} \qquad (2.56)$$

where P_{He} is the polarization of ^{3}He, $[He]$ is the ^{3}He number density, μ_{He} is the magnetic moment of ^{3}He, and G is a geometrical factor characterizing the target cell. For example, $G = 8\pi/3$ for spherical volumes. The term $\mathbf{I}\cdot\mathbf{S}$ dominates the Hamiltonian. $A = 1012$ MHz in comparison to $g_S\mu_B B/h = 50$ MHz at $B = 18$ G. The $\mathbf{I}\cdot\mathbf{B}$ term is even more diminutive since $\mu_N/\mu_B = m_e/m_p \approx 1/1836$. Consequently, in considering eigenstates of $\mathcal{H}$, it is reasonable to invoke the eigenstates of total angular momentum $\mathbf{F} = \mathbf{I} + \mathbf{S}$. Their energies are given exactly by the Breit-Rabi formula [90–92] for an intermediate field, that is the interaction between the external magnetic field and the atom is comparable to the hyperfine interaction,

$$E(F = I \pm 1/2, M_F) = -\frac{hA}{4} - g_I \mu_N B M_F \pm \frac{hA}{4}(2I+1) \times \sqrt{1 + \frac{4M_F}{2I+1}x + x^2} \quad (2.57)$$

where $x = 2(g_S \mu_B B + g_I \mu_N B + h\alpha\langle K \rangle)/hA(2I+1)$. The energy difference between adjacent energy levels is

$$\Delta E = E(F, M_F) - E(F, M_F - 1) \quad (2.58)$$

$$= \frac{hA}{4}(2I+1)\left[\sqrt{1 + \frac{4M_F}{2I+1}x + x^2} - \sqrt{1 + \frac{4(M_F-1)}{2I+1}x + x^2}\right] \quad (2.59)$$

$x \ll 1$ at low magnetic field, so x^2 can be dropped in expanding the radical terms in Taylor series.

$$h\nu = \Delta E = \frac{hA}{2}x = \frac{(g_S \mu_B + g_I \mu_N)(B + \delta B) + h\alpha\langle K \rangle}{2I+1} \quad (2.60)$$

where the classical magnetic field δB of the polarized ^{3}He is shown explicitly. The frequencies for each polarization direction are

$$\nu^{\uparrow} = \frac{g_S \mu_B (B + \delta B) + h\alpha\langle K \rangle}{h(2I+1)} \quad (2.61)$$

$$\nu^{\downarrow} = \frac{g_S \mu_B (B - \delta B) - h\alpha\langle K \rangle}{h(2I+1)} \quad (2.62)$$

where the $g_I \mu_N$ term was ignored since it is much smaller then the corresponding $g_S \mu_B$ term. The EPR frequency shift is then

$$\Delta\nu_{EPR} = \nu^{\uparrow} - \nu^{\downarrow} = \frac{g_S \mu_B}{h(2I+1)}\delta B + \frac{\alpha\langle K \rangle}{2I+1} \quad (2.63)$$

The EPR frequency shift is usually written as [93]

$$\Delta\nu_{EPR} = \frac{g_S \mu_B}{h(2I+1)} \frac{8\pi}{3} \kappa_0 \mu_{He} [He] P_{He} \quad (2.64)$$

where κ_0 is a constant that depends on temperature only [94]

$$\kappa_0 = (5.17 \pm 0.37)\left[1 + \frac{T - 100°C}{(563 \pm 30)°C}\right] \quad (2.65)$$

Measuring the ^{3}He polarization is reduced to measuring the difference in EPR frequencies for each polarization orientation.

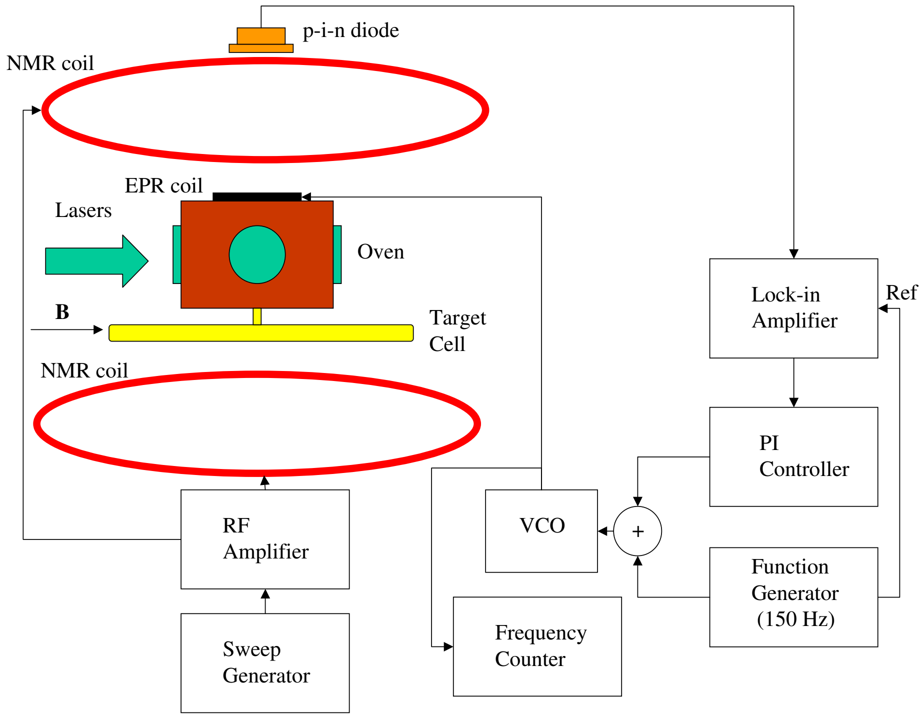

Figure 2.40: Instrumentation for EPR polarimetry. The p-i-n diode picks up the EPR signal from a window on top of the oven. That signal is extracted with a lock-in amplifier, then sent to a PI controller box which outputs the frequency at which the signal is zero (EPR resonance frequency). The resulting signal is mixed with a modulation source, then sent to a VCO to provide the frequency that drives the EPR coil. The EPR coil provides the RF excitation to induce EPR transitions of Rb in the target cell.

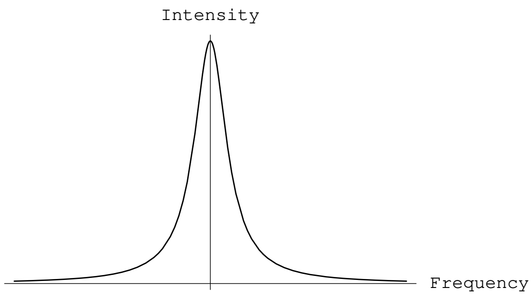

Figure 2.41: EPR lineshape.

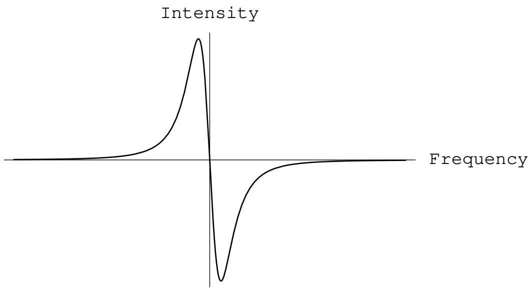

Figure 2.42: First derivative of EPR lineshape.

Instrumentation

The apparatus to detect the EPR resonance of rubidium is shown in Fig. 2.40. A RF field of 6 kHz modulated at 200 Hz was applied via the EPR coil. The field is transverse to the main holding field. The effect of the RF field is to induce the transition $M_F = 3 \rightarrow 2$ in rubidium. The electrons in the state $M_F = 2$ are then optically pumped to the excited P-states. Most of these excited electrons decay back to the ground S-state radiationlessly with the help of the buffer gas (nitrogen). However, a small minority, typically 3 to 5%, decays by emitting a $D_1 = 795$ nm or $D_2 = 780$ nm fluorescence photon. Due to frequency modulation of the magnetic field, the intensity of the fluorescence is proportional to the first derivative of the EPR resonance with respect to the excitation frequency [95]. The EPR lineshape and its first derivative are shown in Figs. 2.41 and 2.42. To avoid stray D_1 radiation from the pumping lasers, a D_2 filter is placed in front of the p-i-n diode or photodiode that monitors the fluorescence of the pumping chamber. The EPR signal from the photodiode is extracted with a lock-in amplifier, then sent to a PI (proportional-integral) controller. The PI controller locks in to the EPR resonance frequency which is the frequency at which the first derivative of the EPR lineshape is zero. The resonance frequency is mixed with a low frequency modulation source, then fed to a frequency counter and a VCO (voltage-controlled oscillator) to drive the EPR coil. The purpose of the feedback circuit (PI controller) is to account for drifts in the holding field and hence drifts in the EPR resonance frequency. The particulars of the feedback circuit are exposed in Fig. 2.43. A typical EPR data taking session consisted of sweeping the frequency through EPR resonance using the technique of AFP (Adiabatic Fast Passage) to flip

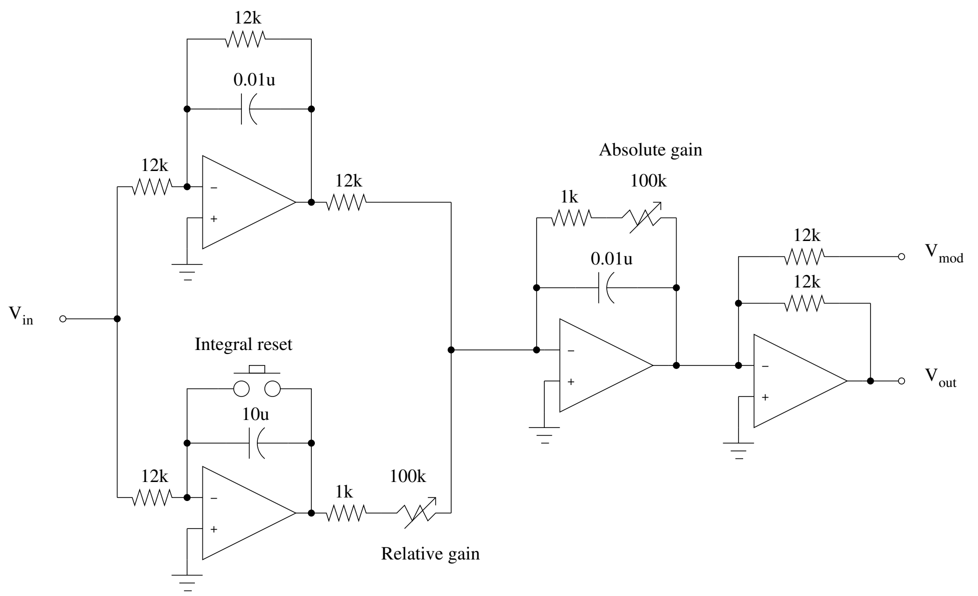

Figure 2.43: The proportional-integral controller output coupled with the modulation source V_{mod} adjusts the input to the voltage-controlled oscillator at V_{out} to keep the input to the lock-in amplifier V_{in} at zero [89].

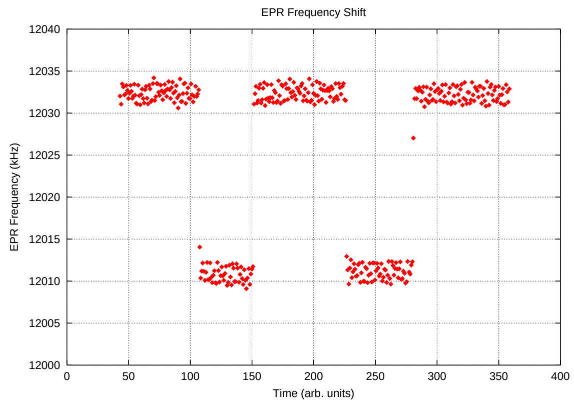

Figure 2.44: Representative EPR frequency shift data set taken on 9/28/1998 at 9:53 pm. The difference in the EPR resonance frequencies between the alternate spin directions is proportional to the ^{3}He polarization. Here the EPR frequency shift is roughly 21 kHz out of 12 MHz.

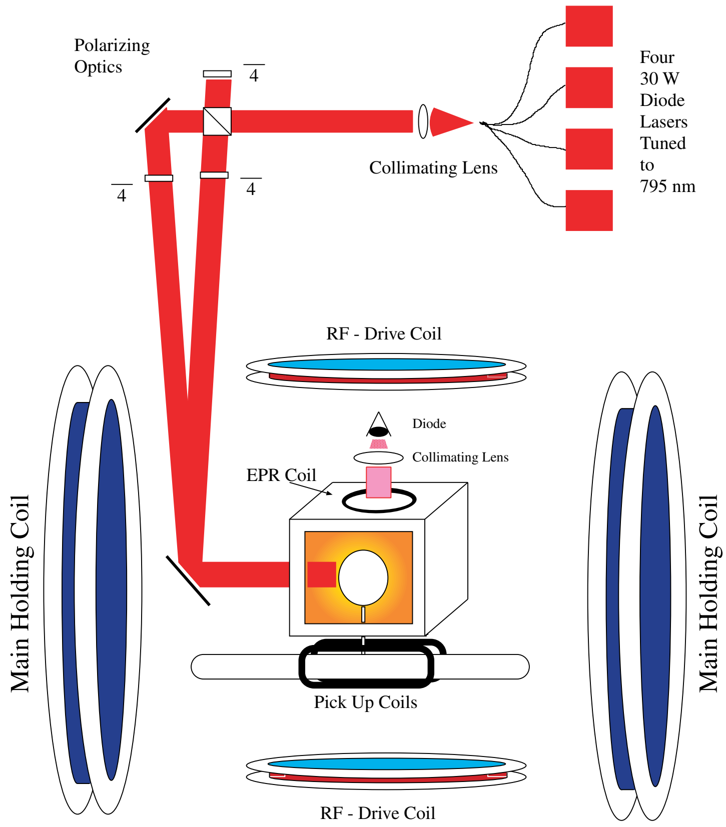

Figure 2.45: Schematic of the polarized ^{3}He target used during E94-010. The upper right features a set of high-power lasers. The upper left displays the polarizing optics. Only one set of Helmholtz coils is shown. The RF drive coils are used for both EPR and NMR measurements. The target cell sits at the center with its pumping chamber located inside an oven.

the spins at intervals of about a minute. A sample EPR data set is shown in Fig. 2.44. The difference in EPR resonance frequencies is proportional to the ^{3}He polarization.

2.6.6 Polarized ^{3}He Target Setup

The setup of the polarized ^{3}He target is shown in Fig. 2.45. A set of high-power diode lasers is shown on the upper right. They are used for optical pumping of the target cell. Four lasers are used for each pumping direction: longitudinal and transverse. In the upper left is shown the polarizing optics which consists of focusing lenses, mirrors, half-wave plates and quarter-wave plates. The latter are used to polarize the laser beam. The beam polarization achieved is close to 100%. The oven, in the center of the diagram, holds the pumping chamber. The oven is used to bring the rubidium in the pumping chamber to a temperature of 170°C and in its gaseous state, to be used in spin-exchange collisions with the helium in the target cell. There are two sets of Helmholtz (main holding) coils, but only one set is shown in the diagram. The other set is perpendicular to the first one. The combination of all four Helmholtz coils provide a main holding magnetic field in any direction in the horizontal plane. The field is utilized to define the polarization direction. The RF drive coils provide a radio frequency field of 91 kHz during a NMR target polarization measurement. The EPR drive coils achieve a similar purpose but for the EPR target polarization measurement technique. The EPR p-i-n diode reads the shift in the rubidium optical transition which is proportional to polarization. The pick-up coils, along the length of the target chamber, are used to read the induced signal during an AFP/NMR measurement of the target polarization. Not shown is the target ladder that includes the reference cell and other targets used for calibration.

Chapter 3

ANALYSIS

There are two fundamental quantities of interest that are sought after in many experimental nuclear and particle physics experiments: cross section and asymmetry. From these two observables, much of the physics being investigated can be readily extracted. These quantities bridge the gap between experiment and theory in physics. The experimental differential cross section is obtained with the following formula:

$$\left(\frac{d^2\sigma}{d\Omega dE'}\right)_{\text{exp}} = \frac{N}{N_{\text{inc}}N_{\text{target}}\Delta\Omega\Delta E'}, \tag{3.1}$$

where σ is the total cross section, $\Delta\Omega = \Delta\theta\Delta\phi$ is the angular acceptance of the spectrometer, $\Delta E'$ is the bin size in scattered electron energy, N is the number of scattered electrons, $N_{\text{inc}} = Q/e$ is the number of incident electrons and is simply the accumulated charge Q normalized by the electronic charge e, and N_{target} is the number of target nuclei per unit area. The experimental asymmetry is calculated with the following formula:

$$A_{\text{exp}} = \frac{1}{fP_{\text{b}}P_{\text{t}}}\frac{N^+/Q^+ - N^-/Q^-}{N^+/Q^+ + N^-/Q^-}, \tag{3.2}$$

where f is a dilution factor introduced by unpolarized nuclei in the target cell, notably nitrogen, P_{b} is the beam polarization, P_{t} is the target polarization, and $N^{+(-)}$ is the number of detected scattered electrons with positive (negative) helicity.

3.1 Procedure of Analysis

A grand overview of the analysis procedure is illustrated in Fig. 3.1. The raw counting rates N^+ and N^- for particles detected in the spectrometers may contain pions and other unwanted particles besides electrons. Thus, the events are subjected to particle identification with the shower and Cherenkov counters. Events that fail to provide a good track reconstruction by the drift chambers are also eliminated. In addition, each detector introduces a detection efficiency which must be corrected for. Normalizing the resulting scattered electrons counting rates N_e^+ and N_e^- by the total beam charge, the dilution factor, the beam and target polarization, the target density, the angular acceptance of the spectrometer obtained by Monte Carlo simulations, the beam energy, and the radiative corrections provide the cross sections and asymmetries. Suitable combinations of the cross sections and various kinematical factors give the structure functions and GDH sum rule for ^{3}He. The corresponding physics quantities for the neutron are extracted from ^{3}He by accounting for nuclear effects with the convolution approach of C. Ciofi degli Atti *et al.* [32].

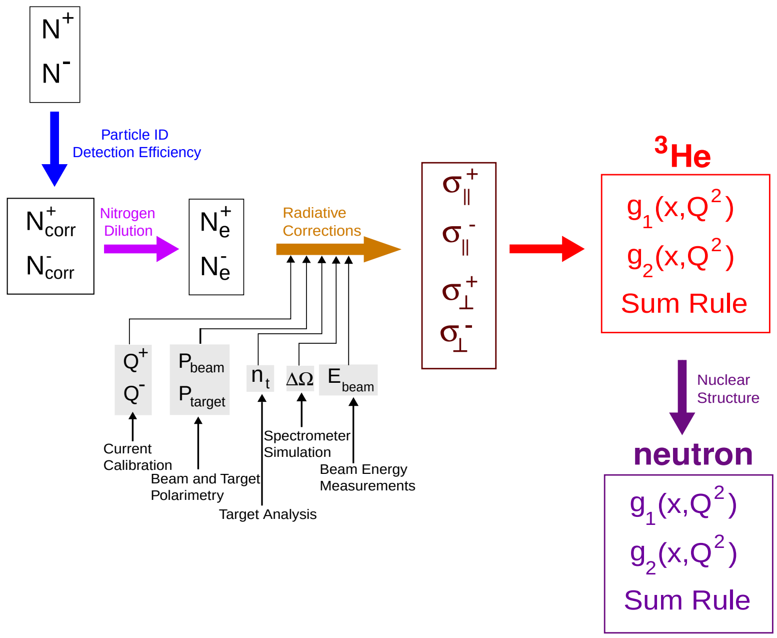

Figure 3.1: Analysis flowchart from raw counting rates to neutron structure functions and the GDH sum rule.

3.2 Data Reduction

The event mode data goes through several stages of filtering in the process of extracting cross sections and scattering asymmetries. These stages include:

1. Event acquisition is limited by the data readout and data transferred rates, requiring normalization to the raw trigger rate, as described in a later section.

2. Events are selected for processing by requiring the reconstruction of a good event track in the wire chamber. Multiple tracks are rejected by the algorithm. The results are renormalized to account for the events not analyzed and other deadtime corrections.

3. "Good events" are further filtered by geometrical cuts and particle ID cuts discussed further in the following sections.

4. The cross section generated must then be normalized for luminosity and acceptance. Most of these corrections are standard to event mode in Hall A HRS event analysis.

Here only the cuts specific to this experiment will be discussed.

3.2.1 Geometrical Cuts

The main purpose of the geometrical cuts is to get rid of events coming from the target windows and to cut off the edges of the spectrometer acceptance. That is, it is desirable to stay within a well-understood part of the acceptance and keep away from regions such as the edges of the acceptance where poor statistics yield large errors and the acceptance is not well understod. The geometrical cuts are applied on target variables θ, ϕ, y, and δ. Two two-dimensional cuts were applied to the data from both the Electron and Hadron spectrometers. The first is a cut on the transverse acceptance variables ϕ and y. The second is a cut on the bend plane observables θ and δ. The geometrical cuts used in the final analysis are shown in Fig. 3.2.

3.2.2 Electron Arm Shower Counters

Calibration of the shower counters is essential in order to determine pion rejection rates (π/e ratio). Cuts on the lead glass calorimeters along with cuts on the Cherenkov counters can separate pions from electrons by several orders of magnitude. An understanding of the issues associated with these detectors such as detector efficiencies and pion suppression abilities is of paramount importance. The calibration of the

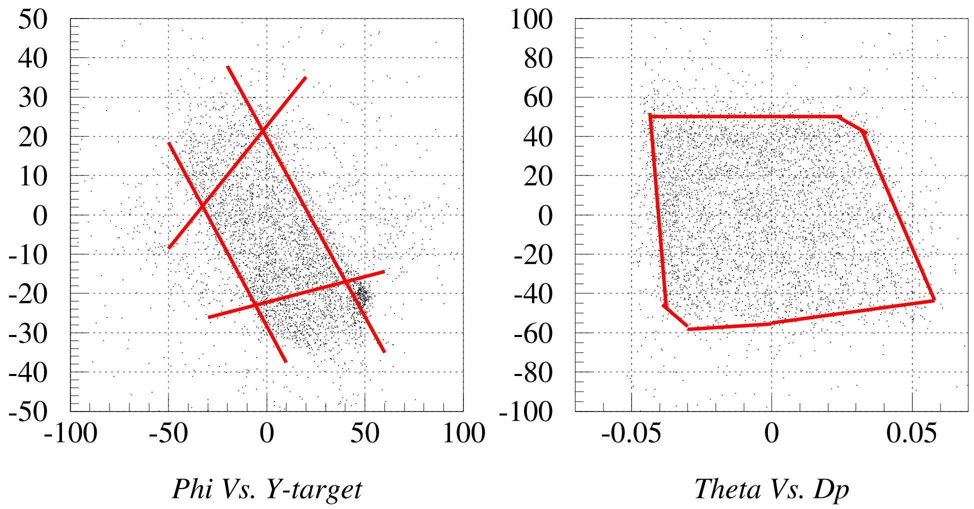

Figure 3.2: Geometrical cuts on target variables θ (Theta), ϕ (Phi), y (Y-target), and δ (Dp) used in the final analysis. The concentration of events in the lower right-hand quadrant outside the cut region in the left figure is due to the target windows.

shower counters for both the Electron and Hadron Arms during E94-010 is detailed in Ref. [96]. The technique employed is described in detail in Ref. [97].

Calibration

Einstein's relation, $E^2 = p^2 + m^2$, simplifies to $E \approx p$ or $E/p \approx 1$ for electrons ($m_e = 0.511$ MeV) at the high beam energies of E94-010 (0.862-5.070 GeV). This is verified in the plot of E/p vs. p in Fig. 3.3. The low data points come from runs taken near the end of the experiment when the scintillator threshold was lowered due to efficiency problems. It is believed that some of the helium which was used to fill the target chamber escaped and corrupted the vacuum of the phototubes of the scintillator counters thereby lowering their efficiency. The immediate solution was to lower the threshold of the trigger scintillators which caused some noise in trigger. However, after final cuts, this was no longer a problem. The high data points come from runs with momentum settings near the limits of the spectrometers. The NMR probe of the dipole proves unreliable and a gaussmeter must be used instead. The difference can be attributed in part to a systematic error between the NMR probe and the gaussmeter. The fractional resolution σ/E scales inversely as the square root of energy E. This is because electromagnetic showers obey a Poisson distribution, for which the variance σ^2 is equal to the mean energy E. A shower counter's fractional resolution is then:

$$\frac{\sigma}{E} = \frac{\sqrt{E}}{E} = \frac{1}{\sqrt{E}}. \tag{3.3}$$

An additional factor is needed to account for various fundamental processes that lead to energy deposition in the detector [98, 99]. In particular for lead-glass shower counters, $\sigma/E \sim 5\%/\sqrt{E}$ as indicated in Table 27.5 of Ref. [100]. This agrees well with the measured values shown in Fig. 3.3 ($\sigma/p \sim 5.3\%/\sqrt{p}$) and Fig. 3.7 ($\sigma/p \sim 4.2\%/\sqrt{p}$) for the Electron Arm and Hadron Arm, respectively.

Detection Efficiency

A T1 event is recorded when paddles from scintillator planes S1 and S2 fire in an acceptable pattern, and the Cherenkov counter fires. The recipe for calculating the efficiency of the calorimeter after selecting T1 events that pass the geometrical cuts described above is:

$$\text{efficiency} = \frac{\text{events registered in preshower, shower, and Cherenkov counters}}{\text{events registered in Cherenkov counter}}. \tag{3.4}$$

As can be seen in Fig. 3.4, the detection efficiency is consistently better than 99% except at low energy (862 MeV) where a few events are omitted by the cluster formation algorithm. This fact is dramatically illustrated in Fig. 3.5. Many events to the left of the histogram never enter the data acquisition system. A possible remedy for the situation is to use the output of the raw ADCs instead. The E/p and preshower$/p$ cuts introduced in Fig. 3.5 excludes certain good electron events. Nonetheless, the inefficiency of these cuts was kept below 1%. [

Pion Suppression

The estimate for pion contamination is achieved by applying cuts on different detectors:

1. Cut on the preshower: An initial anti-Cherenkov cut, i.e. selection of all particles that fail to trigger the Cherenkov, is submitted. Ideally, no electrons are left in the histogram. A cut is now made on the preshower where the pion peak

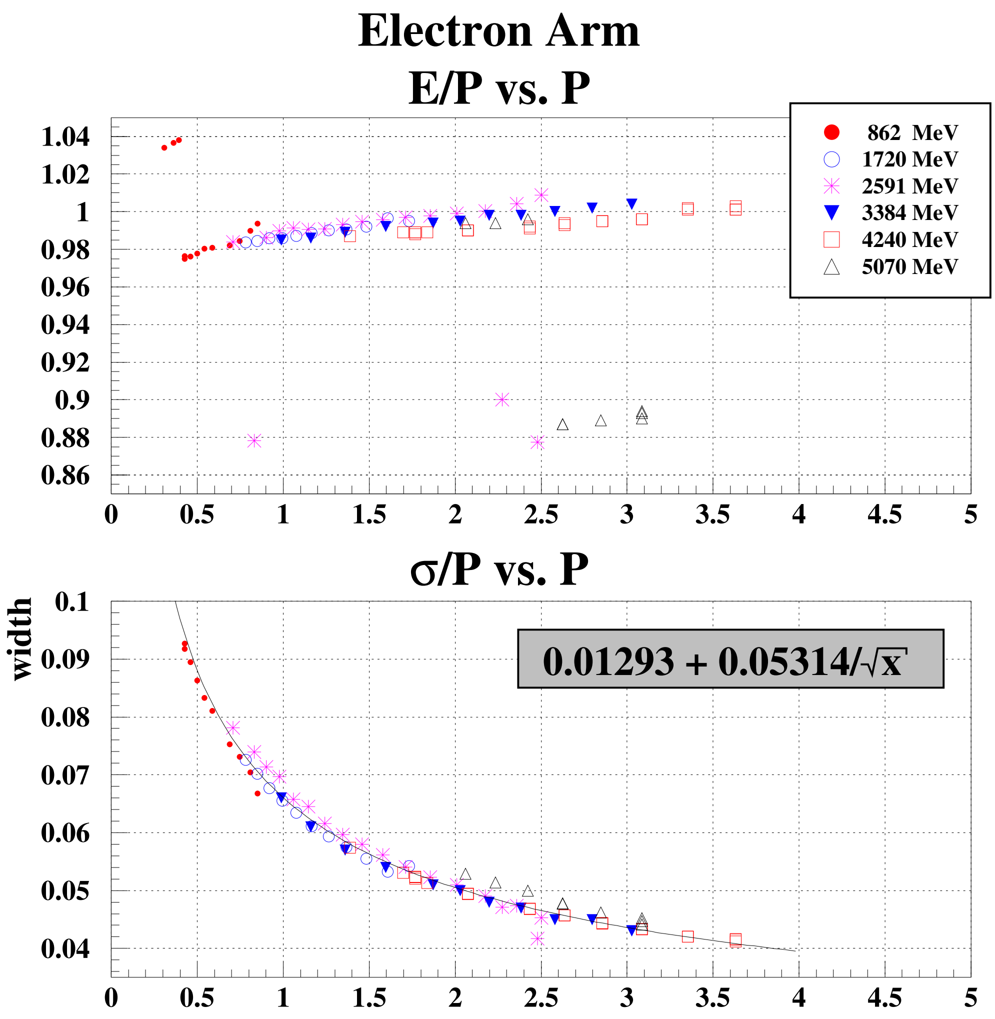

Figure 3.3: Plots of E/p (top) and σ/p (bottom) *vs.* p showing proper calibration of the shower counters in the Electron Arm.

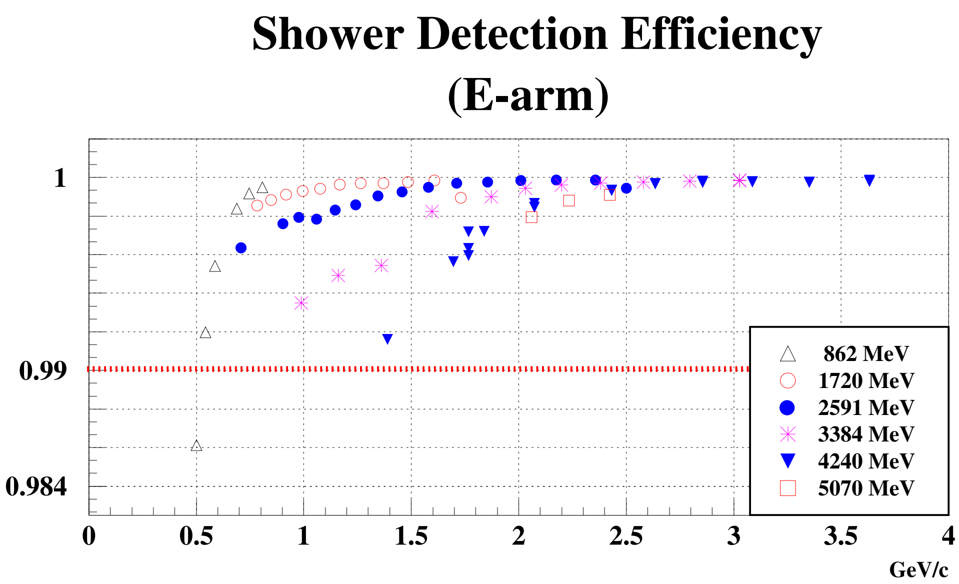

Figure 3.4: Detection efficiency for the Electron Arm. At low energy (862 MeV) the cluster formation algorithm drops a few events.

is much more pronounced since not all of the pion energy is absorbed in this first stage of the shower counter. The ratio of pions before to after the preshower cut is the preshower pion suppression factor. It is typically around 4–5.

2. Cut on the Cherenkov: An E/p plot reveals two peaks. Pions are on the left and electrons on the right. An E/p cut then separates pions from electrons. A further anti-Cherenkov cut then selects pions. The ratio of pions before to after the anti-Cherenkov cut is the Cherenkov pion suppression factor.

to obtain suppression factors. The results are shown in Fig. 3.6. The final pion contamination is the ratio of pions to electrons inside the E/p cut, divided by the preshower and Cherenkov suppression factors.

3.2.3 Hadron Arm Shower Counter

A calorimeter consisting of 32 (16×2) lead-glass blocks was added to the rear of the detector stack in the Hadron Arm prior to E94-010.

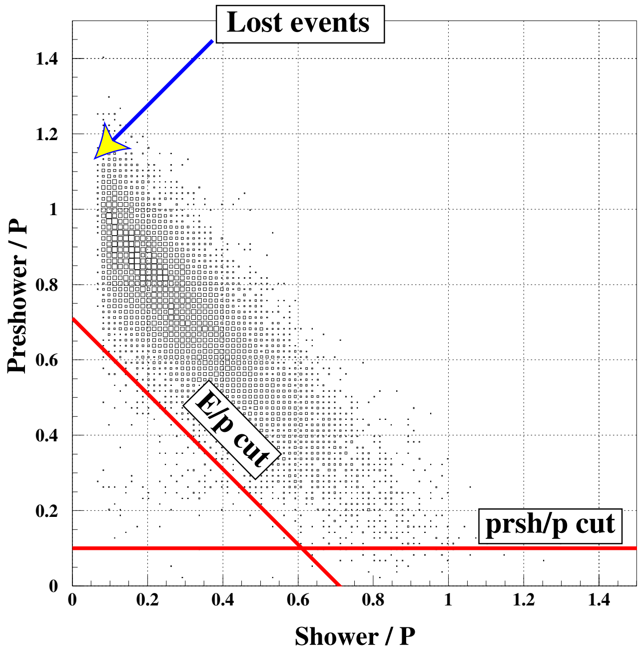

Figure 3.5: Two-dimensional histogram of preshower/p vs. shower/p at 862 MeV showing E/p and preshower/p cuts, where E =preshower+shower. The cluster formation algorithm drops some events on the left as is discussed in the left hand spectrum, resulting in a reduced efficiency.

Calibration

The shower counter in the Hadron Arm is not a total absorption calorimeter. The method used to calibrate the Electron Arm calorimeter cannot be used here. For calibration purpose, only events that fire in a single block are examined. This is to avoid miscalibration with events that pass through fissures between adjacent blocks in the calorimeter. The method of analysis is fully described in Ref. [96]. The software gain of each block is then manually adjusted to normalize the shower output by particle momentum to unity. The results are displayed in Fig. 3.7. The detector resolution σ/E of the Hadron Arm calorimeter is worse than that of the Electron Arm by about 1%.

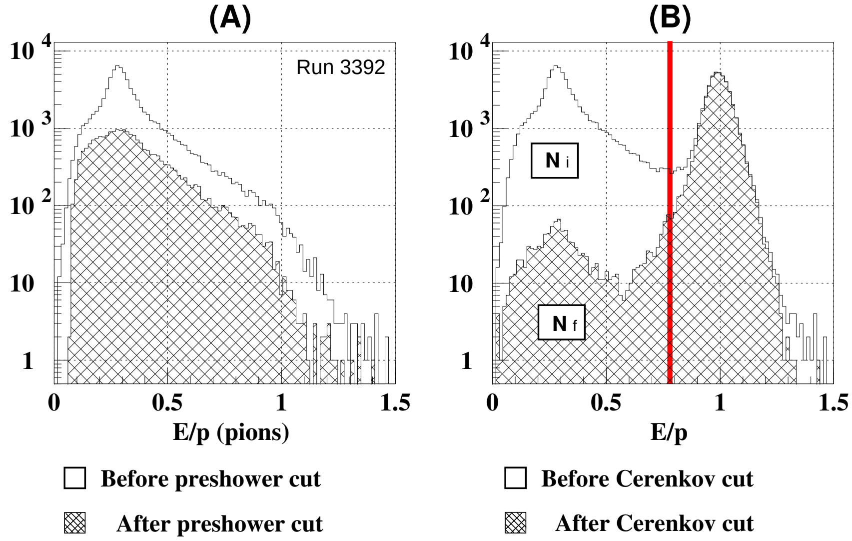

Figure 3.6: **(A)** Pion suppression with a preshower cut. An anti-Cherenkov cut is applied to the initial data sample to isolate pions. A preshower cut is made on the pion population. A factor of 4-5 is obtained in this fashion for the ratio of pions before to after the preshower cut. **(B)** Pion suppression with a Cherenkov cut. Pions are identified as those particles to the left of the E/p cut. An anti-Cherenkov cut is then applied to the pion sample. The resulting ratio of pions before and after the anti-Cherenkov cut is of a couple of orders of magnitude.

Detection Efficiency

The detection efficiency of the Hadron Arm shower counter is reduced by the loss of electrons that pass through the spacing between adjacent lead-glass blocks. However, the detector efficiency is kept higher than 99%. The result is shown in Fig. 3.8.

Cut Efficiency

The cut on the Hadron shower was chosen in such a way to preserve inefficiency below 0.5%. The π/e ratios and detector efficiencies for both the Electron and Hadron Arms are tabulated in Ref. [96].

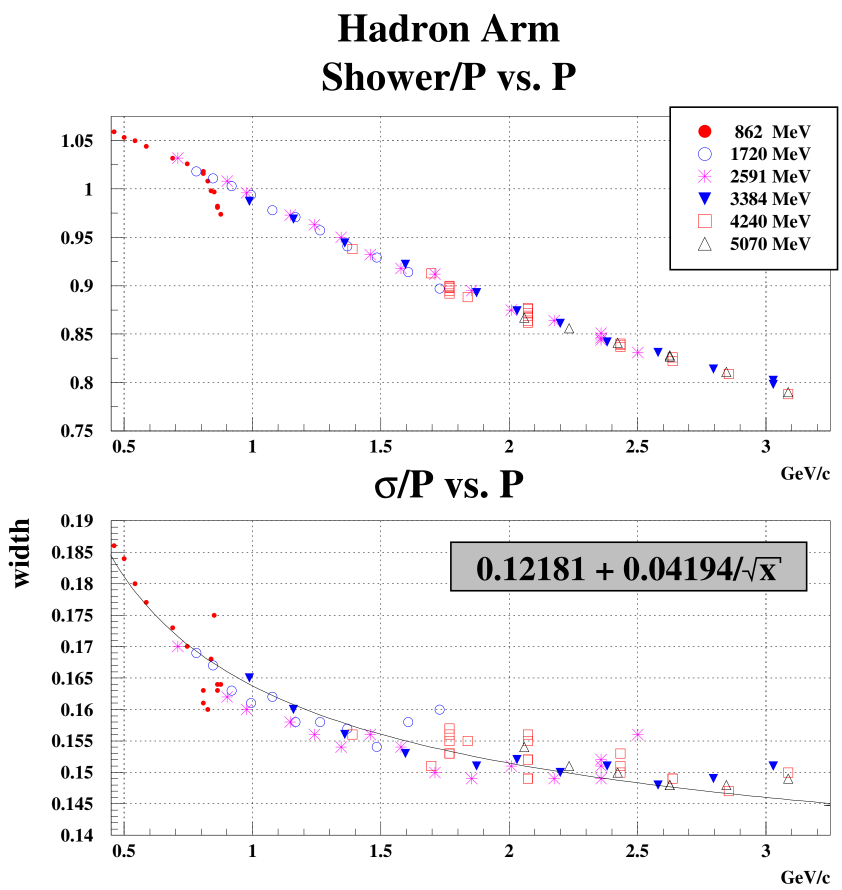

Figure 3.7: Plots of E/p and σ/p *vs.* p for the Hadron Arm. Note the shower counter in the Hadron Arm is not a total absorption calorimeter.

3.2.4 Cherenkov Detectors

Calibration

Calibrating the Cherenkov detectors entails adjusting the offsets and gains of the individual phototube ADCs. Since some electrons will fire several phototubes, one needs to sum over all phototubes to obtain a good collection efficiency. Histograms of the raw and calibrated Cherenkov ADCs are shown in Figs. 3.9 and 3.10. Note the location of the single photoelectron peak on the left before and after calibration.

Stability

It was found that the output of the Cherenkov ADCs was reasonably stable over the momentum range of E94-010 (see Fig. 3.11).

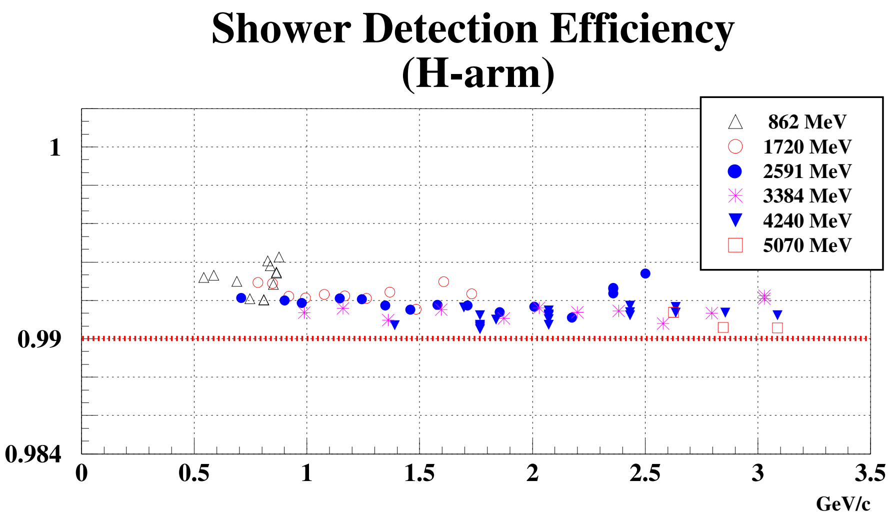

Figure 3.8: Detection efficiency of the Hadron Arm shower counter. Electrons lost in the spacing between blocks effectively reduce the detector efficiency. Nevertheless, an efficiency of better than 99% is maintained throughout.

Detection Efficiency

The detection efficiency ϵ for a Poisson process like the emission of Cherenkov radiation is:

$$\epsilon = 1 - e^{-\mu}, \tag{3.5}$$

where μ is the average number of photoelectrons produced per meter, $e^{-\mu}$ is the probability of emitting no photoelectron, and $\mu \approx 9$ [102] yields $\epsilon \approx 99.99\%$. The method used to calculate efficiencies in the Electron and Hadron Arms is illustrated in Figs. 3.12 and 3.13. For the Electron Arm (Fig. 3.12), a tight two-dimensional cut is applied to the preshower *vs.* shower to select good electrons, followed by a cut on the Cherenkov signal. The Cherenkov detection efficiency is the is the ratio of events that pass the Cherenkov cut to these that pass the two-dimensional preshower *vs.* shower cut:

$$\text{Detection efficiency} = \frac{\text{events registered in the Cherenkov detector}}{\text{events that pass the preshower } vs. \text{ shower 2-D cut}}. \tag{3.6}$$

For the Hadron Arm (Fig. 3.13), a shower/p cut is made to select good electrons. The Cherenkov detection efficiency is the number of events that fire the Cherenkov

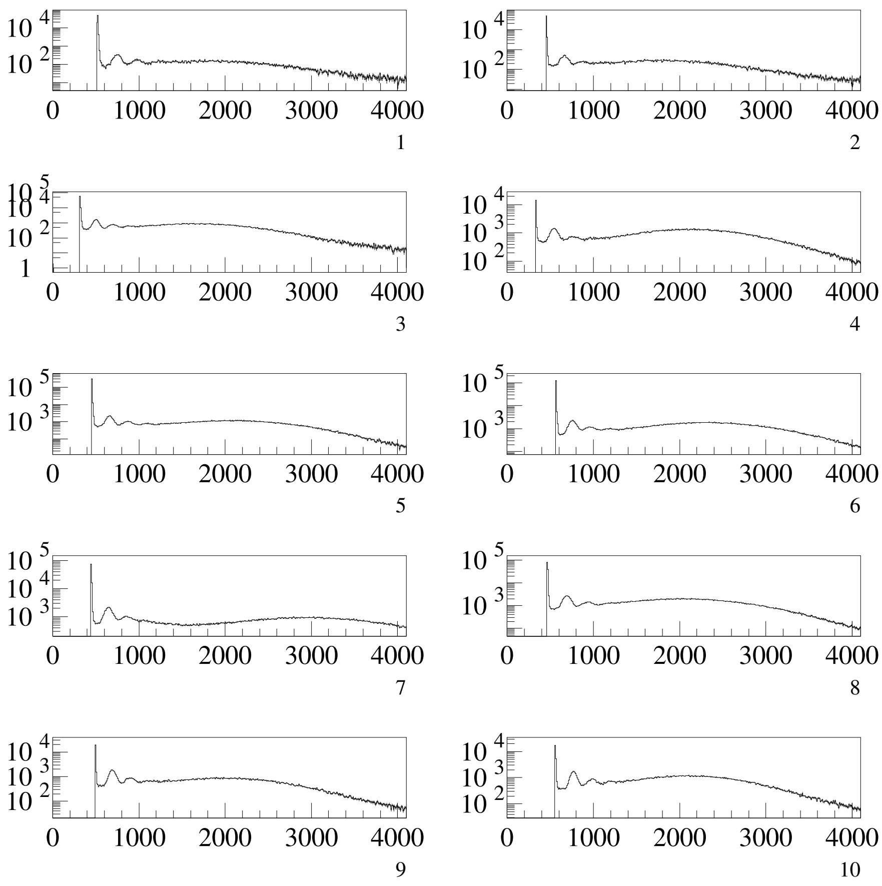

Figure 3.9: Raw Cherenkov ADC spectra.

counter to the number of events that pass the shower/p cut:

$$\text{Detection efficiency} = \frac{\text{events registered in the Cherenkov detector}}{\text{events that pass the shower cut}}. \tag{3.7}$$

The efficiencies as a function of momentum were also investigated with the results shown in Fig. 3.14. Pion contamination is more pronounced at lower momenta. See tables in Ref. [96]. This degrades the detection efficiency.

Cut Efficiency

Values for detection and cut efficiencies are tabulated for all kinematics in the appendix of Ref. [101].

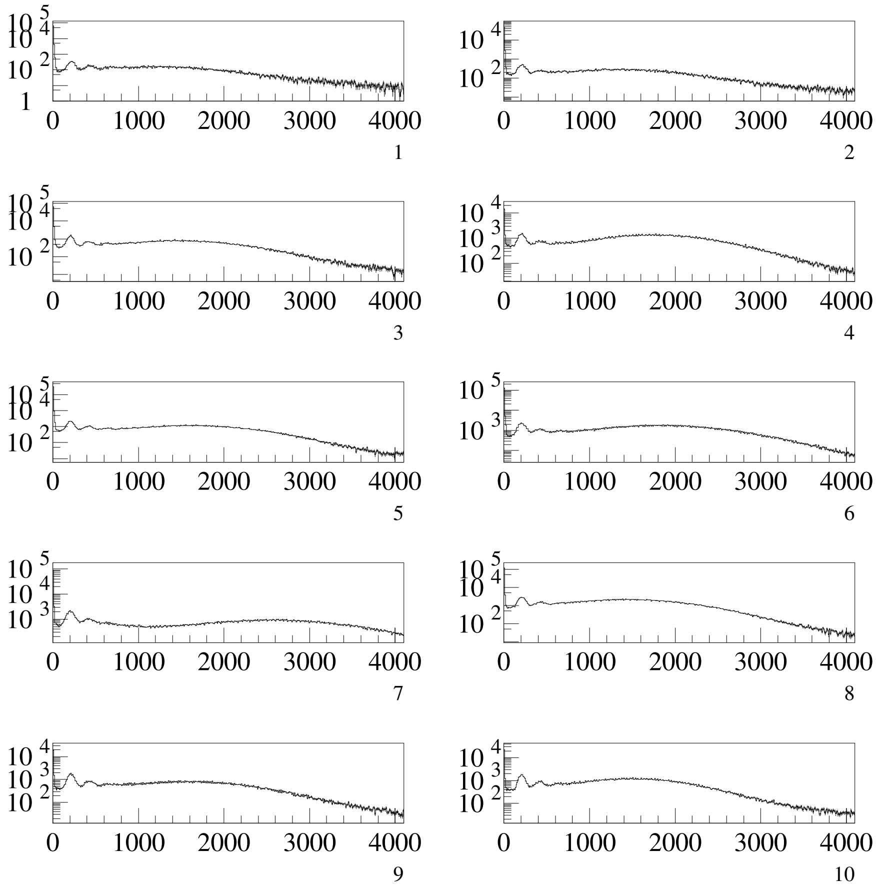

Figure 3.10: Calibrated Cherenkov ADC spectra.

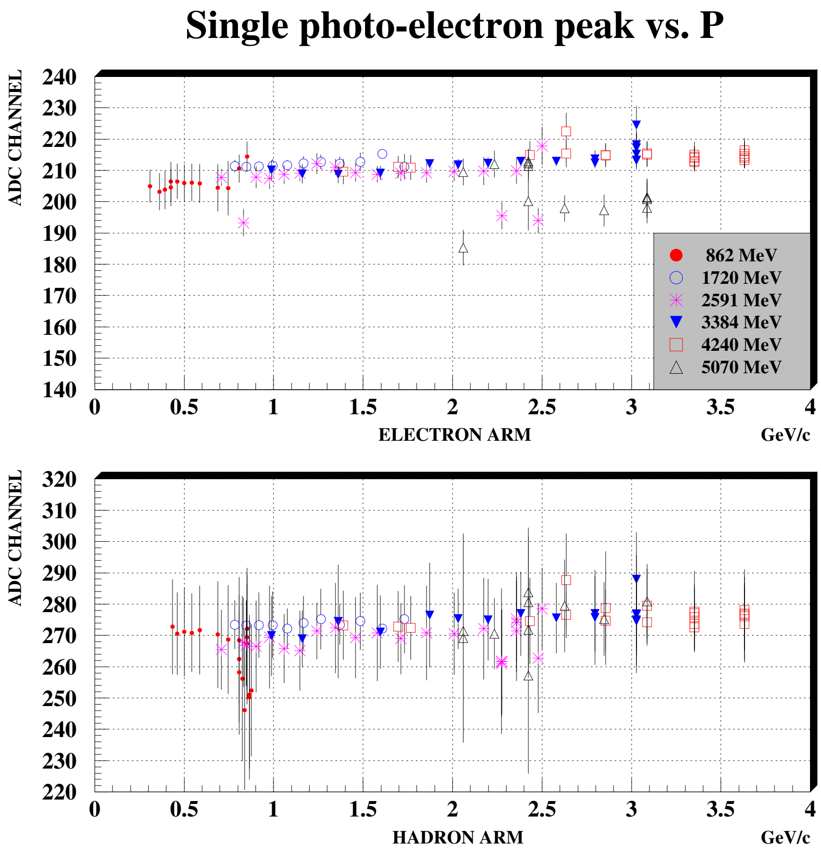

Figure 3.11: Stability of the Electron and Hadron Arm Cherenkov detectors. The data points are averages of the 10 single photoelectron peaks. The low data points in the top plot are mostly from the 2.591 GeV and 5.070 GeV runs near the end of the experiment when the threshold on the trigger scintillators had to be lowered.

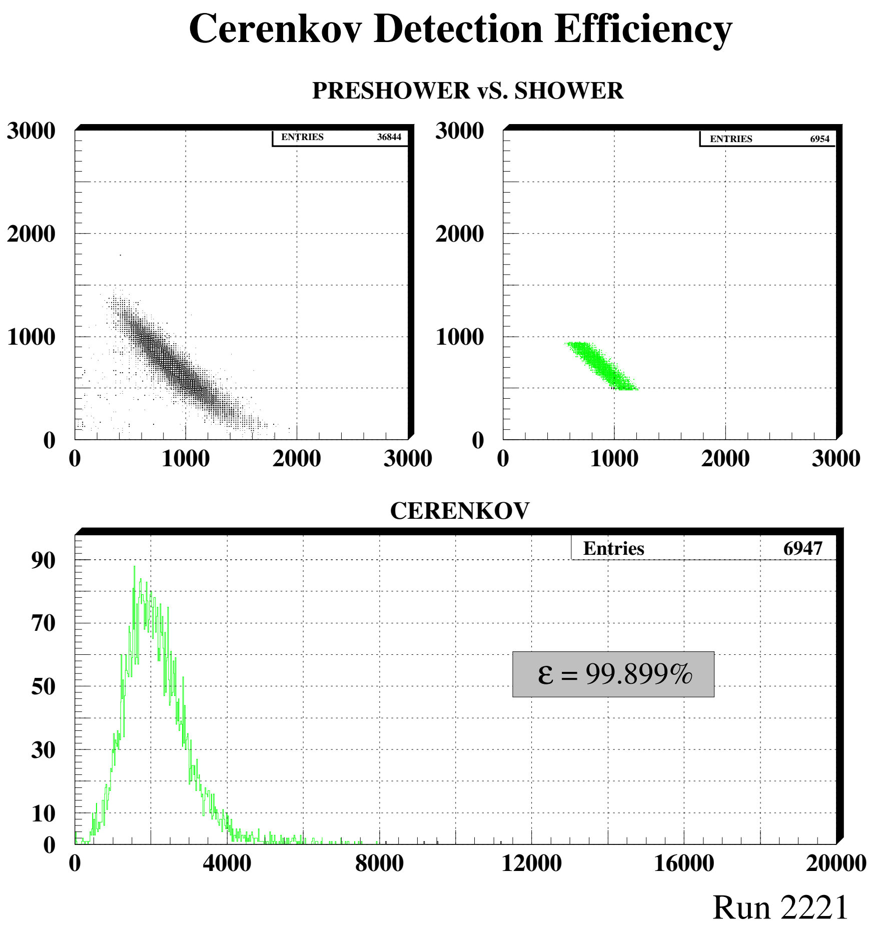

Figure 3.12: Detection efficiency of the Cherenkov detector for the Electron Arm. The plot in the upper left shows preshower *vs.* shower output without any cuts. A tight two-dimensional cut is applied to the preshower *vs.* shower histogram resulting in the plot in the upper right. The bottom plot shows the output of the Cherenkov counter with the previous cut. The efficiency is the number of electrons that fire the Cherenkov counter to the number of events that pass the preshower *vs.* shower cut.

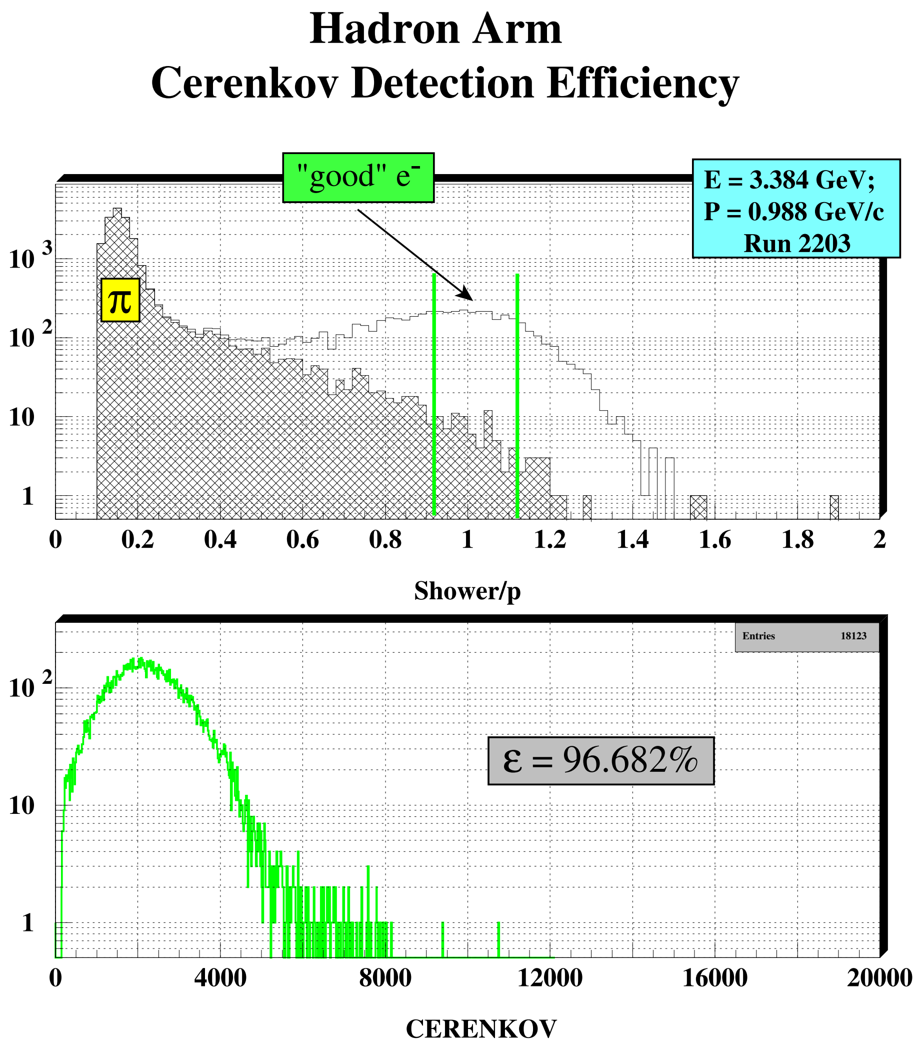

Figure 3.13: Detection efficiency of the Cherenkov detector for the Hadron Arm. The upper plot shows the cuts used to select good electron events. The lower graph shows the output of the Cherenkov with the previous cut. The efficiency is the number of events that fire the Cherenkov to the number of events that pass the shower cut. The events in the hashed area are pions obtained with an anti-Cherenkov cut and serve only to illustrate the amount of pion contaminants.

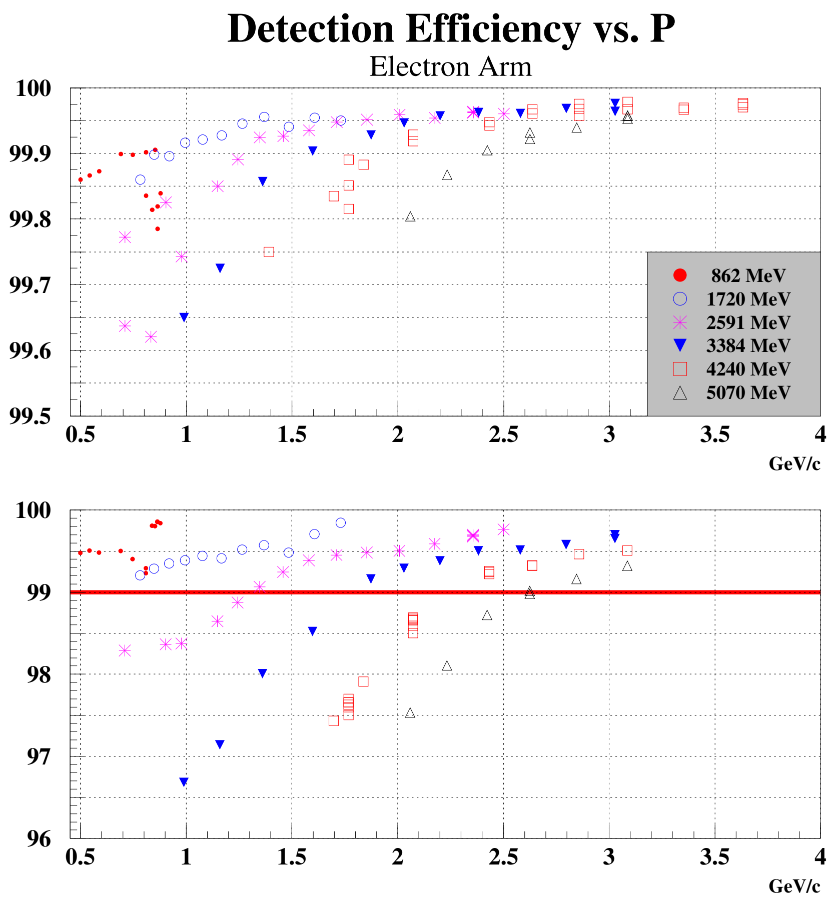

Figure 3.14: Cherenkov detection efficiency *vs.* momentum p. The top plot is for the Electron Arm and the bottom plot is for the Hadron Arm. The efficiency is decreased at lower momenta because of pion contamination [96].

3.3 Charge Determination

The beam charge is determined from a particular V/F (voltage-to-frequency) scaler as the product of the current and the duration of the run:

$$Q = I \times T = R_{\mathrm{V/F}} \times \frac{T}{\alpha_I}, \tag{3.8}$$

where $R_{\mathrm{V/F}}$ is the V/F rate and α_I is a calibration constant. The charge is accurate to better than 1%.

3.4 Acceptance

In order to understand the acceptance of the spectrometer, a simulation of the ^{12}C data was done and subsequently compared with data runs. The results are shown in Fig. 3.15.

3.5 Monte Carlo Techniques

The Monte Carlo method is a powerful tool to simulate electron scattering on a computer. Such a program was developed by A. Deur [103,104] and subsequently used to understand the acceptance of the Jefferson Lab Hall A High Resolution Spectrometers during E94-010 [105]. Often, in a Monte Carlo simulation, it is desired to generate some distribution with a certain probability density function. Of particular interest is the Gaussian or normal distribution. A popular algorithm for generating two independent, normally distributed random numbers z_1 and z_2 with mean 0 and variance 1 is to generate two uniformly distributed random variables u_1 and u_2 in the interval (0,1), then calculate $z_1 = \cos 2\pi u_1 \sqrt{-2\ln u_2}$ and $z_2 = \sin 2\pi u_1 \sqrt{-2\ln u_2}$ [87,106–108]. Repeated evaluations of the trigonometric functions is somewhat inefficient, so faster algorithms have been developed and implemented. See for instance the Fortran routine **RNORML** (V120) from CERNLIB [109].

3.6 Passage of Electrons Through Matter

The dominant physical processes for energy loss by electrons traversing a layer of material at the incident energies of E94-010 are:

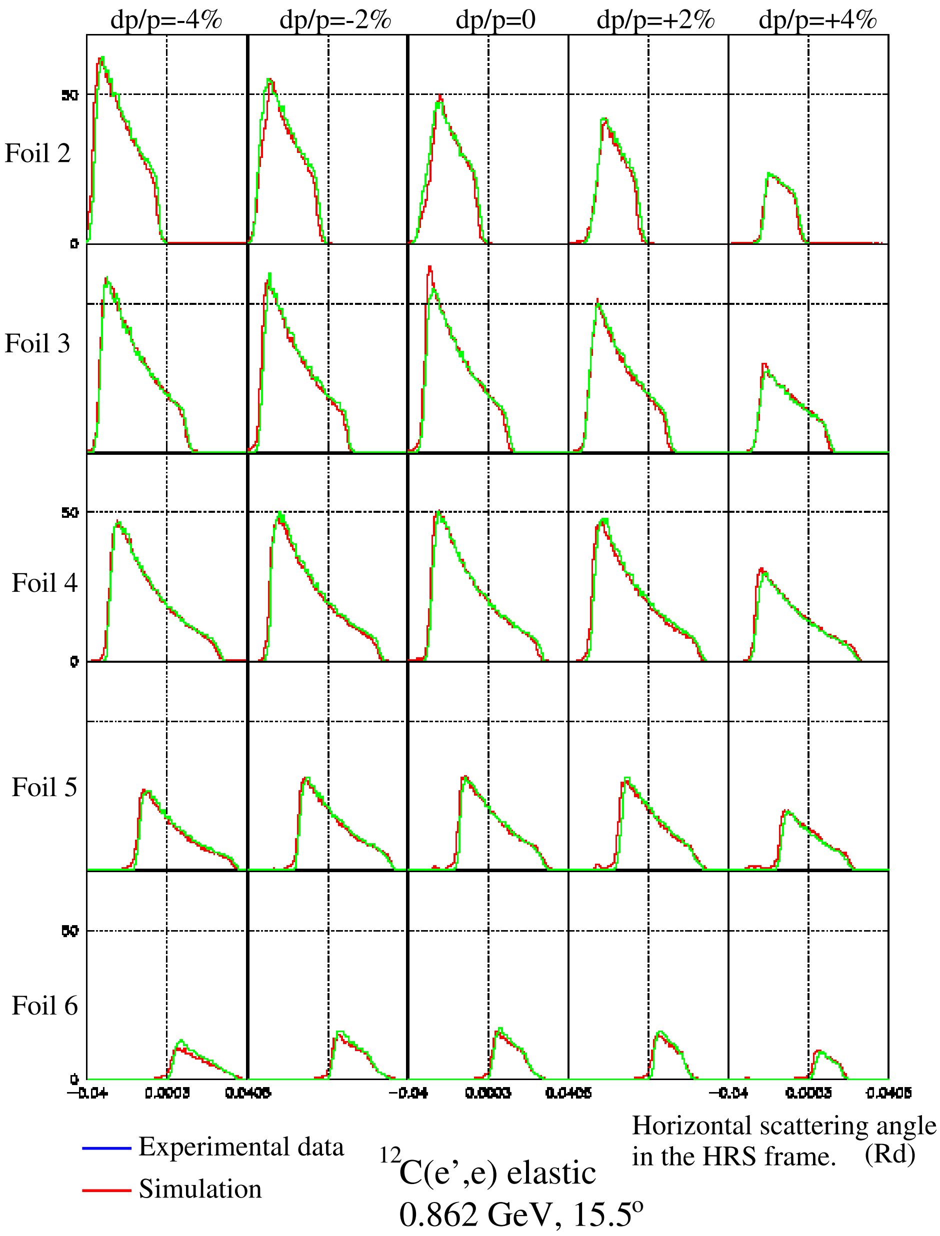

Figure 3.15: Fractional momentum $\delta = dp/p$ spectra of carbon data for experimental data (in green) and simulation (in red) as measured in the Electron Arm.

- Ionization
- External bremsstrahlung
- Internal bremsstrahlung

3.6.1 Ionization

Energy loss by ionization is a consequence of inelastic collisions with the atomic electrons of the material. The expression for the average energy loss per unit path length also known as stopping power was first worked out using classical arguments by Bohr. Later Bethe, Bloch and others developed a formula based on quantum mechanics. The Bethe-Bloch formula [87, 98] is

$$-\frac{dE}{dx} = 2\pi N_A r_e^2 m_e c^2 \rho \frac{Z}{A}\frac{z^2}{\beta^2}\left[\ln\left(\frac{2m_e c^2\beta^2\gamma^2 T_{\max}}{I^2}\right) - 2\beta^2\right] \tag{3.9}$$

where

$$2\pi N_A r_e^2 m_e c^2 = 0.1535 \text{ MeV/g cm}^{-2} \tag{3.10}$$

and

N_A is Avogadro's number $6.02214199(47) \times 10^{23}$ mol^{-1}.

r_e is the classical electron radius $2.817940285(31) \times 10^{-13}$ cm.

m_e is the mass of the electron 0.510998902(21) MeV/c^2.

ρ is the density of the material.

Z is the atomic number of the material.

A is the atomic weight of the material.

z is the charge of the incident particle in e.

$\beta = v/c$ is the speed of the incident particle.

$\gamma = 1/\sqrt{1-\beta^2}$

$T_{\max}$ is the maximum kinetic energy per collision.

$I = I_0 Z$ is the mean excitation potential and $I_0 \approx 13.5$ eV.

The energy loss by ionization of particles crossing a thin absorber, where the energy lost by the particle is small compared to its incident energy, is a statistical process and spread out according to a distribution which was first calculated by Landau. This Landau straggling follows a distribution [98, 110, 111]:

$$f(x, \Delta) = \frac{1}{\xi}\phi(\lambda) \tag{3.11}$$

where

$$\begin{aligned} \xi &= 2\pi N_A r_e^2 m_e c^2 \rho \frac{Z}{A}\frac{z^2}{\beta^2} x && (3.12) \\ \phi(\lambda) &= \frac{1}{2\pi i}\int_{\epsilon - i\infty}^{\epsilon + i\infty} e^{z\ln z + \lambda z} dz && (3.13) \\ \lambda &= \frac{1}{\xi}\left[\Delta - \xi\left(\ln\frac{\xi}{\epsilon} + 1 - \gamma_E\right)\right] && (3.14) \\ \ln\epsilon &= \ln\left(\frac{I^2}{2m_e c^2\beta^2\gamma^2}\right) + \beta^2 && (3.15) \end{aligned}$$

and

x is the thickness of the absorber.

Δ is the energy loss.

ξ is approximately the mean energy loss.

λ is a dimensionless variable.

$\phi(\lambda)$ is the probability density function.

γ_E is the Euler-Mascheroni constant 0.577216.

Often in Monte Carlo simulations of the energy loss it is desired to generate random numbers according to the Landau distribution. It is useful to introduce a distribution function $\Phi(\lambda)$ of the density $\phi(\lambda)$, and its inverse $\Psi(x)$:

$$\begin{aligned} \Phi(\lambda) &= \int_{-\infty}^{\lambda} \phi(\lambda')d\lambda' && (3.16) \\ \Psi(x) &= \Phi^{-1}(x) && (3.17) \end{aligned}$$

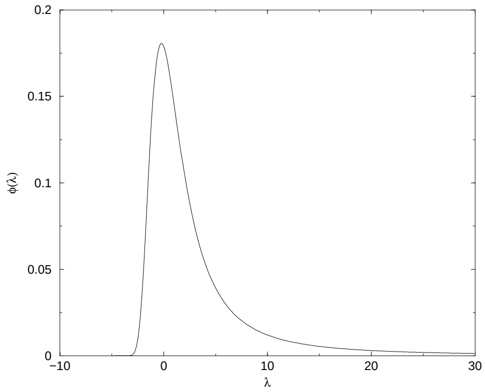

Figure 3.16: Landau density

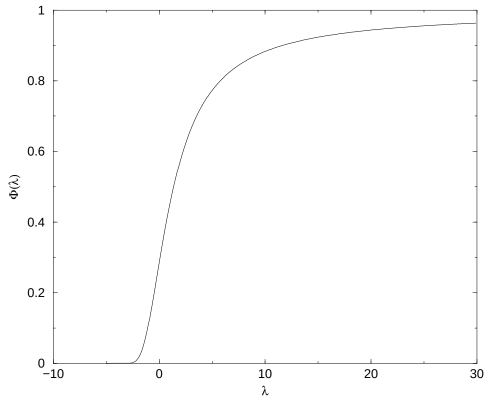

Figure 3.17: Landau distribution

If x is a random variable distributed uniformly between 0 and 1, then $\Psi(x)$ is the corresponding is distributed according to the Landau density $\Phi(\lambda)$. The energy loss can then be deduced from λ using Eq. (3.14). Figs. 3.16 and 3.17 show the Landau density and distribution, respectively. The Landau density peaks at $\lambda = -0.222782$ with $\phi(\lambda) = 0.180655$. The corresponding most probable energy loss is:

$$\Delta_{\mathrm{mp}} = \xi \left[\ln \frac{\xi}{\epsilon} + 0.200002 \right] \tag{3.18}$$

For the purpose of evaluating $\phi(\lambda)$ a couple of integral representations of the Landau distribution function have been derived [112]:

$$\begin{aligned} \phi(\lambda) &= \frac{1}{\pi} e^{-\sigma} \int_0^\infty \exp\left[\frac{\sigma}{2} \ln\left(1 + \frac{u^2}{\sigma^2}\right) - u \arctan \frac{u}{\sigma} \right] \\ &\quad \cos\left[\frac{u}{2} \ln\left(1 + \frac{u^2}{\sigma^2}\right) - u + \sigma \arctan \frac{u}{\sigma} \right] du \\ \phi(\lambda) &= \frac{1}{\pi} \int_0^\infty e^{-\lambda u} u^{-u} \sin \pi u du \end{aligned}$$

where $\sigma = e^{-\lambda-1}$ and the first formula is used for negative λ while the second formula is used for positive λ. The CERNLIB program library contains the **LANDAU** (G110) package which includes the Fortran routines **DENLAN**, **DISLAN**, and **RANLAN** for evaluating $\phi(\lambda)$, $\Phi(\lambda)$, and $\Psi(x)$ respectively [109].

3.6.2 External Bremsstrahlung

The emission of radiation by scattering from nuclei other than the target nucleon is termed external bremsstrahlung [113]. Let $I_e(E, \Delta, t)\ d\Delta$ represent the probability of an electron with incident energy E traversing a material with thickness t in units of radiation length to lose energy between Δ and $\Delta + d\Delta$. The density function $I_e(E,\Delta,t)$ is [114, 115]:

$$I_e(E,\Delta,t) = \frac{1}{\Gamma(bt)}\frac{1}{\Delta}\left(\frac{\Delta}{E}\right)^{bt}\phi\left(\frac{\Delta}{E}\right) \tag{3.19}$$

where

$$b = \frac{4}{3}\left\{1+\frac{1}{9}[(Z+1)/(Z+\xi)][\ln(183Z^{-1/3})]^{-1}\right\} \tag{3.20}$$

$$\xi = \ln(1440Z^{-2/3})/\ln(183Z^{-1/3}) \tag{3.21}$$

$$\phi(v) = 1 - v + \frac{3}{4}\,v^2 \tag{3.22}$$

and $\phi(v)$ is due to the screening of nuclear potentials by atomic electrons. For the purpose of Monte Carlo simulations the integral of $I_e(E,\Delta,t)$ is:

$$\int_0^{\Delta} I_e(E,\Delta',t)\;d\Delta' = \frac{1}{\Gamma(1+bt)}\left(\frac{\Delta}{E}\right)^{bt} + O\left(\frac{\Delta}{E}\right)^{1+bt} \tag{3.23}$$

Following the transformation method [106, 107], if R is a random number in [0,1] let $R = (\Delta/E)^{bt}$. Therefore the formula:

$$\Delta = ER^{\frac{1}{bt}} \tag{3.24}$$

will generate energy losses Δ according to the external bremsstrahlung distribution $I_e(E,\Delta,t)$ provided:

$$\frac{1}{\Gamma(1+bt)} \sim 1 \quad \text{and} \quad \left(\frac{\Delta}{E}\right)^{1+bt} \ll \left(\frac{\Delta}{E}\right)^{bt}. \tag{3.25}$$

3.6.3 Internal Bremsstrahlung

Internal bremsstrahlung refers to the real photons emitted during scattering with the target nucleon. The scattering process has an angular distribution of $1/\gamma$ and therefore strongly peaked along the direction of the incident and outgoing electrons. The Feynman diagrams representing these processes are displayed in Fig. 3.18. This effect can be approximated by placing an effective or virtual before and after the target, each of thickness [114]:

$$bt = \frac{\alpha}{\pi}\left[\ln\left(\frac{Q^2}{m_e^2}\right) - 1\right] \tag{3.26}$$

where Q^2 is the momentum transfer squared.

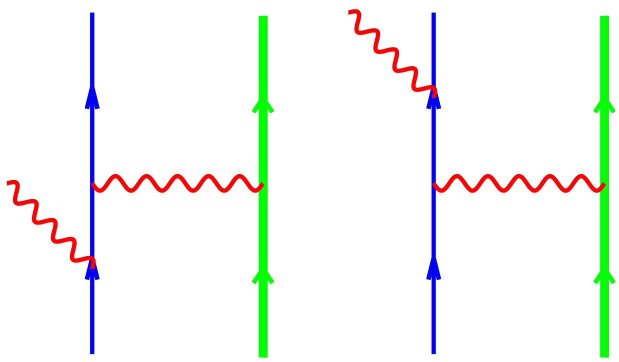

Figure 3.18: Lowest order Feynman diagrams for real bremsstrahlung.

3.6.4 Multiple Scattering Through Small Angles

Charged particles traveling through a certain material suffer deflections due to multiple Coulomb scatterings from nuclei. The distribution of scattering angles is described by the theory of Molière and is approximately Gaussian for small angles with a tail that follows a $1/\sin^4(\theta/2)$ dependence as a result of Rutherford single scatterings. The width of the central Gaussian is given by [87, 116]:

$$\theta_0 = \frac{13.6\text{ MeV}}{\beta^2 \gamma m_e c^2} \sqrt{t}\ [1 + 0.038 \ln t] \tag{3.27}$$

where t is the target thickness in radiation lengths.

3.7 Radiators

In order to be able to calculate radiation loss by electrons going through various materials, a list of materials and some of their atomic and nuclear properties is required. Such a list was originally compiled by F. Xiong [118] and reproduced in Fig. 3.19, and Table 3.1 and 3.2. Corning 1720 [119] is an aluminosilicate glass used for the construction of the reference cell. GE 180 [120] is another type of glass used for the construction of the target cell Armageddon. The composition of both glasses and some of their properties are listed in Table 3.4 and 3.5. The effective atomic number, atomic weight, and X_0 for compounds and mixtures were calculated using the

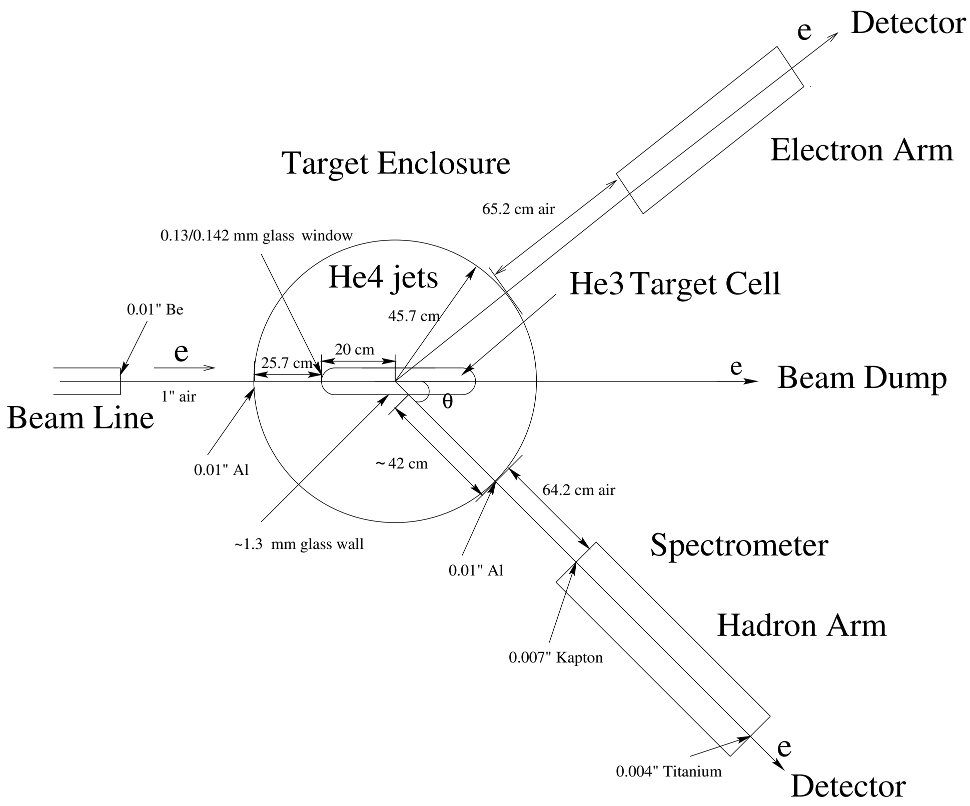

Figure 3.19: Radiators for E94-010.

Material	Length (cm)	Thickness (g/cm^2)	Thickness (radiation length)
Beryllium	0.0254	4.694×10^{-2}	7.200×10^{-4}
Air	2.54	3.060×10^{-3}	8.347×10^{-5}
Aluminum	0.0254	6.855×10^{-2}	2.855×10^{-3}
Helium	25.7	4.274×10^{-3}	4.532×10^{-5}
Corning 1720	0.013	3.302×10^{-2}	1.229×10^{-3}
or GE 180	0.013	3.588×10^{-2}	1.846×10^{-3}
Nitrogen	20	2.331×10^{-2}	6.135×10^{-4}

Table 3.1: Radiators before scattering for Electron and Hadron arms.

following formulas [98]:

$$Z_{\text{eff}} = \sum a_i Z_i, \tag{3.28}$$

$$A_{\text{eff}} = \sum a_i A_i, \tag{3.29}$$

$$\frac{1}{X_0} = \sum \frac{w_i}{X_i}, \tag{3.30}$$

where a_i is the number of atom of the ith element in the compound, $w_i = a_i A_i / A_{\text{eff}}$ is the fraction by weight of the ith element, Z_i is the atomic number of the ith element, and A_i is the atomic weight of the ith element. Values of Z, A, and X_0 for elements are taken from Table III.6 of Ref. [121]. Their densities are from Ref. [122]. Compositions and densities of air and kapton were obtained from Ref. [123] and reproduced in Table 3.6 and 3.7. X_0 for air and kapton are taken from Ref. [87].
The data and simulation are displayed in red and blue respectively in Figs. 3.20 and 3.21. The simulation is normalized by area to the data. δ_{tg} and y_{tg} of the simulation are slightly shifted to the left with respect to the data. θ_{tg} and ϕ_{tg} yield rather good agreement between simulation and data. The excitation energy E_X is defined by:

$$E_X = W - M, \tag{3.31}$$

$$W = \sqrt{M^2 - Q^2 + 2M\nu}, \tag{3.32}$$

$$Q^2 = 4EE' \sin^2 \frac{\theta}{2}, \tag{3.33}$$

$$\nu = E - E', \tag{3.34}$$

Material	Length (cm)	Thickness (g/cm^2)	Thickness (radiation length)
Corning 1720	0.4865	1.236	4.602×10^{-2}
or GE 180	0.4865	1.343	6.908×10^{-2}
Helium	42	6.985×10^{-3}	7.406×10^{-5}
Aluminum	0.0254	6.855×10^{-2}	2.855×10^{-3}
Air (Electron Arm)	65.2	7.855×10^{-2}	2.143×10^{-3}
Air (Hadron Arm)	64.2	7.735×10^{-2}	2.110×10^{-3}
Kapton	0.0178	2.528×10^{-2}	6.232×10^{-4}
Titanium	0.0102	4.631×10^{-2}	2.864×10^{-3}

Table 3.2: Radiators after scattering for Electron and Hadron arms

Material	Z	A	Density (g/cm^3)	X_0 (g/cm^2)
Helium	2	4.002602	1.6632×10^{-4}	94.32
Beryllium	4	9.012182	1.848	65.19
Nitrogen	7	14.00674	1.1653×10^{-3}	37.99
Aluminum	13	26.981538	2.6989	24.01
Titanium	22	47.867	4.54	16.17
Kapton	6.35993	12.70147	1.42	40.56
Air	7.372747	14.801088	1.20479×10^{-3}	36.66
Corning 1720	33.0586	66.7270	2.54	26.86
GE 180	33.5138	82.9943	2.76	19.44

Table 3.3: Atomic and Nuclear Properties of Materials.

Material	Weight Percentage	Z	A	X_0 (g/cm^2)
SiO_2	60.7	30	60.0843	27.05
Al_2O_3	17.3	50	101.961276	17.29
B_2O_3	5.0	34	69.6202	38.42
Na_2O	1.0	30	61.97894	29.17
K_2O	0.2	46	94.196	18.90
MgO	7.4	20	40.3044	28.03
CaO	8.6	28	56.0774	19.01
As_2O_3	0.5	90	197.8414	14.18

Table 3.4: Composition of Corning 1720.

Material	Weight Percentage	Z	A	X_0 (g/cm^2)
SiO_2	60.3	30	60.0843	27.05
CaO	6.5	28	56.0774	19.01
BaO	18.2	34	153.3264	9.02
SrO	0.25	46	103.6194	12.04
Al_2O_3	14.3	50	101.961276	17.29

Table 3.5: Composition of GE 180.

Material	Fraction by weight
Carbon	0.000124
Nitrogen	0.755267
Oxygen	0.231781
Argon	0.012827

Table 3.6: Composition of air.

Material	Fraction by weight
Hydrogen	0.026362
Carbon	0.691133
Nitrogen	0.073270
Oxygen	0.209235

Table 3.7: Composition of kapton.

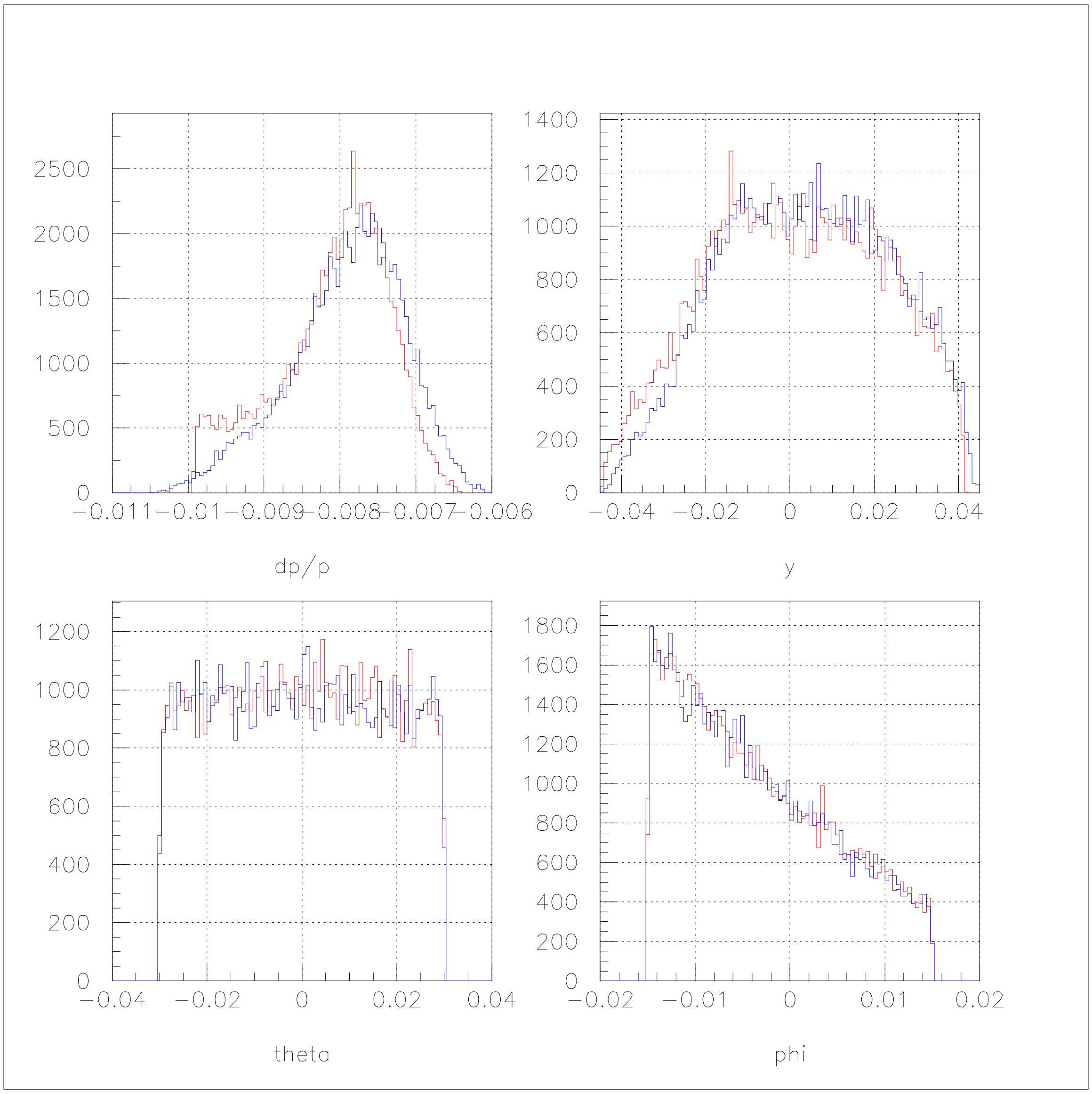

Figure 3.20: $\delta_{\rm tg}$, $y_{\rm tg}$, $\theta_{\rm tg}$, and $\phi_{\rm tg}$ for nitrogen elastic peak at $E_{\rm beam}$=1.7169 GeV.

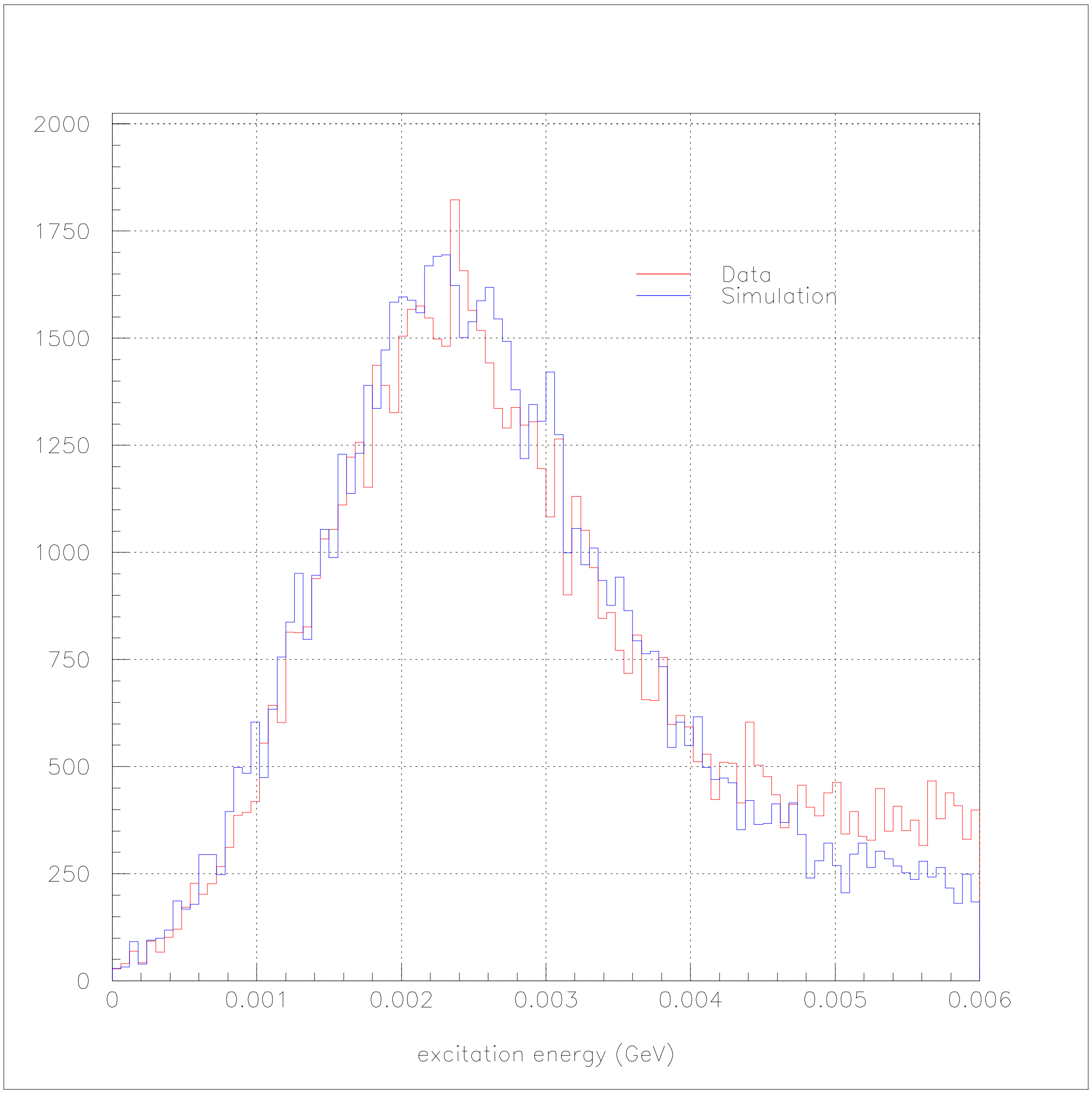

Figure 3.21: Excitation energy spectrum in GeV for nitrogen elastic peak at E_{beam}=1.7169 GeV.

where W is the missing mass, M is the target mass (in this case nitrogen), Q^2 is the four-momentum transfer squared, E is the beam energy, E' is the scattered energy, θ is the scattering angle, and ν is the energy loss. The simulated excitation energy spectrum agrees well with the data, with the provision that the beam energy dispersion be 3×10^{-4}.

3.8 Radiative Corrections

The measured cross section contains radiative effects. The method utilized to extract the Born cross section from the experimentally measured cross section consists of three main steps:

1. Subtract the elastic radiative tail.
2. Subtract the radiative tails of discrete levels such as the quasielastic and the Δ.
3. Unfold the Born cross section from the continuous spectrum by considering external and internal radiative effects.

The contribution of the elastic radiative tail to the cross section is much more significant than that of the discrete levels. The elastic radiative tail runs throughout the entire spectrum whereas the effects of the radiative tails of the discrete levels are only felt by neighboring levels.

3.8.1 Elastic Radiative Tail

Following the treatment of Stein *et al.* [125], the elastic radiative tail in the peaking approximation may be written as:

$$\sigma_{\mathrm{pk\ tail}} = (\sigma_{\mathrm{p}} + \sigma_{\mathrm{b}})F_{\mathrm{soft}}, \tag{3.35}$$

where σ_{p} is the elastic radiative tail in the angle-peaking approximation with internal radiation only and σ_{b} is the elastic radiative tail with straggling caused by target bremsstrahlung and ionization loss only (external radiation). These cross sections are calculated by:

$$
\begin{aligned}
\sigma_{\rm p} &\equiv \left(\frac{d^2\sigma}{d\Omega dE_p}\right)_{\rm p} \\
&= \frac{M_T + (E_s - \omega_s)(1-\cos\theta)}{M_T - E_p(1-\cos\theta)}\tilde{\sigma}_{\rm el}(E_s - \omega_s)\left[\frac{bt_r\phi(v_s)}{\omega_s}\right] \\
&\quad + \tilde{\sigma}_{\rm el}(E_s)\left[\frac{bt_r\phi(v_p)}{\omega_p}\right], && (3.36)\\
\sigma_{\rm b} &\equiv \left(\frac{d^2\sigma}{d\Omega dE_p}\right)_{\rm b} \\
&= \frac{M_T + (E_s - \omega_s)(1-\cos\theta)}{M_T - E_p(1-\cos\theta)}\tilde{\sigma}_{\rm el}(E_s - \omega_s)\left[\frac{bt_r\phi(v_s)}{\omega_s} + \frac{\xi}{2\omega_s^2}\right] \\
&\quad + \tilde{\sigma}_{\rm el}(E_s)\left[\frac{bt_r\phi(v_p)}{\omega_p} + \frac{\xi}{2\omega_p^2}\right], && (3.37)\\
\omega_s &= E_s - \frac{E_p}{1-(E_p/M_T)(1-\cos\theta)}, && (3.38)\\
\omega_p &= \frac{E_s}{1+(E_s/M_T)(1-\cos\theta)} - E_p, && (3.39)\\
v_s &= \omega_s/E_s, && (3.40)\\
v_p &= \omega_p/(E_p+\omega_p), && (3.41)\\
\xi &= \frac{\pi m}{2\alpha}\frac{t_a+t_b}{(Z+\eta)\ln(183Z^{-1/3}}, && (3.42)\\
b &= \frac{4}{3}1+\frac{1}{9}[(Z+1)/(Z+\eta)][\ln(183Z^{-1/3}]^{-1}, && (3.43)\\
\eta &= \ln(1440Z^{-2/3})/\ln(183Z^{-1/3}), && (3.44)\\
t_r &= \frac{1}{b}\frac{\alpha}{\pi}\left[\ln\left(\frac{Q^2}{m_e^2}\right) - 1\right], && (3.45)
\end{aligned}
$$

where $\tilde{\sigma}_{\rm el}(E) = \tilde{F}(Q^2)\sigma_{\rm el}(E)$ is the elastic cross section corrected by a factor $\tilde{F}(Q^2)$. The function $\phi(v) = 1 - v + \frac{3}{4}v^2$ characterizes the shape of the bremsstrahlung spectrum. The variables t_b and t_a designate the total path lengths in units of radiation lengths before and after scattering, respectively.

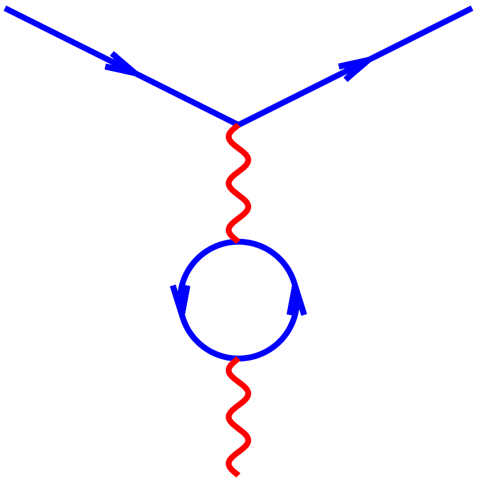

Figure 3.22: Vacuum polarization.

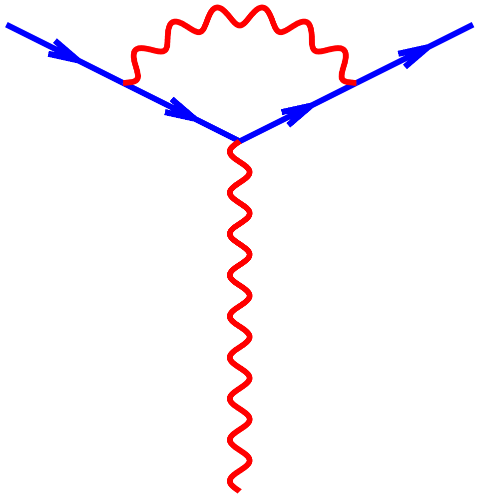

Figure 3.23: Vertex correction.

Factor $\tilde{F}(Q^2)$

The factor $\tilde{F}(Q^2)$ represents all other corrections independent of $\Delta E = E_p^{\text{peak}} - E_p^{\text{min}}$. It is given by:

$$
\begin{aligned}
\tilde{F}(Q^2) \quad = \quad & 1 + \gamma_E bT \\
& + \frac{2\alpha}{\pi}\left[-\frac{14}{9} + \frac{13}{12}\ln\left(\frac{Q^2}{m_e^2}\right)\right] \\
& - \frac{\alpha}{2\pi}\ln^2\left(\frac{E_s}{E_p}\right) \\
& + \frac{\alpha}{\pi}\left[\frac{\pi^2}{6} - \Phi\left(\cos^2\frac{\theta}{2}\right)\right],
\end{aligned}
\tag{3.46}
$$

where $\gamma_E \approx 0.577216$ is the Euler-Mascheroni constant [126]. The first term is an approximation:

$$
1/\Gamma(1 + bT) \approx 1 + \gamma_E bT. \tag{3.47}
$$

The second term is the sum of the vacuum polarization (Fig. 3.22) and vertex correction (Fig. 3.23) diagrams:

$$
\delta_{\text{vacuum}} = \frac{2\alpha}{\pi}\left[-\frac{5}{9} + \frac{1}{3}\ln\left(\frac{Q^2}{m_e^2}\right)\right], \tag{3.48}
$$

$$
\delta_{\text{vertex}} = \frac{2\alpha}{\pi}\left[-1 + \frac{3}{4}\ln\left(\frac{Q^2}{m_e^2}\right)\right]. \tag{3.49}
$$

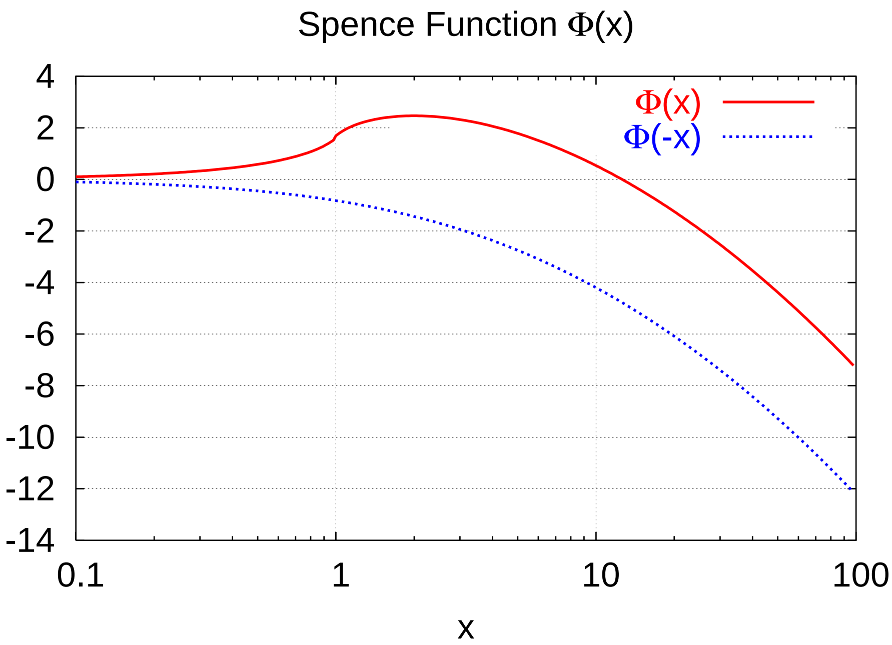

Figure 3.24: The Spence function $\Phi(x)$. Note the logarithmic scale on the x-axis.

The third term is an approximation to the sum of a couple of Spence functions:

$$\Phi\left(\frac{E_p - E_s}{E_p}\right) + \Phi\left(\frac{E_s - E_p}{E_s}\right) \approx -\frac{1}{2}\ln^2\left(\frac{E_s}{E_p}\right). \tag{3.50}$$

The last term is the Schwinger correction. The definition of the Spence function, shown in Fig. 3.24, is

$$\Phi(x) = \int_0^x \frac{-\ln|1-y|}{y}dy. \tag{3.51}$$

Below are properties of the Spence function used in computer codes for the purpose of its evaluation:

$$\Phi(1) = \frac{\pi^2}{6}, \tag{3.52}$$

$$\Phi(-1) = -\frac{\pi^2}{12}, \tag{3.53}$$

$$\Phi(x) = \sum_{n=1}^{\infty}\frac{x^n}{n^2} = x + \frac{x^2}{4} + \frac{x^3}{9} + \cdots \quad \text{if} \quad |x| \leq 1, \tag{3.54}$$

$$\Phi(x) = -\frac{1}{2}\ln^2|x| + \frac{\pi^2}{3} - \Phi\left(\frac{1}{x}\right) \quad \text{if} \quad x > 1, \tag{3.55}$$

$$\Phi(x) = -\frac{1}{2}\ln^2|x| - \frac{\pi^2}{6} - \Phi\left(\frac{1}{x}\right) \quad \text{if} \quad x < -1. \tag{3.56}$$

Elastic Cross Section

The elastic cross section is defined as

$$\sigma_{\text{el}} \equiv \left(\frac{d\sigma}{d\Omega}\right)_{\text{el}} = \sigma_{\text{Mott}}\frac{E'}{E}|F(Q^2,\theta)|^2, \tag{3.57}$$

where the Mott cross section in the ultrarelativistic limit and the recoil factor are

$$\sigma_{\text{Mott}} \equiv \left(\frac{d\sigma}{d\Omega}\right)_{\text{Mott}} = \frac{Z^2\alpha^2}{4E^2}\frac{\cos^2(\theta/2)}{\sin^4(\theta/2)}, \tag{3.58}$$

$$\frac{E'}{E} = \left[1+\frac{2E}{M_T}\sin^2\frac{\theta}{2}\right]^{-1}, \tag{3.59}$$

respectively. The form factor $F(Q^2,\theta)$ depends on the target.

3.8.2 Elastic Form Factor of ^{14}N

The elastic form factors of ^{14}N used in the simulation are those of Ref. [124], where data was taken at incident beam energy 250 MeV and scattering angles from 40 to 90°, and incident beam energy 400 MeV and scattering angles from 32 to 85°. The data was then analyzed with a harmonic-well shell model in the Born approximation. The Q^2 and θ dependence of the elastic form factor can be explicitly separated by introducing two separate form factors:

$$F^2(Q^2,\theta) = F_L^2(Q^2) + \left[\frac{1}{2}+\tan^2\frac{\theta}{2}\right]F_T^2(Q^2), \tag{3.60}$$

where $F_L^2(Q^2)$ is the longitudinal or Coulomb form factor and $F_T^2(Q^2)$ is the transverse form factor. Multipole expansions of the form factors gives:

$$F_L^2(Q^2) = \sum_{\lambda=0}^{\infty} F_{C\lambda}^2(Q^2), \tag{3.61}$$

$$F_T^2(Q^2) = \sum_{\lambda=1}^{\infty}[F_{E\lambda}^2(Q^2) + F_{M\lambda}^2(Q^2)]. \tag{3.62}$$

In the case of elastic scattering, only the C0, C2, and M1 terms contribute:

$$F^2_{C0}(Q^2) = \left|\left(1 - \frac{2\alpha}{2+3\alpha}\right) e^{-(x+d)}\right|^2, \tag{3.63}$$

$$F^2_{C2}(Q^2) = \frac{Q^4}{180}\frac{(J+1)(2J+3)}{J(2J-1)}\left(\frac{Q}{Z}\right)^2 e^{-2(x+d)}, \tag{3.64}$$

$$F^2_{M1}(Q^2) = \frac{2}{3}\frac{J+1}{J}\frac{x}{a^2 m_p^2}\left(\frac{\mu}{Z}\right)^2\left[1 - \frac{2}{3}x + \alpha\frac{2}{3}x\right]^2 e^{-2(x+d)}, \tag{3.65}$$

$$x = \frac{1}{4}Q^2 a^2, \tag{3.66}$$

$$d = \frac{1}{4}Q^2\left(a_p^2 - \frac{a^2}{A}\right), \tag{3.67}$$

$$a_p = \frac{2}{3}\sqrt{\langle r_p^2\rangle}, \tag{3.68}$$

where the parameters for ^{14}N are summarized in Table 3.8. The experimental

Parameter	Value
a	1.75 ± 1.2 fm
$\lvert\mu\rvert$	$30 \pm 65\ \mu_N$
α	0.44 ± 0.35
Q	1.52 ± 4.2 fm^2
a$_p$	0.63 fm
J	1
Z	7
A	14

Table 3.8: Parameters of elastic form factors for ^{14}N.

points along with the corresponding calculated values for the ^{14}N form factor are displayed in Tables 3.9 and 3.10 for incident energies 250 and 400 MeV, respectively. Figs. 3.25 and 3.26 are graphs of the data along with two theoretical fits. Both fits are harmonic-well models. The fit by Ref. [124] uses the electric monopole (C0), electric quadrupole (C2) and magnetic dipole (M1) terms. The fit by Ref. [125] only uses the electric monopole term.

θ (deg)	q (fm^{-1})	$10^4 \times F^2(q^2)$ (experimental)	$10^4 \times F^2(q^2)$ (calculated)
40	0.86	1643 ± 63	1840
50	1.07	637 ± 16	679
60	1.26	195 ± 6	209
70	1.45	42.3 ± 1.2	44.4
80	1.62	7.25 ± 0.54	7.84
90	1.78	3.50 ± 0.31	3.34

Table 3.9: Elastic form factors of ^{14}N at $E_{\mathrm{beam}} = 250$ MeV.

θ (deg)	q (fm^{-1})	$10^4 \times F^2(q^2)$ (experimental)	$10^4 \times F^2(q^2)$ (calculated)
32	1.12	500 ± 15	496
35	1.22	261 ± 7	262
38	1.32	120 ± 4	126
40	1.38	73.2 ± 2.3	76.6
43	1.48	28.8 ± 0.9	30.0
45	1.55	14.7 ± 0.5	14.4
48	1.64	6.18 ± 0.19	5.67
50	1.70	3.56 ± 0.10	3.72
53	1.80	3.03 ± 0.13	3.33
55	1.86	3.32 ± 0.11	3.67
65	2.16	3.43 ± 0.15	3.39
75	2.44	1.72 ± 0.11	1.34
80	2.58	0.799 ± 0.076	0.686
85	2.70	0.310 ± 0.060	0.354

Table 3.10: Elastic form factors of ^{14}N at $E_{\mathrm{beam}} = 400$ MeV.

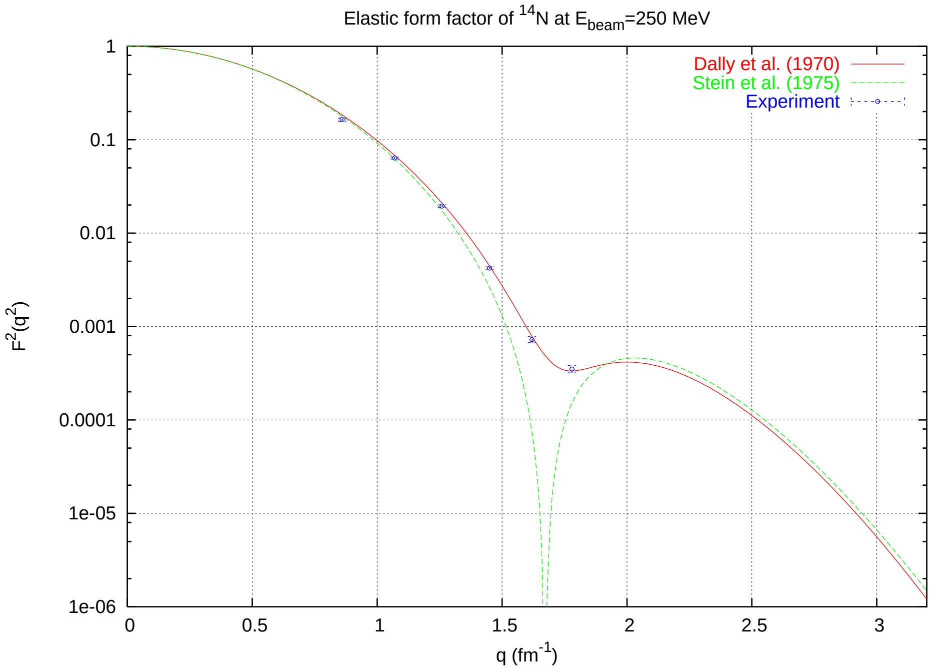

Figure 3.25: Elastic form factor of ^{14}N at $E_{\mathrm{beam}} = 250$ MeV. The fits by Dally *et al.* [124] and Stein *et al.* [125] are harmonic-well models.

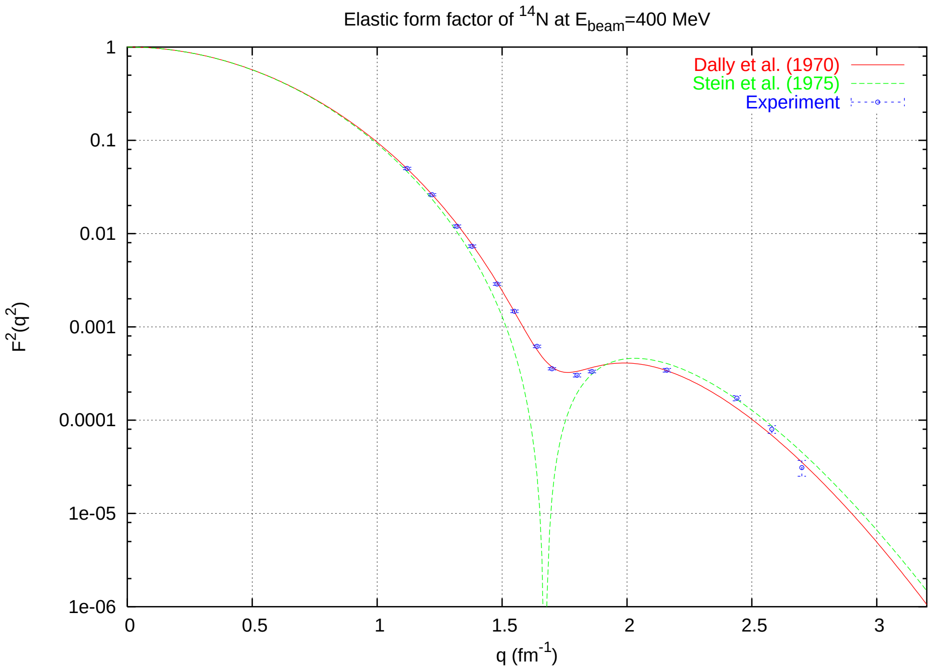

Figure 3.26: Elastic form factor of ^{14}N at $E_{\mathrm{beam}} = 400$ MeV. The fits by Dally *et al.* [124] and Stein *et al.* [125] are harmonic-well models.

Electric	Magnetic
a=0.675 ± 0.008 fm	a=0.654 ± 0.024 fm
b=0.366 ± 0.025 fm	b=0.456 ± 0.029 fm
c=0.836 ± 0.032 fm	c=0.821 ± 0.053 fm
d=(-6.78 ± 0.83) × 10^{-3}	
q_0=3.98 ± 0.09 fm^{-1}	
p=0.90 ± 0.16 fm^{-1}	

Table 3.11: Parameters for ^{3}He elastic form factors.

3.8.3 Elastic Form Factor of ^{3}He

In order to estimate the contribution of the ^{3}He elastic radiative tail in the raw cross section the ^{3}He elastic form factor must be known. The ^{3}He elastic form factor is taken from Refs. [128] and [129]. Here, the differential cross section is given by:

$$\begin{aligned}
\sigma_{\text{el}} &= \sigma_{\text{Mott}} \frac{E'}{E} \left[W_2(q^2) + 2W_1(q^2) \tan^2 \frac{\theta}{2} \right], && (3.69)\\
W_2(q^2) &= \frac{F_e^2(q^2) + \tau F_m^2(q^2)(1+K)^2}{1+\tau}, && (3.70)\\
W_1(q^2) &= \tau F_m^2(q^2)(1+K)^2, && (3.71)\\
\tau &= q^2/4M^2, && (3.72)\\
F(q^2) &= e^{-a^2q^2} - b^2q^2e^{-c^2q^2}, && (3.73)\\
\Delta F &= d \exp\left[-\left(\frac{q-q_0}{p} \right)^2 \right], && (3.74)
\end{aligned}$$

where $1 + K = -2.127624857$ is the anomalous magnetic moment of the ^{3}He nucleus [43]. Here, $F(q^2)$ is the form factor and $\Delta F(q^2)$ is a modification to the electric form factor needed to reproduce the diffraction minimum in the fit. The parameters used to fit the form factors are shown in Table 3.11. The experimental points with errors are graphed in Figs. 3.27 and 3.28, and tabulated in Tables 3.12 and 3.13.

3.8.4 Elastic Radiative Tail Contributions

Using the elastic form factors of ^{14}N and ^{3}He established in the previous sections, the amount of contamination in the raw data by the elastic radiative tails can be

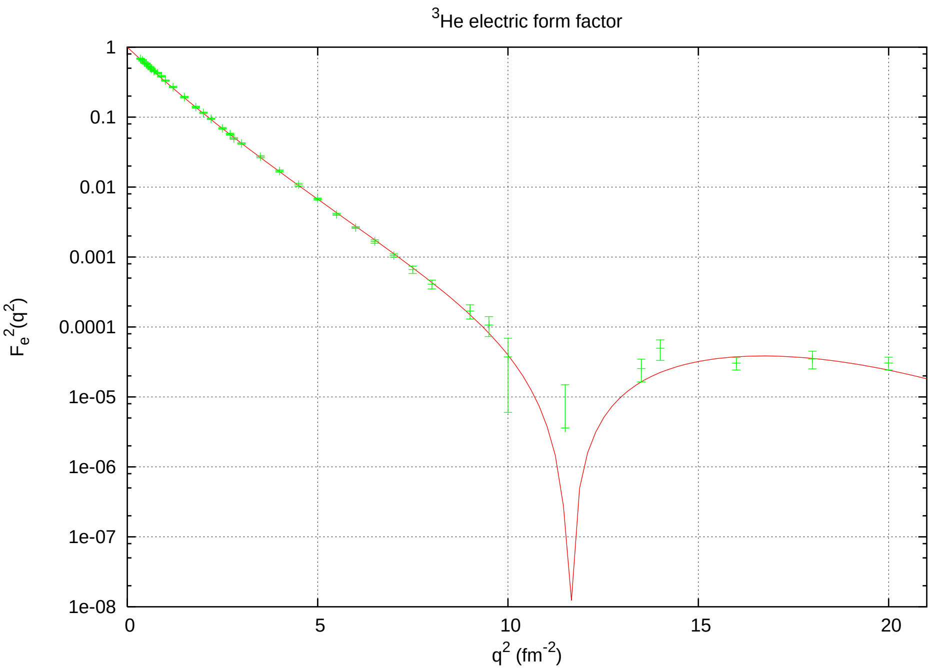

Figure 3.27: ^{3}He electric form factor.

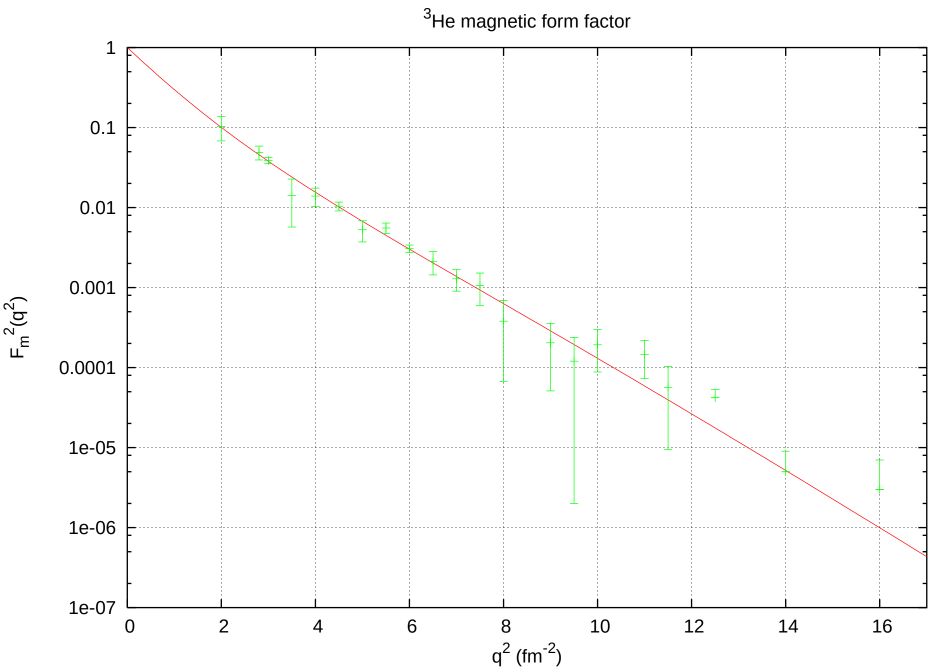

Figure 3.28: ^{3}He magnetic form factor.

q^2 (fm^{-2})	$F_e^2(q^2)$	q^2 (fm^{-2})	$F_e^2(q^2)$
0.347	$(6.82 \pm 0.17) \times 10^{-1}$	3.50	$(2.72 \pm 0.09) \times 10^{-2}$
0.400	$(6.51 \pm 0.16) \times 10^{-1}$	4.00	$(1.70 \pm 0.06) \times 10^{-2}$
0.451	$(6.02 \pm 0.15) \times 10^{-1}$	4.50	$(1.08 \pm 0.05) \times 10^{-2}$
0.500	$(5.82 \pm 0.15) \times 10^{-1}$	5.00	$(6.76 \pm 0.23) \times 10^{-3}$
0.542	$(5.48 \pm 0.14) \times 10^{-1}$	5.50	$(4.07 \pm 0.14) \times 10^{-3}$
0.600	$(5.16 \pm 0.13) \times 10^{-1}$	6.00	$(2.64 \pm 0.08) \times 10^{-3}$
0.639	$(4.87 \pm 0.12) \times 10^{-1}$	6.50	$(1.67 \pm 0.10) \times 10^{-3}$
0.700	$(4.55 \pm 0.11) \times 10^{-1}$	7.00	$(1.05 \pm 0.06) \times 10^{-3}$
0.800	$(4.26 \pm 0.11) \times 10^{-1}$	7.50	$(6.61 \pm 0.80) \times 10^{-4}$
0.900	$(3.85 \pm 0.10) \times 10^{-1}$	8.00	$(4.09 \pm 0.59) \times 10^{-4}$
1.000	$(3.32 \pm 0.08) \times 10^{-1}$	9.00	$(1.69 \pm 0.39) \times 10^{-4}$
1.100	$(2.97 \pm 0.08) \times 10^{-1}$	9.50	$(1.07 \pm 0.34) \times 10^{-4}$
1.200	$(2.69 \pm 0.07) \times 10^{-1}$	10.00	$(3.75 \pm 3.15) \times 10^{-5}$
1.500	$(1.93 \pm 0.05) \times 10^{-1}$	11.00	$(0.0 + 2.29, -0.00) \times 10^{-5}$
1.800	$(1.39 \pm 0.04) \times 10^{-1}$	11.50	$(3.6 + 15, -3.6) \times 10^{-6}$
2.000	$(1.15 \pm 0.03) \times 10^{-1}$	12.50	$(0.0 + 1.5, -0.0) \times 10^{-5}$
2.20	$(9.43 \pm 0.24) \times 10^{-2}$	13.50	$(2.55 \pm 0.91) \times 10^{-5}$
2.50	$(6.91 \pm 0.18) \times 10^{-2}$	14.00	$(4.95 \pm 1.62) \times 10^{-5}$
2.70	$(5.71 \pm 0.17) \times 10^{-2}$	16.00	$(3.05 \pm 0.62) \times 10^{-5}$
2.80	$(4.94 \pm 0.16) \times 10^{-2}$	18.00	$(3.51 \pm 0.99) \times 10^{-5}$
3.00	$(4.19 \pm 0.11) \times 10^{-2}$	20.00	$(3.06 \pm 0.64) \times 10^{-5}$

Table 3.12: ^{3}He electric form factors.

q^2 (fm^{-2})	$F_m^2(q^2)$	q^2 (fm^{-2})	$F_m^2(q^2)$
2.00	$(1.03 \pm 0.35) \times 10^{-1}$	7.50	$(1.06 \pm 0.46) \times 10^{-3}$
2.80	$(4.90 \pm 0.97) \times 10^{-2}$	8.00	$(3.80 \pm 3.13) \times 10^{-4}$
3.00	$(3.88 \pm 0.35) \times 10^{-2}$	9.00	$(2.04 \pm 1.53) \times 10^{-4}$
3.50	$(1.42 \pm 0.85) \times 10^{-2}$	9.50	$(1.20 \pm 1.18) \times 10^{-4}$
4.00	$(1.39 \pm 0.36) \times 10^{-2}$	10.00	$(1.93 \pm 1.05) \times 10^{-4}$
4.50	$(1.04 \pm 0.13) \times 10^{-2}$	11.00	$(1.46 \pm 0.73) \times 10^{-4}$
5.00	$(5.28 \pm 1.57) \times 10^{-3}$	11.50	$(5.66 \pm 4.71) \times 10^{-5}$
5.50	$(5.56 \pm 0.85) \times 10^{-3}$	12.50	$(4.2 + 5.3, -4.2) \times 10^{-5}$
6.00	$(3.07 \pm 0.33) \times 10^{-3}$	14.00	$(0.5 + 0.9, -0.5) \times 10^{-5}$
6.50	$(2.13 \pm 0.69) \times 10^{-3}$	16.00	$(0.3 + 0.7, -0.3) \times 10^{-5}$
7.00	$(1.29 \pm 0.39) \times 10^{-3}$		

Table 3.13: ^{3}He magnetic form factors.

estimated. Fig. 3.29 shows such an example for $E_{\rm beam}$=862 MeV and θ=15.5°. The ^{14}N cross section has been normalized by the factor 2[N]/[He] where the factor of 2 is a correction for nitrogen being a diatomic molecule, and [N] and [He] represent the partial pressures of nitrogen and helium, respectively. Notice that the rise of the tail in the raw data at high energy loss is not due to the elastic radiative tails of ^{14}N or ^{3}He. The rise of the tail was later proved to originate from multiple scattering of electrons in the target materials [130].

3.8.5 Radiative Tail of a Discrete Level

The radiative tails of excited states was investigated and found to be negligible. In addition, the contribution of rubidium to the radiative corrections is insignificant since only trace amounts of the element enter the target cells.

3.8.6 Continuum Radiative Corrections

External Bremsstrahlung

External bremsstrahlung is the result of energy loss by electrons due to bremsstrahlung in the field of atomic nuclei other than the nucleus causing the large angle scattering.

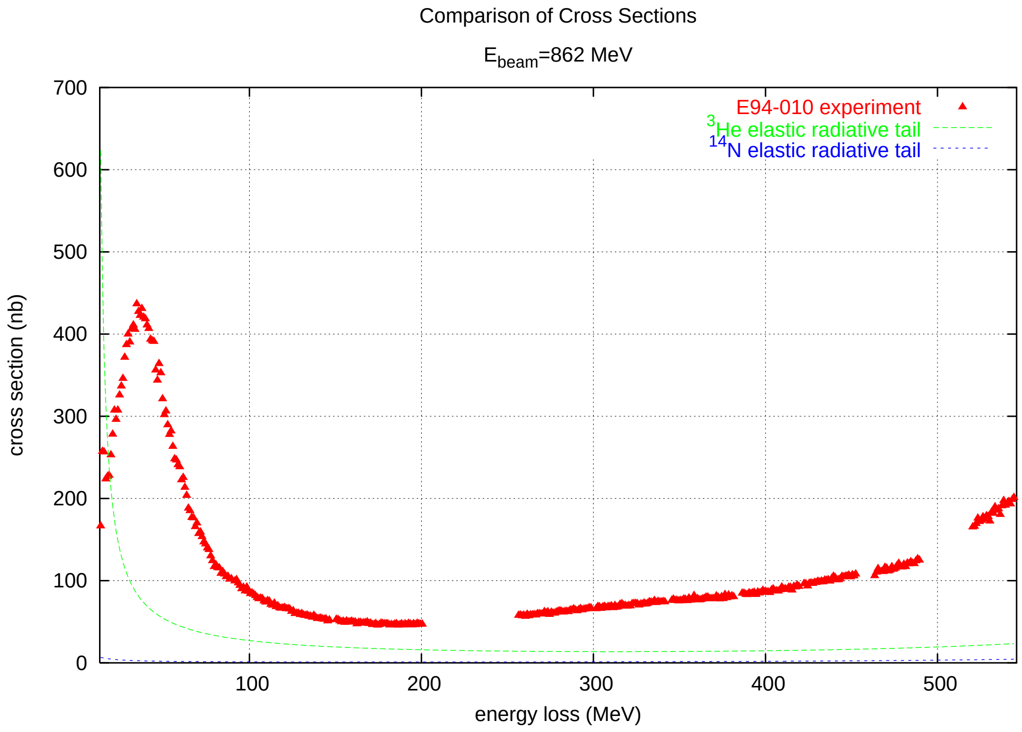

Figure 3.29: Raw cross section at E_{beam}=862 MeV.

This process is illustrated in the Feynman diagrams of Figs. 3.30 and 3.31 where the electron traverses a radiator before and after scattering, respectively. In order to remove external radiation to the continuum state, the following prescription of Mo and Tsai [115] was employed:

$$\begin{aligned}
\sigma_{\mathrm{rad}}(E_s, E_p, T) &= \int_0^T \frac{dt}{T} \int_{E_{s_{\min}}(E_p)}^{E_s} dE'_s \int_{E_p}^{E_{p_{\max}}(E'_s)} dE'_p \\
&\quad \times I_e(E_s, E'_s, t)\sigma(E'_s, E'_p, t) I_e(E'_p, E_p, T-t), \qquad (3.75)\\
I_e(E_0, E, t) &= \frac{bt}{E_0 - E}\left[\frac{E}{E_0} + \frac{3}{4}\left(\frac{E_0 - E}{E_0}\right)^2\right]\left[\ln\left(\frac{E_0}{E}\right)\right]^{bt}, \qquad (3.76)\\
E_{s_{\min}}(E_p) &= \frac{m_\pi^2 + 2Mm_\pi + 2ME_p}{2M - 2E_p(1-\cos\theta)}, \qquad (3.77)\\
E_{p_{\max}}(E'_s) &= \frac{2ME'_s - 2Mm_\pi - m_\pi^2}{2M + 2E'_s(1-\cos\theta)}, \qquad (3.78)
\end{aligned}$$

where $I_e(E_0, E, t)dE$ is the probability of finding an electron in the energy interval dE after an electron with initial energy E_0 and final energy E travels a distance t in units of radiation lengths. The unradiated cross section σ is the quantity sought.

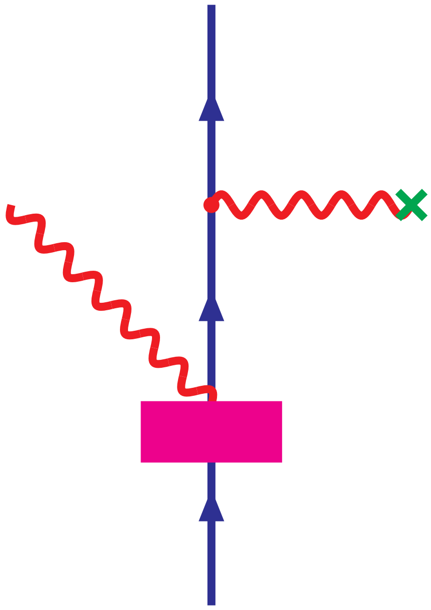

Figure 3.30: External bremsstrahlung before scattering.

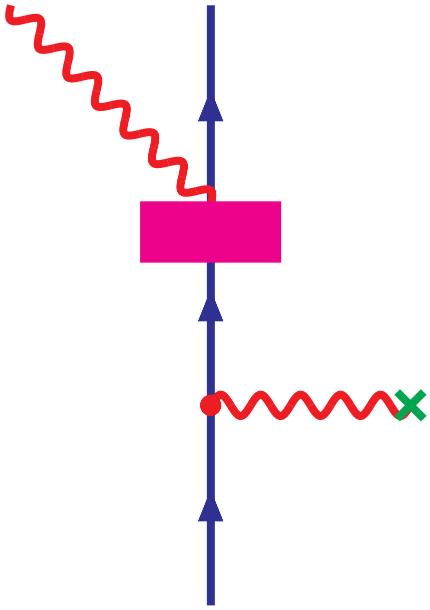

Figure 3.31: External bremsstrahlung after scattering.

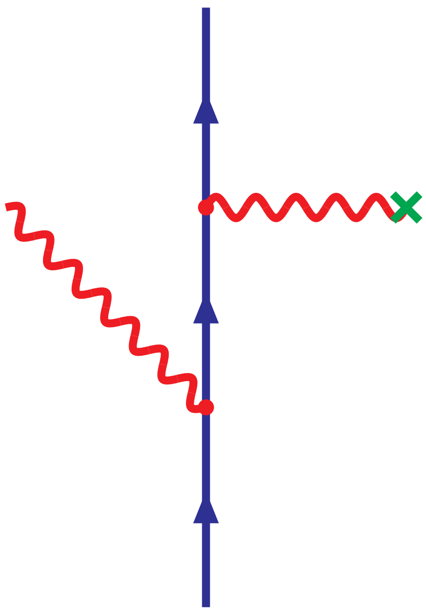

Figure 3.32: Internal bremsstrahlung before scattering.

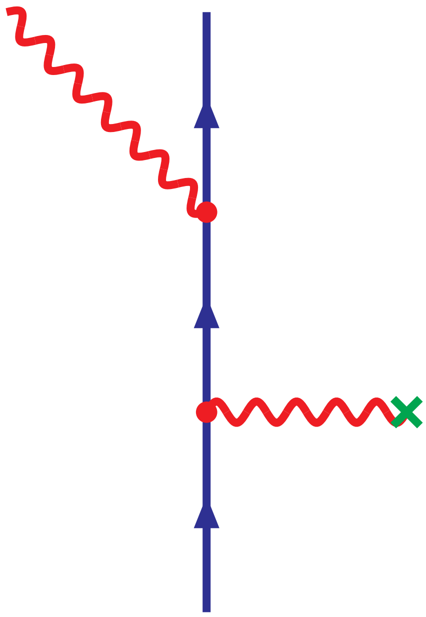

Figure 3.33: Internal bremsstrahlung after scattering.

The unfolding procedure consists of solving for σ by iteration. The technique goes as follows. The experimentally measured cross section σ_{exp} is used as a starting guess for σ and inserted into the multidimensional integral above. A radiated cross section σ_{rad} is obtained in this fashion. Next, the unradiated cross section σ is corrected by a factor $\sigma_{\text{exp}}/\sigma_{\text{rad}}$:

$$\sigma \leftarrow \frac{\sigma_{\text{exp}}}{\sigma_{\text{rad}}} \times \sigma. \tag{3.79}$$

The integration process is restarted and the entire unfolding procedure is repeated a number of times until a satisfactory convergence is achieved. Typically, five passes are sufficient [127].

Internal Bremsstrahlung

Internal bremsstrahlung constitutes the emission of a real photon before and after scattering as in Figs. 3.32 and 3.33, respectively. Internal radiative corrections were treated using a modified version of POLRAD [131] to account for the polarizations of the beam and target.

Chapter 4

RESULTS

4.1 Experimental Cross Sections and Asymmetries

4.1.1 Inclusive Spin-Averaged Cross Sections

The spin-averaged inclusive inelastic cross section can be expressed in terms of two invariant structure functions as follows [133–135]:

$$\frac{d^2\sigma}{d\Omega dE'} = \left(\frac{d\sigma}{d\Omega}\right)_{\mathrm{NS}} \left[W_2(\nu, Q^2) + 2W_1(\nu, Q^2)\tan^2\frac{\theta}{2}\right], \tag{4.1}$$

$$\left(\frac{d\sigma}{d\Omega}\right)_{\mathrm{NS}} = \left(\frac{d\sigma}{d\Omega}\right)_{\mathrm{Mott}} \frac{E'}{E}, \tag{4.2}$$

$$\left(\frac{d\sigma}{d\Omega}\right)_{\mathrm{Mott}} = \frac{\alpha^2}{4E^2}\frac{\cos^2(\theta/2)}{\sin^4(\theta/2)}. \tag{4.3}$$

The structure functions $W_1(\nu, Q^2)$ and $W_2(\nu, Q^2)$ embody the physics of interest. The inclusive unpolarized inelastic cross sections for the six incident beam energies of this experiment (862, 1717.9, 2580.5, 3381.8, 4238.6, and 5058.2 MeV) are shown in Fig. 4.1. Displayed are the unpolarized cross sections after averaging over both spectrometer arms and after removal of the elastic peak and its radiative tail. The solid lines show the raw inelastic cross section before radiative corrections whereas the dashed lines indicate cross sections after inelastic radiative corrections are applied. The spectra are characterized by several important features, namely, the quasielastic, resonance and deep inelastic regions. The quasielastic peak, centered at $\nu = Q^2/2M$, dominates the spectrum at the lower energies. The width of this peak is due to Fermi motion of the constituent nucleons. As the beam energy is increased, contribution

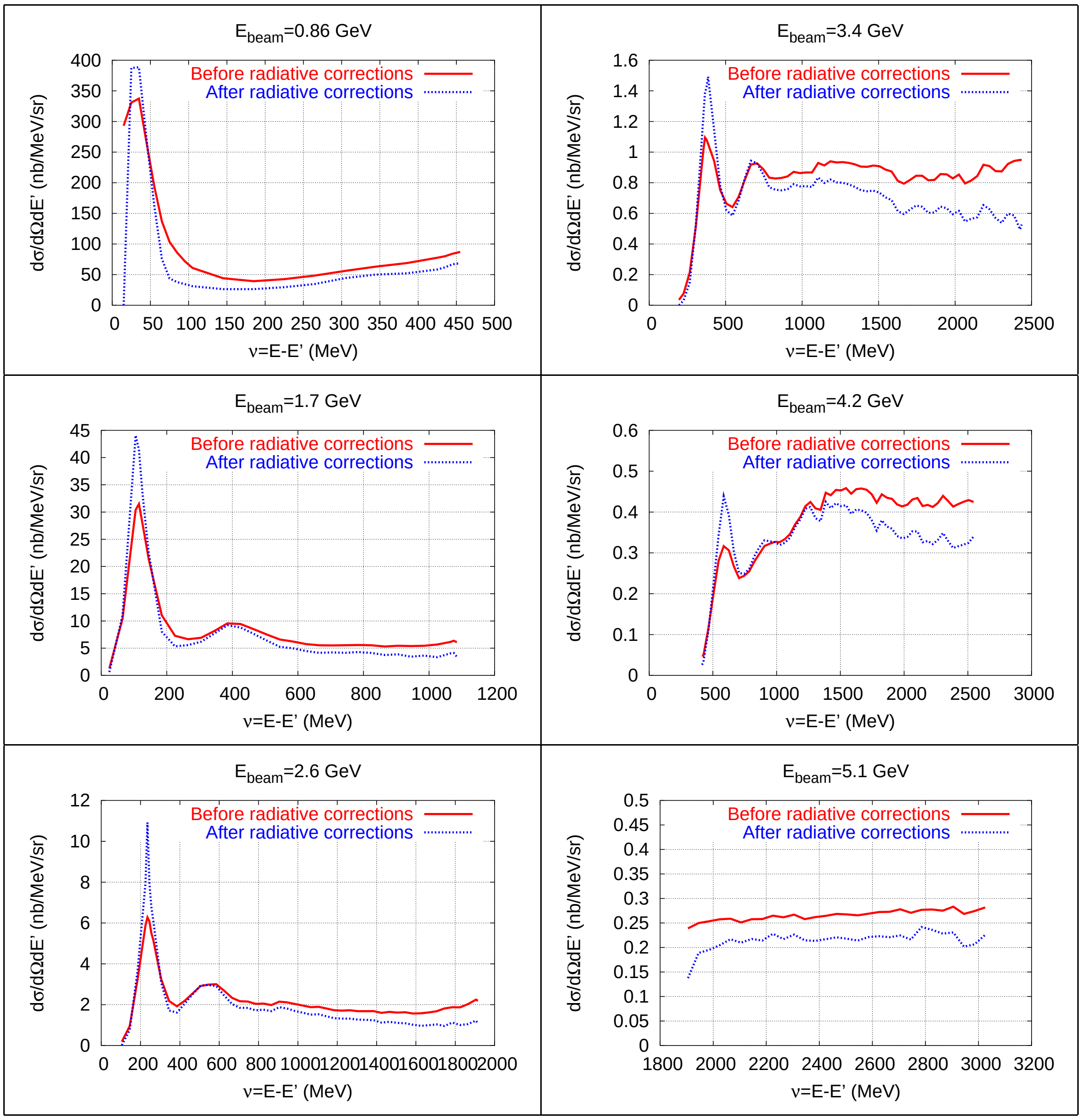

Figure 4.1: Inclusive spin-averaged inelastic cross sections before (solid red lines) and after (dashed blue lines) radiative corrections for the six beam energies of this experiment. Indicated on the plots are the quasielastic, the first and second resonance regions, and the deep inelastic scattering region. The elastic tail has already been removed from this figure.

from the first resonance region dominated by the $\Delta(1232)$ or P_{33} resonance becomes apparent at an energy loss $\nu \approx Q^2/2M + 300$ MeV. As beam energy increases further, additional resonances at increasing excitation energies become visible. At yet higher energies, the quasielastic peak and resonance peaks diminish due to the falloff with Q^2 of their respective form factors. For $W > 2$ GeV scattering from point-like partons occurs. In the deep inelastic scattering (DIS) region, as $\nu, Q^2 \to \infty$ but finite Q^2/ν, the form factors $W_1(\nu, Q^2)$ and $W_2(\nu, Q^2)$ follow simple scaling limits to first order in QCD:

$$MW_1(\nu, Q^2) \rightarrow F_1(x), \tag{4.4}$$
$$\nu W_2(\nu, Q^2) \rightarrow F_2(x). \tag{4.5}$$

$F_1(x)$ and $F_2(x)$ are now functions of a single dimensionless variable $x = Q^2/2M\nu$ known as the Bjorken scaling variable. Moreover, in the quark parton model, the scaling structure functions $F_1(x)$ and $F_2(x)$ obey the Callan-Gross relation [136]:

$$2xF_1(x) = F_2(x). \tag{4.6}$$

Nowadays, these partons are identified as due to point-like quark constituents. Note that even below this point, the overlapping resonances appear to scale as predicted by the Bloom-Gilman duality arguments. At the highest beam energies of 4.2 and 5.1 GeV, the contribution from the scaling region dominates the spectra.

4.1.2 Scattering Asymmetries

Traditionally, the asymmetries have been the easier physical quantities to extract, chiefly, because various normalization factors cancel each other out. The asymmetries were defined in the theory chapter as:

$$A_{\parallel} = \frac{\sigma^{\downarrow\Uparrow} - \sigma^{\uparrow\Uparrow}}{\sigma^{\downarrow\Uparrow} + \sigma^{\uparrow\Uparrow}}, \tag{4.7}$$
$$A_{\perp} = \frac{\sigma^{\downarrow\Rightarrow} - \sigma^{\uparrow\Rightarrow}}{\sigma^{\downarrow\Rightarrow} + \sigma^{\uparrow\Rightarrow}}, \tag{4.8}$$

where the first arrow superscript on the polarized cross sections refers to the beam polarization and the second arrow superscript refers to the target polarization. For the parallel asymmetry $A_{\parallel}$, the target polarization is kept fixed along the beam direction and the beam polarization, longitudinal to the beamline, is pseudo-randomly flipped.

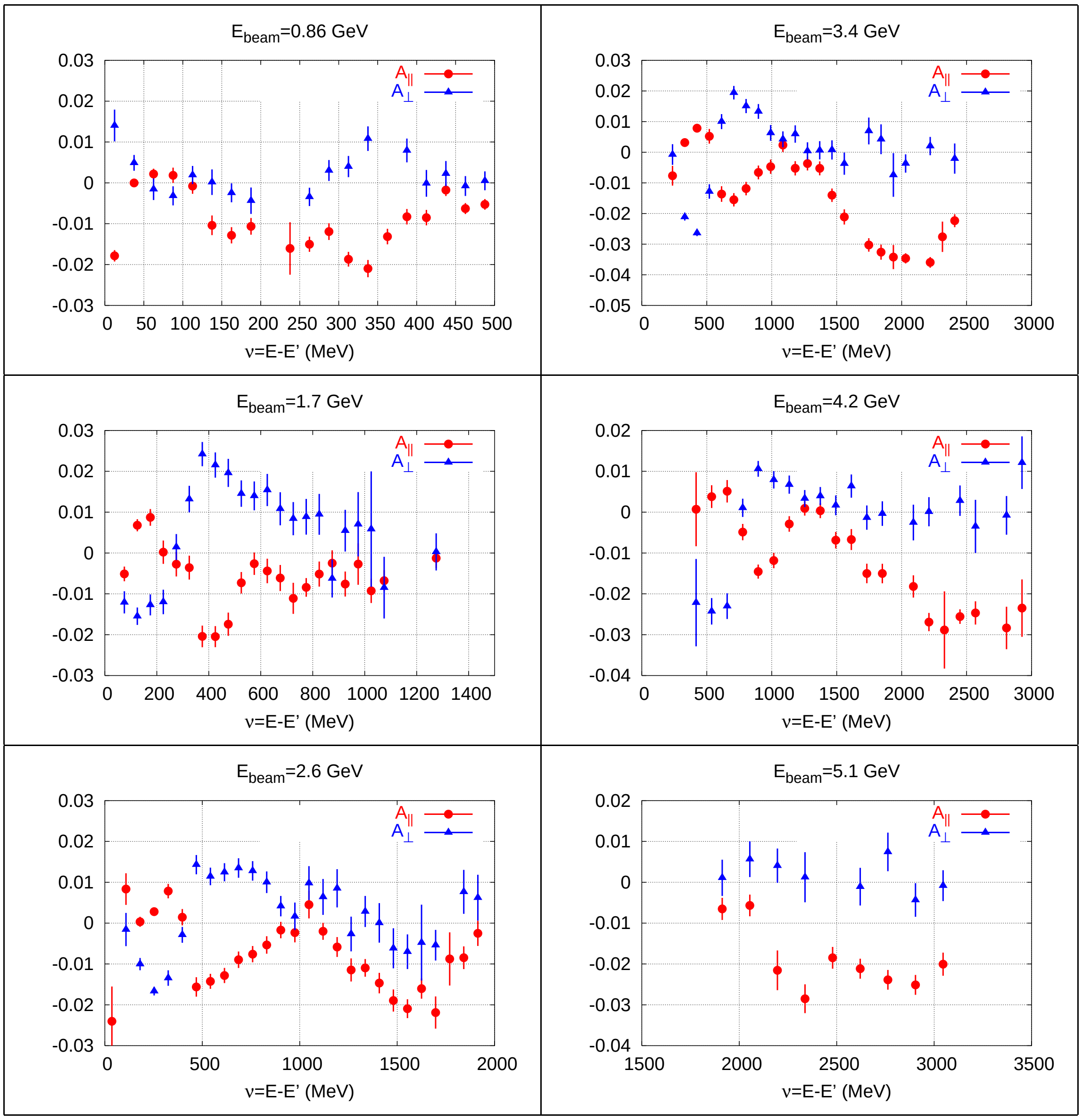

Figure 4.2: Parallel (red circles) and perpendicular (blue triangles) asymmetries as a function of energy loss. The error bars are statistical only.

For the perpendicular asymmetry $A_\perp$, the target polarization is maintained transverse to the beam direction and the beam polarization is again pseudo-randomly flipped. $A_\parallel$ has a large negative value at the Δ ($\approx 2\%$) and is Q^2-independent. Similarly $A_\perp$ has a large positive value at the Δ. It is interesting to note that $A_\parallel$ and $A_\perp$ are rough mirror images of each other in the resonance region. In the deep inelastic scattering regime, $A_\parallel$ becomes large whereas $A_\perp$ quickly dies out. The measured asymmetries are diluted by contribution from unpolarized backgrounds such as nitrogen. However, the results presented here have been corrected for dilution and radiative corrections.

4.2 Polarized Spin Structure Functions g_1 and g_2

The polarized structure functions $G_1(\nu, Q^2)$ and $G_2(\nu, Q^2)$ are related to the measured polarized cross sections in the following way [133]:

$$\frac{d^2\sigma}{d\Omega dE'}(\uparrow\downarrow - \uparrow\uparrow) = \frac{4\alpha^2}{M^3Q^2}\frac{E'}{E}[M(E+E'\cos\theta)G_1 - Q^2G_2], \tag{4.9}$$

$$\frac{d^2\sigma}{d\Omega dE'}(\uparrow\rightarrow - \uparrow\leftarrow) = \frac{4\alpha^2}{M^3Q^2}\frac{E'^2}{E}\sin\theta[MG_1 + 2EG_2]. \tag{4.10}$$

Like their unpolarized counterparts, in the scaling limit, the polarized structure functions $G_1(\nu, Q^2)$ and $G_2(\nu, Q^2)$ are replaced by the scaling polarized structure functions $g_1(x)$ and $g_2(x)$ [133]:

$$\frac{\nu}{M}G_1(\nu, Q^2) \rightarrow g_1(x), \tag{4.11}$$

$$\frac{\nu^2}{M^2}G_2(\nu, Q^2) \rightarrow g_2(x). \tag{4.12}$$

Plots of the g_1 and g_2 structure functions for ^{3}He as a function of energy loss ν are shown in Fig 4.3. It is to be noted that the quasielastic region does not contribute significantly to the structure functions. However, the Δ and resonance regions play a major role for both g_1 and g_2. In the scaling region, g_1 dominates. Plots of g_1 and g_2 as a function of the Bjorken scaling variable x are shown in Fig. 4.4 at the six beam energies of this experiment and at six chosen and equally spaced Q^2: 0.10, 0.26, 0.42, 0.58, 0.74, and 0.90 GeV^2. The evaluation of g_1 and g_2 from constant beam energy to constant Q^2 was done by interpolation and in a few instances by extrapolation [137].

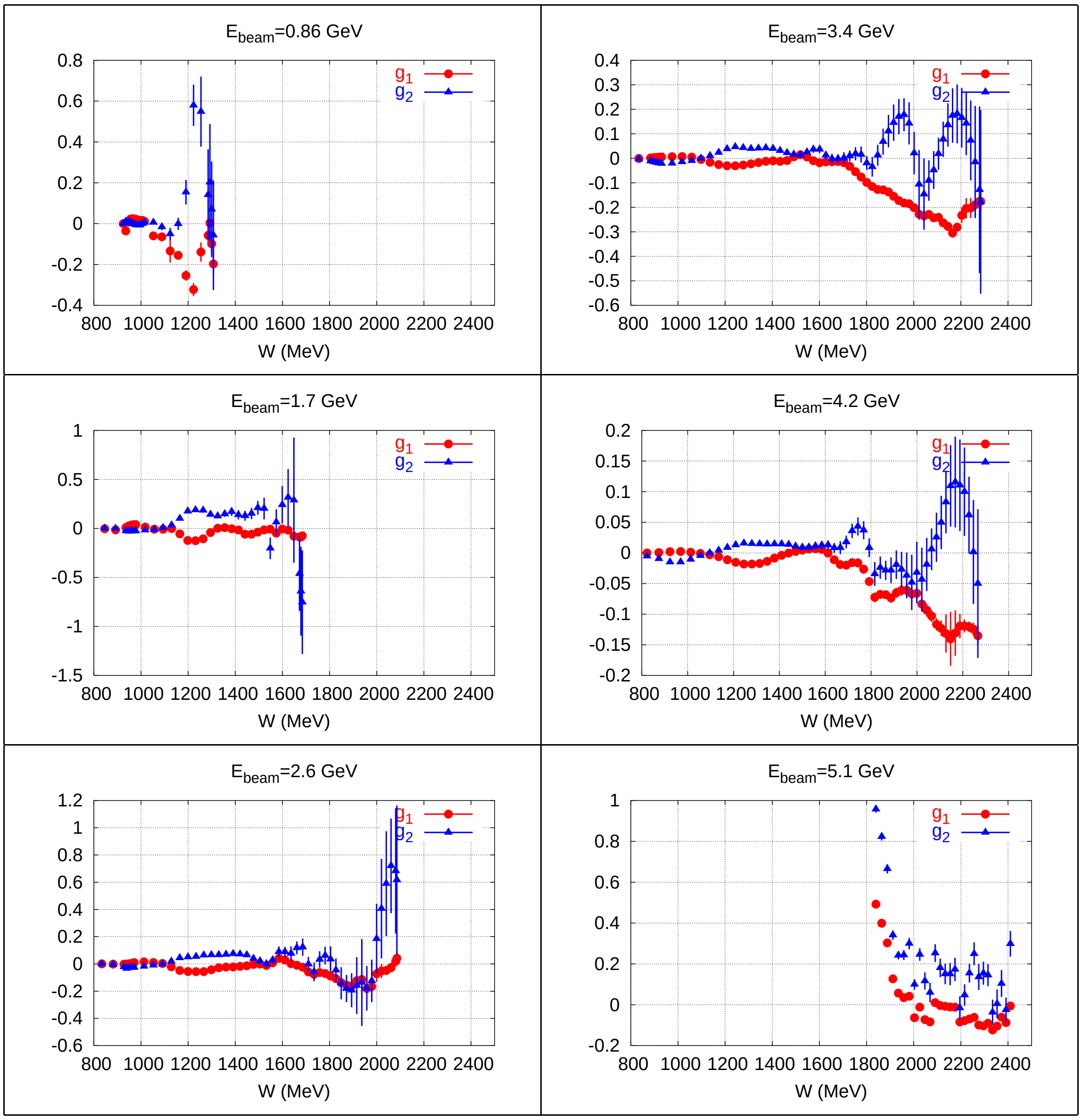

Figure 4.3: The ^{3}He polarized structure functions g_1 (red circles) and g_2 (blue triangles) as a function of invariant mass. The error bars are statistical only.

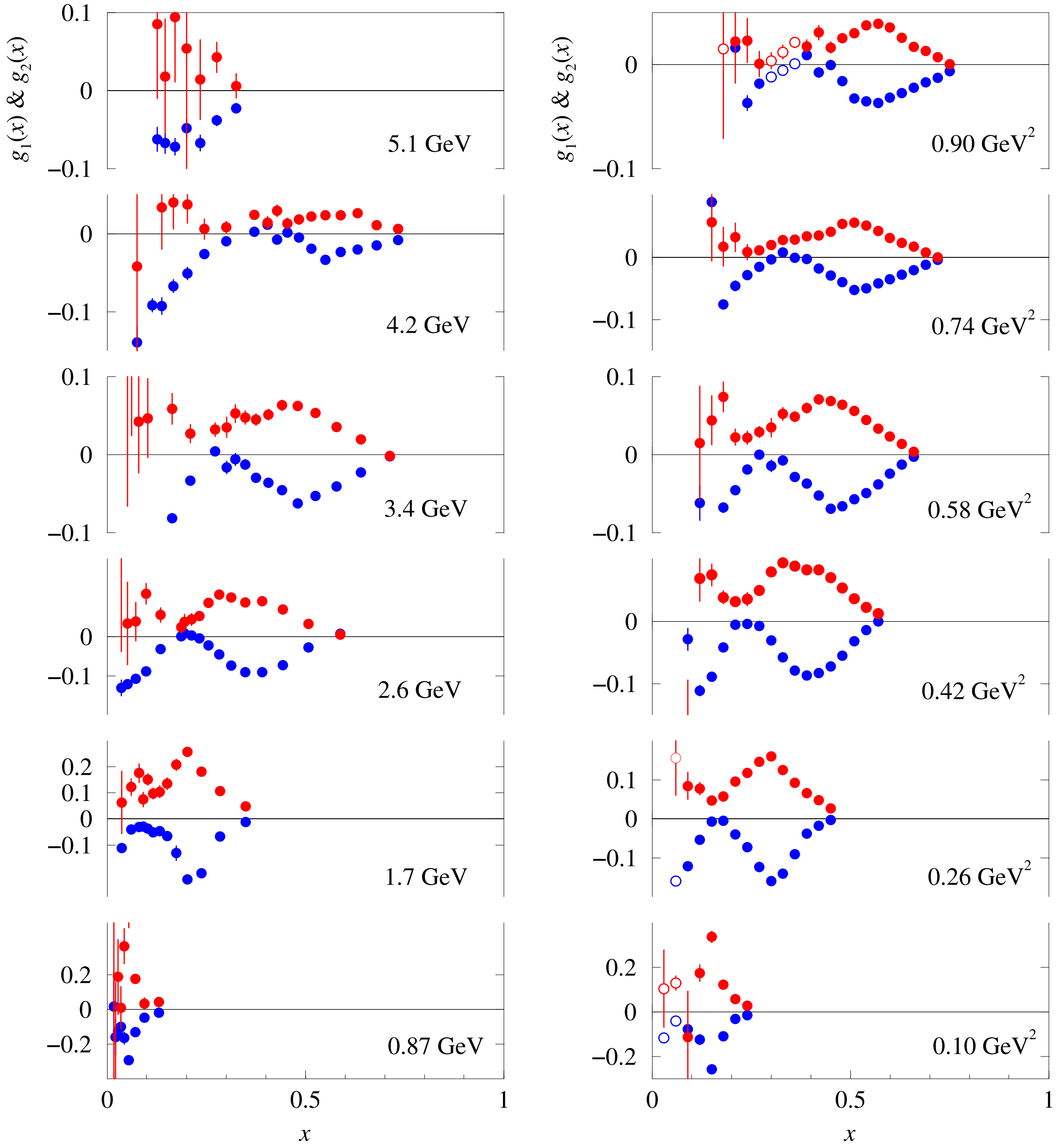

Figure 4.4: $g_1(x)$ (blue solid circles) and $g_2(x)$ (red solid circles) as a function of the Bjorken scaling variable x at the six beam energies of this experiment (left plot) and at six chosen fixed Q^2 (right plot).

4.3 Extraction of Neutron from ^{3}He

In this experiment, all measurements were performed on a polarized ^{3}He target. Hence spin structure functions and asymmetries extracted so far are those of ^{3}He. However, in a naïve model of the ^{3}He nucleus, all nucleons sit in a S-wave state. In this picture, both protons carry opposite' spins and cancel each other out. What is left is the spin of the neutron. Thus, to a large extent, the neutron may be approximated by a ^{3}He nucleus. The spin structure functions and asymmetries for ^{3}He and the neutron are then identical. Unfortunately, the scenario just described is not completely accurate. In a realistic model of the ^{3}He wave function, where effective nucleon polarizations are taken into account but not nuclear effects, the S state is augmented by an admixture of S'- and D-wave components, with a negligible P-wave contribution. World calculations on the three-body system for the extra wave function percentages give $P_D = 9.8\%$ and $P_{S'} = 1.4\%$. The prescription for getting at the neutron spin structure functions and asymmetries from those of ^{3}He and the proton is [33]:

$$\begin{aligned} g_1^{^3\text{He}} &= 2p_p g_1^p(x) + p_n g_1^n(x), & (4.13)\\ A_{^3\tilde{\text{He}}} &= 2f_p p_p A_{\vec{p}} + f_n p_n A_{\vec{n}}, & (4.14) \end{aligned}$$

Here the important quantities are the effective nucleon polarizations p_p and p_n of the proton and neutron, respectively. Their values from world calculations are $p_p = -0.028 \pm 0.004$ and $p_n = 0.86 \pm 0.02$. The dilution factor of the proton(neutron) is defined as $f_{p(n)} = F_2^{p(n)}/(2F_2^p + F_2^n)$, and the asymmetry is $A_{\vec{p}(\vec{n})} = 2xg_1^{p(n)}/F_2^{p(n)}$. In the same fashion, a formula for the GDH integral is developed [33]:

$$I^{^3\text{He}}(Q^2) = 2p_p I^p(Q^2) + p_n I^n(Q^2). \qquad (4.15)$$

In order to introduce nuclear effects, namely Fermi motion and binding effects, a convolution approach [33] is employed. The method consists of defining the spin structure function of ^{3}He as a convolution of the spin structure function of the nucleon and its spectral functions, summed over the constituent nucleons. This last convolution approach differ from the method of effective nucleon polarizations by at most 5%. However, the correction to the GDH integral of the neutron from ^{3}He may be as large as 30%. All the cross sections, asymmetries, and structure functions presented in this thesis do not include corrections for nuclear effects. However, results for the GDH integral are presented for both the neutron in ^{3}He (no correction for nuclear effects) and the free neutron (corrections for nuclear effects included). The extraction of the neutron GDH integral from ^{3}He was obtained by multiplying by a factor $I^n_{\mathrm{GDH}}/I^{^3\mathrm{He}}_{\mathrm{GDH}}$ acquired from Ref. [33].

4.4 GDH Integrand

The polarized cross sections measured in this experiment are connected to the transverse-transverse interference term σ'_{TT} and the longitudinal-transverse interference term σ'_{LT} by [138]:

$$\sigma^{\downarrow\uparrow} - \sigma^{\uparrow\uparrow} \equiv \frac{d^2\sigma^{\downarrow\uparrow}}{d\Omega dE'} - \frac{d^2\sigma^{\uparrow\uparrow}}{d\Omega dE'} = 2\Gamma D(1+\epsilon R)(\sigma'_{TT} + \eta\sigma'_{LT}), \tag{4.16}$$

$$\sigma^{\downarrow\rightarrow} - \sigma^{\uparrow\rightarrow} \equiv \frac{d^2\sigma^{\downarrow\rightarrow}}{d\Omega dE'} - \frac{d^2\sigma^{\uparrow\rightarrow}}{d\Omega dE'} = 2\Gamma d(1+\epsilon R)(\sigma'_{LT} - \zeta\sigma'_{TT}), \tag{4.17}$$

where

$$\Gamma = \frac{\alpha}{4\pi^2}\frac{K}{Q^2}\frac{E'}{E}\frac{2}{1-\epsilon}. \tag{4.18}$$

The photon depolarization factor $D = (1-\epsilon E'/E)/(1+\epsilon R)$, $d = D\sqrt{2\epsilon/(1+\epsilon)}$, $\eta = \epsilon\sqrt{Q^2}/(E-\epsilon E')$, $\zeta = \eta(1+\epsilon)/2\epsilon$, $\epsilon^{-1} = 1+2(1+\gamma^{-2})\tan^2(\theta/2)$, $\gamma = 2Mx/\sqrt{Q^2}$, $R = \sigma_L/\sigma_T$, and K is the photon flux and is convention-dependent. In this experiment, the convention picked is the so-called Hand convention and is defined as $K = \nu - Q^2/2M$. Substituting D and d in the equations for the differences of polarized cross sections above yield a new set of linear equations:

$$\sigma^{\downarrow\uparrow} - \sigma^{\uparrow\uparrow} = 2\Gamma(1-\epsilon E'/E)(\sigma'_{TT} + \eta\sigma'_{LT}), \tag{4.19}$$

$$\sigma^{\downarrow\rightarrow} - \sigma^{\uparrow\rightarrow} = 2\Gamma(1-\epsilon E'/E)(\sigma'_{LT} - \zeta\sigma'_{TT}). \tag{4.20}$$

This removes the dependency of R and obviates the need to obtain experimentally measured values for $R = \sigma_L/\sigma_T$. This experiment measured the quantities $\sigma^{\downarrow\uparrow}$, $\sigma^{\uparrow\uparrow}$, $\sigma^{\downarrow\rightarrow}$, and $\sigma^{\uparrow\rightarrow}$. All the other factors (Γ, ϵ, η, and ζ) depend only on the kinematics. The GDH integrand σ'_{TT} and σ'_{LT} may now be extracted from the set of linear equations above. For completeness sake, the spin-averaged cross section in the above formalism is simply:

$$\frac{d^2\sigma}{d\Omega dE'} = \Gamma(\sigma_T + \epsilon\sigma_L). \tag{4.21}$$

Thus, having measured the polarized cross sections, the interference terms required by the GDH sum rule are readily extracted. Fig. 4.5 shows σ'_{TT} as a function of invariant mass W at the six constant beam energies of this experiment (left plot) and σ'_{TT} as a function of energy loss ν as a function of six chosen and equally spaced Q^2 values. All values are averaged over both the Electron and Hadron arms. The dominant feature of σ'_{TT} is the $\Delta(1232)$ or P_{33} resonance. It is by far the single largest contributor to the GDH integral.

4.5 GDH Sum Rule and Integral

The GDH sum rule links the total photoabsorption cross-section difference to the nucleon anomalous magnetic moment [16]. This relationship is captured in the following equation:

$$\int_{\nu_0}^{\infty} \frac{d\nu}{\nu}(\sigma_{1/2} - \sigma_{3/2}) = -\frac{2\pi^2\alpha}{M^2}\kappa^2. \tag{4.22}$$

$\sigma_{1/2(3/2)}$ is the total photoabsorption cross section where the index represents the projection of total angular momentum along the quantization axis for the photon-nucleon pair. Here, ν is the energy loss and ν_0 is the threshold of pion production. M is the mass of the nucleon and κ is the anomalous magnetic moment of the nucleon. The prediction of the GDH sum rule is restricted to real photons only, that is $Q^2 = 0$. In this experiment, a beam of electrons interacted with the target nucleons via virtual photons. Thus it is necessary to extend the GDH sum rule to virtual photons if a meaningful dialogue between theory and experiment is to be engaged. This is traditionally done by redefining the GDH integral for finite Q^2. Several definitions of the GDH integral exist in the literature [26, 31]. The one chosen for this experiment is [139]:

$$I(Q^2) = 2\int_{\nu_0}^{\infty} \frac{d\nu}{\nu}(1 - x)\sigma'_{TT}. \tag{4.23}$$

$x = Q^2/2M\nu$ is the Bjorken scaling variable. As defined above, the real photon limit for the GDH integral is:

$$I(0) = -\frac{2\pi^2\alpha}{M^2}\kappa^2. \tag{4.24}$$

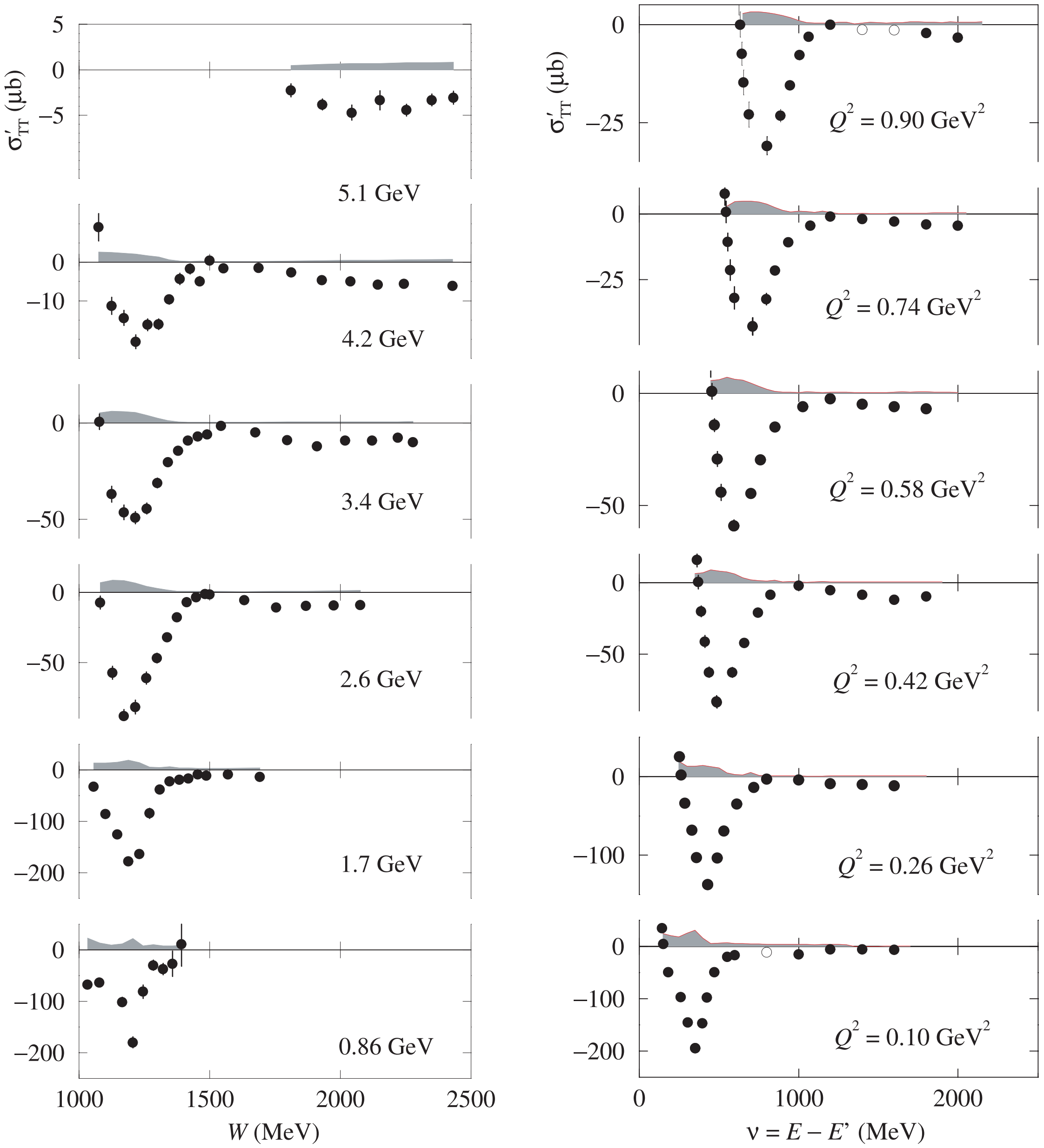

Figure 4.5: σ'_{TT} as a function of invariant mass W at the six beam energies of this experiment (left) and σ'_{TT} as a function of energy loss ν for six chosen, equally spaced Q^2 values (right). Statistical errors are represented by the error bars on the data points and systematic errors are represented by the error bands on the horizontal axes. The open circles represent interpolated points.

Q^2 (GeV^2)	I_{GDH} (μb)	Statistical (μb)	Systematic (μb)
0.10	-187.50	5.23	28.43
0.26	-109.92	2.04	13.77
0.42	-53.51	1.21	5.48
0.58	-31.68	0.74	3.72
0.74	-18.27	0.64	2.42
0.90	-10.47	0.46	1.52

Table 4.1: Experimentally measured values for $I^{^3\text{He}}_{\text{GDH}}(Q^2)$ before nuclear corrections along with their corresponding statistical and systematic errors; see Ref. [1].

On the other side of the momentum spectrum,

$$I(Q^2) \to 16\pi^2\alpha\frac{\Gamma_1(Q^2)}{Q^2} \quad \text{as} \quad Q^2 \to \infty, \tag{4.25}$$

where $\Gamma_1(Q^2) = \int_0^1 g_1(x, Q^2)dx$. This experiment measured values of the GDH integral for the neutron from ^{3}He. If, in addition, measurements of the GDH integral for the proton are obtained, the difference,

$$\Gamma_1^p(Q^2) - \Gamma_1^n(Q^2) = \frac{1}{6}\left|\frac{g_A}{g_V}\right|\left[1 - \frac{\alpha_s(Q^2)}{\pi}\right], \tag{4.26}$$

is the well-known Bjorken sum rule [7] and has been calculated to high accuracy in the fundamental theory of quantum chromodynamics (QCD). Here, g_A/g_V is the ratio of the axial to vector coupling constant in the β decay of the neutron and α_s is the strong coupling constant. Table 4.1 contains values for the GDH integral measured in this experiment. These values have been evaluated at fixed Q^2 by interpolating between values of constant beam energies. In addition, alongside the experimental points, theoretical predictions for both the GDH sum rule and integral are plotted in Fig. 4.6. Note the GDH integral of the model of Ref. [26] does not match the GDH sum rule at $Q^2 = 0$. This is possibly due to some missing resonances or insufficient strengths of certain resonances in their model.

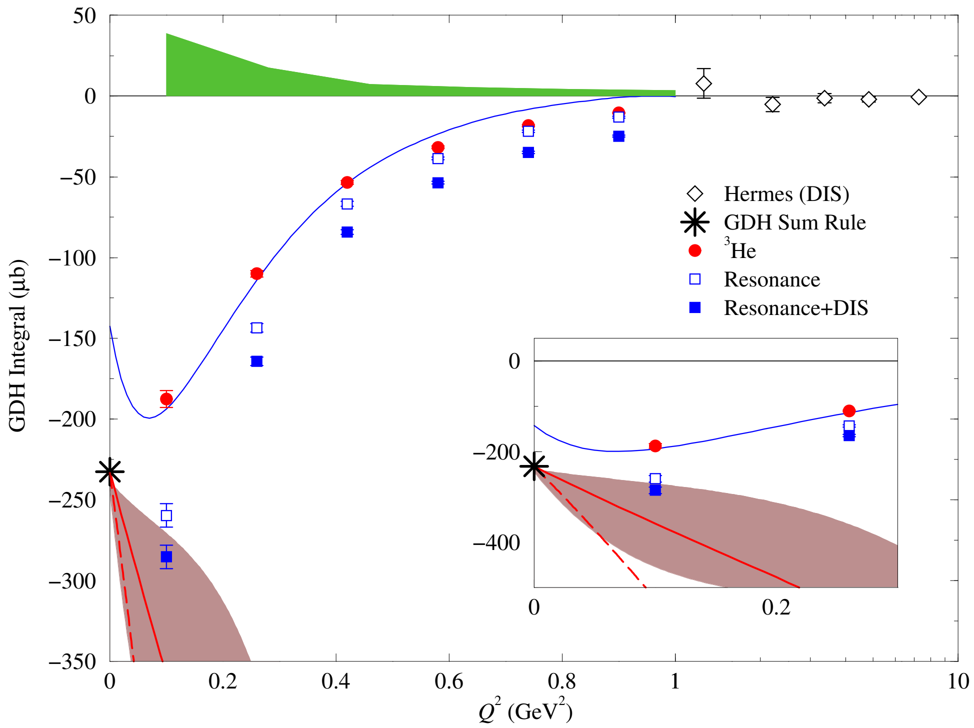

Figure 4.6: GDH integral as a function of Q^2 for this experiment. The red solid circles represent $I_{\rm GDH}$ without any nuclear corrections. The blue hollow squares represent $I_{\rm GDH}$ corrected for nuclear effects but with resonance contribution only. The blue solid squares represent $I_{\rm GDH}$ corrected for nuclear effects including resonance and DIS contributions. The hollow diamonds are DIS data from the HERMES collaboration [140]. The star is the value of the GDH integral for the neutron. The solid blue curve is a calculation based on the MAID model [26]. The red dashed line in the lower left corner represents ChPT calculations of Ref. [31]. The red solid line and pink band represent ChPT calculations of Ref. [141]. The band includes uncertainties in resonance parameters used. The green error band on the horizontal axis represents systematic errors. The statistical errors are represented by error bars on the data points. When absent, the error bars are simply smaller than the data points shown. Note that beyond a Q^2 of 1 GeV^2, the data points are plotted with a semi-log scale.

4.6 Conclusion and Outlook

This dissertation describes the first experiment to measure g_1, g_2, σ'_{TT}, and $I^n_{\mathrm{GDH}}(Q^2)$ in the low Q^2 range of 0.1 to 0.9 GeV^2. The low Q^2 evolution of the GDH integral may be compared with model predictions from different phenomenologies: chiral perturbation theory, lattice quantum chromodynamics (when available), and high twist expansion. Future experiments at Jefferson Lab aim to extend these measurements to lower Q^2 [142] to answer the question whether the GDH integral makes the expected dramatic turnover at Q^2 below 0.1 GeV^2 and meets the predicted value for the GDH sum rule of $I(0) = -232.8\ \mu$b.

Experiment E94-010 is the first of a series of many successful experiments in Hall A to use the polarized ^{3}He target. As part of that programme, a polarized ^{3}He target facility has been built at Jefferson Laboratory and a target cell building facility has been setup at the College of William and Mary under the auspices of T. Averett. The latter is an ongoing active research effort and target cells with record ever increasing polarization have been developed. In addition, the accelerator group has been breaking new grounds by achieving ever higher beam polarization at high luminosity and reliability. One can only wait with anticipation at the physics results pouring out of this program in the next few years.

Chapter 5

ADDENDUM

An experiment of this magnitude involves a large collaborative effort and many years of preparation. I would like to thank the co-spokepersons, Prof. Z.-E. Meziani, Prof. G. Cates, and Dr. J.-P. Chen, for proposing the experiment and for the dedication and effort to bring the experiment to fruition and build the required polarized ^{3}He target system specifically needed for this measurement. I would like to acknowledge Jefferson Laboratory Accelerator Division for providing high-quality polarized beam using the Continuous Electron Accelerator Facility. Thanks also to the entire Hall A Collaboration and its leader Dr. Kees de Jager for providing the standard experimental High-Resolution Spectrometers and additional apparatus needed, and the manpower.

Such a large experiment is, of necessity, a collective endeavor of numerous people, not the least significant of which is the work of my fellow Ph.D. thesis students, K. Slifer, A. Deur, S. Jensen, and I. Kominis, and a cadre of postdocs, notably, Drs. D. Pripstein, S. Choi, and X. Jiang. A complete list of collaborators is presented at the end of this section, extracted from the first publication of the work described in this thesis. Space prohibits my mentioning all by name.

In the work of this magnitude, the question arises as to the specific contribution of any one individual, namely myself. At the request of Prof. J.D. Walecka, I would like to acknowledge a partial list of specific contributions I have made to this project:

1. I participated in the initial construction and installation of the polarized ^{3}He target and its initial calibration. Some specific contributions I made include: cabling for target ladder controller, building of the oven by working closely with

the design team, and assisting with early water polarimetry.

2. I also made very significant contributions of both the commissioning and production run for E94-010. This includes taking 55 shifts on the experiment, more than any other individual collaborator. My primary contribution during data acquisition was that of Target Operator and Data Acquisition Shift Worker.

3. Contributions to the subsequent analysis included much of the work needed to obtain the absolute cross section, including extraction scintillator inefficiencies, nitrogen dilution factors, deadtime analysis, and elastic radiative tail corrections. Normalized cross sections are important for extracting the GDH integrand. In addition, I did a thorough investigation of all the runs to check the scaler data and cross-check target polarization orientations, as well as eliminating bad data.

4. Last, but not least important, is my work and love of this thesis which has taken so many years of my time and from which I have learned so much. In the process, I have learned to write an important document, and I would like to thank the members of my thesis committee for their feedback and patience. These people are College of William and Mary Profs. J.M. Finn, T.D. Averett, D.S. Armstrong, K.A. Griffioen, Distinguished Prof. J.D. Walecka, and the external examinator Dr. J.-P. Chen from Jefferson Laboratory.

Q^2 Evolution of the Generalized Gerasimov-Drell-Hearn Integral for the Neutron using a ^{3}He Target

M. Amarian,[5] L. Auerbach,[20] T. Averett,[6,23] J. Berthot,[4] P. Bertin,[4] W. Bertozzi,[11] T. Black,[11] E. Brash,[16] D. Brown,[10] E. Burtin,[18] J. R. Calarco,[13] G. D. Cates,[15,22] Z. Chai,[11] J.-P. Chen,[6] Seonho Choi,[20] E. Chudakov,[6] E. Cisbani,[5] C.W. de Jager,[6] A. Deur,[4,6,22] R. DiSalvo,[4] S. Dieterich,[17] P. Djawotho,[23] M. Finn,[23] K. Fissum,[11] H. Fonvieille,[4] S. Frullani,[5] H. Gao,[11] J. Gao,[1] F. Garibaldi,[5] A. Gasparian,[3] S. Gilad,[11] R. Gilman,[6,17] A. Glamazdin,[9] C. Glashausser,[17] E. Goldberg,[1] J. Gomez,[6] V. Gorbenko,[9] J.-O. Hansen,[6] F.W. Hersman,[13] R. Holmes,[19] G. M. Huber,[16] E.W. Hughes,[1] T. B. Humensky,[15] S. Incerti,[20] M. Iodice,[5] S. Jensen,[1] X. Jiang,[17] C. Jones,[1] G. M. Jones,[8] M. Jones,[23] C. Jutier,[4,14] A. Ketikyan,[24] I. Kominis,[15] W. Korsch,[8] K. Kramer,[23] K. S. Kumar,[12,15] G. Kumbartzki,[17] M. Kuss,[6] E. Lakuriqi,[20] G. Laveissiere,[4] J. Lerose,[6] M. Liang,[6] N. Liyanage,[6,11] G. Lolos,[16] S. Malov,[17] J. Marroncle,[18] K. McCormick,[14] R. McKeown,[1] Z.-E. Meziani,[20] R. Michaels,[6] J. Mitchell,[6] Z. Papandreou,[16] T. Pavlin,[1] G. G. Petratos,[7] D. Pripstein,[1] D. Prout,[7] R. Ransome,[17] Y. Roblin,[4] D. Rowntree,[11] M. Rvachev,[11] F. Sabatie,[14] A. Saha,[6] K. Slifer,[20] P. A. Souder,[19] T. Saito,[21] S. Strauch,[17] R. Suleiman,[7] K. Takahashi,[21] S. Teijiro,[21] L. Todor,[14] H. Tsubota,[21] H. Ueno,[21] G. Urciuoli,[5] R. Van der Meer,[6,16] P. Vernin,[18] H. Voskanian,[24] B. Wojtsekhowski,[6] F. Xiong,[11] W. Xu,[11] J.-C. Yang,[2] B. Zhang,[11] and P. Zolnierczuk[8]

(Jefferson Lab E94010 Collaboration)

[1]*California Institute of Technology, Pasadena, California 91125*
[2]*Chungnam National University, Taejon 305-764, Korea*
[3]*Hampton University, Hampton, Virginia 23668*
[4]*LPC IN2P3/CNRS, Université Blaise Pascal, F-63170 Aubière CEDEX, France*
[5]*Istituto Nazionale di Fiscica Nucleare, Sezione Sanità, 00161 Roma, Italy*
[6]*Thomas Jefferson National Accelerator Facility, Newport News, Virginia 23606*
[7]*Kent State University, Kent, Ohio 44242*
[8]*University of Kentucky, Lexington, Kentucky 40506*
[9]*Kharkov Institute of Physics and Technology, Kharkov 310108, Ukraine*
[10]*University of Maryland, College Park, Maryland 20742*
[11]*Massachusetts Institute of Technology, Cambridge, Massachusetts 02139*
[12]*University of Massachusetts–Amherst, Amherst, Massachusetts 01003*
[13]*University of New Hampshire, Durham, New Hampshire 03824*
[14]*Old Dominion University, Norfolk, Virginia 23529*
[15]*Princeton University, Princeton, New Jersey 08544*
[16]*University of Regina, Regina, Canada SK S4S 0A2*
[17]*Rutgers, The State University of New Jersey, Piscataway, New Jersey 08855*
[18]*CEA Saclay, DAPNIA/SPhN, F-91191 Gif sur Yvette, France*
[19]*Syracuse University, Syracuse, New York 13244*
[20]*Temple University, Philadelphia, Pennsylvania 19122*
[21]*Tohoku University, Sendai 980, Japan*
[22]*University of Virginia, Charlottesville, Virginia 22904*
[23]*The College of William and Mary, Williamsburg, Virginia 23187*
[24]*Yerevan Physics Institute, Yerevan 375036, Armenia*
(Received 15 May 2002; published 26 November 2002)

We present data on the inclusive scattering of polarized electrons from a polarized ^{3}He target at energies from 0.862 to 5.06 GeV, obtained at a scattering angle of 15.5°. Our data include measurements from the quasielastic peak, through the nucleon resonance region, and beyond, and were used to determine the virtual photon cross-section difference $\sigma_{1/2} - \sigma_{3/2}$. We extract the extended Gerasimov-Drell-Hearn integral for the neutron in the range of four-momentum transfer squared Q^2 of 0.1–0.9 GeV^2.

DOI: 10.1103/PhysRevLett.89.242301 PACS numbers: 25.30.–c, 11.55.Hx

Sum rules involving the spin structure of the nucleon offer an important opportunity to study quantum chromodynamics (QCD). At long distance scales or in the confinement regime, a sum rule of great interest is that due to Gerasimov, Drell, and Hearn (GDH) [1,2]. The GDH sum rule relates an integral over the full excitation spectrum of the spin-dependent total photoabsorption cross section to the nucleon's anomalous magnetic

Figure 5.1: Cover page from initial publication of this work showing the Jefferson Laboratory E94-010 collaborators and their respective institutions.

Appendix A

Tables of $g_1(x)$, $g_2(x)$, and σ'_{TT}

Presented in this chapter are tables of the physics quantities measured in this experiment. Tables 1-6 include values of $g_1(x)$ at constant beam energy. Tables 7-12 include values of $g_2(x)$ at constant beam energy. Tables 13-18 include values of $g_1(x)$ at constant Q^2. Tables 19-24 include values of $g_2(x)$ at constant Q^2. Tables 25-30 include values of σ'_{TT} *vs.* W at constant beam energy. Tables 31-36 include values of σ'_{TT} *vs.* ν at constant Q^2. The last column of each table represents statistical errors only.

Table A.1: $g_1(x)$ at $E_{\text{beam}} = 0.86$ GeV

x	$g_1(x)$	Statistical
1.12	0.14182250E-01	0.26234046E-02
0.35	0.91571636E-01	0.60040797E-02
0.20	0.11382457E-01	0.82934806E-02
0.13	0.10658792E-02	0.81755072E-02
0.09	-0.49901415E-01	0.40711936E-01
0.07	-0.13679247E+00	0.24238409E-01
0.06	-0.22968970E+00	0.33332061E-01
0.04	-0.17004804E+00	0.47813617E-01
0.03	-0.10828505E+00	0.50857317E-01
0.03	-0.33049781E-01	0.59056628E-01
0.02	-0.90949327E-01	0.16542999E+00
0.02	-0.23331431E+00	0.30727485E+00

Table A.2: $g_1(x)$ at $E_{\text{beam}} = 1.7$ GeV

x	$g_1(x)$	Statistical
4.51	-0.16306395E-02	0.10699913E-03
1.46	-0.22705919E-02	0.21377730E-02
0.85	0.34619238E-01	0.79466505E-02
0.59	0.41623883E-01	0.72399811E-02
0.44	0.34726663E-02	0.59218481E-02
0.35	-0.16102279E-01	0.77965166E-02
0.29	-0.18617181E-01	0.89896452E-02
0.24	-0.11674576E+00	0.13463100E-01
0.20	-0.13845623E+00	0.22265524E-01
0.17	-0.10323865E-01	0.25535723E-01
0.15	0.19927669E-01	0.16946007E-01
0.13	0.14430597E-01	0.18075427E-01
0.12	-0.42113303E-02	0.16524276E-01
0.10	-0.34073610E-01	0.21528162E-01
0.09	0.51094666E-01	0.28412353E-01
0.08	-0.13106216E-01	0.25847560E-01
0.07	-0.20000676E-02	0.29022532E-01
0.06	-0.63624866E-01	0.39962627E-01
0.06	0.70814778E-04	0.39350338E-01
0.05	-0.12766827E-01	0.77100240E-01
0.05	-0.72170891E-01	0.51351890E-01
0.04	0.57972752E-01	0.44542219E-01
0.04	0.50687820E+00	0.19393364E+00
0.03	0.10037500E+01	0.27364549E+00
0.03	0.14831458E+01	0.21846020E+00
0.02	0.19500046E+01	0.33972446E-01

Table A.3: $g_1(x)$ at $E_{\text{beam}} = 2.6$ GeV

x	$g_1(x)$	Statistical
10.22	0.36296681E-01	0.63235092E-03
3.34	0.35186585E-02	0.10241738E-04
1.96	0.32382572E-03	0.20288014E-03
1.37	-0.13550362E-02	0.11910818E-02
1.05	0.26851977E-03	0.35099837E-02
0.84	0.17225698E-02	0.46784608E-02
0.69	0.20381914E-01	0.39229984E-02
0.59	0.14061023E-01	0.40358393E-02
0.51	-0.94419662E-02	0.55401931E-02
0.44	-0.44636104E-01	0.98728212E-02
0.39	-0.53154502E-01	0.12776713E-01
0.35	-0.82318485E-01	0.13364040E-01
0.31	-0.59743538E-01	0.16884565E-01
0.28	-0.58646314E-01	0.14159492E-01
0.26	-0.42269982E-01	0.12391546E-01
0.23	0.18245949E-02	0.15401202E-01
0.21	0.22452618E-02	0.16328041E-01
0.19	0.15153727E-01	0.15674304E-01
0.18	-0.60126376E-02	0.20183455E-01
0.16	0.10961683E-01	0.20105746E-01
0.15	0.16520057E-01	0.18633366E-01
0.14	0.23036931E+00	0.22658363E-01
0.13	0.55162704E+00	0.21369396E-01
0.12	0.84337813E+00	0.24912560E-01
0.11	0.12172891E+01	0.21434600E-01
0.10	0.15553987E+01	0.23642356E-01
0.09	0.19741496E+01	0.22993388E-01
0.09	0.16165129E+01	0.24930939E-01
0.08	-0.13816418E+00	0.25629917E-01
0.07	-0.16858179E-01	0.28302766E-01

Table A.3: $g_1(x)$ at $E_{\text{beam}} = 2.6$ GeV

x	$g_1(x)$	Statistical
0.07	-0.40372554E-01	0.28958468E-01
0.06	-0.68981551E-01	0.33252705E-01
0.06	-0.90578087E-01	0.33722520E-01
0.05	-0.73108234E-01	0.29512106E-01
0.05	-0.54406628E-01	0.40314399E-01
0.05	-0.15339199E+00	0.54153755E-01
0.04	0.21072589E+00	0.13131882E+00
0.04	-0.18311450E+00	0.50190572E-01
0.03	-0.16698907E+00	0.18729267E+00

Table A.4: $g_1(x)$ at $E_{\text{beam}} = 3.4$ GeV

x	$g_1(x)$	Statistical
1.84	-0.26862817E-04	0.54414594E-03
1.48	-0.69356535E-03	0.34488586E-03
1.23	-0.21423807E-03	0.74801873E-03
1.05	0.28862262E-02	0.14576418E-02
0.91	0.58034372E-01	0.22032454E-02
0.80	0.68118731E-02	0.21556602E-02
0.71	0.38112768E-02	0.31887873E-02
0.64	-0.95562711E-02	0.38042590E-02
0.58	-0.23624588E-01	0.48740194E-02
0.53	-0.37551660E-01	0.66223340E-02
0.48	-0.46644263E-01	0.65085799E-02
0.44	-0.23888119E-01	0.62438259E-02
0.41	-0.21869641E-01	0.65440098E-02
0.38	-0.82710752E-03	0.79535833E-02
0.35	0.18345626E-01	0.79408344E-02
0.32	-0.17569920E+00	0.84132487E-02
0.30	-0.57906967E+00	0.92388699E-02

Table A.4: $g_1(x)$ at $E_{\text{beam}} = 3.4$ GeV

x	$g_1(x)$	Statistical
0.28	-0.71906912E+00	0.11570845E-01
0.26	-0.79048979E+00	0.10951820E-01
0.25	-0.73019654E+00	0.11092637E-01
0.23	-0.59086710E+00	0.13427658E-01
0.22	-0.40579370E+00	0.14305437E-01
0.20	-0.20995156E+00	0.14672418E-01
0.19	0.64403981E-01	0.15120492E-01
0.18	-0.12374887E-01	0.17340321E-01
0.17	-0.23902573E-01	0.15521068E-01
0.16	-0.22538722E-01	0.15925694E-01
0.15	-0.41337423E-01	0.21149745E-01
0.14	-0.22313419E+00	0.15706538E+00
0.13	-0.14013819E+00	0.55227943E-01
0.13	-0.82780495E-01	0.31293456E-01
0.12	-0.62498111E-01	0.18735601E-01
0.11	-0.83540969E-01	0.23571163E-01
0.11	-0.18613680E+00	0.59740413E-01
0.10	-0.10718542E+00	0.37500184E-01
0.09	-0.69411345E-01	0.31711966E-01
0.09	-0.80979288E-01	0.23585496E-01
0.08	-0.99490821E-01	0.35758894E-01
0.08	-0.11014149E+00	0.45921136E-01
0.07	-0.11045226E+00	0.45349233E-01
0.07	-0.93336336E-01	0.27916530E-01
0.06	-0.82355820E-01	0.47905438E-01
0.06	-0.61615016E-01	0.40889718E-01
0.06	-0.56889951E-01	0.38737681E-01
0.05	-0.48980452E-01	0.48134804E-01

Table A.5: $g_1(x)$ at $E_{\text{beam}} = 4.2$ GeV

x	$g_1(x)$	Statistical
1.30	0.80808077E-03	0.16237996E-02
1.16	-0.62457827E-03	0.18325783E-02
1.05	0.52421396E-02	0.34310624E-02
0.95	0.19452974E-01	0.38110972E-02
0.87	0.53533177E+01	0.52270875E-02
0.80	-0.95838638E+02	0.40947930E-02
0.73	-0.72953491E+02	0.24826899E-02
0.68	-0.53496925E+02	0.24193737E-02
0.63	-0.43318588E+02	0.33312179E-02
0.59	-0.36649883E+02	0.38725245E-02
0.55	-0.31842117E+02	0.54022931E-02
0.52	-0.28248373E+02	0.56709526E-02
0.48	-0.25304966E+02	0.55362713E-02
0.45	-0.22956518E+02	0.52327006E-02
0.43	-0.20864058E+02	0.53148521E-02
0.40	-0.15755212E+02	0.65190136E-02
0.38	0.76201224E+00	0.72898748E-02
0.36	0.71846750E-02	0.79123322E-02
0.34	0.16173370E-03	0.74368124E-02
0.32	-0.42652260E-02	0.83301868E-02
0.31	-0.73306621E-02	0.10533367E-01
0.29	-0.17781585E-01	0.11892070E-01
0.28	0.81141023E-02	0.11807044E-01
0.26	0.14994864E-01	0.11533692E-01
0.25	-0.11311520E-03	0.14761130E-01
0.24	-0.32201316E-01	0.16177498E-01
0.23	-0.48282448E-01	0.16572295E-01
0.22	-0.31293787E-01	0.15804337E-01
0.21	-0.15409846E-01	0.20686787E-01
0.20	-0.68948515E-01	0.38399711E-01

Table A.5: $g_1(x)$ at $E_{\text{beam}} = 4.2$ GeV

x	$g_1(x)$	Statistical
0.19	0.15892087E-01	0.49721401E-01
0.18	0.53825393E-01	0.64382814E-01
0.17	0.35791159E-01	0.46547893E-01
0.16	-0.31354681E-01	0.20832958E-01
0.16	-0.68346553E-01	0.18339409E-01
0.15	-0.71198612E-01	0.24392886E-01
0.14	-0.10926700E+00	0.50926276E-01
0.14	-0.36866434E-01	0.90590693E-01
0.13	-0.81900870E-02	0.50177231E-01
0.12	-0.63442580E-01	0.25287675E-01
0.12	-0.36305726E-01	0.23834264E-01
0.11	0.68128407E-02	0.30182019E-01
0.11	-0.32328241E-01	0.57840478E-01
0.10	0.23692858E+00	0.14878465E+00
0.10	0.98638915E-01	0.14331158E+00
0.09	-0.13922465E-01	0.17079030E+00
0.09	-0.66735268E-01	0.12662871E+00
0.08	-0.64184606E-01	0.44997573E-01
0.08	-0.13073483E+00	0.46533972E-01
0.07	-0.13420624E+00	0.47769587E-01

Table A.6: $g_1(x)$ at $E_{\text{beam}} = 5.1$ GeV

x	$g_1(x)$	Statistical
0.35	-0.10876932E-01	0.38251005E-01
0.33	-0.17921032E-01	0.17171517E-01
0.32	-0.39308652E-01	0.15422063E-01
0.31	-0.25113815E-01	0.15015876E-01
0.29	-0.38317807E-01	0.13653855E-01
0.28	-0.23837000E-01	0.15711963E-01

Table A.6: $g_1(x)$ at $E_{\text{beam}} = 5.1$ GeV

x	$g_1(x)$	Statistical
0.27	-0.32783128E-01	0.24473397E-01
0.26	-0.46943195E-01	0.37591878E-01
0.25	-0.28414562E-01	0.32654881E-01
0.24	-0.72196223E-01	0.34150403E-01
0.23	-0.47591273E-01	0.27213020E-01
0.22	-0.51551163E-01	0.29033868E-01
0.21	-0.42569071E-01	0.28567731E-01
0.20	-0.34861658E-01	0.27691448E-01
0.20	-0.30992478E-01	0.25501471E-01
0.19	-0.35756044E-01	0.23836128E-01
0.18	-0.78248248E-01	0.24240701E-01
0.17	-0.57427771E-01	0.23874903E-01
0.17	-0.72669260E-01	0.27138056E-01
0.16	0.63001132E-02	0.38236555E-01
0.15	-0.71755931E-01	0.40560432E-01
0.15	-0.72652660E-01	0.40890533E-01
0.14	-0.37801217E-01	0.32166842E-01
0.14	-0.27906664E-01	0.29541388E-01
0.13	-0.57806838E-02	0.28385323E-01
0.13	-0.43886282E-01	0.33899467E-01

Table A.7: $g_2(x)$ at $E_{\text{beam}} = 0.86$ GeV

x	$g_2(x)$	Statistical
1.12	0.27885041E-02	0.47925930E-03
0.35	-0.65823947E-03	0.26677263E-02
0.20	0.18484594E-01	0.48397072E-02
0.13	0.11621362E-01	0.94528040E-02
0.09	0.25718626E-01	0.62590532E-01
0.07	0.94635196E-01	0.38580269E-01

Table A.7: $g_2(x)$ at $E_{\text{beam}} = 0.86$ GeV

x	$g_2(x)$	Statistical
0.06	0.22264320E+00	0.81016377E-01
0.04	0.33829698E+00	0.13896564E+00
0.03	0.19557568E+00	0.19038598E+00
0.03	0.31593511E+00	0.31553167E+00
0.02	-0.70127529E+00	0.11809517E+01
0.02	-0.13266039E+01	0.27056563E+01

Table A.8: $g_2(x)$ at $E_{\text{beam}} = 1.7$ GeV

x	$g_2(x)$	Statistical
4.51	0.13113629E-03	0.67125989E-05
1.46	-0.25170215E-02	0.60995331E-03
0.85	-0.47840908E-01	0.34291146E-02
0.59	-0.88774245E-02	0.39000800E-02
0.44	-0.54638605E-02	0.33809291E-02
0.35	0.22773990E-01	0.53295195E-02
0.29	0.55060979E-01	0.80480902E-02
0.24	0.11348634E+00	0.13998950E-01
0.20	0.19289444E+00	0.22120127E-01
0.17	0.17270193E+00	0.29828928E-01
0.15	0.17572418E+00	0.28791560E-01
0.13	0.96148312E-01	0.34437601E-01
0.12	0.95983885E-01	0.39344389E-01
0.10	0.10395623E+00	0.52595701E-01
0.09	0.89846887E-01	0.57348460E-01
0.08	0.33866489E+00	0.84321029E-01
0.07	0.17358233E+00	0.10964624E+00
0.06	0.10261069E+00	0.13286522E+00
0.06	0.93905151E-01	0.13542095E+00
0.05	0.64683771E+00	0.29728234E+00

Table A.8: $g_2(x)$ at $E_{\mathrm{beam}} = 1.7$ GeV

x	$g_2(x)$	Statistical
0.05	0.83249402E+00	0.29097408E+00
0.04	-0.29760832E+00	0.27344880E+00
0.04	-0.24869750E+01	0.54956543E+00
0.03	-0.49600582E+01	0.71932501E+00
0.03	-0.72450256E+01	0.65940708E+00
0.02	-0.93047047E+01	0.61662209E+00

Table A.9: $g_2(x)$ at $E_{\mathrm{beam}} = 2.6$ GeV

x	$g_2(x)$	Statistical
10.22	-0.10347107E-02	0.61112063E-04
3.34	0.35251534E-03	0.18192650E-05
1.96	-0.40775496E-04	0.10988500E-03
1.37	-0.25275792E-02	0.44954079E-03
1.05	-0.21270551E-01	0.15252163E-02
0.84	-0.37918430E-01	0.27365880E-02
0.69	-0.29802185E-01	0.30924613E-02
0.59	-0.46039494E-02	0.36086801E-02
0.51	0.18219635E-01	0.41933530E-02
0.44	0.47052942E-01	0.77798334E-02
0.39	0.58717731E-01	0.11652213E-01
0.35	0.37495442E-01	0.12453332E-01
0.31	0.75240046E-01	0.18154012E-01
0.28	0.10294256E+00	0.19714605E-01
0.26	0.52345145E-01	0.18813258E-01
0.23	0.76889649E-01	0.26884345E-01
0.21	0.70254341E-01	0.30220868E-01
0.19	0.44259496E-01	0.31125495E-01
0.18	0.28168401E-01	0.44181269E-01
0.16	0.73325068E-01	0.52295960E-01

Table A.9: $g_2(x)$ at $E_{\mathrm{beam}} = 2.6$ GeV

x	$g_2(x)$	Statistical
0.15	-0.10655407E+00	0.52053329E-01
0.14	-0.20818665E+01	0.75569667E-01
0.13	-0.47278953E+01	0.85708342E-01
0.12	-0.76890163E+01	0.93827710E-01
0.11	-0.10788750E+02	0.73560975E-01
0.10	-0.13958464E+02	0.90141393E-01
0.09	-0.17440351E+02	0.12539820E+00
0.09	-0.15735399E+02	0.14307803E+00
0.08	0.81296331E+00	0.15095492E+00
0.07	0.24216191E+00	0.18065728E+00
0.07	0.35254613E+00	0.18235725E+00
0.06	-0.19724467E+00	0.31993115E+00
0.06	-0.51721507E+00	0.45744944E+00
0.05	0.38586816E+00	0.34145319E+00
0.05	0.63905513E+00	0.41788423E+00
0.05	-0.48829159E+00	0.53447092E+00
0.04	0.25086136E+01	0.20694494E+01
0.04	-0.81686592E+00	0.63964081E+00
0.03	-0.22445283E+01	0.28045101E+01

Table A.10: $g_2(x)$ at $E_{\mathrm{beam}} = 3.4$ GeV

x	$g_2(x)$	Statistical
1.84	0.29848295E-03	0.17503301E-03
1.48	-0.34626466E-03	0.12407143E-03
1.23	-0.42937514E-02	0.33455272E-03
1.05	-0.20335959E-01	0.77853008E-03
0.91	-0.11331205E+00	0.13307380E-02
0.80	-0.26349830E-01	0.15091615E-02
0.71	-0.10966114E-01	0.22690326E-02

Table A.10: $g_2(x)$ at $E_{\text{beam}} = 3.4$ GeV

x	$g_2(x)$	Statistical
0.64	0.20481190E-01	0.27423869E-02
0.58	0.38339611E-01	0.38444058E-02
0.53	0.50096646E-01	0.58071609E-02
0.48	0.50954200E-01	0.65254192E-02
0.44	0.55072680E-01	0.73112561E-02
0.41	0.66082060E-01	0.81934277E-02
0.38	0.64914674E-01	0.10758860E-01
0.35	0.13039641E+00	0.11625396E-01
0.32	-0.17603824E+01	0.12963668E-01
0.30	-0.68226404E+01	0.14430132E-01
0.28	-0.11640256E+02	0.20093977E-01
0.26	-0.16408232E+02	0.20593785E-01
0.25	-0.20772755E+02	0.22581417E-01
0.23	-0.25280010E+02	0.28784575E-01
0.22	-0.29810057E+02	0.31858865E-01
0.20	-0.23608360E+02	0.33077598E-01
0.19	0.12676399E+01	0.36305796E-01
0.18	0.27158186E-01	0.47217242E-01
0.17	0.15589987E+00	0.60150422E-01
0.16	0.94048403E-01	0.64455770E-01
0.15	0.45180198E-01	0.88895760E-01
0.14	0.10360028E+00	0.13962804E+00
0.13	0.11749584E+00	0.18079364E+00
0.13	0.15545757E+00	0.13835025E+00
0.12	0.22148925E+00	0.88642843E-01
0.11	0.45845095E-01	0.11474291E+00
0.11	-0.12874320E+00	0.27480280E+00
0.10	-0.25832298E+00	0.21276821E+00
0.09	-0.17790152E+00	0.19411911E+00
0.09	0.14818901E+00	0.14897765E+00

Table A.10: $g_2(x)$ at $E_{\mathrm{beam}} = 3.4$ GeV

x	$g_2(x)$	Statistical
0.08	0.12458502E+00	0.23466431E+00
0.08	0.17584492E+00	0.32869774E+00
0.07	0.10173831E+00	0.34428817E+00
0.07	-0.87773368E-01	0.22449318E+00
0.06	0.22429270E+00	0.40544233E+00
0.06	0.11109690E+00	0.46351609E+00
0.06	0.22788687E+00	0.48341268E+00
0.05	0.63306129E+00	0.64937007E+00

Table A.11: $g_2(x)$ at $E_{\mathrm{beam}} = 4.2$ GeV

x	$g_2(x)$	Statistical
1.84	0.29848295E-03	0.17503301E-03
1.48	-0.34626466E-03	0.12407143E-03
1.23	-0.42937514E-02	0.33455272E-03
1.05	-0.20335959E-01	0.77853008E-03
0.91	-0.11331205E+00	0.13307380E-02
0.80	-0.26349830E-01	0.15091615E-02
0.71	-0.10966114E-01	0.22690326E-02
0.64	0.20481190E-01	0.27423869E-02
0.58	0.38339611E-01	0.38444058E-02
0.53	0.50096646E-01	0.58071609E-02
0.48	0.50954200E-01	0.65254192E-02
0.44	0.55072680E-01	0.73112561E-02
0.41	0.66082060E-01	0.81934277E-02
0.38	0.64914674E-01	0.10758860E-01
0.35	0.13039641E+00	0.11625396E-01
0.32	-0.17603824E+01	0.12963668E-01
0.30	-0.68226404E+01	0.14430132E-01
0.28	-0.11640256E+02	0.20093977E-01

Table A.11: $g_2(x)$ at $E_{\mathrm{beam}} = 4.2$ GeV

x	$g_2(x)$	Statistical
0.26	-0.16408232E+02	0.20593785E-01
0.25	-0.20772755E+02	0.22581417E-01
0.23	-0.25280010E+02	0.28784575E-01
0.22	-0.29810057E+02	0.31858865E-01
0.20	-0.23608360E+02	0.33077598E-01
0.19	0.12676399E+01	0.36305796E-01
0.18	0.27158186E-01	0.47217242E-01
0.17	0.15589987E+00	0.60150422E-01
0.16	0.94048403E-01	0.64455770E-01
0.15	0.45180198E-01	0.88895760E-01
0.14	0.10360028E+00	0.13962804E+00
0.13	0.11749584E+00	0.18079364E+00
0.13	0.15545757E+00	0.13835025E+00
0.12	0.22148925E+00	0.88642843E-01
0.11	0.45845095E-01	0.11474291E+00
0.11	-0.12874320E+00	0.27480280E+00
0.10	-0.25832298E+00	0.21276821E+00
0.09	-0.17790152E+00	0.19411911E+00
0.09	0.14818901E+00	0.14897765E+00
0.08	0.12458502E+00	0.23466431E+00
0.08	0.17584492E+00	0.32869774E+00
0.07	0.10173831E+00	0.34428817E+00
0.07	-0.87773368E-01	0.22449318E+00
0.06	0.22429270E+00	0.40544233E+00
0.06	0.11109690E+00	0.46351609E+00
0.06	0.22788687E+00	0.48341268E+00
0.05	0.63306129E+00	0.64937007E+00

Table A.12: $g_2(x)$ at $E_{\text{beam}} = 5.1$ GeV

x	$g_2(x)$	Statistical
0.35	0.52131038E-01	0.91907576E-01
0.33	-0.57930150E-02	0.41470263E-01
0.32	-0.23541455E-02	0.37955854E-01
0.31	0.16747264E-01	0.36695741E-01
0.29	0.27337383E-01	0.35714973E-01
0.28	0.14536730E-01	0.39873265E-01
0.27	0.19663107E+00	0.72203971E-01
0.26	0.19686541E+00	0.11647356E+00
0.25	-0.70491433E-01	0.10067608E+00
0.24	0.15292150E+00	0.10452728E+00
0.23	-0.13596360E+00	0.12561518E+00
0.22	-0.68554848E-01	0.19777824E+00
0.21	-0.99554108E-02	0.29942465E+00
0.20	0.35385232E-01	0.33802202E+00
0.20	0.59309892E-01	0.30401003E+00
0.19	0.63493766E-01	0.19983892E+00
0.18	0.36037505E-01	0.18797620E+00
0.17	0.32597390E+00	0.20682092E+00
0.17	0.25173798E+00	0.20582953E+00
0.16	0.42220491E+00	0.20934789E+00
0.15	0.43642411E+00	0.19858848E+00
0.15	-0.32202285E-01	0.18603705E+00
0.14	0.21568009E+00	0.17659219E+00
0.14	-0.31669974E+00	0.18677635E+00
0.13	0.41004401E+00	0.21848904E+00
0.13	-0.49650133E-01	0.23953831E+00

Table A.13: $g_1(x)$ at $Q^2 = 0.10$ GeV^2

x	$g_1(x)$	Statistical
0.10	-0.11158335E+00	0.33910330E-01
0.15	0.91623388E-01	0.19273477E-01
0.20	0.87445276E-02	0.14562094E-01
0.25	-0.40141199E-01	0.11834145E-01
0.30	-0.73109843E-01	0.12622668E-01
0.35	-0.88818818E-01	0.89337444E-02
0.40	-0.36289845E-01	0.62139235E-02
0.45	-0.59278817E-02	0.46057347E-02
0.50	-0.21221477E-03	0.44207717E-02
0.55	0.94467849E-02	0.37835811E-02
0.60	0.19764334E-01	0.38501890E-02
0.65	0.29139536E-01	0.41699368E-02
0.70	0.35288587E-01	0.53482326E-02
0.75	0.33862803E-01	0.49535735E-02
0.80	0.31187534E-01	0.49312972E-02
0.85	0.29211586E-01	0.55696662E-02
0.90	0.26823286E-01	0.66894284E-02
0.95	0.22984846E-01	0.61996030E-02

Table A.14: $g_1(x)$ at $Q^2 = 0.26$ GeV^2

x	$g_1(x)$	Statistical
0.10	-0.10570808E+00	0.25326915E-01
0.15	0.52386034E+00	0.12479737E-01
0.20	-0.37882370E+00	0.10843997E-01
0.25	0.66024768E+00	0.11966434E-01
0.30	0.50666946E+00	0.93274387E-02
0.35	0.34497440E+00	0.11277024E-01
0.40	0.20483106E+00	0.12257409E-01
0.45	0.46421710E-01	0.96706720E-02

Table A.14: $g_1(x)$ at $Q^2 = 0.26$ GeV^2

x	$g_1(x)$	Statistical
0.50	-0.12514859E-01	0.51027434E-02
0.55	0.56925188E-02	0.38009030E-02
0.60	0.15419142E-01	0.36185225E-02
0.65	0.19628642E-01	0.29490222E-02
0.70	0.20956535E-01	0.35138694E-02
0.75	0.18645603E-01	0.32254371E-02
0.80	0.13134829E-01	0.35591449E-02
0.85	0.87130368E-02	0.41020927E-02
0.90	0.76945447E-02	0.37823445E-02
0.95	0.67869220E-02	0.34091338E-02

Table A.15: $g_1(x)$ at $Q^2 = 0.42$ GeV^2

x	$g_1(x)$	Statistical
0.10	0.13680476E+00	0.12765191E+00
0.15	-0.74600279E-01	0.23415986E-01
0.20	-0.12037601E+00	0.11956813E-01
0.25	-0.65469432E+00	0.86461101E-02
0.30	0.97238129E+00	0.66386112E-02
0.35	0.11716455E+01	0.63631930E-02
0.40	0.13357460E+01	0.76234397E-02
0.45	0.15121013E+01	0.73071662E-02
0.50	0.17252523E+01	0.64880042E-02
0.55	0.20518212E+01	0.38151927E-02
0.60	0.23197465E+01	0.31982264E-02
0.65	0.23596463E+01	0.30912017E-02
0.70	0.12295235E+01	0.25412766E-02
0.75	-0.97585849E-01	0.30892177E-02
0.80	-0.29237071E+00	0.28113280E-02
0.85	-0.19934699E+00	0.37345823E-02

Table A.15: $g_1(x)$ at $Q^2 = 0.42$ GeV^2

x	$g_1(x)$	Statistical
0.90	0.12203064E-01	0.36789952E-02
0.95	0.16542977E-01	0.30200544E-02

Table A.16: $g_1(x)$ at $Q^2 = 0.58$ GeV^2

x	$g_1(x)$	Statistical
0.20	-0.86336493E-01	0.47594175E-01
0.25	-0.19080795E-01	0.33664674E-01
0.30	0.26197352E-02	0.14296498E-01
0.35	0.14267374E+01	0.35996050E-01
0.40	0.17098308E+01	0.17387846E-01
0.45	-0.28271429E+02	0.91032395E-02
0.50	-0.29098772E+02	0.57925927E-02
0.55	-0.30869200E+02	0.52279127E-02
0.60	-0.33662571E+02	0.36466890E-02
0.65	-0.37869530E+02	0.34515772E-02
0.70	-0.45245285E+02	0.29849573E-02
0.75	-0.54063557E+02	0.28785029E-02
0.80	-0.48988483E+02	0.34480547E-02
0.85	-0.37596872E+01	0.35678432E-02
0.90	0.80572739E+01	0.31267202E-02
0.95	-0.67427512E-02	0.35038802E-02

Table A.17: $g_1(x)$ at $Q^2 = 0.74$ GeV^2

x	$g_1(x)$	Statistical
0.05	0.63121833E-01	0.41306160E-01
0.10	-0.77485493E-02	0.45814771E-01
0.15	-0.21547560E+00	0.22742502E-01

Table A.17: $g_1(x)$ at $Q^2 = 0.74$ GeV^2

x	$g_1(x)$	Statistical
0.20	-0.53406775E-01	0.25159264E-01
0.25	-0.77850656E-02	0.99901194E-02
0.30	0.10345538E-01	0.67646303E-02
0.35	0.18542362E-01	0.79092160E-02
0.40	0.52164655E-01	0.65356041E-02
0.45	0.80583312E-01	0.57434482E-02
0.50	0.10205472E+00	0.62014181E-02
0.55	0.10617282E+00	0.63711382E-02
0.60	0.97173735E-01	0.57250606E-02
0.65	0.87161496E-01	0.51632957E-02
0.70	0.77240378E-01	0.47535789E-02
0.75	0.67876227E-01	0.44901352E-02
0.80	0.59203159E-01	0.43141469E-02
0.85	0.51386595E-01	0.42469059E-02
0.90	0.44400983E-01	0.42559928E-02
0.95	0.38186539E-01	0.43122913E-02

Table A.18: $g_1(x)$ at $Q^2 = 0.90$ GeV^2

x	$g_1(x)$	Statistical
0.05	-0.14199643E+00	0.60775027E-01
0.10	0.29183605E+00	0.23046233E-01
0.15	-0.23845188E-01	0.15655419E-01
0.20	-0.34096723E-02	0.13631987E-01
0.25	-0.13730502E+00	0.17146252E-01
0.30	-0.55133384E-01	0.81176423E-02
0.35	-0.79683028E-02	0.63012172E-02
0.40	-0.94402311E-02	0.64572166E-02
0.45	0.21825559E-02	0.52648708E-02
0.50	0.16462233E-01	0.51988554E-02

Table A.18: $g_1(x)$ at $Q^2 = 0.90$ GeV^2

x	$g_1(x)$	Statistical
0.55	0.30430946E-01	0.53742323E-02
0.60	0.41934077E-01	0.71663549E-02
0.65	0.43159720E-01	0.64593698E-02
0.70	0.42208087E-01	0.59206695E-02
0.75	0.40133584E-01	0.60364809E-02
0.80	0.37483141E-01	0.68156514E-02
0.85	0.34600057E-01	0.79451595E-02
0.90	0.30443974E-01	0.74470900E-02
0.95	0.26665734E-01	0.67661600E-02

Table A.19: $g_2(x)$ at $Q^2 = 0.10$ GeV^2

x	$g_2(x)$	Statistical
0.10	0.12194709E+00	0.13832770E+00
0.15	-0.31062260E+01	0.61504032E-01
0.20	0.99042714E-01	0.27027769E-01
0.25	0.10783166E+00	0.17068695E-01
0.30	0.82483746E-01	0.12050298E-01
0.35	0.89692600E-01	0.79599964E-02
0.40	0.49045198E-01	0.49481601E-02
0.45	0.22050608E-01	0.33259396E-02
0.50	0.56787180E-02	0.29660200E-02
0.55	-0.87576769E-02	0.23893828E-02
0.60	-0.16801247E-01	0.22787480E-02
0.65	-0.19467810E-01	0.25289252E-02
0.70	-0.21609116E-01	0.30398797E-02
0.75	-0.31646512E-01	0.26643896E-02
0.80	-0.40825237E-01	0.26116108E-02
0.85	-0.48648432E-01	0.29014924E-02
0.90	-0.53878304E-01	0.33300612E-02

Table A.19: $g_2(x)$ at $Q^2 = 0.10$ GeV^2

x	$g_2(x)$	Statistical
0.95	-0.47613263E-01	0.29236584E-02

Table A.20: $g_2(x)$ at $Q^2 = 0.26$ GeV^2

x	$g_2(x)$	Statistical
0.10	0.16111828E-02	0.14529759E+00
0.15	-0.37826653E+01	0.50831605E-01
0.20	-0.95934515E+01	0.26241340E-01
0.25	0.33655887E+01	0.20694267E-01
0.30	0.22607601E+01	0.12930835E-01
0.35	0.13544909E+01	0.11195152E-01
0.40	0.74159914E+00	0.11143207E-01
0.45	0.25076681E+00	0.75538391E-02
0.50	0.20902367E-01	0.38793965E-02
0.55	0.38774167E-02	0.29397334E-02
0.60	-0.93250489E-02	0.30979468E-02
0.65	-0.21647885E-01	0.23475040E-02
0.70	-0.29490806E-01	0.26431421E-02
0.75	-0.32160521E-01	0.21674030E-02
0.80	-0.36253773E-01	0.21135961E-02
0.85	-0.38868431E-01	0.22891257E-02
0.90	-0.40171839E-01	0.20224652E-02
0.95	-0.37741497E-01	0.17327776E-02

Table A.21: $g_2(x)$ at $Q^2 = 0.42$ GeV^2

x	$g_2(x)$	Statistical
0.10	-0.13044302E+00	0.51859683E+00
0.15	0.14145450E+00	0.89858763E-01

Table A.21: $g_2(x)$ at $Q^2 = 0.42$ GeV^2

x	$g_2(x)$	Statistical
0.20	-0.17344654E+02	0.27359808E-01
0.25	-0.11961409E+02	0.16797574E-01
0.30	0.46070409E+01	0.10490685E-01
0.35	0.45887179E+01	0.83883340E-02
0.40	0.43412995E+01	0.75572166E-02
0.45	0.41858869E+01	0.65618176E-02
0.50	0.41406817E+01	0.50992812E-02
0.55	0.43159342E+01	0.28813274E-02
0.60	0.43877325E+01	0.24303959E-02
0.65	0.40861335E+01	0.26875539E-02
0.70	0.19300663E+01	0.21031226E-02
0.75	-0.22757466E+00	0.24280045E-02
0.80	-0.49474898E+00	0.19682252E-02
0.85	-0.34057862E+00	0.23155320E-02
0.90	-0.48821401E-01	0.21489353E-02
0.95	-0.31104621E-01	0.16467809E-02

Table A.22: $g_2(x)$ at $Q^2 = 0.58$ GeV^2

x	$g_2(x)$	Statistical
0.20	-0.57851095E-01	0.30260411E+00
0.25	0.99303648E-01	0.10016484E+00
0.30	-0.31412456E-01	0.34675408E-01
0.35	0.44941292E+02	0.76308027E-01
0.40	0.17895435E+02	0.30597277E-01
0.45	-0.12956802E+03	0.13536014E-01
0.50	-0.11001259E+03	0.74252598E-02
0.55	-0.99715714E+02	0.54675457E-02
0.60	-0.95487503E+02	0.35912110E-02
0.65	-0.96324020E+02	0.30817136E-02

Table A.22: $g_2(x)$ at $Q^2 = 0.58$ GeV^2

x	$g_2(x)$	Statistical
0.70	-0.10476864E+03	0.24369508E-02
0.75	-0.11589037E+03	0.23065964E-02
0.80	-0.98393379E+02	0.28031957E-02
0.85	-0.65585346E+01	0.27594806E-02
0.90	0.14679336E+02	0.22682690E-02
0.95	-0.21313158E+00	0.24980090E-02

Table A.23: $g_2(x)$ at $Q^2 = 0.74$ GeV^2

x	$g_2(x)$	Statistical
0.05	-0.13976388E+00	0.20013879E+00
0.10	0.75830728E-01	0.13706098E+00
0.15	0.17025550E+00	0.33826094E-01
0.20	0.37782088E-01	0.28502582E-01
0.25	0.12376348E-01	0.90431813E-02
0.30	0.93531236E-02	0.47495365E-02
0.35	0.11848436E-01	0.38457653E-02
0.40	0.65943873E-02	0.29525224E-02
0.45	0.79393742E-03	0.26272102E-02
0.50	-0.45842249E-02	0.27438232E-02
0.55	-0.58788061E-02	0.25815379E-02
0.60	-0.46865167E-02	0.21555198E-02
0.65	-0.34723934E-02	0.18461179E-02
0.70	-0.23865860E-02	0.16425387E-02
0.75	-0.12635161E-02	0.15110556E-02
0.80	0.21950458E-03	0.14135010E-02
0.85	0.13833352E-02	0.13489298E-02
0.90	0.22817883E-02	0.13027670E-02
0.95	0.29650258E-02	0.12658676E-02

Table A.24: $g_2(x)$ at $Q^2 = 0.90$ GeV^2

x	$g_2(x)$	Statistical
0.05	0.18815590E+00	0.50781012E+00
0.10	-0.73557359E+00	0.88587388E-01
0.15	0.88600405E-01	0.32265611E-01
0.20	0.15494074E+00	0.19301601E-01
0.25	0.15451050E+00	0.15492702E-01
0.30	0.68237647E-01	0.72828676E-02
0.35	0.30764911E-01	0.47556204E-02
0.40	0.11073907E-01	0.40764292E-02
0.45	-0.39705583E-02	0.30529476E-02
0.50	-0.92766648E-02	0.28173872E-02
0.55	-0.10068273E-01	0.30287791E-02
0.60	-0.10345665E-01	0.38474146E-02
0.65	-0.21109315E-01	0.32337641E-02
0.70	-0.30541271E-01	0.28591915E-02
0.75	-0.38111959E-01	0.28577512E-02
0.80	-0.43877102E-01	0.31086362E-02
0.85	-0.47907863E-01	0.34308776E-02
0.90	-0.42536244E-01	0.30367081E-02
0.95	-0.36688864E-01	0.26140495E-02

Table A.25: σ'_{TT} *vs.* W at $E_{\text{beam}} = 0.86$ GeV

W (MeV)	σ'_{TT} (μb)	Statistical
935.30	0.00000000E+00	0.00000000E+00
985.77	0.23872638E+03	0.58040337E+02
1033.79	-0.51506783E+02	0.19571472E+02
1079.66	-0.12003312E+02	0.11697751E+02
1123.67	-0.41153759E+02	0.35602165E+02
1166.02	-0.85515076E+02	0.13989582E+02
1206.88	-0.11695153E+03	0.15533202E+02
1246.40	-0.81075706E+02	0.17916586E+02
1284.71	-0.40148804E+02	0.16091085E+02
1321.91	-0.17325794E+02	0.16250257E+02
1358.09	-0.86456604E+01	0.39949593E+02
1393.33	-0.34033348E+02	0.65946007E+02

Table A.26: σ'_{TT} *vs.* W at $E_{\text{beam}} = 1.7$ GeV

W (MeV)	σ'_{TT} (μb)	Statistical
846.01	0.00000000E+00	0.00000000E+00
903.22	0.00000000E+00	0.00000000E+00
957.01	0.40638672E+04	0.27370477E+03
1007.94	0.16117961E+03	0.41239220E+02
1056.42	0.22450829E+02	0.12935129E+02
1102.77	-0.46995949E+02	0.98287964E+01
1147.25	-0.56235802E+02	0.80386019E+01
1190.06	-0.10546619E+03	0.87497435E+01
1231.39	-0.10960032E+03	0.10481890E+02
1271.38	-0.39343872E+02	0.99150219E+01
1310.14	-0.20133341E+02	0.59196520E+01
1347.80	-0.64882026E+01	0.53764439E+01
1384.42	-0.81688213E+01	0.43842978E+01
1420.11	-0.12585336E+02	0.49459610E+01

Table A.26: σ'_{TT} *vs.* W at $E_{\rm beam} = 1.7$ GeV

W (MeV)	σ'_{TT} (μb)	Statistical
1454.92	0.54177108E+01	0.56496258E+01
1488.91	-0.13339189E+02	0.48546782E+01
1522.15	-0.47516394E+01	0.49905319E+01
1554.67	-0.11339153E+02	0.62061977E+01
1586.53	-0.14793873E+01	0.56571012E+01
1617.76	-0.97990427E+01	0.10354173E+02
1648.40	-0.17177513E+02	0.65067768E+01
1678.48	0.91022625E+01	0.52986503E+01
1708.03	0.71789955E+02	0.21749601E+02
1737.08	0.13083112E+03	0.29167950E+02
1765.65	0.17838147E+03	0.22186171E+02
1793.77	0.21737479E+03	0.31750927E+01

Table A.27: σ'_{TT} *vs.* W at $E_{\rm beam} = 2.6$ GeV

W (MeV)	σ'_{TT} (μb)	Statistical
669.02	0.00000000E+00	0.00000000E+00
742.16	0.00000000E+00	0.00000000E+00
808.71	0.00000000E+00	0.00000000E+00
870.19	0.00000000E+00	0.00000000E+00
927.60	0.00000000E+00	0.00000000E+00
981.66	0.58845844E+03	0.42722424E+02
1032.89	0.16803969E+03	0.14988063E+02
1081.70	0.21362612E+02	0.84011898E+01
1128.40	-0.28664665E+02	0.60918913E+01
1173.25	-0.57396259E+02	0.75078468E+01
1216.44	-0.50613792E+02	0.76114731E+01
1258.15	-0.39880058E+02	0.61663799E+01
1298.52	-0.36283302E+02	0.65777822E+01
1337.67	-0.34385960E+02	0.49771271E+01

Table A.27: σ'_{TT} *vs.* W at $E_{\mathrm{beam}} = 2.6$ GeV

W (MeV)	σ'_{TT} (μb)	Statistical
1375.71	-0.17039873E+02	0.37420244E+01
1412.72	-0.83510008E+01	0.41390100E+01
1448.79	-0.58426433E+01	0.38519399E+01
1483.98	-0.56841964E+00	0.33018134E+01
1518.36	-0.25546432E+01	0.38618681E+01
1551.98	-0.18014046E+01	0.35818310E+01
1584.88	0.63375568E+01	0.30369565E+01
1617.11	0.95541229E+02	0.34748108E+01
1648.72	0.19172987E+03	0.31008217E+01
1679.73	0.26702914E+03	0.32705314E+01
1710.17	0.33400858E+03	0.25785139E+01
1740.09	0.38192947E+03	0.26843841E+01
1769.50	0.42971164E+03	0.25357070E+01
1798.42	0.33322974E+03	0.25845962E+01
1826.89	-0.20523111E+02	0.25033047E+01
1854.93	-0.34975870E+01	0.26249590E+01
1882.54	-0.59243984E+01	0.25464399E+01
1909.76	-0.43723145E+01	0.28281002E+01
1936.59	-0.43302326E+01	0.27573090E+01
1963.06	-0.72732735E+01	0.22794085E+01
1989.17	-0.64762383E+01	0.29798372E+01
2014.95	-0.91607323E+01	0.38520107E+01
2040.40	0.70946126E+01	0.88742371E+01
2065.54	-0.10084033E+02	0.33070204E+01
2090.37	-0.59392753E+01	0.11871027E+02

Table A.28: σ'_{TT} *vs.* W at $E_{\mathrm{beam}} = 3.4$ GeV

W (MeV)	σ'_{TT} (μb)	Statistical
725.29	0.00000000E+00	0.00000000E+00

Table A.28: σ'_{TT} *vs.* W at $E_{\mathrm{beam}} = 3.4$ GeV

W (MeV)	σ'_{TT} (μb)	Statistical
795.09	0.00000000E+00	0.00000000E+00
859.24	0.00000000E+00	0.00000000E+00
918.92	0.00000000E+00	0.00000000E+00
974.96	0.16423141E+04	0.18086731E+02
1027.95	0.11481177E+03	0.64880748E+01
1078.33	0.25211567E+02	0.51368699E+01
1126.47	-0.30182846E+02	0.39203565E+01
1172.63	-0.40859558E+02	0.36994786E+01
1217.04	-0.41318871E+02	0.39545796E+01
1259.88	-0.34874180E+02	0.32229073E+01
1301.32	-0.22792971E+02	0.26629767E+01
1341.48	-0.20222073E+02	0.23579597E+01
1380.47	-0.11609659E+02	0.24799991E+01
1418.38	-0.14610475E+02	0.21773667E+01
1455.31	0.16673625E+03	0.20347669E+01
1491.33	0.53138525E+03	0.19729800E+01
1526.50	0.77244006E+03	0.22643285E+01
1560.87	0.92287390E+03	0.19633154E+01
1594.51	0.10029381E+04	0.18332040E+01
1627.44	0.10580249E+04	0.20444658E+01
1659.73	0.10878901E+04	0.20132287E+01
1691.40	0.74621735E+03	0.19114623E+01
1722.48	-0.28635044E+02	0.18479316E+01
1753.02	-0.19229591E+01	0.20126452E+01
1783.03	-0.56074438E+01	0.17863615E+01
1812.55	-0.38219185E+01	0.17206304E+01
1841.59	-0.44121585E+01	0.21510484E+01
1870.18	-0.20560553E+02	0.14024057E+02
1898.34	-0.12980453E+02	0.48807950E+01
1926.09	-0.82439232E+01	0.26929195E+01

Table A.28: σ'_{TT} *vs.* W at $E_{\text{beam}} = 3.4$ GeV

W (MeV)	σ'_{TT} (μb)	Statistical
1953.45	-0.68931818E+01	0.15421171E+01
1980.43	-0.65441875E+01	0.18537123E+01
2007.04	-0.12286748E+02	0.44809809E+01
2033.31	-0.56621461E+01	0.27235620E+01
2059.24	-0.35772011E+01	0.22172558E+01
2084.85	-0.60161457E+01	0.15869985E+01
2110.15	-0.68256893E+01	0.23201444E+01
2135.15	-0.74445133E+01	0.28795536E+01
2159.86	-0.69192796E+01	0.27498357E+01
2184.29	-0.50861406E+01	0.16387496E+01
2208.45	-0.52798953E+01	0.27254982E+01
2232.34	-0.36576624E+01	0.22489214E+01
2255.99	-0.35621371E+01	0.20636330E+01
2279.39	-0.38600247E+01	0.24866321E+01

Table A.29: σ'_{TT} *vs.* W at $E_{\text{beam}} = 4.2$ GeV

W (MeV)	σ'_{TT} (μb)	Statistical
781.89	0.00000000E+00	0.00000000E+00
848.88	0.00000000E+00	0.00000000E+00
910.95	0.00000000E+00	0.00000000E+00
969.06	0.33305702E+02	0.30901402E+02
1023.88	-0.30003561E+05	0.13140122E+02
1075.90	0.25850167E+06	0.62946572E+01
1125.53	0.12826684E+06	0.25537138E+01
1173.05	0.68435883E+05	0.18545702E+01
1218.73	0.42741395E+05	0.20131516E+01
1262.75	0.29155834E+05	0.18945949E+01
1305.29	0.21110795E+05	0.21555500E+01
1346.49	0.16033922E+05	0.19566722E+01

Table A.29: σ'_{TT} *vs.* W at $E_{\mathrm{beam}} = 4.2$ GeV

W (MeV)	σ'_{TT} (μb)	Statistical
1386.46	0.12582608E+05	0.17186161E+01
1425.31	0.10180604E+05	0.14431522E+01
1463.13	0.83677607E+04	0.13112220E+01
1500.00	0.56980332E+04	0.14445028E+01
1535.98	-0.19754628E+03	0.14573374E+01
1571.14	-0.24642427E+01	0.14214426E+01
1605.53	-0.39629109E+01	0.12263510E+01
1639.20	-0.10454947E+01	0.12600607E+01
1672.19	-0.22424088E+01	0.14865228E+01
1704.54	-0.15933988E+01	0.15961498E+01
1736.29	0.40521827E+00	0.14933943E+01
1767.47	-0.25750408E+00	0.13623844E+01
1798.10	0.29280770E+00	0.16400646E+01
1828.23	-0.31437540E+01	0.16900610E+01
1857.87	-0.33141983E+01	0.16232817E+01
1887.04	-0.39910483E+01	0.14678764E+01
1915.76	-0.29133797E+01	0.18222896E+01
1944.07	-0.65906911E+01	0.32124660E+01
1971.96	0.29129739E+01	0.40505409E+01
1999.47	0.58340383E+01	0.50280604E+01
2026.60	0.25919595E+01	0.34879522E+01
2053.38	-0.46365991E+01	0.15199368E+01
2079.81	-0.57374058E+01	0.12798226E+01
2105.91	-0.45197983E+01	0.16373482E+01
2131.69	-0.42621431E+01	0.33028479E+01
2157.16	-0.11484808E+01	0.55676789E+01
2182.33	-0.54382908E+00	0.30194767E+01
2207.22	-0.44589071E+01	0.14911675E+01
2231.83	-0.32495971E+01	0.13601984E+01
2256.17	0.17455764E+00	0.16622009E+01

Table A.29: σ'_{TT} *vs.* W at $E_{\text{beam}} = 4.2$ GeV

W (MeV)	σ'_{TT} (μb)	Statistical
2280.25	-0.82317406E+00	0.31232882E+01
2304.08	0.12863067E+02	0.77130637E+01
2327.67	0.52200379E+01	0.72459517E+01
2351.02	-0.68557596E+00	0.84128628E+01
2374.14	-0.32480986E+01	0.60836191E+01
2397.03	-0.29474616E+01	0.21072907E+01
2419.71	-0.57322569E+01	0.21256075E+01
2442.18	-0.57593422E+01	0.21294460E+01

Table A.30: σ'_{TT} *vs.* W at $E_{\text{beam}} = 5.1$ GeV

W (MeV)	σ'_{TT} (μb)	Statistical
1765.07	-0.29578459E+01	0.47500529E+01
1796.58	-0.15268990E+01	0.19875954E+01
1827.54	-0.35153534E+01	0.16763963E+01
1857.99	-0.26131589E+01	0.15307620E+01
1887.95	-0.38210886E+01	0.13279629E+01
1917.44	-0.22077000E+01	0.14373534E+01
1946.48	-0.61478081E+01	0.21728075E+01
1975.10	-0.67587619E+01	0.31911206E+01
2003.31	-0.97094178E+00	0.26340632E+01
2031.13	-0.70761366E+01	0.26248944E+01
2058.57	-0.14885625E+01	0.21282835E+01
2085.65	-0.25550830E+01	0.23797996E+01
2112.38	-0.25611489E+01	0.26111257E+01
2138.78	-0.24483323E+01	0.25379467E+01
2164.85	-0.23355691E+01	0.21450121E+01
2190.62	-0.25456409E+01	0.16540686E+01
2216.09	-0.46114674E+01	0.15689034E+01
2241.26	-0.52678785E+01	0.15079292E+01

Table A.30: σ'_{TT} *vs.* W at $E_{\text{beam}} = 5.1$ GeV

W (MeV)	σ'_{TT} (μb)	Statistical
2266.16	-0.53606730E+01	0.15992177E+01
2290.79	-0.20403736E+01	0.20963972E+01
2315.15	-0.58384333E+01	0.21389573E+01
2339.26	-0.33935263E+01	0.20863252E+01
2363.13	-0.27438452E+01	0.16048216E+01
2386.76	-0.22350153E-01	0.14392922E+01
2410.15	-0.17873483E+01	0.13541114E+01
2433.32	-0.17810215E+01	0.15661767E+01

Table A.31: σ'_{TT} *vs.* ν at $Q^2 = 0.10$ GeV^2

ν (MeV)	σ'_{TT} (μb)	Statistical
25.00	0.00000000E+00	0.00000000E+00
75.00	0.23872638E+03	0.58040337E+02
125.00	-0.51506783E+02	0.19571472E+02
175.00	-0.12003312E+02	0.11697751E+02
225.00	-0.41153759E+02	0.35602165E+02
275.00	-0.85515076E+02	0.13989582E+02
325.00	-0.11695153E+03	0.15533202E+02
375.00	-0.81075706E+02	0.17916586E+02
425.00	-0.40148804E+02	0.16091085E+02
475.00	-0.17325794E+02	0.16250257E+02
525.00	-0.86456604E+01	0.39949593E+02
575.00	-0.34033348E+02	0.65946007E+02

Table A.32: σ'_{TT} *vs.* ν at $Q^2 = 0.26$ GeV^2

ν (MeV)	σ'_{TT} (μb)	Statistical
25.00	0.00000000E+00	0.00000000E+00

Table A.32: σ'_{TT} *vs.* ν at $Q^2 = 0.26$ GeV^2

ν (MeV)	σ'_{TT} (μb)	Statistical
75.00	0.00000000E+00	0.00000000E+00
125.00	0.40638672E+04	0.27370477E+03
175.00	0.16117961E+03	0.41239220E+02
225.00	0.22450829E+02	0.12935129E+02
275.00	-0.46995949E+02	0.98287964E+01
325.00	-0.56235802E+02	0.80386019E+01
375.00	-0.10546619E+03	0.87497435E+01
425.00	-0.10960032E+03	0.10481890E+02
475.00	-0.39343872E+02	0.99150219E+01
525.00	-0.20133341E+02	0.59196520E+01
575.00	-0.64882026E+01	0.53764439E+01
625.00	-0.81688213E+01	0.43842978E+01
675.00	-0.12585336E+02	0.49459610E+01
725.00	0.54177108E+01	0.56496258E+01
775.00	-0.13339189E+02	0.48546782E+01
825.00	-0.47516394E+01	0.49905319E+01
875.00	-0.11339153E+02	0.62061977E+01
925.00	-0.14793873E+01	0.56571012E+01
975.00	-0.97990427E+01	0.10354173E+02
1025.00	-0.17177513E+02	0.65067768E+01
1075.00	0.91022625E+01	0.52986503E+01
1125.00	0.71789955E+02	0.21749601E+02
1175.00	0.13083112E+03	0.29167950E+02
1225.00	0.17838147E+03	0.22186171E+02
1275.00	0.21737479E+03	0.31750927E+01

Table A.33: σ'_{TT} *vs.* ν at $Q^2 = 0.42$ GeV^2

ν (MeV)	σ'_{TT} (μb)	Statistical
25.00	0.00000000E+00	0.00000000E+00

Table A.33: σ'_{TT} *vs.* ν at $Q^2 = 0.42$ GeV^2

ν (MeV)	σ'_{TT} (μb)	Statistical
75.00	0.00000000E+00	0.00000000E+00
125.00	0.00000000E+00	0.00000000E+00
175.00	0.00000000E+00	0.00000000E+00
225.00	0.00000000E+00	0.00000000E+00
275.00	0.58845844E+03	0.42722424E+02
325.00	0.16803969E+03	0.14988063E+02
375.00	0.21362612E+02	0.84011898E+01
425.00	-0.28664665E+02	0.60918913E+01
475.00	-0.57396259E+02	0.75078468E+01
525.00	-0.50613792E+02	0.76114731E+01
575.00	-0.39880058E+02	0.61663799E+01
625.00	-0.36283302E+02	0.65777822E+01
675.00	-0.34385960E+02	0.49771271E+01
725.00	-0.17039873E+02	0.37420244E+01
775.00	-0.83510008E+01	0.41390100E+01
825.00	-0.58426433E+01	0.38519399E+01
875.00	-0.56841964E+00	0.33018134E+01
925.00	-0.25546432E+01	0.38618681E+01
975.00	-0.18014046E+01	0.35818310E+01
1025.00	0.63375568E+01	0.30369565E+01
1075.00	0.95541229E+02	0.34748108E+01
1125.00	0.19172987E+03	0.31008217E+01
1175.00	0.26702914E+03	0.32705314E+01
1225.00	0.33400858E+03	0.25785139E+01
1275.00	0.38192947E+03	0.26843841E+01
1325.00	0.42971164E+03	0.25357070E+01
1375.00	0.33322974E+03	0.25845962E+01
1425.00	-0.20523111E+02	0.25033047E+01
1475.00	-0.34975870E+01	0.26249590E+01
1525.00	-0.59243984E+01	0.25464399E+01

Table A.33: σ'_{TT} *vs.* ν at $Q^2 = 0.42$ GeV^2

ν (MeV)	σ'_{TT} (μb)	Statistical
1575.00	-0.43723145E+01	0.28281002E+01
1625.00	-0.43302326E+01	0.27573090E+01
1675.00	-0.72732735E+01	0.22794085E+01
1725.00	-0.64762383E+01	0.29798372E+01
1775.00	-0.91607323E+01	0.38520107E+01
1825.00	0.70946126E+01	0.88742371E+01
1875.00	-0.10084033E+02	0.33070204E+01
1925.00	-0.59392753E+01	0.11871027E+02

Table A.34: σ'_{TT} *vs.* ν at $Q^2 = 0.58$ GeV^2

ν (MeV)	σ'_{TT} (μb)	Statistical
225.00	0.00000000E+00	0.00000000E+00
275.00	0.00000000E+00	0.00000000E+00
325.00	0.00000000E+00	0.00000000E+00
375.00	0.00000000E+00	0.00000000E+00
425.00	0.16423141E+04	0.18086731E+02
475.00	0.11481177E+03	0.64880748E+01
525.00	0.25211567E+02	0.51368699E+01
575.00	-0.30182846E+02	0.39203565E+01
625.00	-0.40859558E+02	0.36994786E+01
675.00	-0.41318871E+02	0.39545796E+01
725.00	-0.34874180E+02	0.32229073E+01
775.00	-0.22792971E+02	0.26629767E+01
825.00	-0.20222073E+02	0.23579597E+01
875.00	-0.11609659E+02	0.24799991E+01
925.00	-0.14610475E+02	0.21773667E+01
975.00	0.16673625E+03	0.20347669E+01
1025.00	0.53138525E+03	0.19729800E+01
1075.00	0.77244006E+03	0.22643285E+01

Table A.34: σ'_{TT} *vs.* ν at $Q^2 = 0.58$ GeV^2

ν (MeV)	σ'_{TT} (μb)	Statistical
1125.00	0.92287390E+03	0.19633154E+01
1175.00	0.10029381E+04	0.18332040E+01
1225.00	0.10580249E+04	0.20444658E+01
1275.00	0.10878901E+04	0.20132287E+01
1325.00	0.74621735E+03	0.19114623E+01
1375.00	-0.28635044E+02	0.18479316E+01
1425.00	-0.19229591E+01	0.20126452E+01
1475.00	-0.56074438E+01	0.17863615E+01
1525.00	-0.38219185E+01	0.17206304E+01
1575.00	-0.44121585E+01	0.21510484E+01
1625.00	-0.20560553E+02	0.14024057E+02
1675.00	-0.12980453E+02	0.48807950E+01
1725.00	-0.82439232E+01	0.26929195E+01
1775.00	-0.68931818E+01	0.15421171E+01
1825.00	-0.65441875E+01	0.18537123E+01
1875.00	-0.12286748E+02	0.44809809E+01
1925.00	-0.56621461E+01	0.27235620E+01
1975.00	-0.35772011E+01	0.22172558E+01
2025.00	-0.60161457E+01	0.15869985E+01
2075.00	-0.68256893E+01	0.23201444E+01
2125.00	-0.74445133E+01	0.28795536E+01
2175.00	-0.69192796E+01	0.27498357E+01
2225.00	-0.50861406E+01	0.16387496E+01
2275.00	-0.52798953E+01	0.27254982E+01
2325.00	-0.36576624E+01	0.22489214E+01
2375.00	-0.35621371E+01	0.20636330E+01
2425.00	-0.38600247E+01	0.24866321E+01

Table A.35: σ'_{TT} *vs.* ν at $Q^2 = 0.74$ GeV^2

ν (MeV)	σ'_{TT} (μb)	Statistical
475.00	0.00000000E+00	0.00000000E+00
525.00	0.00000000E+00	0.00000000E+00
575.00	0.00000000E+00	0.00000000E+00
625.00	0.33305702E+02	0.30901402E+02
675.00	-0.30003561E+05	0.13140122E+02
725.00	0.25850167E+06	0.62946572E+01
775.00	0.12826684E+06	0.25537138E+01
825.00	0.68435883E+05	0.18545702E+01
875.00	0.42741395E+05	0.20131516E+01
925.00	0.29155834E+05	0.18945949E+01
975.00	0.21110795E+05	0.21555500E+01
1025.00	0.16033922E+05	0.19566722E+01
1075.00	0.12582608E+05	0.17186161E+01
1125.00	0.10180604E+05	0.14431522E+01
1175.00	0.83677607E+04	0.13112220E+01
1225.00	0.56980332E+04	0.14445028E+01
1275.00	-0.19754628E+03	0.14573374E+01
1325.00	-0.24642427E+01	0.14214426E+01
1375.00	-0.39629109E+01	0.12263510E+01
1425.00	-0.10454947E+01	0.12600607E+01
1475.00	-0.22424088E+01	0.14865228E+01
1525.00	-0.15933988E+01	0.15961498E+01
1575.00	0.40521827E+00	0.14933943E+01
1625.00	-0.25750408E+00	0.13623844E+01
1675.00	0.29280770E+00	0.16400646E+01
1725.00	-0.31437540E+01	0.16900610E+01
1775.00	-0.33141983E+01	0.16232817E+01
1825.00	-0.39910483E+01	0.14678764E+01
1875.00	-0.29133797E+01	0.18222896E+01
1925.00	-0.65906911E+01	0.32124660E+01

Table A.35: σ'_{TT} *vs.* ν at $Q^2 = 0.74$ GeV^2

ν (MeV)	σ'_{TT} (μb)	Statistical
1975.00	0.29129739E+01	0.40505409E+01
2025.00	0.58340383E+01	0.50280604E+01
2075.00	0.25919595E+01	0.34879522E+01
2125.00	-0.46365991E+01	0.15199368E+01
2175.00	-0.57374058E+01	0.12798226E+01
2225.00	-0.45197983E+01	0.16373482E+01
2275.00	-0.42621431E+01	0.33028479E+01
2325.00	-0.11484808E+01	0.55676789E+01
2375.00	-0.54382908E+00	0.30194767E+01
2425.00	-0.44589071E+01	0.14911675E+01
2475.00	-0.32495971E+01	0.13601984E+01
2525.00	0.17455764E+00	0.16622009E+01
2575.00	-0.82317406E+00	0.31232882E+01
2625.00	0.12863067E+02	0.77130637E+01
2675.00	0.52200379E+01	0.72459517E+01
2725.00	-0.68557596E+00	0.84128628E+01
2775.00	-0.32480986E+01	0.60836191E+01
2825.00	-0.29474616E+01	0.21072907E+01
2875.00	-0.57322569E+01	0.21256075E+01
2925.00	-0.57593422E+01	0.21294460E+01

Table A.36: σ'_{TT} *vs.* ν at $Q^2 = 0.90$ GeV^2

ν (MeV)	σ'_{TT} (μb)	Statistical
1825.00	-0.29578459E+01	0.47500529E+01
1875.00	-0.15268990E+01	0.19875954E+01
1925.00	-0.35153534E+01	0.16763963E+01
1975.00	-0.26131589E+01	0.15307620E+01
2025.00	-0.38210886E+01	0.13279629E+01
2075.00	-0.22077000E+01	0.14373534E+01

Table A.36: σ'_{TT} *vs.* ν at $Q^2 = 0.90$ GeV^2

ν (MeV)	σ'_{TT} (μb)	Statistical
2125.00	-0.61478081E+01	0.21728075E+01
2175.00	-0.67587619E+01	0.31911206E+01
2225.00	-0.97094178E+00	0.26340632E+01
2275.00	-0.70761366E+01	0.26248944E+01
2325.00	-0.14885625E+01	0.21282835E+01
2375.00	-0.25550830E+01	0.23797996E+01
2425.00	-0.25611489E+01	0.26111257E+01
2475.00	-0.24483323E+01	0.25379467E+01
2525.00	-0.23355691E+01	0.21450121E+01
2575.00	-0.25456409E+01	0.16540686E+01
2625.00	-0.46114674E+01	0.15689034E+01
2675.00	-0.52678785E+01	0.15079292E+01
2725.00	-0.53606730E+01	0.15992177E+01
2775.00	-0.20403736E+01	0.20963972E+01
2825.00	-0.58384333E+01	0.21389573E+01
2875.00	-0.33935263E+01	0.20863252E+01
2925.00	-0.27438452E+01	0.16048216E+01
2975.00	-0.22350153E-01	0.14392922E+01
3025.00	-0.17873483E+01	0.13541114E+01
3075.00	-0.17810215E+01	0.15661767E+01

BIBLIOGRAPHY

[1] A. Amarian *et al.*, *Phys. Rev. Lett.* **89**, 242301 (2002).

[2] M.E. Peskin and D.V. Schroeder, *An Introduction to Quantum Field Theory*, Addison-Wesley Publishing Company, Reading, Massachusetts, 1995.

[3] F. Halzen and A.D. Martin, *Quarks & Leptons: An Introductory Course in Modern Particle Physics*, John Wiley & Sons, New York, 1984.

[4] W. Greiner and A. Schäfer, *Quantum Chromodynamics*, Springer-Verlag, Berlin, 1994.

[5] L.N. Hand, *Phys. Rev.* **129**, 1834 (1963).

[6] F.J. Gilman, *Phys. Rev.* **167**, 1365 (1968).

[7] J.D. Bjorken, *Phys. Rev.* **148**, 1467 (1966); J.D. Bjorken, *Phys. Rev. D* **1**, 1376 (1971); J.D. Bjorken and E.A. Paschos, *Phys. Rev. D* **1**, 3151 (1970).

[8] Particle Data Group, R.M. Barnett *et al.*, *Phys. Rev. D* **54**, 1 (1996); http://pdg.lbl.gov/.

[9] M. Gell-Mann, *Phys. Rev.* **125**, 1062 (1962); R. Feynman, M. Gell-Mann, G. Zweig, *Phys. Rev. Letters* **13**, 678 (1964).

[10] E. Hughes and R. Voss, *Annu. Rev. Nucl. Part. Sci.* **49**, 303-339 (1999).

[11] SMC, B. Adeva *et al.*, *Phys. Rev. D* **58**, 112002 (1998).

[12] E154 Collaboration, K. Abe *et al.*, *Phys. Lett. B* **405**, 180 (1997).

[13] S.A. Larin and J.A.M. Vermaseren, *Phys. Lett. B* **259**, 345 (1991).

[14] A.L. Kataev and V.V. Starshenko, CERN-TH-7190/94 (1994); hep-ph/9405294.

[15] I. Hinchliffe and A.V. Manohar, *Annu. Rev. Nucl. Part. Sci.* **50**, 643-678 (2000); hep-ph/0004186.

[16] S.B. Gerasimov, *Yad. Fiz.* **2**, 839 (1965) [*Sov. J. Nucl. Phys.* **2**, 589 (1966)]; S.D. Drell and A.C. Hearn, *Phys. Rev. Lett.* **16**, 908 (1966).

[17] R. Pantförder, *Ph.D. Thesis*, Universität Bonn, 1998 (unpublished); hep-ph/9805434.

[18] M. Gell-Mann, M.L. Goldberger, and W. Thirring, *Phys. Rev.* **95**, 1612 (1954).

[19] F.E. Low, *Phys. Rev.* **96**, 1428 (1954); M. Gell-Mann and M.L. Goldberger, *Phys. Rev.* **96**, 1433 (1954).

[20] D. Drechsel, *Prog. Part. Nucl. Phys.* **34**, 181-200 (1995), nucl-th/9411034.

[21] D. Drechsel, in *Hadronic Structure*, edited by J.L. Goity, World Scientific, Singapore, 2001.

[22] A.M. Baldin, *Nucl. Phys.* **18**, 310 (1960).

[23] I. Karliner, *Phys. Rev. D* **7**, 2717 (1973).

[24] R.L. Walker, *Phys. Rev.* **182**, 1729 (1969).

[25] K.M. Watson, *Phys. Rev.* **85**, 852 (1952).

[26] D. Drechsel, S.S. Kamalov, and L. Tiator, *Phys. Rev. D* **63**, 114010 (2001); hep-ph/0008306.

[27] D. Drechsel *et al.*, *Nucl. Phys. A* **645**, 145-174 (1999); nucl-th/9807001; MKPH-T-98-10; MAID, An Interactive Program for Pion Electroproduction; http://www.kph.uni-mainz.de/MAID/.

[28] J.F. Donoghue, E. Golowich, and B. Holstein, *Dynamics of the Standard Model*, Cambridge University Press, Cambridge, 1992.

[29] B. Holstein, in *Hadronic Structure*, edited by J.L. Goity, World Scientific, Singapore, 2001.

[30] V. Bernard, N. Kaiser, and Ulf-G. Meissner, *Phys. Rev. D* **48**, 3062 (1993).

[31] X. Ji and J. Osborne, *J. Phys. G* **27**, 127 (2001); hep-ph/9905410; X. Ji, C.-W. Kao, and J. Osborne, *Phys. Lett. B* **472**, 1-4 (2000); hep-ph/9910256.

[32] C. Ciofi degli Atti and S. Scopetta, *Phys. Rev. C* **48**, 968-972 (1993).

[33] C. Ciofi degli Atti and S. Scopetta, *Phys. Lett. B* **404**, 223-229 (1997).

[34] R.G. Sachs, *Nuclear Theory*, Addison-Wesley, Cambridge, Massachusetts, 1953.

[35] G. Derrick and J.M. Blatt, *Nucl. Phys.* **8**, 310-324 (1958).

[36] J.L. Friar, B.F. Gibson, G.L. Payne, A.M. Bernstein, and T.E. Chupp, *Phys. Rev. C* **42**, 2310 (1990).

[37] I.R. Afnan and N.D. Birrell, *Phys. Rev. C* **16**, 823 (1977).

[38] L.D. Faddeev, ZhETF **39** (1960); (JETP (Sov. Phys.) **12**, 1014 (1961)).

[39] T.A. Osborn, *SLAC Report No. 79*; Ph.D. Thesis, Stanford (1968); http://www.slac.stanford.edu/pubs/slacreports/slac-r-079.html.

[40] R.A. Malfliet and J.A. Tjon, *Nucl. Phys.* **A127**, 161-168 (1969).

[41] B. Blankleider and R.M. Woloshyn, *Phys. Rev. C* **29**, 538 (1984).

[42] R.V. Reid, *Ann. Phys.*, **50**, 411 (1968).

[43] R. Firestone *et al.*, *Table of Isotopes*, 8th Ed., John Wiley, New York (1996).

[44] R.-W. Schultze and P.U. Sauer, *Phys. Rev. C* **48**, 38 (1993).

[45] V. Burkert and Z. Li, *Phys. Rev. D* **47**, 46 (1993); V. Burkert and B.L. Ioffe, *Phys. Lett. B* **296**, 223 (1992).

[46] J. Ahrens *et al.* (GDH and A2 Collaborations), *Phys. Rev. Lett.* **87**, 022003-1 (2001).

[47] N. Bianchi and T. Thomas, *Phys. Lett. B* **450**, 439 (1999).

[48] O. Hanstein *et al.*, *Nucl. Phys.* **A632**, 561 (1998).

[49] R.A. Arndt *et al.*, *Phys. Rev. C* **53**, 430 (1996).

[50] J. Alcorn *et al.* (The Jefferson Lab Hall A Collaboration), *Basic Instrumentation for Hall A at Jefferson Lab*, 2003, submitted to Nucl. Instr. and Meth.

[51] Z.-E. Meziani, G. Cates, and J.-P. Chen, *Measurement of the Neutron (^{3}He) Spin Structure Function at Low Q^2; a Connection between the Bjorken and Drell-Hearn-Gerasimov Sum Rules*, Jefferson Lab PR-94-010 Proposal (1994); http://www.jlab.org/e94010/.

[52] J.D. Jackson, *Classical Electrodynamics*, 2nd Ed., John Wiley & Sons, New York, 1975.

[53] F. Xiong, *E94-010 Technical Note #5*, 1998.

[54] C.K. Sinclair, *TJNAF-TN-96-032*, 1996.

[55] C.K. Sinclair, *TJNAF-TN-97-021*, 1997.

[56] The Electron Gun Group, http://www.jlab.org/accel/inj_group/

[57] J.S. Price *et al.*, *5 MeV Mott Polarimeter for Rapid Precise Electron Beam Measurements*, Jefferson Lab Technical Report JLAB-ACC-96-22, 1996; http://www.jlab.org/div_dept/admin/publications/.

[58] J.S. Price *et al.*, *5 MeV Mott Polarimeter Development at Jefferson Lab*, Jefferson Lab Technical Report JLAB-ACC-97-27, 1997; http://www.jlab.org/div_dept/admin/publications/.

[59] M. Steigerwald, *MeV Mott Polarimetry at Jefferson Lab*, 2000; http://www.jlab.org/accel/inj_group/mott/mott.pdf.

[60] J. Kessler, *Polarized Electrons*, Second Edition, Springer-Verlag, Berlin, 1985.

[61] N. Sherman, *Phys. Rev.* **103**, 1601 (1956).

[62] J.W. Motz, H. Olsen, and H.W. Koch, *Rev. Mod. Phys.* **36**, 881 (1964).

[63] N.F. Mott and H.S. Massey, *The Theory of Atomic Collisions*, Third Edition, Oxford University Press, London, 1965.

[64] H. Überall, *Electron Scattering from Complex Nuclei*, Academic Press, New York, 1971.

[65] P.G. Burke and C.J. Joachain, *Theory of Electron-Atom Collisions*, Plenum Press, New York, 1995.

[66] A. Saha, *Hall A Beam and Polarimeters*;
http://hallaweb.jlab.org/equipment/beam.html.

[67] D. Marchand, *Ph.D. Thesis*, Université Blaise Pascal, 1998.

[68] http://www.jlab.org/˜moller/.

[69] http://hallaweb.jlab.org/equipment/HRS.htm.

[70] The Hall A Collaboration, *ESPACE Manual Version 2.9.0β*, August 12, 2002.

[71] N. Liyanage, http://www.jlab.org/˜nilanga/physics/optimization.ps.

[72] K. Wijesooriya, *Ph.D. Thesis*, The College of William & Mary, 1999 (unpublished).

[73] K.G. Fissum *et al.*, *Nucl. Instr. and Meth. A* **474**, 108 (2001).

[74] *CEBAF Online Data Acquisition*;
http://coda.jlab.org/.

[75] R. Michaels, *Online Codes: DATASPY and DHIST for Hall A Spectrometers*, January 2001;
http://hallaweb.jlab.org/equipment/daq/dplot.html.

[76] KUIP, CERN Program Library Long Writeup I102, Version 2.05;
http://wwwinfo.cern.ch/asdoc/kuip/kuipoverview.html.

[77] PAW, CERN Program Library Long Writeup Q121;
http://wwwinfo.cern.ch/asd/paw/.

[78] T.B. Smith, *Ph.D. Thesis*, University of Michigan, 1998 (unpublished).

[79] D.J. Griffiths, *Introduction to Quantum Mechanics*, Prentice-Hall, Englewood Cliffs, New Jersey, 1995.

[80] J.R. Taylor, C.D. Zafiratos, *Modern Physics for Scientists and Engineers*, Prentice Hall, Englewood Cliffs, New Jersey, 1991.

[81] H.L. Middleton, *Ph.D. Thesis*, Princeton University, 1991 (unpublished).

[82] A. Abragam, *The Principles of Nuclear Magnetism*, Oxford University Press, London, 1961.

[83] B. Cowan, *Nuclear Magnetic Resonance and Relaxation*, Cambridge University Press, Cambridge, 1997.

[84] F. Bloch, *Phys. Rev.* **70**, 460 (1946).

[85] H. Haken and H.C. Wolf, *The Physics of Atoms and Quanta: Introduction to Experiments and Theory*, 5th Ed., Springer-Verlag, Berlin, 1996.

[86] National Institute of Standards and Technology, *The NIST Reference on Constants, Units, and Uncertainty*; http://physics.nist.gov/constants.

[87] D.E. Groom *et al.*, *The European Physical Journal* **C15** 1, (2000).

[88] J.K. Tuli, *Nuclear Wallet Cards*, 6th Ed., Brookhaven National Laboratory, Upton, New York, 2000.

[89] M.V. Romalis, *Ph.D. Thesis*, Princeton University, 1997 (unpublished).

[90] A. Corney, *Atomic and Laser Spectroscopy*, Oxford University Press, 1979.

[91] G.K. Woodgate, *Elementary Atomic Structure*, McGraw-Hill, London, 1970.

[92] G. Breit and I.I. Rabi, *Phys. Rev.* **38**, 2002 (1930).

[93] A.S. Barton *et al.*, *Phys. Rev.* **A49**, 2766 (1994).

[94] N.R. Newbury *et al.*, *Phys. Rev.* **A48**, 558 (1993).

[95] C.P. Poole, Jr., *Electron Spin Resonance: A Comprehensive Treatise on Experimental Techniques*, 2nd Ed., John Wiley & Sons, New York, 1983.

[96] K. Slifer, *E94-010 Technical Note #31: Shower Detector Calibration and Cut Optimization for E94-010*, May 2, 2000, unpublished; http://www.jlab.org/e94010/tech_notes.html.

[97] A. Ketikyan, H. Voskanyan, and B. Wojtsekhowski, *About Shower Detector Software*, September 1997, unpublished; http://www.jlab.org/~armen/sh_web_page/general.html.

[98] W.R. Leo, *Techniques for Nuclear and Particle Physics Experiments*, 2nd Ed., Springer-Verlag, New York, 1994.

[99] U. Fano, *Phys. Rev.* **72**, 26 (1947).

[100] K. Hagiwara *et al.*, *Phys. Rev. D* **66**, 010001 (2002).

[101] K. Slifer, *E94-010 Technical Note #32: Analysis of the Hall A HRS Čerenkov Detectors for E94-010*, July 2000, unpublished; http://www.jlab.org/e94010/tech_notes.html.

[102] M. Iodice *et al.*, *The CO_2 Gas Čerenkov Detectors for the Jefferson Lab Hall A Spectrometers*, Elsevier Preprint (January 1998).

[103] A. Deur, *E94-010 Technical Note #33* (2000), unpublished.

[104] X. Jiang, *Ph.D. Thesis*, University of Massachusetts, Amherst, 1998 (unpublished).

[105] A. Deur, *E94-010 Technical Note #36* (2000), unpublished.

[106] W.H. Press *et al.*, *Numerical Recipes in C*, Cambridge University Press, Cambridge, 1988.

[107] B.P. Roe, *Probability and Statistics in Experimental Physics*, Springer-Verlag, New York, 1992.

[108] F. James, *Reports on Progress in Physics* **43**, 1145-1189 (1980); in: T. Ferbel, *Experimental Techniques in High Energy Physics*, Addison-Wesley, Reading, 1987.

[109] http://wwwinfo.cern.ch/asdoc/cernlib.html.

[110] L.D. Landau, *J. Phys. (USSR)* **8**, 201 (1944); in: L.D. Landau, *Collected Papers*, ed. D. ter Haar (Pergamon Press, Oxford, 1965) p. 417.

[111] G. Cowan, *Statistical Data Analysis*, Clarendon Press, Oxford, 1998.

[112] K.S. Kölbig and B. Schorr, *Comp. Phys. Comm.* **31**, 97-111 (1984).

[113] H.A. Bethe and W. Heitler, *Proc. Roy. Soc. London Ser.* **A146**, 83-112 (1934); in: H.A. Bethe, *Selected Works of Hans A. Bethe: With Commentary*, World Scientific, Singapore, 1997, p. 187.

[114] Y.S. Tsai, *SLAC-PUB-0848*, January 1971.

[115] L.W. Mo and Y.S. Tsai, *Rev. Mod. Phys.* **41**, 205 (1969).

[116] E. Segrè, *Nuclei and Particles*, W.A. Benjamin, Inc., New York, 1964.

[117] J. Schwinger, *Phys. Rev.* **76**, 760 (1949).

[118] F. Xiong, *private communication*, 1999.

[119] C.T. Lynch, Ed., *CRC Handbook of Materials Science*, CRC Press, Inc., Boca Raton, Florida, 1989.

[120] I. Kominis, *private communication*, 2000.

[121] Y.S. Tsai, *Rev. Mod. Phys.* **46**, 815 (1974).

[122] R.M. Sternheimer *et al.*, *Atomic Data and Nuclear Data Tables* **30**, 261-271 (1984).

[123] http://www.physics.nist.gov/cgi-bin/Star/compos.pl.

[124] E.B. Dally, M.G. Croissiaux, and B. Schweitz, *Phys. Rev. C* **2**, 2057 (1970).

[125] S. Stein, W.B. Atwood, E.D. Bloom, R.L.A. Cottrell, H. DeStaebler, C.L. Jordan, H.G. Piel, C.Y. Prescott, R. Siemann, and R.E. Taylor, *Phys. Rev. D* **12**, 1884 (1975).

[126] G. Arfken, *Mathematical Methods for Physicists*, Third Edition, Academic Press, Inc., San Diego (1985).

[127] I. Kominis, *Ph.D. Thesis*, Princeton University, (2001), unpublished.

[128] J.S. McCarthy, I. Sick, R.R. Whitney, and M.R. Yearian, *Phys. Rev. Lett.* **25**, 884 (1970).

[129] J.S. McCarthy, I. Sick, and R.R. Whitney, *Phys. Rev. C* **15**, 1396 (1977).

[130] A. Deur, *private communication* (2002).

[131] I. Akushevich, A. Ilyichev, N. Shumeiko, A. Soroko, and A. Tolkachev, *Comp. Phys. Comm.* **104**, 201-244 (1997).

[132] A. Deur, *Ph.D. Thesis*, Université Blaise Pascal (2000), unpublished.

[133] R.G. Roberts, *The Structure of the Proton*, Cambridge University Press, Cambridge (1990).

[134] F.E. Close, *An Introduction to Quarks and Partons*, Academic Press, London (1979).

[135] S. Boffi, C. Giusti, F.D. Pacati, and M. Radici, *Electromagnetic Response of Atomic Nuclei*, Clarendon Press, Oxford (1996).

[136] C.G. Callan and D.J. Gross, *Phys. Rev. Lett.* **22**, 156 (1969).

[137] S. Choi, *private communication*, 2002.

[138] K. Abe *et al.* (The E143 Collaboration), *SLAC-PUB-7753* (1998).

[139] M. Anselmino, B.L. Ioffe, and E. Leader, *Sov. J. Nucl. Phys.* **49**, 136 (1989).

[140] K. Ackerstaff *et al.* (The HERMES Collaboration), *Phys. Lett. B* **444**, 531 (1998).

[141] V. Bernard, T.R. Hemmert, and Ulf.-G. Meißner, *hep-ph/0203167*.

[142] J.-P. Chen, A. Deur, and F. Garibaldi, *Jefferson Laboratory Proposal PR-97-010*.

VITA

Pibero Djawotho

Born in Aungba, Orientale, Democratic Republic of Congo, September 18, 1970. Graduated from Atlantic City High School in Atlantic City, New Jersey, May 1988, B.S., The Richard Stockton College of New Jersey, May 1996.

In September 1996, the author started graduate studies at the College of William and Mary in the Department of Physics.